The geometry and kinematics of baryonic feedback

Thesis by

Nikolaus Zen Prusinski

In Partial Fulfillment of the Requirements for the
Degree of
Doctor of Philosophy

CALIFORNIA INSTITUTE OF TECHNOLOGY
Pasadena, California

2026
Defended May 13, 2026

Nikolaus Zen Prusinski
ORCID: 0000-0001-5847-7934

ACKNOWLEDGEMENTS

This thesis is the written realization of an aspiration that started many years ago, well before I had a remotely clear concept of what it means to be an astrophysicist. Growing up, I was fortunate to have excellent teachers and role models who encouraged me to think critically and pursue my wide array of interests. Innumerable individuals have donated their time, knowledge, experience, kindness, and resources toward my education and humanity, and for their largesse I am extremely grateful. It would be nearly impossible to thank them all, and in many cases words would not do justice; what follows will be constrained to the past ~decade and I humbly apologize in advance to anyone I may miss.

On the academic front, I owe a great deal to my advisor Chuck Steidel, who has supported me throughout the duration of my PhD and has shown through example what it means to be a good scientist. Thank you Chuck for your availability; your insight, especially when we delved into the minutiae; and your patience as I learned about and started contributing to the high-z universe. Thank you for allowing me the freedom to branch out and explore new research areas as opportunities presented themselves, while always having KBSS as the strong backbone of my thesis.

Whereas Chuck made me truly appreciate high S/N spectra, Chris Martin gave me the opportunity to work with them. Thank you Chris for being my co-advisor and opening the door to the instrumentation side of astronomy. KCWI red channel AIT, commissioning, and the experiences stemming from that success are among the highlights of my PhD. I am tremendously grateful for your support and encouragement during these past few years.

My thesis committee: Chuck, Chris, Phil Hopkins, Lynne Hillenbrand, and Dimitri Mawet deserves acknowledgment for providing advice and guidance throughout this PhD. I am in particular indebted to Lynne, for providing timely direction and insight at critical stages throughout this endeavor. I also thank Shri Kulkarni for his advice and support at various points during my time at Caltech.

It is impossible to talk about KCWI without mentioning Matt Matuszewski and Don Neill who were critical in developing my expertise on both the hardware and software side of the instrument. Their mentorship and intuition have made me the spectroscopist I am today. I thank Rosalie McGurk and Max Brodheim (not to mention Max Davis and the entire Keck Observatory staff) for their hospitality and support when I spent the better part of a summer in Hawaii as a visiting scholar working on KCWI.

I thank the members of Chuck's group over the years — Yuguang Chen, Zhihui Li, Sofia Gallego, Zhuyun Zhuang, Evan Nuñez-Cravin, Yuanze Ding, Charis Hall, Isaac Cheng, Mandy Chen, Ricky Mendez — who are some of the most thoughtful individuals I know working on (primarily high-z) galaxy evolution and who I am honored to call my friends. It has been a pleasure to get to know some of Chuck's former students and collaborators over the years including (but not limited to) Allison Strom, Gwen Rudie, Ryan Trainor, Yuichi Matsuda, Hideki Umehata, and Sebastiano Cantalupo who have been consistently kind, generous, and welcoming. The story has been the same in Chris' group and those affiliated with it. I thank Zeren Lin, Xihan Deng, Vincent Picouet, Marty Crabill, Hector Rodriguez, Ray Zarzaca, Jason Fucik, and especially Drew Miles.

Dawn Erb deserves a special thank you for introducing me to galaxy evolution research during my undergraduate at the University of Wisconsin – Milwaukee (UWM). Dawn was extremely patient answering my many questions in the beginning and her methodical approach to research and unwavering support in many forms over my research career to date has been an inspiration. Jean Creighton sparked my curiosity in astronomy at a very young age through her shows at the UWM Manfred Olson Planetarium and has played a pivotal role ever since then in shaping my trajectory in the field. Thank you Jean for your sage advice over the years. David Kaplan, John Friedman, Aaron Geller, Christopher Berry, and Nancy Aggarwal also deserve a mountain of appreciation for their time, generosity, and expertise during my undergraduate.

It has been an honor and privilege to call the Caltech astronomy department home these past six years and to have the opportunity to explore our cosmos with those at the forefront of the astronomical enterprise. Outreach with Cameron Hummels has been a blast and our discussions on galaxies especially apropos these thesis projects have always been very helpful. Gita Patel, Judy McClain, Anthony, Brick Hale, and Stephanie Cha-Ramos are the real individuals keeping Cahill in business; thank you for everything you do. Similarly Patrick Shopbell, Anu Mahabal, and James Lansdown have kept me digitally sane (and never pixel-limited!) with all of their IT support over the years.

The true highlight of being at Caltech has always been the people, and I have been privileged to know so many that are not only highly accomplished scientists in their own right with accolades that could span pages, but are simultaneously wonderful, kind, and compassionate human beings that make me cherish the fun times we have together. I am first and foremost indebted to my fellow astronomy graduate students, especially those in my cohort. I cannot think of a better group of people to spend these past six years with. Tony, Adolfo, Jean, Kaustav, Yashvi, Jerry, Peter, Yash, Ryan, Max, Kishalay, and Kaew all deserve special shout-outs.

The orchestra and the other musical ensembles here at Caltech have been a source of much joy these past six years. I have Glenn, Maia, and Barb to thank for making such creative outlets possible and in particular André, Kiran, Sarah, Chandler, Carlos, Janice, Warren, and Peter for making them fun. Like orchestra, improv has been a weekly source of respite for the past number of years. I am indebted to Sofia, Sara, and Viraj for inviting me the first time and Brian, Adam, Kari, Eli, Auden, Tal, Max, Chandru, and the rest of the gang for making me not want to leave.

In my first year, by luck of the draw, I got matched with Prat who has been a fantastic roommate for our entire time in grad school and an even better sounding board during many moments of uncertainty. Niyati and Lorenzo are some of the warmest people and best friends one could ask for and I have been lucky to share many fond moments with them over the years. I cannot imagine grad school without Alec, Elisabetta, Jimmy, Martijn, Shivansh, and Vi who have all enriched this experience tremendously in their own way. I am indebted to my parents, Gail and Bob, and my extended family (especially Rachel, Anita, and Alex) for encouraging critical thinking and exploration from a young age. This PhD exists because of their time, support, and guidance during my formative years.

ABSTRACT

This thesis addresses the connection between the physics of galactic-scale baryonic feedback, the morphology and kinematics of gas in the multiphase circumgalactic medium (CGM), and host galaxy properties. Broadly speaking, each of the projects in this thesis attempts (through different datasets and techniques) to quantify how star formation is regulated in galaxies; the relevant observable being the gas and metal distributions in and around galaxies. The geometry and kinematics of interstellar, circumgalactic, and intergalactic gas provide insight into the efficacy and timescales over which galaxy-driven baryonic feedback processes operate.

Chapter 2 features the highest fidelity maps of the average $z \sim 2$ CGM to date using foreground/background galaxy pairs with angular separations $\leq 30''$ in the Keck Baryonic Structure Survey (KBSS). The maps of covering fraction vs. transverse distance and line-of-sight velocity chart the changing gravitational influence the galaxy has over its CGM. Lyα absorption shows a distinct transition near the virial radius of the average foreground galaxy and overall, dark matter halo mass appears to strongly modulate the kinematics, covering fraction, and spatial extent of CGM gas, a significant fraction of which may be unbound.

Chapter 3 presents new results on the spatial distribution and kinematics of nonresonant emission in and around $z \sim 2$ KBSS galaxies observed with the Keck Cosmic Web Imager (KCWI). Nonresonant Si II* emission lines have velocity spreads most consistent with a zero-velocity offset "ISM" component fit to their corresponding resonant Si II absorption lines. Extended Si II* halos are observed for the first time at $z \sim 2$ with a decreasing velocity spread with increasing transverse distance. At large radii, photon conservation appears to hold in that the flux "removed" by resonant absorption approximately equals the flux contributed by nonresonant emission.

Chapter 4 outlines the data reduction procedures needed to produce the integral field spectra used in this thesis. The KCWI data reduction pipeline stages I have improved or still need improvement are discussed. I introduce `KCWIKit`, a toolkit for mosaicking and correcting common systematics in integral field unit datacubes.

Finally, Chapter 5 introduces two ongoing projects considering how supermassive black holes couple to their host galaxies, their CGM, and intergalactic media (IGM) via Mpc-scale jets. Using KCWI, I am investigating the driving mechanisms behind Mpc-scale jets and searching for collisionally-excited emission from the giant jet bow shock. Such a detection would be the first detection of the warm-hot IGM (WHIM) in rest-frame UV emission and would open up a new means of mapping the distribution of metals in the IGM. The latter remains a critical frontier in accounting for the baryons in the universe and understanding the large-scale effects of galactic feedback.

PUBLISHED CONTENT AND CONTRIBUTIONS

Prusinski, N. Z., Steidel, C. C., & Chen, Y. (2026). Nonresonant emission in KBSS-KCWI galaxies at $z \sim 2$. *in prep*.

NZP conducted some of the observations, performed all of the analysis, and wrote the manuscript.

Prusinski, N. Z., Steidel, C. C., & Chen, Y. (2025). Mapping the $z \sim 2$ Circumgalactic Medium with KBSS Galaxy Pairs. *The Astrophysical Journal*, *994*(1), Article 85, 85. https://doi.org/10.3847/1538-4357/ae0921

NZP conducted some of the observations, performed all of the analysis, and wrote the manuscript.

Prusinski, N. Z., & Chen, Y. (2024, April). *KCWIKit: KCWI Post-Processing and Improvements*.

NZP is the lead developer of this toolkit used for correcting systematics in and stacking 3-D data cubes from integral field units.

TABLE OF CONTENTS

LIST OF ILLUSTRATIONS

LIST OF TABLES

Chapter 1

THE CIRCUMGALACTIC MEDIUM AS THE KEY TO UNDERSTANDING BARYONIC FEEDBACK

1.1 Introduction

According to the most recent cosmological estimates, the universe today contains $\simeq$ 70% dark energy, $\simeq$ 25% dark matter, and $\simeq$ 5% baryonic matter (e.g. Planck Collaboration et al., 2020). Dark energy (described by the cosmological constant, Λ) results in expansion on the largest scales ($\gtrsim$ 100 Mpc), counteracted by gravity which works to coalesce cold dark matter (CDM) and baryons. In the current concordance cosmology, Λ–CDM, primordial fluctuations in the (largely uniform) dark matter density field are the "seeds" of large-scale structure in the universe. Overdensities collapse leading to the earliest dark matter halos, which continue to grow via mergers, eventually resulting in the "cosmic web" we observe today. Since most of the mass in the universe is in dark matter, it drives structure formation; the baryons "come along for the ride," generally tracing the dark matter distribution on the largest scales, and eventually fall into the centers of the dark matter halos. The baryons cool, condense, and collapse to form the first stars and galaxies.

While gravity has long been recognized as the primary driver of structure formation in the universe, small-scale baryonic processes, collectively referred to as "feedback", have been shown to dramatically impact the formation and evolution of galaxies and, in turn, the large-scale environment in which they reside (H.-W. Chen & Zahedy, 2024; Tumlinson et al., 2017). Acquiring a detailed understanding of these feedback processes is challenging because they operate on a wide range of length and time scales, often simultaneously, and are expected to interact in a complex, nonlinear fashion (e.g. Hopkins et al., 2012). The principal goal in the field of galaxy evolution is to develop a predictive framework connecting the assembly history of galaxies and their dark matter halos with their stellar populations, gaseous structures, metal content, and black holes at interstellar, circumgalactic, and intergalactic scales over cosmic time.

The balance between feedback and gravitationally-driven processes has direct impacts on star formation, chemical enrichment, and the diffuse gas in a galaxy's circumgalactic medium (CGM). This intrinsically connects studies of feedback to numerous areas in astrophysics. On interstellar scales, feedback affects the efficiency of star and planet formation by regulating how gas cools, loses its angular momentum, and mixes with other gas. By extension, dust formation, supernova diversity, and high-energy transients (e.g. fast radio bursts) are all fundamentally linked to galactic feedback. In cosmology, stellar feedback is invoked to describe the effects of reionization in the early universe and the global matter power spectrum (e.g. Bigwood et al., 2024; Siegel et al., 2025). Given its effect on many subfields, it is no surprise that the *Astro2020* Decadal Survey listed "unveiling the drivers of galaxy growth and cosmic ecosystems" as a priority area in the current decade.

In the past two decades, considerable progress has been made connecting the cycling of baryons in and out of galaxies with their underlying dark matter halos. The current picture places galaxies at the center of a "cosmic ecosystem" where pristine gas flows in from the cosmic web, sustaining star formation. Various forms of galactic feedback such as supernovae (e.g. Leitherer et al., 1999; Veilleux et al., 2005), radiation pressure from stars on acting on gas (Murray et al., 2011), cosmic ray pressure (e.g. Hopkins, 2025), and active galactic nuclei (AGN; Faucher-Giguère and Quataert 2012; Silk and Rees 1998) in the most massive galaxies can expel metal-enriched gas to circumgalactic and potentially intergalactic scales. The CGM contains the majority of gas associated with galaxies (Peeples et al., 2014; Shull et al., 2012) and, like the galactic winds that inject mass, energy, and momentum into it, has been shown to be metal-rich (R. Dutta et al., 2020, 2021; Péroux & Howk, 2020) and multiphase (e.g. Byrohl & Nelson, 2023; Faucher-Giguère & Oh, 2023). The CGM acts as a nexus between the interstellar medium (ISM) of a galaxy and the diffuse intergalactic medium (IGM), making it an excellent laboratory for studying the effects of baryonic feedback.

Constraints on baryonic feedback in the CGM come from several cosmic epochs: many in the low-redshift universe (e.g. H.-W. Chen et al. 2020a; Werk et al. 2012), and some, with the advent of *JWST*, out to $z \sim 6$ (e.g. Bordoloi, Simcoe, Matthee, Kashino, Mackenzie, Lilly, Eilers, Liu, DePalma, Yue, and P. Naidu 2024a). The so-called "cosmic noon" (i.e. $z \sim 2$) is both scientifically and observationally compelling. Perhaps most significant is the fact that at $z \sim 2 - 3$, the global star formation rate surface density, baryonic accretion rate, and supermassive black hole (SMBH) growth all reached their peak (e.g. Behroozi et al. 2013; Faucher-Giguère et al. 2011; Madau and Dickinson 2014; Richards et al. 2006) meaning baryonic feedback is likely to have its most significant impact on galaxies and their environment during this epoch. Indeed, extended H I and metallic halos (in absorption and emission) and large-scale galactic outflows are ubiquitous in $z \sim 2$ star-forming galaxies (Y. Chen et al., 2020, 2021; Prusinski et al., 2025; Rudie et al., 2019; Steidel et al., 2010). At the same time, this redshift range is observationally conducive since many of the rest-frame far-UV and optical diagnostics fall into wavelength ranges with high atmospheric throughput and can therefore be observed with ground-based telescopes (see e.g. Steidel et al. 2014).

1.2 CGM Observations

The concept of a CGM was first proposed by Lyman Spitzer (Bahcall & Spitzer, 1969; Spitzer, 1956) who hypothesized that the Milky Way had a "galactic corona" with temperature $T \sim 10^6$ K and density $n_e \sim 10^{-4}$ cm^{-2} that would explain the extended Na I in the Milky Way halo (Münch & Zirin, 1961). Ensuing observations in the coming years would confirm the general validity of these values. Today, the CGM can be thought of as an extended gaseous structure that is effectively the galaxy's "sphere of influence." Gas has been shown to exist at densities $n_e \sim 10^{-5} - 10^{-1}$ cm^{-3} and temperatures $T \sim 10^4 - 10^7$ K. The diffuse nature of the CGM makes it difficult to observe and the wide range of scales involved makes it hard to simulate (e.g. Hopkins et al., 2014).

CGM observations span the wavelength range including the radio (Connor & Ravi, 2021; Faber et al., 2024; Ravi, 2019), far-IR (Le Fèvre et al., 2020), IR (Freeman et al., 2019), and X-ray (Anderson et al., 2015; J.-T. Li et al., 2017) but the bulk are in the UV and optical where there are numerous transitions from astrophysically abundant ions that are sensitive to the appropriate ranges of temperature and density (e.g. Lyα, C IV, O VI). The canonical way of observing the CGM is to use a relatively bright background source (e.g. a QSO) whose sightline passes through the CGM of a foreground galaxy that imparts absorption on the background spectrum at $z_{\rm fg}$. Since the QSO is bright ($V \sim 16 - 17$ for KBSS QSOs), high S/N and high resolution spectra are attainable.

Thanks to many dedicated observational campaigns with multi-object spectrometers (MOS) and integral field units (IFUs), our knowledge of the CGM has increased significantly in recent years. One approach is to identify absorption systems in background sightlines and search for foreground galaxies at that redshift that may be the cause of such absorption (Bergeron & Boissé, 1991). While it is fairly straightforward to identify absorption systems, the connection between that absorption and a particular galaxy is always uncertain. A less biased (galaxy-centered) approach is to reverse the process i.e. to start with a sample of well-characterized galaxies near a QSO sightline and search for the corresponding absorption system in the QSO spectrum (e.g. Adelberger et al., 2003; H.-W. Chen et al., 2020b; Crighton et al., 2011b; Lofthouse et al., 2020; Rudie et al., 2012; Turner et al., 2014; Werk et al., 2012).

1.3 This Thesis

While there exists a general understanding of how baryonic feedback shapes galaxies, the details remain largely unconstrained. Fundamentally, *how is star formation regulated in galaxies?* Galactic-scale outflows and AGN are the primary agents modulating the efficiency of star formation in low- and high-mass galaxies, respectively. However, a detailed understanding of both feedback mechanisms and their efficacy requires knowing *the geometry of the gas and metal distributions in and around galaxies and the timescales over which such processes operate.* The projects in this thesis make significant headway in these areas using several novel techniques.

Chapter 2 takes a relatively unexplored tack in CGM absorption line studies using background *galaxies* instead of background QSOs. The limit of using background QSOs is that the line of sight through the foreground galaxy's CGM is only as wide as the QSO accretion disk (diameter $\simeq 1$ pc). Individual QSOs therefore sample the CGM on ~pc scales making their measurements highly stochastic. An alternative to using background QSOs is to use background *galaxies* as the sightlines through the CGM of a foreground galaxy. Galaxies are considerably more numerous than QSOs ($50-100\times$ in the KBSS) which allows for finer spatial sampling at the cost of lower spectral resolution and lower S/N spectra since they are intrinsically fainter. Spectra of galaxies also average over several kpc (the half-light radius of the average $z \sim 2$ galaxy) and thus converge to the true CGM gas distribution faster than QSO sightlines (Rubin, Diamond-Stanic, Coil, Crighton, & Moustakas, 2018; Rubin, Diamond-Stanic, Coil, Crighton, & Stewart, 2018; Steidel et al., 2010).

With the advent of IFUs like Keck/KCWI and VLT/MUSE, the current observational frontier is to study the CGM in *emission*. Observations to date have primarily focused on Lyα halos around high-z star-forming galaxies, since it is by far the brightest spectral line (Y. Chen et al., 2021; Wisotzki et al., 2016, 2018). Nonresonant transitions (e.g. Si II*, C II*) offer a new means of understanding optically thick regions of the CGM, but studies of these transitions have been more rare owing to the lower S/N (in general) of these transitions. In Chapter 3, I make concrete advancements in our understanding of Si II* halos using the largest sample to date of $z \sim 2$ nonresonantly emitting star-forming galaxies.

Chapters 2 and 3 of this thesis make heavy use of galaxies in the Keck Baryonic Structure Survey (KBSS; e.g. Y. Chen et al. 2020; Rudie et al. 2012; Steidel et al. 2014; Strom et al. 2017; R. F. Trainor et al. 2015), in particular those observed with the Keck Cosmic Web Imager (KCWI; Y. Chen et al. 2021). KBSS comprises 15 survey fields with extensive multiwavelength coverage (rest-UV to radio wavelengths), each subtending $\sim 5' \times 5'$ on the sky. Every survey field contains at least one hyperluminous quasar (HLQSO); HIRES spectra of those HLQSOs have been used to chart foreground circumgalactic gas at $z \sim 2$ (Rudie et al., 2012, 2019). Galaxies in KBSS were largely selected photometrically using the Lyman break technique (i.e. Lyman break galaxies [LBGs]; Adelberger et al. 2004; Steidel et al. 2003, 2004; Strom et al. 2017), with a smaller subset discovered through narrow-band photometry (R. Trainor & Steidel, 2013; R. F. Trainor & Steidel, 2012; R. F. Trainor et al., 2015). Over 3500 galaxies have been spectroscopically identified to date.

The remaining chapters in this thesis address the data reduction that makes these results possible (Chapter 4), two ongoing projects investigating the origin, effects, and usefulness of Mpc-scale jets in probing AGN feedback (Chapter 5), and I conclude in Chapter 6 with the broader context in which these results sit.

Where appropriate, I adopt a flat Λ-CDM cosmology with $H_0 = 70$ km s^{-1}

Mpc^{-1}, $\Omega_m = 0.3$, $\Omega_\Lambda = 0.7$. Unless otherwise stated, distances are measured in physical units. For Chapters 2 and 3 of this thesis relying on KBSS data (KBSS average redshift $\langle z \rangle = 2.3$), 1″ corresponds to 8.2 (physical) kpc. I use $D_{\rm tran}$ to represent the projected distance along the LOS to a galaxy or sightline.

Chapter 2

MAPPING THE $z \sim 2$ CIRCUMGALACTIC MEDIUM WITH KBSS GALAXY PAIRS

Prusinski, N. Z., Steidel, C. C., & Chen, Y. (2025). Mapping the $z \sim 2$ Circumgalactic Medium with KBSS Galaxy Pairs. *The Astrophysical Journal*, *994*(1), Article 85, 85. https://doi.org/10.3847/1538-4357/ae0921

Nikolaus Z. Prusinski: Cahill Center for Astronomy and Astrophysics, California Institute of Technology, MC 249-17, Pasadena, CA 91125, USA; nik@astro.caltech.edu

Charles C. Steidel: Cahill Center for Astronomy and Astrophysics, California Institute of Technology, MC 249-17, Pasadena, CA 91125, USA; ccs@astro.caltech.edu

Yuguang Chen: Department of Physics, The Chinese University of Hong Kong, Shatin, N.T., Hong Kong SAR, China; yuguangchen@cuhk.edu.hk

ABSTRACT

We present new results on the spatial structure and kinematics of the circumgalactic medium (CGM) of $z \sim 2$ star-forming galaxies drawn from the Keck Baryonic Structure Survey, using Lyα and metallic ion absorption recorded in spectra of background galaxies whose sightlines are projected within $\theta \sim 30''$ (physical distances $D_{\rm tran} \lesssim 250$ kpc) of the foreground galaxy. The sample of 1033 foreground galaxies ($\langle z_{\rm fg} \rangle = 2.03 \pm 0.36$; $8 \lesssim \log(M_*/M_\odot) \lesssim 11$) is probed by the spectra of 736 background galaxies obtained using Keck/KCWI ($R \sim 1800$) and Keck/LRIS ($R \sim 1200$). Using the galaxy pair ensemble, we present measurements of absorption strength (W_λ) and line-of-sight velocity dispersion (σ) as a function of $D_{\rm tran}$, which together with "down-the-barrel" spectra of the foreground galaxies provide unprecedented maps of neutral hydrogen and ionized metals throughout the CGM of star-forming galaxies at "cosmic noon". A 2D map of Lyα absorption depth (vs. line-of-sight velocity and $D_{\rm tran}$) for the full ensemble shows a distinct transition near $D_{\rm tran} \sim 80$ kpc (close to the virial radius of the average foreground galaxy) where the line-of-sight velocity dispersion reaches a minimum and beyond which the Lyα absorption depth flattens. Splitting the sample into subsets based on properties of the foreground galaxies, we find a strong and monotonic correlation of both W_λ(C IV) and σ(C IV) with stellar mass (M_*) at all $D_{\rm tran}$ including DTB (i.e., $D_{\rm tran} \sim 0-250$ kpc). Taken together, our results suggest that the kinematics, covering fraction, and spatial extent of CGM gas traced by Lyα and (especially) C IV are modulated primarily by halo mass, and that a significant fraction of the CGM gas may be unbound.

2.1 Introduction

Galaxies evolve via the cycling of baryons between gas reservoirs in the intergalactic medium (IGM) and their own interstellar media (ISM). The circumgalactic medium (CGM) represents the sphere of influence for a galaxy and acts as a boundary layer where one can directly observe the exchange of baryons to and from the IGM. Despite its importance in galaxy formation, the CGM and the underlying processes driving its evolution with time remain largely unconstrained (Tumlinson et al., 2017).

Observational and theoretical work has established that the CGM of star-forming galaxies comprises metal-enriched gas (e.g., R. Dutta et al., 2020, 2021; Peeples et al., 2014; Péroux & Howk, 2020) in a clumpy morphology (e.g., Erb et al., 2023; Z. Li et al., 2024; Rubin, Diamond-Stanic, Coil, Crighton, & Stewart, 2018; Rudie et al., 2019) across a range of temperatures, densities, and ionization states (e.g., Byrohl & Nelson, 2023; Faucher-Giguère & Oh, 2023). The multiphase nature of the CGM is the result of a combination of baryonic feedback processes i.a., supernova ejecta (Leitherer et al., 1999; Veilleux et al., 2005), active galactic nuclei (Faucher-Giguère & Quataert, 2012), and radiation pressure (Murray et al., 2011) from massive stars all acting in concert to shape the gas distribution and physical conditions. Numerous studies across a range of redshifts have observed outflows which inject energy and momentum into the ISM and CGM of their host galaxy (e.g., Erb et al., 2012; Martin et al., 2012; Prusinski et al., 2021; Shapley et al., 2003; Steidel et al., 2010; Weiner et al., 2009); signatures of inflowing material are much less common (e.g., Bouché et al., 2013; Kereš et al., 2005; Rubin et al., 2012), but the connections between such baryonic flows, the underlying CGM gas distribution, and the host galaxy properties remain uncertain.

A natural epoch in which to study the CGM around galaxies is at $z \sim 2-3$ where the global star formation rate, baryonic accretion rate, and supermassive black hole growth all reached their peak (e.g., Behroozi et al., 2013; Faucher-Giguère et al., 2011; Madau & Dickinson, 2014; Richards et al., 2006). At these redshifts, many of the rest-frame far-UV and optical diagnostics fall into wavelength windows with high atmospheric transmission and can therefore be observed using ground-based telescopes (see e.g., Steidel et al., 2014). Indeed, galaxies in this redshift range show prominent outflows, extended H I halos in both emission and absorption, and substantial metal absorption in their CGM (Bouche et al., 2007; Y. Chen et al., 2021; Leclercq et al., 2020; Rudie et al., 2012; Steidel et al., 2010, 2011; Weldon et al., 2022).

Prior to the early 1990s, the connection between diffuse, metal-enriched gas and galaxies was based largely on the statistical incidence of various classes of intervening absorption systems in spectroscopic surveys of QSOs – the characteristic "size" of extended gas in galaxy halos was derived from a combination of the observed incidence per unit redshift path length of absorption systems (e.g. Mg II, C IV, damped Lyα) and the space density of galaxies with which the gas was assumed to be bound, yielding "predicted" halo sizes of $R_{\rm gal} \simeq 20 - 100$ pkpc, depending on the sensitivity of the QSO absorption system samples, the tracer ion, and the assumed scaling relation between galaxy luminosity and galaxy gaseous cross-section. More direct association of QSO absorption systems and intervening galaxies began at low redshift: deep CCD images of QSO sightlines with known $z \simeq 0.2 - 0.5$ Mg II absorption systems were used to identify candidate absorbing galaxies within several arcsec of the QSO, followed by spectroscopic observations of the relatively faint ($R \gtrsim 20$) galaxies to confirm their redshifts (Bergeron & Boissé, 1991). The initial success in identifying $\simeq L^*$ galaxies within $\lesssim 50$ kpc of the QSO sightline appeared to support the general expectations that had been based on simple statistical arguments.

However, the small samples of identified absorbing galaxies, in addition to being observationally expensive, were subject to potential observational selection biases – e.g., one cannot be certain that the galaxy identified is the one responsible for the absorption system, or simply the most easily-observed galaxy at the same redshift near the QSO sightline. A less biased means of establishing the connection between galaxies and absorbers would be to first observe galaxies near QSO sightlines, where each would have known luminosity, stellar mass, SFR, etc., as well as separation from the QSO sightline $D_{\rm tran}$, and subsequently look for absorption signatures (or sensitive limits) in the QSO spectrum for each (e.g. Adelberger et al., 2003; H.-W. Chen et al., 2020b; Crighton et al., 2011a; Lofthouse et al., 2020; Rudie et al., 2012; Turner et al., 2014; Werk et al., 2012). Such a "galaxy-centered" approach – where galaxy samples are observed in fields deliberately chosen to have one or more bright background sources (usually QSOs) that can provide high-quality measurements of diffuse gas over the relevant range of redshift – has become more practical on large telescopes equipped with efficient multi-object spectrographs (MOS) or integral field units (IFUs).

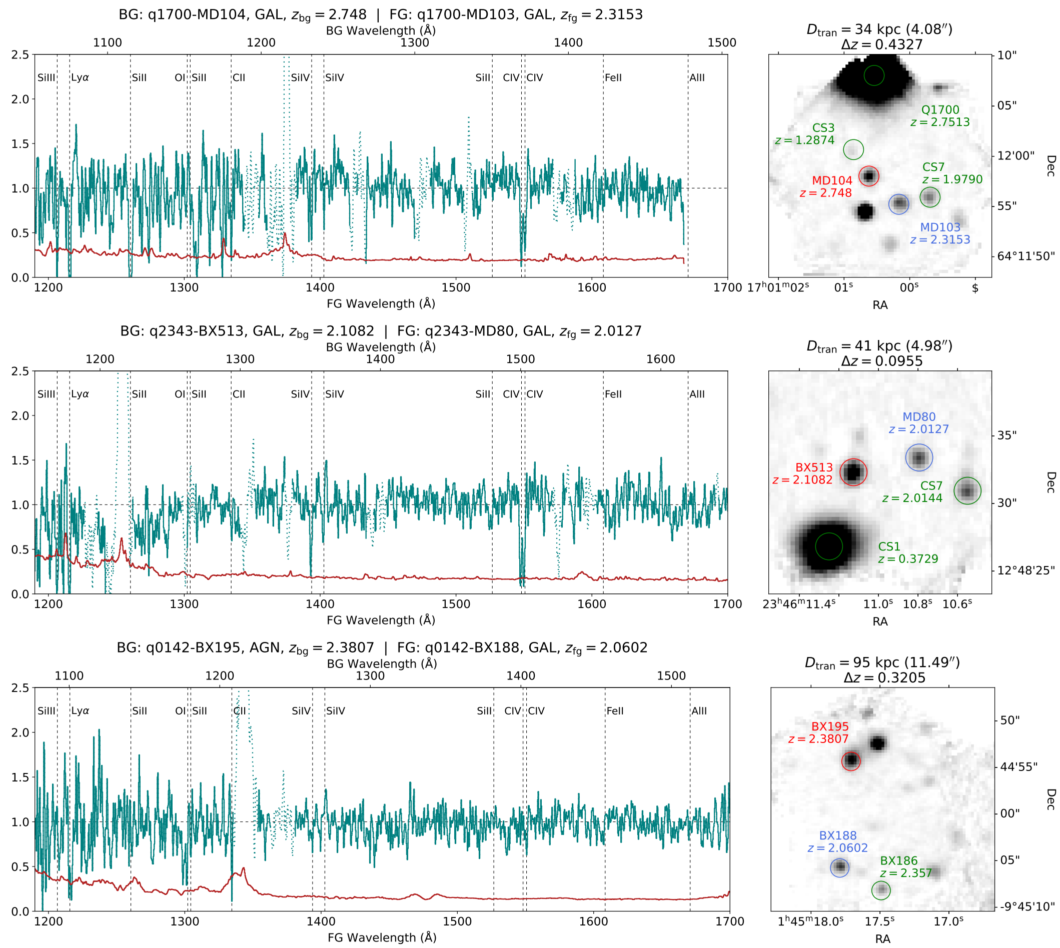

Figure 2.1: Example KCWI background galaxy spectra, normalized and shifted to the rest frame of the foreground galaxy of the pair, from the KBSS-KCWI sample. The righthand images show the white light (3530 – 5530 Å) image from the relevant KCWI pointing, where the background galaxy is labeled in red and the foreground galaxy in blue; green labels indicate other galaxies with spectroscopic identifications within the field of view. Spectral features at the redshift of the FG in each pair are indicated with vertical dashed lines and labels. The location of the same set of features at the BG redshift have been highlighted with a dotted line style. The three cases have $D_{tran} \simeq 34$, 41, and 95 kpc, respectively.

An alternative to using background QSOs is to use unrelated foreground-background galaxy pairs, which are 50–100 times more numerous within the Keck Baryonic Structure Survey (KBSS) than QSO-galaxy sightlines (e.g. Adelberger et al. 2005; Y. Chen et al. 2020; Steidel et al. 2010; see also Bordoloi et al. 2011; Méndez-Hernández et al. 2022; Rubin, Diamond-Stanic, Coil, Crighton, and Moustakas 2018; Rubin, Diamond-Stanic, Coil, Crighton, and Stewart 2018). The CGM of a particular foreground galaxy (at $z_{\rm fg}$) can be probed using spectroscopy of background galaxies ($z_{\rm bg} > z_{\rm fg}$), each of which forms a sightline through the foreground CGM. The use of faint galaxies as background sources, while individually of much lower S/N and typically of significantly lower spectral resolution compared to a QSO spectrum, has additional advantages other than the larger number of foregound-background pairs that complement QSO-based measurements. As emphasized by Steidel et al. (2010), using background galaxies is equivalent to averaging over a beam with a diameter of several kpc passing through the CGM of the foreground galaxy (e.g. Afruni et al., 2023; Rubin, Diamond-Stanic, Coil, Crighton, & Stewart, 2018), whereas the projected beam of a background QSO sightline is ~ 1 pc; this means that, in principle, spectra of an ensemble of resolved background sources converge more quickly to a spatially averaged absorption strength and representative kinematics of gas associated with a foreground galaxy, in a statistical sense – albeit without resolving the individual velocity components necessary for measuring accurate column densities within a foreground galaxy's CGM. An ensemble of foreground/background galaxy pairs is thus highly complementary to surveys of galaxies near the lines of sight to bright QSOs. Three representative examples of foreground/background galaxy pairs are shown in Figure 2.1, in order to illustrate the technique. Note that the projected distance ($D_{\rm tran}$) for the Q0142-BX195-BX188 pair is $\simeq 2-3$ times larger that of the pairs in the top two panels and has comparatively weaker absorption features at the redshift of the foreground galaxy. An ensemble of such pairs can be used to characterize the CGM absorption as a function of both $D_{\rm tran}$ and with respect to the properties of the foreground galaxies.

Galaxy foreground-background close angular pairs drawn from what would become the KBSS survey were used by both Adelberger et al. (2005) and Steidel et al. (2010); the latter study constructed a sample of 512 galaxy pairs with angular separations $\theta \leq 15''$ from a sample of $z \sim 2-3$ star forming galaxies. The galaxy pairs were subdivided into three composite spectra ($\langle D_{\rm tran} \rangle \in [31, 63, 103]$ kpc) to make a low resolution map of absorption as a function of $D_{\rm tran}$ (their Figure 21). They used the measurements of absorption line equivalent widths (W_λ) versus $D_{\rm tran}$, combined with the stack of "down the barrel" (DTB; $D_{\rm tran} = 0$ kpc) spectra of the foreground galaxies in each angular pair, to model the velocity field and galactocentric radial distribution of absorbing gas in the "mean" CGM surrounding galaxies at $\langle z \rangle = 2.2$. They found that all of the observed metallic species were observable to $D_{\rm tran} \simeq 70 - 100$ kpc, at which point the equivalent widths fell below the detection limit of $W_\lambda \simeq 0.1$ Å. Excess Lyα absorption remained detectable to at least $D_{\rm tran} \sim 250$ kpc, as expected given the earlier results using background QSOs to probe similar galaxies in the same fields (Adelberger et al., 2003, 2005).

Y. Chen et al. (2020) extended the galaxy pair technique by incorporating a larger sample of galaxy spectra ($N \simeq 3000$ with $1.7 \lesssim z \lesssim 3.4$), with an increased range of pair separations, drawn from the KBSS survey regions. The authors assembled more than 200,000 foreground/background galaxy pairs with angular separations $\Delta\theta \simeq 3 - 500''$ ($20 \lesssim D_{\rm tran}/{\rm kpc} \lesssim 4000$) and produced maps of Lyα absorption strength as a function of line of sight velocity (with respect to the foreground galaxy systemic redshifts) $v_{\rm LOS}$ and $D_{\rm tran}$. They found that, if expressed as a single power law, $W_\lambda({\rm Ly}\alpha) \propto D_{\rm tran}^{-0.4}$ over the full range of impact parameters, in agreement with Steidel et al. (2010). The number of galaxy pairs sampling separations $D_{\rm tran} \leq 100$ kpc – i.e., the range over which metal lines had been detected by Steidel et al. (2010) – was not significantly larger, so only the distribution and kinematics of Lyα were analyzed.

In the present work, our goal has been to construct an ensemble of foreground/background galaxy pairs that provides improved sampling of gas within $D_{\rm tran} \leq 250$ kpc, the approximate scale of the CGM surrounding individual $L^*_{\rm uv}$ galaxies at $z \simeq 2 - 3$ established by previous work using KBSS QSO sightlines. We are also interested in improving the constraints on CGM gas-phase kinematics (both H I and metals) and its relation to the properties of the foreground galaxies; to this end, from Y. Chen et al. (2020) we include only the subset ($\sim 30\%$) of background galaxy spectra observed with the higher spectral resolving power configuration of LRIS-B ($\langle R \rangle \sim 1300$; see Appendix B of Y. Chen et al. 2020). The most significant improvement – the one that has motivated our revisiting the use of close angular pairs of galaxies – comes from incorporating deep IFU pointings using the Keck Cosmic Web Imager (KCWI; Morrissey et al. 2018). The KCWI data set

(KBSS-KCWI; see Y. Chen et al. 2021) consists of IFU observations of many contiguous $\sim 20''$ diameter ($\simeq 170$ kpc at $z \sim 2$) regions within the KBSS survey fields. The KBSS-KCWI subsample provides deep ($\gtrsim 5$ hour total integrations per pointing) spectra with resolving power $\langle R \rangle \simeq 1800$ of a large number of galaxy angular pairs with projected separations $\leq 20''$, including previously-known KBSS galaxies as well as fainter galaxies newly-identified from their extracted KCWI spectra. The KCWI pointings are embedded within larger KBSS survey fields, each of which has extensive photometric and spectroscopic ancillary data. All of the galaxy spectra included in the combined LRIS+KCWI sample have resolving power $R \simeq 1500 \pm 300$, such that the C IV $\lambda\lambda 1548, 1550$ doublet is resolved, as are O I $\lambda 1302$ and Si II $\lambda 1304$.

This paper is organized as follows: in Section 3.2, we discuss the observations and data reduction associated with each instrument subsample; Sections 2.3 and 2.4 cover the construction of the galaxy pair sample and stacking of galaxies in bins of $D_{\rm tran}$; Section 2.5 features results from Lyα and metal absorption features in 1-D and 2-D; Section 2.6 presents a semianalytic model that can be used to fit the 1-D composite spectra and the 2-D map of Lyα absorption; Section 2.7 has results from composite spectra binned by inferred foreground galaxy properties; these results are placed in a broader context in Section 3.6; and finally, we summarize our conclusions in Section 2.9. Appendix 2.10 justifies why an explicit redshift cut is not required for our sample; Appendix 2.10 uses pairs generated from HIRES spectra of background QSOs to elucidate the profiles we observe at low resolution; Appendix 2.10 shows how different stacking methods affect the composite spectra; and Appendix 2.10 details how, for galaxy pairs with close angular separations, Lyα emission from the foreground galaxy can modulate the observed background Lyα absorption signal.

Throughout this paper, we adopt the *Planck* 2018 cosmology (Planck Collaboration et al., 2020): a flat ΛCDM model with $H_0 = 67.7$ km s^{-1} Mpc^{-1}, $\Omega_{m,0} = 0.31$, and $\Omega_{\Lambda,0} = 0.69$. In this cosmology, at the median redshift of the sample ($z_{\rm med} = 2.3$), $1''$ corresponds to 8.4 (physical) kpc. We use $D_{\rm tran}$ to represent the projected physical separation between a foreground galaxy and the line of sight to a background object, evaluated at the redshift of the foreground galaxy ($z_{\rm fg}$); we direct the reader to to Figure 23 of Steidel et al.

(2010) for a schematic.

2.2 Observations

KBSS-KCWI

The KBSS-KCWI spectra (Y. Chen et al., 2021, p. 2025) used in this paper comprise 193 galaxies observed in 46 different KCWI pointings, selected to include objects from KBSS. KBSS-KCWI pointings maximize the number of previously identified galaxies in each field, in particular those with data from LRIS-B (Steidel et al., 2004), MOSFIRE (McLean et al., 2012), and *HST* WFC3-IR imaging. Of the 193 targets (excluding QSOs), 7 are optically faint AGN, while the remainder are star-forming galaxies.

KCWI observations were conducted between 2017 September and 2022 June, after which KCWI went offline for red-channel integration. The integral field spectra used in this study were obtained using KCWI's low resolution grating (BL; central wavelength = 4500 Å) and Medium slice resulting in data cubes providing a contiguous $20\farcs4 \times 16\farcs5$ FoV and spectral resolving power $\langle R \rangle \approx 1800$ over the $3530 - 5530$ Å bandpass. Each KBSS-KCWI field was observed for a typical total integration time of five hours, with dithers and/or position angle (PA) rotations between each 20-minute exposure. The final mosaicked data cube for each pointing maps a region with a $20''$ diameter (170 kpc at $\langle z \rangle = 2.3$) with approximately uniform exposure and uniform spatial sampling.

Individual exposures were reduced using a customized version of the IDL KCWI Data Reduction Pipeline (DRP; Neill, Matuszewski, and Martin 2023)[1] described in detail in Y. Chen et al. (2021). Briefly, each twenty minute science frame was converted into a 3D flux and wavelength calibrated, rectified data cube, with the original spatial sampling ($0\farcs3 \times 0\farcs68$ and spectral sampling of 1.0 Å/pixel. All exposures for a given pointing were then combined into a stacked, mosaicked data cube using the `KCWIKit` package (Y. Chen et al., 2021; Prusinski & Chen, 2024). `KCWIKit` reads in a list of cubes to be stacked; a parameter file enumerating e.g. the final stack pixel scale, dimensions, and orientation; and if necessary, a list of pre-alignment cube world coordinate system (WCS) shifts if the header WCS is incorrect or significantly offset from the rest of the stack. The code runs natively in

[1] https://github.com/Keck-DataReductionPipelines/KcwiDRP

a `jupyter` (Kluyver et al., 2016) environment and begins by aligning each cube with respect to a fiducial frame (the first in the list of cubes by default). The code de-rotates and cross-correlates each frame to determine sub-pixel relative offsets, then drizzles them onto a common grid with rectilinear ($0\farcs3 \times 0\farcs3$) spatial sampling, weighted by exposure time using the `Montage`[2] (Jacob et al., 2010) package. Since all data were taken in the KCWI "Medium BL" configuration, each cube has the same common wavelength range (3530-5530 Å) and sampling (1 Å pix^{-1}). The WCS of the stacked cube is then corrected using an external observation (typically *HST* F160W images) to match the astrometry of existing KBSS ancillary data products. The final output is a WCS-registered $\sim 20''$ (170 kpc) diameter pointing.

For each stacked cube, we also constructed a "white light" (3530 – 5530 Å) image and used `Source Extractor` (Bertin & Arnouts, 1996) to detect all significant continuum sources; all detected continuum sources were extracted to 1D from the data cubes by weighting each spatial element within the detected segmentation region by the $(S/N)^2$ of the white light signal. Some of the continuum sources detected in each KCWI pointing were not KBSS catalog objects (normally limited to $\mathcal{R} \leq 25.5$), but yielded spectroscopic redshifts placing them in the targeted range for the present purposes, $1.4 \leq z \leq 3.5$. Very deep photometric catalogs exist in all of the KBSS survey fields (in addition to the KCWI white light images), generally for at least $UG\mathcal{R}JHK_s$ bands as well as one or more deep pointings of HST-WFC3-IR F140W and/or F160W, so that photometry sufficient for constraining the stellar masses of the newly identified galaxies was available. These sources (of which there are 51 in all) have been labeled "CS" (continuum serendipitous) along with their segmentation IDs (e.g., CS3 – see Figure 2.1). Of the 51 galaxies, 22 are fainter than the nominal KBSS catalog continuum limit ($\mathcal{R} \geq 25.5$), with a limiting $\mathcal{R}$-band magnitude of 27.33.[3]

LRIS-B

LRIS-B spectra comprise the bulk of the KBSS rest-frame far-UV spectroscopic sample, having been accumulated over ~two decades, and as such we direct the reader to Steidel et al. (2003, 2004) and Adelberger et al. (2004)

[2] http://montage.ipac.caltech.edu/

[3] A small number of additional serendipitous objects were spectroscopically identified but lacked detections in any of the available near-IR photometric bands necessary to constrain their stellar masses; they have not been included in the analyses below.

for color selection criteria and data reduction strategies of the QSO field observations used in this study. LRIS observations are used to supplement KCWI observations and include a portion of the KBSS galaxy pair sample (KGPS) compiled by Y. Chen et al. (2020), which at the time comprised a broad superset of the galaxies used previously in numerous projects (e.g. Adelberger et al. 2005; Reddy et al. 2006; Steidel et al. 2003, 2004, 2010). Notably, in the current work we include only galaxy pairs with angular separations $\Delta\theta \leq 30''$ ($\sim$ 250 kpc) and background galaxy spectra obtained with the higher resolution 600 lines mm^{-1} LRIS-B grism. The latter condition translates to LRIS-B spectra with $R \sim 1300$ (Y. Chen et al., 2020), somewhat lower resolution than KCWI at the same wavelengths.

All of the LRIS-B data used in this sample were obtained between 2002 and 2016. Of the 2862 spectra used in the KGPS sample, 872 were observed with the 600 lines mm^{-1} grism blazed at 4000 Å, and of those, 400/872 were observed on more than one slitmask. Each slitmask was observed for a minimum of 1.5 hours and 30% of the 600 lines mm^{-1} grism slitmasks have exposure times of > 3 hours. Only the blue channel LRIS data have been used in the present work; the spectral range covered is similar to that of the KCWI data described above, with a red cutoff near 5600 Å extending down to 3400-3500 Å in the UV.

Of the 872 galaxies that make up the LRIS sample ($1.4 \leq z \leq 3.6$), 135 were observed with particularly long total integrations ($\sim 10 - 12$ hours). This “KBSS-LM1” sample was compiled between 2014 and 2016 to be a deep collection of LRIS rest-UV spectra focused on the redshift range $2.10 \leq z_{\rm gal} \leq 2.58$, corresponding to the highest quality existing KBSS-MOSFIRE spectra. Sample selection criteria are described by Steidel et al. (2016) and Theios et al. (2019), but in short, the galaxies were chosen to maximize the overlap with the existing KBSS-MOSFIRE sample, and especially pertinent for this work, the KBSS fields were prioritized so that the largest number of galaxies could be observed on a single slitmask.

2.3 Galaxy Pair Sample

To understand the bulk properties of gas in galaxies’ circumgalactic media, we assembled a sample of galaxy pairs from the KCWI and LRIS subsamples. A galaxy pair consists of a foreground and background galaxy (at redshifts

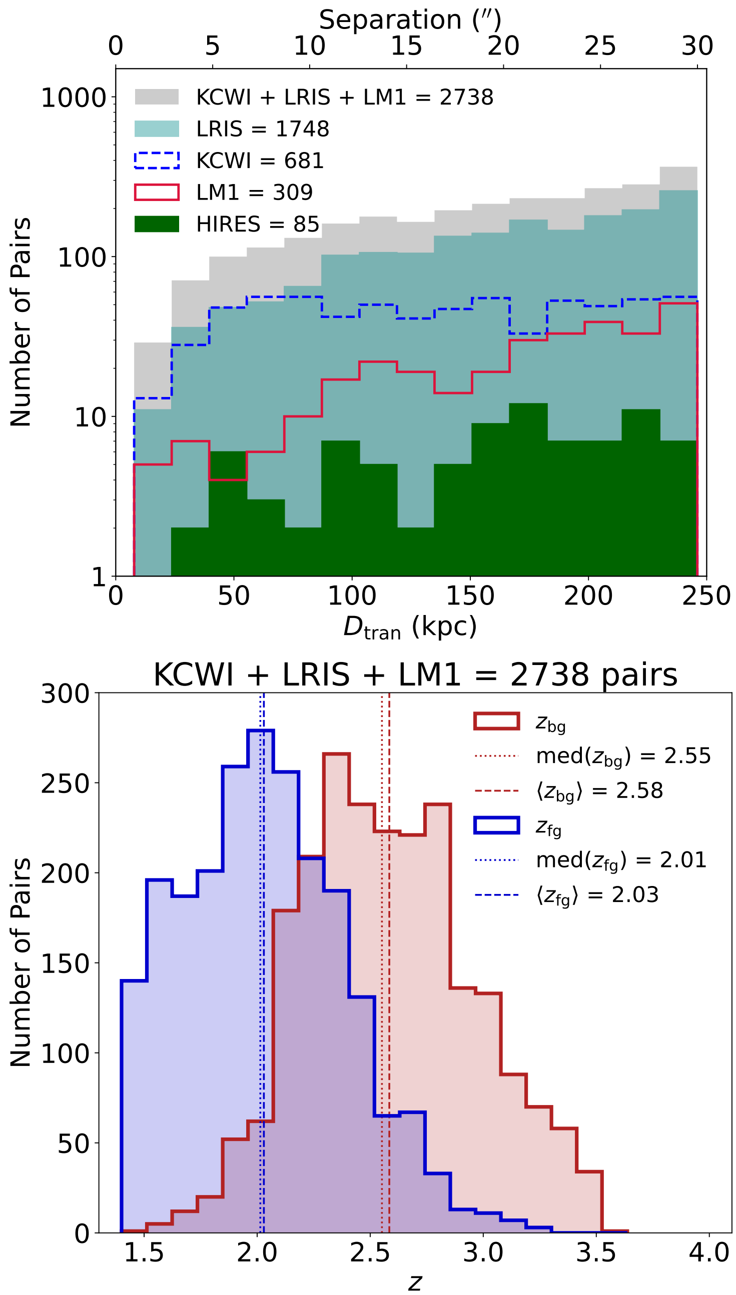

Figure 2.2: *Top:* Histogram of $D_{\rm tran}$ for the galaxy pair sample. The full distribution of projected distances is shown in gray and KCWI pairs are shown in the dashed blue histogram. KCWI background spectra are supplemented by LRIS-B (cyan histogram) and LM1 (red outline) observations, the former of which begins to dominate at $D_{\rm tran} \gtrsim 100$ kpc. There are 2738 pairs in total and respective totals are enumerated in the plot legend. The HIRES pair distribution constructed from background QSOs is shown for comparison in green. *Bottom:* The redshift distribution of foreground (blue) and background (red) galaxies in the galaxy pair sample along with vertical dotted and dashed lines denoting the median and mean redshifts respectively.

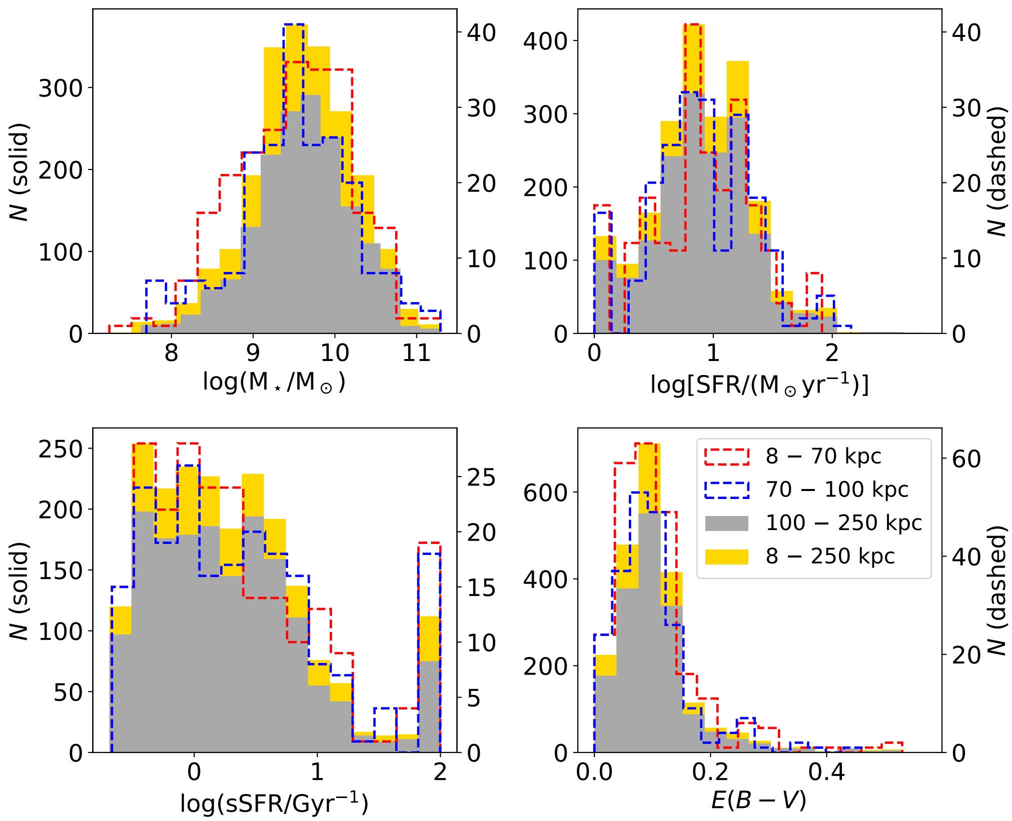

Figure 2.3: Foreground galaxy property distributions for M_* (top left), SFR (top right), sSFR (bottom left), and $E(B-V)$ (bottom right). The yellow histogram shows the properties over the full range of $D_{\rm tran}$ probed in this sample, while the red outline, blue outline, and solid gray histogram correspond to samples drawn from $D_{\rm tran} = 8-70$ kpc, $70-100$ kpc, and $100-250$ kpc, respectively. The number of pairs in the solid histograms is shown on the left vertical axis, while the numbers in the dashed histograms (with considerably fewer pairs but a similar overall distribution) are shown on the right vertical axis.

$z_{\rm fg}$ and $z_{\rm bg}$ respectively) with a projected separation on the sky satisfying the following requirements:

- $\Delta\theta < 30''$ so that the background galaxy probes the foreground galaxy's CGM within 250 kpc.
- $\Delta v = \frac{c\Delta z}{1+z_{\rm bg}} \gtrsim 3{,}000$ km s^{-1}, where $\Delta z = z_{\rm bg} - z_{\rm fg}$ to ensure the foreground and background galaxies are not part of the same large-scale structure (i.e., they are causally disconnected from each other). For the average foreground redshift $\langle z_{\rm fg}\rangle = 2.3$, $\Delta z \gtrsim 0.033$ or 12.9 physical Mpc along the line of sight assuming pure Hubble flow. We do not impose an upper bound on Δv (see Appendix 2.10).
- $z_{\rm fg} > 1.4$, such that at least C IV falls at $\lambda > 3700$ Å, where both LRIS-B and KCWI spectra have relatively low noise.
- The background galaxy has been observed with KCWI or LRIS-B with the 600 line mm^{-1} grism.
- The background object in a pair is not a QSO. The rationale behind this decision is discussed in Section 3.1 and Appendix 2.10: in short, we are using only spatially-resolved background sources because they average over (foreground galaxy) CGM sub-structure on projected scales of 2 – 4 kpc, and so are physically distinct from QSO measurements, which sample a region several thousand times smaller (see Steidel et al. 2010 and Rubin, Diamond-Stanic, Coil, Crighton, and Moustakas 2018; Rubin, Diamond-Stanic, Coil, Crighton, and Stewart 2018 for discussions of this point).
- The foreground object in a foreground-background pair is not classified as an AGN (type 1 or type 2). Although such measurements would be interesting, here we focus solely on star-forming galaxies without evidence for current AGN activity.
- For the purpose of binning the sample by galaxy properties (Section 2.7), we require the foreground galaxy to have an SED fit that allows for a constraint on its stellar mass.

Since we are interested in using background galaxy spectra to measure foreground absorption, a well-determined foreground galaxy redshift is essential to ensure accurate velocity measurements in the shifted spectra. To that end, where possible, nebular redshifts from KBSS-MOSFIRE (Steidel et al., 2014; Strom et al., 2017, 2018) were used to determine galaxy systemic velocities. The KBSS-MOSFIRE nebular redshifts have systemic redshift uncertainties $\Delta v_{\rm MOSFIRE} \simeq 18$ km s^{-1} (Steidel et al., 2014), considerably higher velocity accuracy than either LRIS ($\sigma_{\rm LRIS} \simeq 107$ km s^{-1}) or KCWI ($\sigma_{\rm KCWI} \simeq 71$ km s^{-1}). When nebular emission line measurements were not available, rest-frame UV emission (i.e. Lyα) and low ionization interstellar (LIS) absorption features (e.g. Si II, C II) were used to calculate the systemic redshift, using the redshift calibration rules outlined by Y. Chen et al. (2020); in such cases the typical redshift accuracy is $\sigma_{\rm UV} \simeq 100$ km s^{-1} (Steidel et al., 2018).

To assemble the sample, we started by constructing galaxy pairs for all known foreground galaxies in KBSS where the corresponding background galaxy had been observed with KCWI; 681 pairs with a KCWI-observed background galaxy satisfied the criteria above, 341 (51%) of which had a foreground galaxy with a nebular redshift. The number of KCWI pairs reaches a peak count at $D_{\rm tran} \simeq 50$ kpc and plateaus for $D_{\rm tran} > 100$ kpc (see the blue dashed histogram outline in the left panel of Figure 2.2). The lack of pairs with $D_{\rm tran} > 50$ kpc is an artifact of the KCWI observing strategy: 252/681 (37%) of the KCWI galaxy pairs have their foreground and background galaxies on the same KCWI pointing (which are ≈ 170 kpc in diameter). The remaining 429 (63%) pairs involve a KCWI background galaxy and a foreground galaxy that falls off the KCWI footprint but still probes gas (at $z_{\rm fg}$) in the KCWI background galaxy spectrum.

To supplement the number of pairs sampling larger $D_{\rm tran}$, we then formed pairs where the background galaxy was one observed with LRIS-B (the blue channel of LRIS). This added 1748 galaxy foreground/background pairs from the general LRIS sample ($t_{\rm int} \simeq 1.5 - 4.5$ hours; cyan solid histogram in the left panel of Figure 2.2) and 309 pairs from LM1 masks ($t_{\rm int} \simeq 10 - 12$ hours; red histogram outline in Figure 2.2) to the initial KCWI sample, mostly sampling $100 \lesssim D_{\rm tran}/{\rm kpc} \lesssim 250$; 879 of the 1748 (50%) LRIS pairs and 186/309 (60%) of the LM1 pairs had foreground galaxies with nebular redshifts. In the end, 2738 pairs (1406 [51%] with foreground nebular redshifts) sampling $8 \leq D_{\rm tran}/{\rm kpc} \leq 250$ ($\Delta\theta \sim 1'' - 30''$) met all of our selection criteria. The final sample of galaxy pairs is summarized in Figure 2.2. The foreground galaxy stellar mass (M_*), star formation rate (SFR), specific star formation rate (sSFR ≡ SFR/M_*), and the inferred reddening $E(B-V)$ distributions are shown in Figure 2.3. A thorough description of the SED fitting underlying these measurements can be found in Steidel et al. (2016, 2018) and Theios et al. (2019). We will return to the stellar population parameters of the foreground galaxies in Section 2.7.

2.4 Stacking

Although some background galaxy spectra show clear evidence of intervening absorption at the redshift of the foreground galaxy (see Figure 2.1 for some examples), most of the background spectra do not have sufficient S/N to detect weak absorption ines against the faint continuum. Stacking (in bins of $D_{\rm tran}$) increases the effective S/N and facilitates the detection of weaker (metallic) absorption features. In doing so, however, each constituent background spectrum contributes absorption at $z_{\rm bg}$, $z_{\rm fg}$, and possibly additional "contaminating" redshifts (especially in the Lyα forest) to the stack. Averaging over a sufficiently large number of different ($z_{\rm fg}$, $z_{\rm bg}$) pairs (see Appendix 2.10) can mitigate the effects of contamination because the locations of the discrete contaminating absorption lines from redshifts other than $z_{\rm fg}$ will be "randomized" with respect to the features of interest at $z_{\rm fg}$. It is useful to keep in mind that what one is trying to measure from the stacked background spectrum (redshifted to $z_{\rm fg}$) is the excess absorption signal from a particular transition at a particular redshift ($z_{\rm fg}$) compared to the mean absorption from all lines at other redshifts that happen by chance to coincide in wavelength with the feature of interest. In the limit of a very large number of ($z_{\rm fg}$, $z_{\rm bg}$) pairs, the contamination will eventually manifest as a local continuum that is lowered relative to the original by an amount that depends on both rest wavelength and the particular ensemble of ($z_{\rm fg}$, $z_{\rm bg}$) pairs being combined (see, e.g., Appendix 2.10). For stacks based on the combination of a finite number of ($z_{\rm fg}$, $z_{\rm bg}$) pairs, a significant source of noise in the measurements of interest arises from fluctuations in the local (mean) continuum when the absorption line "background" has not converged to a smooth distribution. These effects are exacerbated by the fact that there is a wide range of S/N among the spectra contributing to a given wavelength pixel in the stacked spectrum, and the number of individual spectra contributing to each wavelength pixel varies according to the distribution of $z_{\rm fg}$, $z_{\rm bg}$, and Δz (the difference between them).

Before stacking, each background galaxy spectrum was trimmed in wavelength. For KCWI pairs, background spectra were restricted to observed wavelengths where all 24 slices were sensitive i.e., 3530 – 5530 Å for the KCWI configuration we used. For the LRIS spectra, similar wavelength cuts were imposed both in the short and long wavelength ends of the blue channel data. The Lyα forest is primarily responsible for noise at the short wavelength end, while the LRIS dichroic cutoff at $\sim$ 5600 Å and the sky subtraction residuals around [O I] λ5577 occasionally introduce undulations in the red end of the blue channel. As for the KCWI spectra, 3500 – 5555 Å turned out to be a good fiducial wavelength to mitigate both effects. In addition to the wavelength endpoints, spectral regions near Lyα in the background galaxy spectrum were masked to avoid contamination in the final stack.[4]

In order to give each background spectrum an approximately equal weight in the composite, each spectrum was normalized with a cubic spline. The spline knots used to fit the background spectrum were chosen via a sparsely sampled median, ignoring wavelength regions near resonance lines. In the Lyα forest, we found points 1σ above the local ($\Delta\lambda \approx 50$ Å) median reliably traced the suppressed continuum. The KCWI and LM1 observations have associated error spectra; for the LRIS galaxies where error spectra do not always exist, we use the local standard deviation of the spectrum to construct a coarse error spectrum. We impose a $S/N \gtrsim 1$ cut on all constituent background spectra, i.e. only spectral regions where the cubic spline fit is greater than the error spectrum contribute to the stack. Background spectra where less than 15% of the bandpass had continuum $S/N \gtrsim 1$ were excluded entirely to avoid adding patches of sporadic noise to the stack.

In stacking, each normalized background galaxy spectrum was shifted to the rest frame of its corresponding foreground galaxy and resampled onto a common wavelength grid with 0.2 Å sampling using linear interpolation. For a given range of $D_{\rm tran}$, the associated background spectra were combined

[4]We experimented with masking other far-UV absorption features (e.g. C IV, Si II) but found that additional wavelength masks added more discontinuities to the constituent spectra and resulted in overall noisier stacks.

to make a final stack using a trimmed mean where spectral pixels above (below) the 95th (5th) percentile were rejected. For the stacks presented below, this resulted in 4 – 6 objects being excluded, comparable to a $\sim 2\sigma$ clipped average, where σ is defined based on the variance of the input spectra at a given wavelength. We experimented with various methods for combining the spectra and several measures of central tendency before deciding on the trimmed mean; further details on the stacking method and the results of these tests are described in Appendix 2.10. Even with stacks of coarsely normalized spectra, the fact that each background spectrum has been shifted to an unrelated foreground redshift necessitates a manual adjustment to the continuum fit of the composite in order to measure accurate absorption profiles (discussed further in Appendix 2.10).

As highlighted above, error spectra for KCWI and LM1 masks exist and can be propagated through to the stacks; however, we adopt a bootstrap approach since it includes sample variance and reveals how much individual spectra contribute to the absorption observed in the combined spectrum. For each background stack, we ran 100 bootstrap realizations with randomly selected galaxy pairs (with replacement) from that bin's range of $D_{\rm tran}$. The error spectrum is then the standard deviation of the 100 bootstrap stacks. As expected, the error spectra qualitatively resemble those propagated from each spectrum's respective noise estimated by the DRP, but there tends to be a spike in variability around strong absorption features due to the variance in foreground absorption between galaxies.

Foreground galaxy spectra within each sub-sample ($D_{\rm tran}$ bin) were used to create a composite "down the barrel" average foreground galaxy spectrum for each. The individual spectra were combined in a similar fashion to their background galaxy counterparts, with a few notable exceptions. To ensure every foreground galaxy had a roughly equal contribution to the stack, each spectrum was approximately normalized based on its median continuum (1410 – 1510 Å) flux density before being combined. Each spectrum with a continuum $S/N \gtrsim 1$ was then shifted to its rest frame and galaxies within the 5th – 95th percentiles (as a function of wavelength) were averaged. The final stack was continuum-normalized by fitting a BPASSv2.2 (Stanway & Eldridge, 2018) constant star formation rate stellar population synthesis model with age 10^8 years, metallicity $Z = 0.14\,Z_{\odot}$, and including the effect of binary evolution of massive stars; an SMC extinction curve[5] was assumed. More details on the choice of model and the fitting procedure can be found in Steidel et al. (2016, 2018) and Theios et al. (2019).

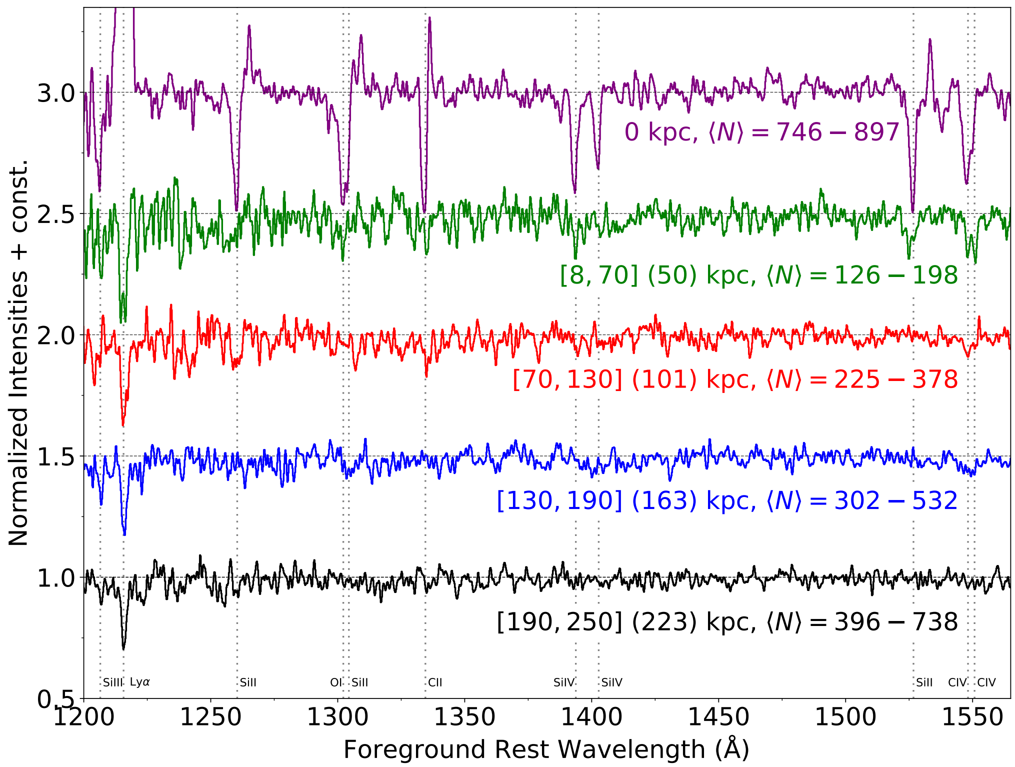

Figure 2.4: Normalized composite spectra of the foreground galaxies in this sample when viewed down the barrel (top, purple) plus four $D_{\rm tran}$ bins ranging from 8 – 250 kpc utilizing background galaxies as a continuum source. The spectra are offset by 0.5 from one another for ease of visualization. Each spectrum's minimum, maximum, and median (shown in parentheses) sampled $D_{\rm tran}$ is labeled in the plot along with the number of pairs contributing to each stack. Note that the number of pairs varies as a function of wavelength with fewer pairs contributing at shorter wavelengths. The two counts specify the number of pairs contributing at Lyα and C IV respectively. Typical far-UV resonant transitions are marked with vertical dotted lines and labeled at the bottom of the plot.

Stacks from several $D_{\rm tran}$ bins are shown in Figure 2.4, offset from one another for clarity. We observe prominent Lyα and C IV over the widest range of impact parameters, plus Si III, Si IV, Si II λ1260, and Si II λ1526 primarily in the small impact parameter bin ($\langle D_{\rm tran}\rangle$ = 50 kpc; green spectrum). The

[5] $A_V = 2.74\,E(B-V)$ for the SMC extinction curve.

number of objects contributing to the final stack varies by a factor of ~ 2, largely due to the underlying redshift distribution ($1.4 \lesssim z_{\rm fg} \lesssim 3.2$; see the right panel of Figure 2.2) and the short wavelength UV cutoff of the spectra (~ 3500 Å). As one moves to higher $z_{\rm fg}$, correspondingly higher $z_{\rm bg}$ objects are required to measure shorter rest-wavelength transitions (e.g. Si III λ1206) which invariably fall in the Lyα forest of the background spectrum. The noise level is also somewhat higher at the short wavelength end of the spectrum as compared with a region around e.g. 1500 Å because many of the spectra cut off at shorter wavelengths and fewer pairs end up being averaged. There is also some small scale variability in the number of spectra contributing at a particular wavelength that arises from trimming and/or masking of particular spectral features at the redshift of the background galaxies.

2.5 Absorption Trends from Composite Spectra

With a method for stacking galaxy pairs in hand, we proceeded to construct a suite of composite spectra for $D_{\rm tran}$ between 8 kpc (the minimum pair separation) and 250 kpc, with the goal of sampling the changing absorption profiles over increasing galactocentric radius. Bins sampling projected distances $D_{\rm tran} \lesssim 100$ kpc are typically 30 kpc wide and are spaced in 10 kpc intervals (i.e. 8 – 40 kpc[6], 20 – 50 kpc, . . . , 100 – 130 kpc). The number of pairs contributing to a particular stack ranges from ~ 50 at $D_{\rm tran} \simeq 30$ kpc to ~ 200 at $D_{\rm tran} \simeq 100$ kpc which ensures any supposed absorption is real and easily discernible (Appendix 2.10). As an illustration, Lyα and C IV absorption in several such stacks is shown in Figure 2.7; we will revisit these spectra in Section 2.5. These bins are not unique however; choosing different bin endpoints and/or spacing does not significantly alter the results presented below because the underlying distribution being sampled is the same.

Since the number of pairs increases with $D_{\rm tran}$ (Figure 2.2), it becomes possible to sample smaller impact parameter intervals while maintaining a comparable continuum S/N. On the other hand, the absorption features become weaker and less variable outside of the virial radius ($R_{\rm vir} \simeq 90$ kpc for a typical halo in our sample). As a compromise, for $100 \lesssim D_{\rm tran}/{\rm kpc} < 250$ we maintain 30 kpc bins but increase the spacing to 15 kpc (i.e. 115 – 145 kpc, 130 – 160 kpc, . . . , 220 – 250 kpc). The 10–15 kpc spacing between

[6] All but one of the ($z_{\rm fg}$,$z_{\rm bg}$) pairs have $D_{\rm tran} > 10$ kpc.

the bins means that every other or every third bin contains a unique set of background/foreground pairs or, depending on $D_{\rm tran}$, at least $\sim 30-50\%$ of the pairs differ between adjacent bins. The benefit to this "moving average" type sampling is a reduced susceptibility to outlier spectra and an increased resolution at small $D_{\rm tran}$. We use these bins for the majority of the analysis with the full pair sample and specify cases for which the binning differs.

Quantitative measurements of absorption features

Absorption features in the stacked composite spectra represent averages over many lines of sight through the CGM of foreground galaxies, each of which is already a spatial average over several kpc as discussed above, so that we do not attempt to measure column densities or Doppler parameters as one might using high resolution QSO spectra. The kinematics of the absorption line profiles convey information about the average velocity distribution (relative to $z_{\rm fg}$) of gas giving rise to a given transition, while the relative depth of the absorption as a function of velocity is proportional to the fraction of the area of the beam footprint with significant optical depth at a particular LOS velocity in the transition; both are affected by the effective resolving power of the composite spectra.

To quantify the absorption features in a model-independent way, for each transition in the composite spectra we measured the rest-frame equivalent width W_λ, the velocity centroid (first moment) of the absorption feature relative to the systemic velocity of the foreground galaxy (Δv), and the second moment (σ) as a proxy for the velocity dispersion. For the DTB composite, each quantity was computed via direct integration over the region where the flux was below the continuum.[7] The $D_{\rm tran} \geq 8$ kpc composites have comparatively lower continuum S/N so each metric was instead computed over the velocity range $|v| \leq 700$ km s^{-1}.[8] Since the background galaxy spectra ($D_{\rm tran} \geq 8$ kpc) measure absorption throughout the foreground galaxy halo and DTB spectra probe only gas "in front" of the galaxy along our line

[7] At this spectral resolution, the DTB σ(C II) measurement is contaminated by the presence of the associated nonresonant C II* λ1335.62 emission line which "fills in" the red side of the absorption feature. To compensate, we fit a double Gaussian to both features and define σ(C II) as the standard deviation of the Gaussian absorption component.

[8] Given their close proximity, the integration region for O I λ1302 and Si II λ1304 was truncated at $\lambda = 1303.3$ Å, the midpoint between the two features. Note that measuring the $D_{\rm tran} > 0$ kpc composites in the same manner as the DTB spectra increases the overall noise but does not significantly alter the results presented below.

of sight, we corrected the DTB W_λ and σ by multiplying the observed DTB quantities by a factor of two (Table 2.1) to approximate the total absorption and velocity spread that would be observed along a line of sight at $D_{\rm tran} = 0$ kpc. Similar to the background error spectrum calculation, we ran 2000 Monte Carlo resamples of the stacked spectrum perturbed by a Gaussian whose width was equal to the pixel noise level at each wavelength. Uncertainties on W_λ, Δv, and σ were determined from the standard deviation of the resulting parameter distributions. Absorption line W_λ, σ, all as functions of $D_{\rm tran}$, are shown in Figures 2.5 and 2.6 , respectively. These figures comprise the principal results of this study, and we will discuss them further in Sections 2.5 and 2.5.

We note that a few of the low ionization lines are detected in only a subset of the $D_{\rm tran}$ bins, leading to some non-uniform sampling. In general, if low ions or Lyα are detected in a stack, then C IV tends to be as well simply because there is a factor of $\simeq 2$ increase in the number of pairs contributing to a stack between Lyα and C IV (recall the S/N is roughly proportional to the number of pairs being averaged). The net result is that Lyα and C IV have the densest sampling in $D_{\rm tran}$, especially at $D_{\rm tran} \lesssim 100$ kpc since bins where the low ionization features are detected can almost always be reused to measure Lyα or C IV.

Instrumental contributions to observed kinematics

In order to evaluate the significance of the observed kinematics of absorption features in the stacked spectra, we first evaluate the contributions of the instrumental resolving power and redshift uncertainties to observed kinematic profiles. As discussed in Section 2.3, 1406/2738 ($f_{\rm neb} = 51\%$) of the foreground galaxies among the foreground/background galaxy pairs have nebular redshift measurements from KBSS-MOSFIRE, which have very small redshift uncertainties $\sigma_{\rm neb} \simeq 18$ km s^{-1}, or $\Delta z \lesssim 0.0002$ at $z \sim 2$ (see Steidel et al., 2014); the remaining ($f_{\rm UV} = 49\%$) have uncertainties $\sigma_{\rm UV} \simeq 100$ km s^{-1} (see Y. Chen et al., 2020; Steidel et al., 2018). Combining the two velocity errors in quadrature weighted by their fractional contribution i.e.

$$\delta v_{\rm sys} = \sqrt{f_{\rm neb}\sigma_{\rm neb}^2 + f_{\rm UV}\sigma_{\rm UV}^2} \tag{2.1}$$

implies the full galaxy pair sample has a systemic velocity uncertainty of $\delta v_{\rm sys} \approx 71$ km s^{-1}.

The spectral resolving power for individual background galaxy spectra depends on the instrument used to obtain them: for spectra obtained with LRIS-B using the 600 line mm^{-1} grism, we adopt $\sigma_{\rm LRIS} = 107$ km s^{-1} ($\langle R \rangle \simeq 1200$; Y. Chen et al. 2020), and for KCWI we use $\sigma_{\rm KCWI} = 71$ km s^{-1}, consistent with a spectral resolution $\langle R \rangle \simeq 1800$.

In a similar fashion to Equation 2.1,

$$\sigma_{\rm comb} = \sqrt{f_{\rm LRIS}\sigma^2_{\rm LRIS} + f_{\rm KCWI}\sigma^2_{\rm KCWI}} \tag{2.2}$$

where $f_{\rm LRIS}$ and $f_{\rm KCWI}$ are the fractional contributions of background spectra from each instrument to the total stack and $\sigma_{\rm inst}$ are the respective spectral resolving power. For the full $D_{\rm tran} < 250$ kpc sample, $\sigma_{\rm comb} \approx 99$ km s^{-1}, and for $D_{\rm tran} < 100$ kpc, $\sigma_{\rm comb} \approx 90$ km s^{-1}.

Combining in quadrature the two sources of line broadening affecting the composite (stacked) spectra – i.e, foreground galaxy systemic redshift uncertainties and spectral resolution of the background galaxy spectra – we find $\sigma_{\rm tot} = \sqrt{\delta v^2_{\rm sys} + \sigma^2_{\rm comb}} \approx 122$ km s^{-1} for the full sample and $\sigma_{\rm tot} \approx 121$ km s^{-1} at $D_{\rm tran} < 100$ kpc.

We adopt $\sigma_{\rm tot} = 122$ km s^{-1} as the effective instrumental resolution for all composite spectra, meaning that the velocity width of any measured (single line) spectral feature must be corrected by subtracting this value in quadrature, and that real spectral features should have second moments larger than $\sigma_{\rm tot}$. In the case of the C IV doublet, which is usually blended in composite spectra, the effective instrumental contribution to a measured second moment for the full absorption feature (assuming each component is broadened by $\sigma_{\rm tot} = 122$ km s^{-1}) is $\sigma_{\rm tot,CIV} \sim 260$ km s^{-1}.

We have subtracted (in quadrature) the appropriate instrumental contribution $\sigma_{\rm tot}$ (or $\sigma_{\rm tot,CIV}$) from all second moment measurements presented (Figure 2.6) to facilitate comparisons between velocity dispersions from different transitions.

Lyα and C IV

Lyα and C IV (in that order) are by far the strongest absorption features detected in the composite spectra of background galaxies. We therefore present these results before moving onto the low ions. Starting in one

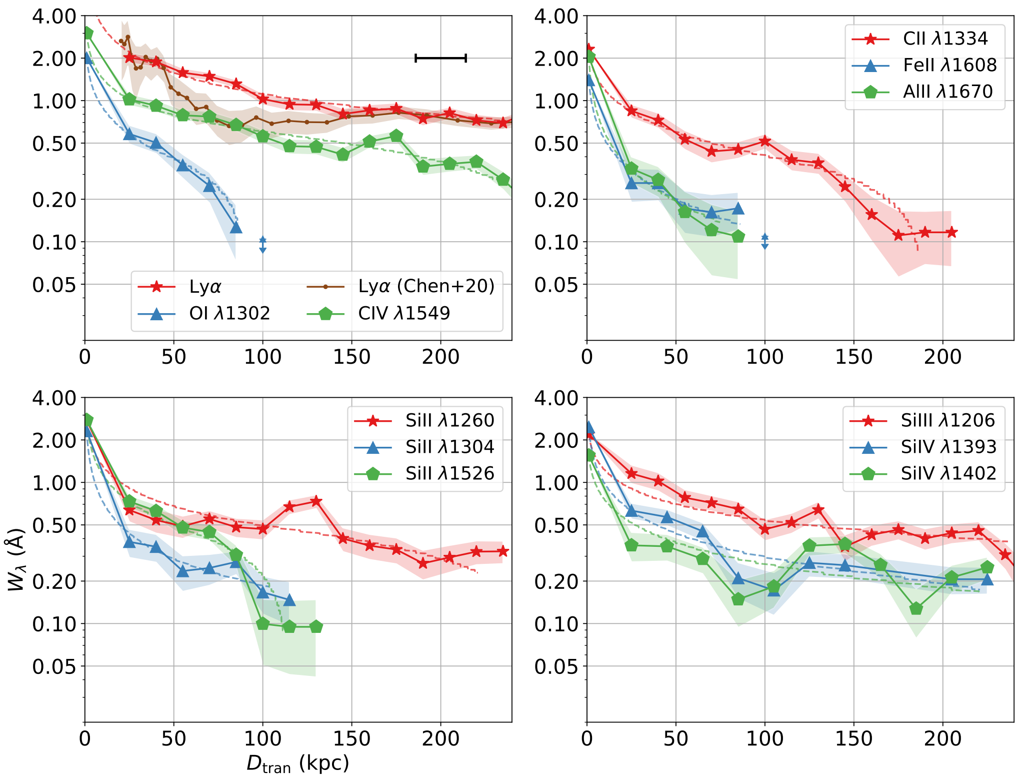

Figure 2.5: Absorption line W_λ vs. $D_{\rm tran}$ for several transitions (labeled in the plot legends). The green C IV $\lambda\,1549$ points show the total equivalent width integrating over the entire feature. Color coded bands show W_λ uncertainties and dashed lines are predicted W_λ from the model described in Section 2.6 (best fit parameters are listed in Table 2.1)
. In the top left plot, the horizontal error bar shows typical bin sizes for all the transitions shown. The Y. Chen et al. (2020) W_λ(Lyα) measurements (with uncertainties) are shown in brown.

dimension, some representative stacks are presented in Figure 2.7 that show how Lyα (left) and C IV (right) change with $D_{\rm tran}$. The same $D_{\rm tran}$ bins are shown for ease of comparison, although as can be seen in, e.g., Figure 2.4, excess Lyα absorption extends well beyond $D_{\rm tran}$ = 100 kpc. For Lyα and C IV, absorption starts out both stronger and more extended in velocity close to the center of the galaxy and the profiles become shallower and narrower with increasing $D_{\rm tran}$. Between $D_{\rm tran} \simeq 30$ kpc and $D_{\rm tran} \simeq 100$ kpc, W_λ(Lyα) drops by a factor of $\simeq$ 2 from 2 Å to 1 Å (Figure 2.5) and σ(Lyα) decreases from 340 km s^{-1} to 270 km s^{-1}; a 21% reduction (Figure 2.6). In the same range of projected distances, W_λ(C IV) drops by a factor of $\simeq$ 2 from 1.0 Å to 0.5 Å and σ(C IV) broadly follows σ(Lyα) with a velocity spread $\simeq$ 300 km s^{-1}. In

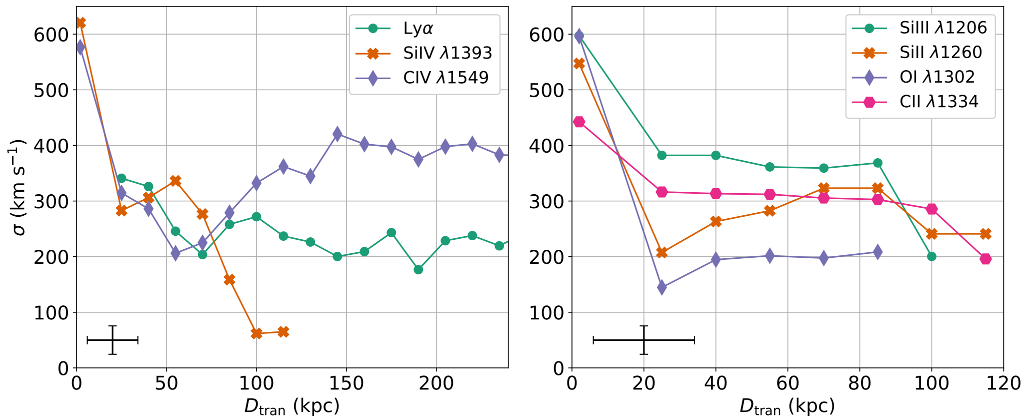

Figure 2.6: Second moment of the normalized absorption profiles (σ) vs. projected distance ($D_{\rm tran}$) for transitions color coded in the legends of each panel. As for Figure 2.5, the C IV λ 1549 (thin purple diamonds) measurements are obtained by integrating over the entire doublet. The values of σ have been corrected for the instrumental contribution as discussed in Section 2.5. The black error bar in the lower lefthand corner of each panel shows typical bin sizes (horizontal) and average bootstrap uncertainties on the second moment (vertical) for each transition.

this case, W_λ(C IV) and σ(C IV) were measured via direct integration over the full doublet, without distinguishing between the individual transitions, and σ(C IV) were corrected as described in Section 2.5.

For Lyα in the left panel of Figure 2.7 (see also Figure 2.8), we observe a shifting velocity centroid with $D_{\rm tran}$: at $D_{\rm tran} \lesssim 50$ kpc, Δv(Lyα) < 0 km s^{-1}; between $D_{\rm tran} \sim 50 - 125$ kpc, Δv(Lyα) $\simeq 100$ km s^{-1}, after which point Δv(Lyα) is consistent with zero. We note that the relative scarcity of galaxy pairs within $\simeq 100$ kpc results in noisier stacks compared with those at $\langle D_{\rm tran} \rangle \gtrsim 100$ kpc where more lines of sight are probed. This can be seen by comparing the dotted red and dotted purple error spectra; the former has fewer (37) pairs contributing than the latter (116) and the corresponding bootstrap uncertainty is increased by a factor of $\simeq 2$. Despite the larger uncertainty in absorption strength, the shifted trough persists across multiple independent bins. We discuss the net blueshifted velocity centroid at $D_{\rm tran} \lesssim 50$ kpc further in Appendix 2.10.

While both Lyα and C IV present a similar trend in decreasing W_λ and σ with increasing $D_{\rm tran}$, the shape of the C IV absorption troughs changes more significantly. In the $D_{\rm tran} = 8 - 40$ kpc bin (right panel of Figure 2.7),

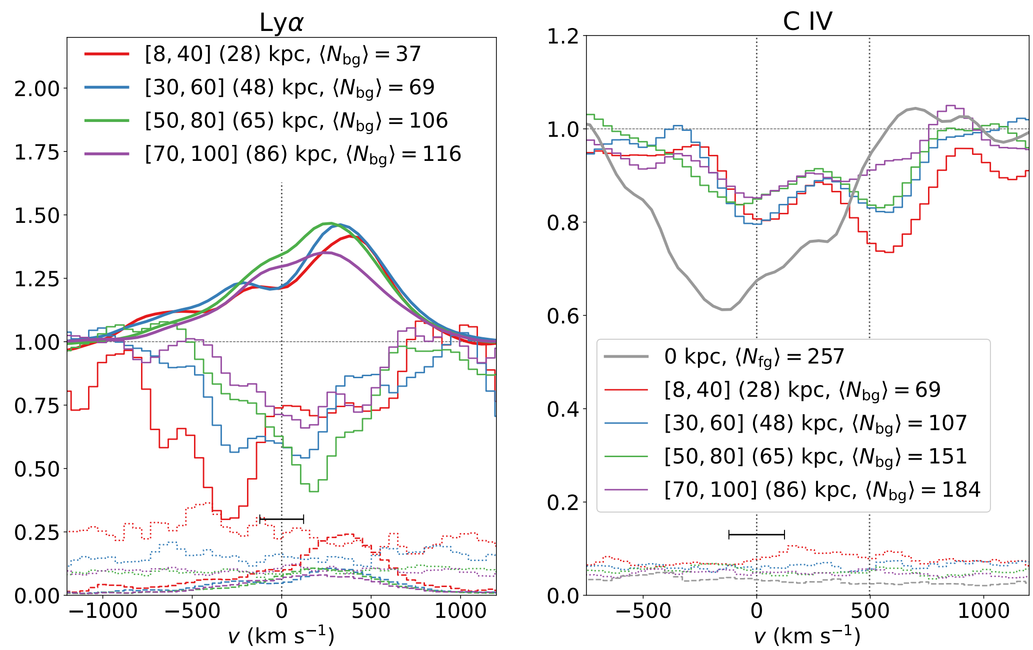

Figure 2.7: *Left:* Normalized and scaled Lyα emission (thick line style; $D_{\rm tran}$ = 0 kpc) and absorption (thin histogram line style; $D_{\rm tran}$ > 0 kpc) profiles plotted for several impact parameter bins. For a given impact parameter range, DTB foreground galaxy spectra were averaged to produce an emission spectrum while background spectra were similarly averaged to measure the absorption induced by the foreground galaxy's CGM. The range of $D_{\rm tran}$ and the median are shown for each bin. Note that the Lyα emission is scaled down by a factor of 15 and translated vertically by +1 for display purposes. *Right:* C IV absorption profiles for the same bins in $D_{\rm tran}$ (with the same color scheme) as the left panel. The DTB (thick gray) spectrum includes all foreground galaxies in pairs with $D_{\rm tran}$ < 100 kpc. In both panels, the number of pairs contributing to each stack at the wavelength of interest is shown in the plot legends; "fg" subscripts correspond to DTB spectra, while "bg" are measurements utilizing background spectra. The vertical dashed lines show $v_{\rm sys}$ = 0 km s^{-1} for each transition and the black error bar shows the effective resolution element of the stack. Note that C IV λ1550 is shown at v = 497 km s^{-1} on the right hand panel. Normalized background (DTB) error spectra from bootstrap resampling are plotted in a dotted (dashed) line style and are color coded to match the stacked spectra.

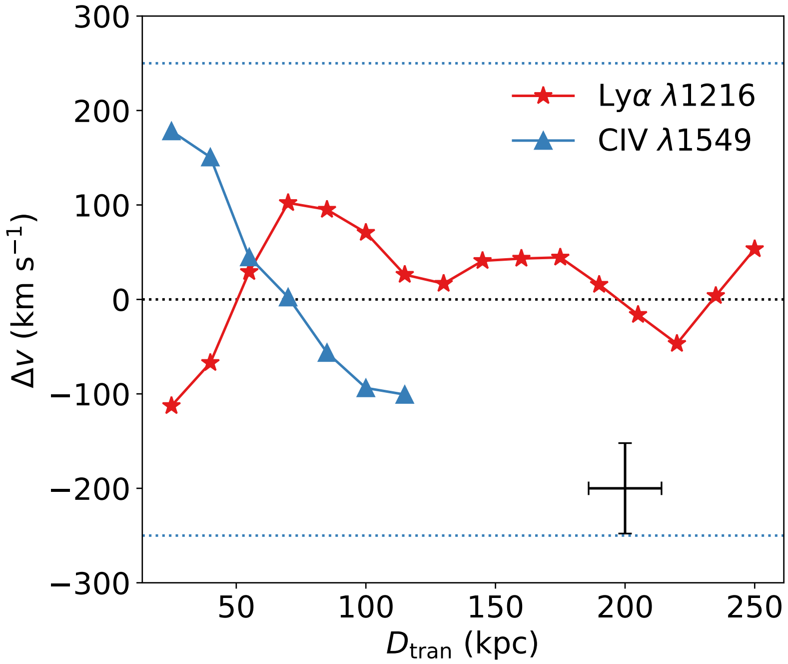

Figure 2.8: Lyα (red) and C IV (blue) velocity centroids (Δv) as a function of $D_{\rm tran}$. The C IV centroid was computed by integrating over the entire doublet and Δv(C IV) = 0 km s^{-1} corresponds to the midpoint between the two C IV transitions ($\lambda \approx 1549.480$ Å). The dotted blue horizontal lines at $\Delta v = -250, +250$ km s^{-1} correspond to C IV λ1548 and C IV λ1550 relative the fiducial velocity. The black error bar shows the average bin width and bootstrap error on the velocity centroid.

both C IV λ1548 and C IV λ1550 present strong absorption near the systemic velocity with an extended trough in velocity space out to $v_{\rm LOS} \simeq -300$ km s^{-1} in C IV λ1548, and $v_{\rm LOS} \simeq +300$ km s^{-1} in C IV λ1550. We note that $W_\lambda(1550)$ is at least a factor of two larger than $W_\lambda(1548)$ which would of course be unphysical if one were measuring a single absorbing complex. In Appendix 2.10, we use stacked HIRES spectra of background QSOs to show how such foreground absorption profiles can arise. At lower S/N, small numbers of galaxy-galaxy pairs with a variety of absorption line strengths and kinematic profiles (e.g. those with σ(C IV) $\gtrsim 500$ km s^{-1}) can result in net $W_\lambda(1548)/W_\lambda(1550) < 1$. At the same time, averages over small numbers of pairs are also more sensitive to contamination by unrelated absorption features from other redshifts. Moving to larger $D_{\rm tran}$, the subsequent bins in Figure 2.7 show a contracting velocity spread centered near zero velocity and an increasing $W_\lambda(1548)/W_\lambda(1550)$ ratio, approaching the DTB presentation.

As an example, between $D_{\rm tran} \simeq 28$ kpc and $D_{\rm tran} \simeq 48$ kpc, $W_\lambda(1550)$ diminishes by $\sim 25\%$ and the velocity dispersion reduces slightly from 300 km s^{-1} to 230 km s^{-1}.

We used the $W_\lambda(1548)/W_\lambda(1550)$ ratio and Δv(C IV) to estimate the change in τ(C IV) with $D_{\rm tran}$. Between $D_{\rm tran} \simeq 30$ kpc and $D_{\rm tran} \simeq 90$ kpc, the average $W_\lambda(1548)/W_\lambda(1550)$ ratio transitions from approximately one to two (Figure 2.7). When σ(C IV) is large, a more robust approach to measuring the gas opacity involves the overall velocity centroid (Δv(C IV)) integrating over the full doublet. Measuring the velocity offset from $\lambda_{\rm cent} = 1549.480$ Å (the average of the two C IV rest wavelengths), we would theoretically expect a velocity centroid of $\Delta v \simeq -90$ km s^{-1} for optically thin C IV absorption with $W_\lambda(1548)/W_\lambda(1550) = 2$. Naturally, the velocity centroid would be centered at $\Delta v = 0$ km s^{-1} for the optically thick doublet ($W_\lambda(1548)/W_\lambda(1550) = 1$).

Between $D_{\rm tran} \simeq 30$ kpc and $D_{\rm tran} \simeq 100$ kpc, Δv(C IV) blueshifts by $\simeq 300$ km s^{-1} from Δv(C IV) $\simeq +200$ km s^{-1} to Δv(C IV) $\simeq -100$ km s^{-1} (Figure 2.8). The majority of the C IV bins show $\Delta v \lesssim -90$ km s^{-1} beyond $D_{\rm tran} \simeq 60$ kpc and the average $W_\lambda(1548)/W_\lambda(1550)$ changes from a 1:1 to a 2:1 ratio, consistent with a transition from optically thick to optically thin gas with increasing $D_{\rm tran}$. The gradient in line strength is largest at $D_{\rm tran} \simeq 50$ kpc, but the noise in both the Δv(C IV) and $W_\lambda(1548)/W_\lambda(1550)$ measurements suggests that some optically thick C IV may persist to $D_{\rm tran} \simeq 90$ kpc.

Beyond $D_{\rm tran} \simeq 100$ kpc, the C IV absorption signal becomes weaker and the marginal S/N prevents an accurate determination of W_λ(C IV) ratios. Physically, the equivalent width ratio likely remains at or around two but the number of pairs in our sample is insufficient to distinguish C IV λ1550 from the continuum. Indeed, the consistently negative Δv(C IV) values at $D_{\rm tran} \gtrsim 80$ kpc indicate that optically thin C IV is still present out to at least $D_{\rm tran} \simeq 125$ kpc; beyond this projected distance, the S/N is not sufficient to make a reliable velocity centroid measurement.

Low Ions

In addition to Lyα and C IV, we attempted to measure additional far-UV low ionization interstellar absorption transitions in the stacked spectra. Figure 2.9 shows several far-UV transitions where the absorption profiles vary significantly with $D_{\rm tran}$ and provides a visualization of the changing W_λ and

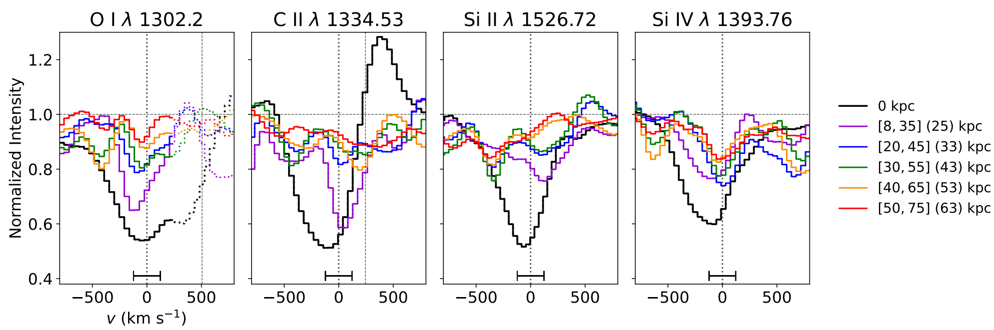

Figure 2.9: Normalized intensity profiles for several strong far-UV transitions, measured DTB (thick black) and at $D_{\rm tran}$ between 8 and 75 kpc (median $D_{\rm tran}$ shown in parentheses). The legend specifies the map between line color and range of $D_{\rm tran}$. The plotted colors move from blue to red across the rainbow with increasing $D_{\rm tran}$ e.g., $D_{\rm tran} \simeq 25$ kpc is blue and $D_{\rm tran} \simeq 63$ kpc is red. Black vertical dotted lines show $v_{\rm sys}$ and dashed lines show nearby transitions where appropriate (Si II λ1304 and C II* λ1335). Regions of the spectrum contaminated by such nearby transitions are shown with a dotted line style. The black error bar shows the effective velocity resolution. This figure is in contrast to Figure 2.10 which shows different transitions within the same bin.

σ measured in Figures 2.5 and 2.6 respectively. As expected, DTB ($D_{\rm tran} = 0$ kpc) absorption is considerably stronger for all transitions when compared with background galaxy sightlines ($D_{\rm tran} > 10$ kpc). Among the $D_{\rm tran} > 10$ kpc spectra, the trend continues: absorption strength for all transitions decreases with $D_{\rm tran}$. In particular, O I and Si IV show the largest change in both absorption strength and velocity extent over the other transitions.

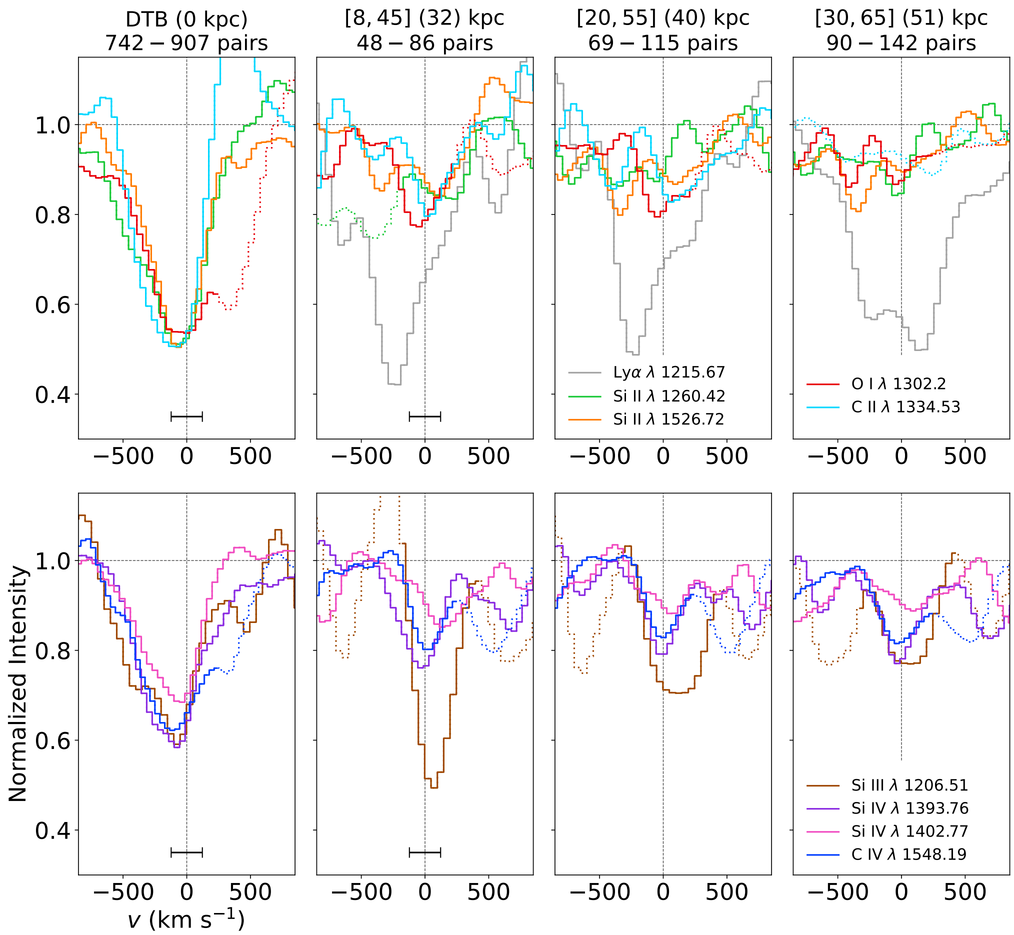

Figure 2.10: Normalized far-UV absorption features on a unified velocity scale for several different transitions DTB ($D_{\mathrm{tran}} = 0$ kpc) and at three nonzero projected distances (separated by column). The range of D_{tran} and number of galaxy pairs in that range are listed in the title in a similar format to previous figures. The ions being compared are shown in the legend. The vertical dashed line shows the systemic velocity of the foreground galaxy stack and the black error bar at the bottom shows the effective spectral resolution. Spectral regions contaminated by neighboring features are shown in a dotted line style. This plot differs from Figure 2.9 in that several transitions are being compared at a fixed D_{tran}, as opposed to comparing the effect of D_{tran} for a fixed transition.

Table 2.1: DTB Equivalent Width Measurements and Model Fits[a]

Line	λ (Å)	W_λ^b (Å)	$W^c_{\lambda,\mathrm{corr}}$ (Å)	γ_{out}	R_{eff} (kpc)	v_1 (km s^{-1})	$f_{c,\mathrm{max,out}}$
Si III	1206.51	1.09 ± 0.06	2.19 ± 0.12	0.19 ± 0.01	> 250	711 ± 102	0.43 ± 0.06
Lyα	1215.67	...	...	0.33 ± 0.02	> 250	734 ± 150	0.67[e]
Si II	1260.42	1.38 ± 0.03	2.75 ± 0.06	0.25 ± 0.03	> 250	709 ± 32	0.52 ± 0.02
O I	1302.2	1.00 ± 0.02[d]	2.01 ± 0.05	0.27 ± 0.03	92 ± 22	616 ± 25	0.43 ± 0.02
Si II	1304.4	1.16 ± 0.02[d]	2.31 ± 0.05	0.41 ± 0.06	123 ± 37	704 ± 28	0.44 ± 0.02
C II	1334.53	1.16 ± 0.02	2.31 ± 0.05	0.20 ± 0.01	191 ± 78	632 ± 23	0.46 ± 0.02
Si IV	1393.76	1.23 ± 0.02	2.47 ± 0.04	0.33 ± 0.03	> 250	685 ± 21	0.44 ± 0.01
Si IV	1402.77	0.78 ± 0.02	1.55 ± 0.04	0.24 ± 0.04	> 250	664 ± 20	0.28 ± 0.01
Si II	1526.72	1.39 ± 0.02	2.77 ± 0.04	0.31 ± 0.02	114 ± 62	655 ± 19	0.48 ± 0.01
C IV	1549.0	1.50 ± 0.02	3.00 ± 0.05	0.27 ± 0.01	> 250	822 ± 26	0.40 ± 0.01
Fe II	1608.45	0.70 ± 0.02	1.40 ± 0.04	0.32 ± 0.07	102 ± 34	596 ± 17	0.25 ± 0.01
Al II	1670.81	1.02 ± 0.03	2.04 ± 0.05	0.44 ± 0.09	100 ± 52	616 ± 20	0.35 ± 0.01

[a] The full set of foreground galaxies in this sample have median stellar mass $\log(M_*/\mathrm{M}_\odot) = 9.6 \pm 0.8$ (Figure 2.3).

[b] W_λ are measured equivalent widths from DTB spectra ($D_{\mathrm{tran}} = 0$ kpc). W_λ(C IV) is computed by integrating over the full doublet.

[c] $W_{\lambda,\mathrm{corr}}$ are corrected equivalent widths assuming one is looking through a full halo endowed with a symmetric velocity distribution (i.e. $W_{\lambda,\mathrm{corr}} = 2\,W_\lambda$). The DTB $W_{\lambda,\mathrm{corr}}$ are used in Figure 2.5.

[d] At the spectral resolution of the sample, the DTB O I λ1302 and Si II λ1304 lines are blended. We measure W_λ(1304.4) by scaling the Si II λ1260 profile to the red wing of the Si II λ1304 absorption feature; W_λ(1302.2) is computed by subtracting off the scaled Si II λ1260 profile from the blended (O I + Si II) profile and measuring the residual absorption.

[e] $f_{c,\mathrm{max}}$(Lyα) is the sum of the two best fit $f_{c,\mathrm{max}}$ components in the 2D model. See Section 2.6 and Table 2.2 for details.

As a group, the high ions (Si III, C IV, and Si IV) have shallower declines in W_λ with $D_{\rm tran}$ compared to the low ions. Whereas the low ions (excluding Si II λ1260) become undetectable within $D_{\rm tran} \leq 250$ kpc, the high ions are present over the full range of $D_{\rm tran}$ sampled. C II, Si II, O I, and Lyα are all consistent with one another in their W_λ dependence (especially at $D_{\rm tran} \lesssim 100$ kpc) while weaker transitions like Al II and Si II λ1526 tend to fall off the fastest with projected distance. The exception to this trend is Si II λ1260 which tracks Si II λ1526 steadily until $D_{\rm tran} \simeq 50$ kpc but maintains a larger W_λ beyond that impact parameter.

We compare the Si II λ1260 and Si II λ1526 W_λ ratios to see how Si II optical depth varies with $D_{\rm tran}$. Down the barrel, $W_\lambda(1260)/W_\lambda(1526) = 1$ (Table 2.1) implying both Si II λ1260 and Si II λ1526 are strongly saturated. However, the DTB spectra in the top left panel of Figure 2.10 show a divergence of velocities between Si II λ1260 (green) and Si II λ1526 (orange) on the blue side of the line suggesting that high velocity outflowing gas may be less strongly saturated than gas at $\Delta v \gtrsim -200$ km s^{-1}. Comparing $W_\lambda(1260)$ and $W_\lambda(1526)$ with $D_{\rm tran}$ (see Figures 2.5 and 2.10), we find Si II remains saturated through $D_{\rm tran} \simeq 50$ kpc, at which point $W_\lambda(1526)$ begins to fall off more rapidly than $W_\lambda(1260)$. At $D_{\rm tran} \simeq 75$ kpc, $W_\lambda(1260)/W_\lambda(1526) \approx 2$ ($\tau(1526) \simeq 1.7$, assuming the flat part of the curve of growth). We note that $W_\lambda(1260)/W_\lambda(1526) = 6.25$ in the optically thin limit so beyond $D_{\rm tran} \simeq 100$ kpc, Si II λ1526 is unsaturated and we measure an optically thin Si II column density of $\log(N(\text{Si II})/\text{cm}^{-2}) \simeq 12.9$. We lack sufficient S/N to measure both transitions beyond $D_{\rm tran} \simeq 125$ kpc.

Figures 2.9 and 2.10 provide two complementary views on how each ion evolves with $D_{\rm tran}$ and how the profiles between transitions compare. While all lines show a decrease in absorption strength and velocity dispersion with increasing $D_{\rm tran}$, the higher ionization lines like C IV and Si IV have a slightly broader velocity range at all $D_{\rm tran}$ than observed for O I and C II. Unlike the other transitions, Si IV has an extended red wing that extends to $v_{\rm LOS} \simeq 700$ km s^{-1} for $D_{\rm tran} \lesssim 50$ kpc and similar to C IV, $W_\lambda(1393)/W_\lambda(1402)$ increases with $D_{\rm tran}$ as $N(\text{Si IV})$ decreases. The dichotomy between lower and higher ionization species is in agreement with previous QSO studies (see e.g. Rauch et al., 2001; Rudie et al., 2019) which have shown that higher ionization species probe a wider range of both $N_{\rm HI}$ and velocity.

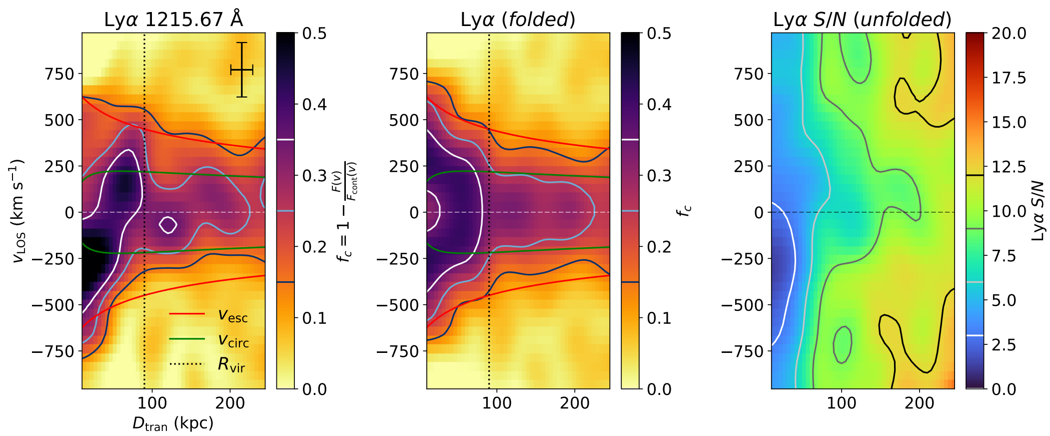

Figure 2.11: *Left:* Maps of Lyα covering fraction (f_c; Equation 2.3) as a function of $v_{\rm LOS}$ and $D_{\rm tran}$. The darker regions correspond to deeper absorption troughs and thus higher covering fractions. *Center:* f_c(Lyα) folded about $v_{\rm LOS} = 0\,{\rm km\,s^{-1}}$. *Right:* The Ly$\alpha$ S/N map, associated with the unfolded Lyα map (computed over the full range of $v_{\rm LOS}$). The escape velocity, circular velocity, and virial radius for a $M_{\rm halo} = 10^{12}$ M$_\odot$ NFW halo are denoted in red, green, and black, respectively. Contours are plotted where applicable on each respective colorbar. Lyα contours are separated by $\Delta f_c = 0.1$ and S/N contours proceed in increments of three i.e., $\Delta(S/N) = 3$. The black error bar in the top right of the left-hand panel shows the average bin size and effective LOS velocity resolution.

Like the DTB spectra, Figure 2.10 shows that all of the low ions and all of the high ions share similar respective profiles. The velocity extent of the metal lines agree to within $\sim$ 100 km s^{-1} in the $D_{\rm tran} \simeq 32$ kpc bin and the amplitudes are consistent to within the bootstrap uncertainties. The decreasing absorption strength with $D_{\rm tran}$ makes this type of comparison more difficult at larger projected distances due to the reduced S/N in each line, so we restrict these plots to $D_{\rm tran} \lesssim 50$ kpc. Of the low ionization lines, O I and C II show the best agreement with one another for $D_{\rm tran} \lesssim 50$ kpc.

2-D Absorption Maps

In addition to one-dimensional spectra, we constructed a two-dimensional map of covering fraction

$$f_c = 1 - \frac{F(v)}{F_{\rm cont}(v)}, \qquad (2.3)$$

as a function of $v_{\rm LOS}$ and $D_{\rm tran}$; this is shown in Figure 2.11. In Equation 2.3, $F(v)$ is the flux density measured for a stacked spectrum and $F_{\rm cont}(v)$ is the level of the continuum. When working with normalized spectra,

$F_{\rm cont}(v)$ would naturally be one. Recall that the covering fraction f_c is best interpreted as an excess optical depth (at a particular velocity and $D_{\rm tran}$) since we do not measure the *total* optical depth along the line of sight. For ease of visualization, we "fold" the Lyα map about $v_{\rm LOS} = 0\,{\rm km\,s^{-1}}$ by taking the average of the red and blue halves of the velocity range. In other words, $f_c(D_{\rm tran}, v_{\rm LOS}) = \langle f_c(D_{\rm tran}, \pm v_{\rm LOS})\rangle$; the folded map is shown in the middle panel of Figure 2.11.

We know from QSO sightlines through the CGM for a fraction of the galaxies in this sample that H I and metals at these projected distances are clumpy and comprise several discrete velocity components (Rudie et al., 2012). Although absorption is seen at velocities $|\Delta v| < 700$ km s^{-1}, the individual velocity components do not span the full range of velocities meaning large swaths of velocity space may show little to no absorption. Where present however, most complexes have $N_{\rm HI} \gtrsim 10^{14.5}$ cm^{-2} such that Lyα is saturated. At low resolution, as in Figure 2.11, the Lyα absorption profile shows the variation in velocity and f_c of the clumps along the line of sight.

On that point, the two-dimensional maps in Figure 2.11 illustrate the spatial and velocity extent of Lyα with the corresponding S/N shown in the right-hand panel. Given that these are compilations of one-dimensional stacks (selected examples of which are shown in Figure 2.7), they support the assertions made in Section 2.5, i.e. Lyα starts out with extended absorption at small $D_{\rm tran}$ which becomes shallower (both in f_c and $v_{\rm LOS}$) as galactocentric radius increases. The two-dimensional representation highlights the location of the velocity centroid and how that evolves with $D_{\rm tran}$. Interestingly, Lyα absorption is the strongest within $D_{\rm tran} \lesssim 50$ kpc at $v_{\rm LOS} \simeq -250\,{\rm km\,s^{-1}}$, indicative of a blue-dominated velocity asymmetry. Moving to larger $D_{\rm tran}$, the velocity centroid shifts to $v_{\rm LOS} \simeq 100$ km s^{-1} by $D_{\rm tran} \simeq 80$ kpc and Lyα absorption appears skewed by $\Delta v \simeq +100$ km s^{-1} for $D_{\rm tran} \lesssim 200$ kpc. Both of these asymmetries are discussed in Appendix 2.10.

2.6 A semianalytic model

In the vein of Steidel et al. (2010) and Y. Chen et al. (2020), we constructed a simple analytic model to reconcile DTB observations and absorption from composite spectra with $D_{\rm tran} > 0$ kpc. This model is empirically motivated and attempts to broadly capture the trends we measure in the foreground and background spectra: a general decrease in LOS velocity spread and covering fraction with D_{tran}. We begin by introducing the model parameters, then establish models for the metal ions that reproduce the measured W_λ vs. D_{tran} distribution observed in Figure 2.5 (Section 2.6). In Section 2.6, we configure the model to output 2-D maps of covering fraction and use it to better understand the main features in measured the 2-D Lyα f_c distribution (Figure 2.11).

Modeling 1-D Composites

Given its simplicity and its prior success in matching the observed change in W_λ with D_{tran}, we apply the Steidel et al. (2010) outflow model to the current dataset. We provide an overview of the model in this work and direct the reader to that study for a complete description and motivation for each parameter. As discussed in Section 2.5, for a saturated transition observed at low resolution (i.e. $R \simeq 1000$ for our sample), the absorption line profile depends on f_c and the velocity (v) of gas along the line of sight. The Steidel et al. (2010) model uses a simple parameterization of these two components (f_c, v) to generate line profiles whose W_λ are consistent with the W_λ vs. D_{tran} distribution. We tailor this model to fit our W_λ measurements (Figure 2.5) below.

The model velocity profile assumes an NFW halo (Navarro et al., 1996, 1997) where outflowing gas is initially accelerated to a maximum velocity v_1 within a galactocentric radius $r \simeq 1$ kpc and subsequently decelerates with increasing D_{tran} solely under the influence of gravity. The outflowing radial velocity field is defined such that

$$v_{\text{out}}(r) = \sqrt{v_1^2 + A\left(-\ln\frac{R_s + 1}{R_s} + \frac{1}{r}\ln\frac{R_s + r}{R_s}\right)}, \tag{2.4}$$

where the NFW scale radius $R_s = 27$ kpc ($R_{\text{vir}} \simeq 90$ kpc, given a concentration parameter $c = 3.3$) and

$$A = \frac{8\pi G\rho_0 R_s^3}{1\,\text{kpc}} \simeq 1.2 \times 10^7\,\text{km}^2\,\text{s}^{-2} \tag{2.5}$$

for a NFW halo at $z \simeq 2.3$ with mass $M_{\text{halo}} = 10^{12}$ M$_\odot$. The NFW halo parameters are from Y. Chen et al. (2020) and were chosen to match the mean KBSS halo.

Analogous to Steidel et al. (2010), the gas opacity depends on a radially varying covering fraction $f_c(r)$ such that $f_{c,\mathrm{out}}(r) = f_{c,\mathrm{max,out}} r^{-\gamma_{\mathrm{out}}}$ where $f_{c,\mathrm{max,out}}$ is the maximum covering fraction used to normalize the distribution, γ_{out} is the power law index, and r is once again the galactocentric radius. The radial power-law form is a natural choice and, based on our experiments, resulted in reasonable W_λ predictions over the range of D_{tran} sampled. Following Steidel et al. (2010), we define $f_{c,\mathrm{max,out}}$ as the deepest part of the absorption trough, relative to the continuum, and measure $f_{c,\mathrm{max,out}}$ for each ion using the composite DTB spectrum (see e.g. Figure 2.4).

Since the velocities we measure relative to the foreground galaxy systemic redshift are projected along our LOS, we set up two grids: one in terms of projected distance (D_{tran}) and the other over a range of line of sight distances (ℓ) such that each combination of of D_{tran} and ℓ form a right triangle satisfying $r^2 = \ell^2 + D_{\mathrm{tran}}^2$. The line of sight velocity for a given component is therefore

$$v_{\mathrm{LOS}}(D_{\mathrm{tran}}, \ell) = \frac{\ell}{r} v(r) = \frac{\ell}{\sqrt{D_{\mathrm{tran}}^2 + \ell^2}} v(r). \tag{2.6}$$

For each $(D_{\mathrm{tran}}, \ell)$ grid point, we measured velocities and covering fractions and projected each into the $v_{\mathrm{LOS}} - D_{\mathrm{tran}}$ plane using Equation 2.6. For the low ions whose W_λ fall off precipitously within $D_{\mathrm{tran}} \leq 250$ kpc, we fit a maximum outflow radius (R_{eff}) beyond which there is no absorption. In the case of the high ions (which extend beyond $D_{\mathrm{tran}} = 250$ kpc), we set $R_{\mathrm{eff}} = 500$ kpc (twice the maximum D_{tran} of the pair sample) or to the radius where f_c was below the noise level of the observed composite spectra to ensure f_c represented absorption associated with the galaxy and not the IGM.

The predicted $W_\lambda(D_{\mathrm{tran}})$ are shown in Figure 2.5 and their associated parameters are in Table 2.1. The uncertainties on the model parameters are derived from bootstrap resampling of the composite spectra (discussed in Sections 2.4 and 2.5). The model captures the shallow dependence of W_λ on D_{tran} reasonably well and the initial gas velocities (v_1) are consistent with the maximum outflow velocities measured in the DTB spectra. We concede that R_{eff} is clearly an unphysical simplification as real outflows are unlikely to have such well-defined "edges", but including this parameter allows for an accurate reproduction of the rapid decline in low ion W_λ with decreasing column densities.

Modeling the 2-D Map

Given the successful fits to W_λ in Figure 2.5, we attempted to fit the 2-D Lyα absorption maps in a manner similar to Y. Chen et al. (2020). Despite having slightly different parameterizations for each component and different output formats, we note that the Steidel et al. (2010) and Y. Chen et al. (2020) models fundamentally operate in the same way: both construct grids of f_c and $v_{\rm LOS}$ to make absorption line profiles as functions of $D_{\rm tran}$; the Steidel et al. (2010) model focuses on fitting W_λ while the Y. Chen et al. (2020) model fits the Lyα kinematics. The similarities between the current and previous two models allowed us to extend the current model to output Lyα absorption maps. Importantly, our sample is restricted to $D_{\rm tran} \leq 250$ kpc, while the Y. Chen et al. (2020) sample extends to $D_{\rm tran} \simeq 4$ Mpc.

We fit the Lyα absorption map using the outflow component defined in Section 2.6, and to add additional opacity near $v_{\rm LOS} = 0$ km s^{-1}, we added a random velocity component that takes on a Gaussian velocity distribution with constant velocity width (σ_v) with radius[9]. In contrast to Y. Chen et al. (2020), we neglect the Hubble expansion due to the close-in range of $D_{\rm tran}$ sampled. This represents the simplest parameterization of the non-outflowing gas motions we observe. Again, we let the covering fraction vary radially such that $f_{c,\rm r}(r) = f_{c,\rm max,r} r^{-\gamma_{\rm r}}$ where each symbol takes on a similar meaning to those defined above. For simplicity, the random velocity component operates independently of the outflowing component. Since Lyα extends beyond $D_{\rm tran} = 250$ kpc, we again set $R_{\rm eff} = 500$ kpc to ensure only absorption associated with the galaxy is considered.

2-D Model Results

The observed Lyα map has $\Delta v_{\rm LOS} = 50$ km s^{-1} and $\Delta D_{\rm tran} = 5$ kpc sampling Given the simplicity of the model and its inability to capture small variations in covering fraction, we smoothed the observed Lyα maps with a 2 pix × 2 pix Gaussian kernel ($\sigma_{D_{\rm tran}} = 10$ kpc and $\sigma_{v_{\rm LOS}} = 100$ km s^{-1}) so the broad

[9]As discussed in Y. Chen et al. (2020) and based on experimentation with the current sample, a one-component "outflow only" model is insufficient to reproduce the observed trends in the 2-D Lyα absorption map.

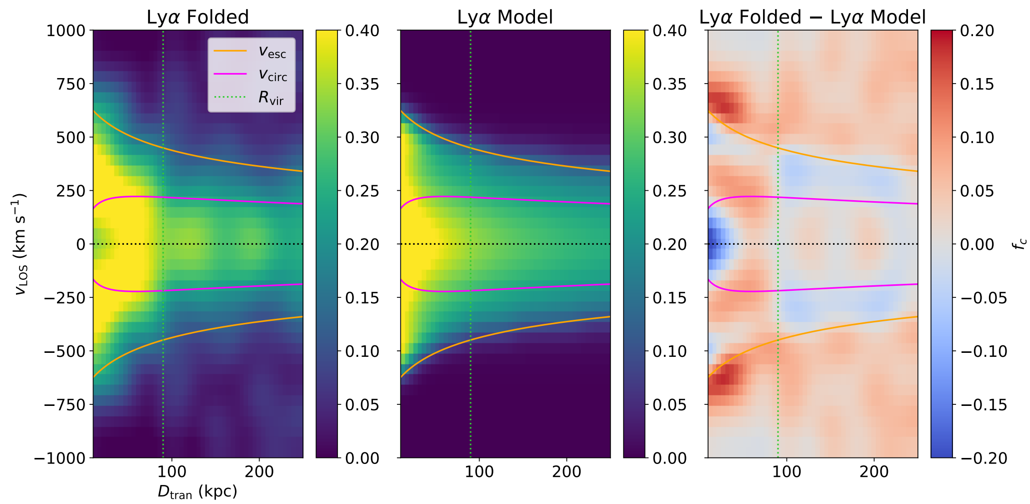

Figure 2.12: *Left:* Measured Lyα covering fraction folded about $v_{\rm LOS} = 0$ km s^{-1}; *Middle:* Lyα best-fit (outflow and random velocity gas) model; *Right:* Lyα absorption residuals (data − model). The observed and model heatmaps have the same colorbar. The escape and circular velocities for a $M_{\rm halo} = 10^{12}$ M$_\odot$ NFW halo are shown in orange and magenta respectively in conjunction with the approximate virial radius (lime green). The best-fit model parameters are listed in Table 2.2.

trends were captured and the fitting procedure was facilitated. Since the model is symmetric around $v_{\rm LOS} = 0$ km s^{-1}, we use the folded map to compensate for the asymmetry in the measured Lyα absorption (especially at $D_{\rm tran} \lesssim 50$ kpc). We argue in Appendix 2.10 that this asymmetry results from foreground Lyα emission contributing to the background absorption feature, so the folded map bears a closer resemblance to the unaffected signal.[10] We employ the `emcee` (Foreman-Mackey et al., 2013) Markov chain Monte Carlo (MCMC) sampler to find the best fit to the six (v_1, σ_v, $f_{c,\rm max,out}$, $f_{c,\rm max,r}$, $\gamma_{\rm out}$, and γ_r) model parameters given the smoothed Lyα covering fraction and uncertainty maps.[11] We require the fit σ_v to have a velocity consistent with the random velocity dispersion of a 10^{12} M$_\odot$ halo. The best fit model is shown in the middle panel of Figure 2.12 and the parameters used to generate it are enumerated in Table 2.2.

[10]The "hole" in the folded Lyα map at $(D_{\rm tran}, v_{\rm LOS}) = (0, 0)$ most likely results from foreground Lyα emission.

[11]Since the observed Lyα map is constructed using overlapping bins, in fitting we boost the measured bootstrap uncertainties by $\simeq 7\%$ (the largest difference in uncertainty between the adopted binning scheme and a set of independent bins) to account for bin-to-bin covariance.

Table 2.2: Best Fit Model Parameters

Component	Parameter	Value
Outflow	v_1 (km s^{-1})	$781\,^{+73}_{-77}$
	$f_{c,\,\mathrm{max,\,out}}$	$0.26\,^{+0.25}_{-0.19}$
	γ_{out}	$0.40\,^{+0.21}_{-0.17}$
Random Velocity	σ_v (km s^{-1})	$219\,^{+32}_{-34}$
	$f_{c,\,\mathrm{max,\,r}}$	$0.41\,^{+0.32}_{-0.38}$
	γ_r	$0.32\,^{+0.36}_{-0.22}$

In comparing the best fit models between Y. Chen et al. (2020) and our study we first recall that the range of D_{tran} sampled in Y. Chen et al. (2020) span galactocentric radii larger by an order of magnitude than our current sample. With this in mind, we note a few distinctions. The initial outflow velocity (v_1) is larger by 30% in the current sample ($781\,^{+73}_{-77}$ km s^{-1} vs. $603\,^{+5}_{-11}$ km s^{-1}) and the velocity of gas near the systemic velocity (σ_v) is a factor of $\simeq 2.6$ greater in magnitude ($219\,^{+32}_{-34}$ km s^{-1} vs. $-84\,^{+6}_{-6}$ km s^{-1}). The finer sampling and higher velocity resolution of the current sample means low-f_c, high-v_{LOS} gas is more readily detectable than in the Y. Chen et al. (2020) sample. Intuitively, the outflowing component in the model establishes a high velocity (relatively low optical depth) envelope while the non-outflowing velocity component adds additional opacity at lower velocities centered around $v = 0$ km s^{-1}. Since the gas with the highest galactocentric velocity in both Y. Chen et al. (2020) and this sample is found at $D_{\mathrm{tran}} \lesssim 60$ kpc, those are the impact parameters that fix the model parameters of the outflowing component. In contrast, an H I overdensity with $|v| < 200$ km s^{-1} was observed throughout the full 4 Mpc range in Y. Chen et al. (2020), gradually decreasing in optical depth with D_{tran}. When restricted to $D_{\mathrm{tran}} < 250$ kpc, the velocity field appears considerably more active than at larger galactocentric radii so the constant velocity component (centered at $v_{\mathrm{LOS}} = 0$ km s^{-1}) will naturally take on a correspondingly higher value to match that velocity spread. It is for this reason that although functionally similar to the "inflow" component of the Y. Chen et al. (2020) model, we associate this component with gas with random velocities or high optical depth non-radial flows since it is unlikely that the excess optical depth at these galactocentric distances and velocities results strictly from "inflowing" material.

The random velocity gas has a covering fraction similar to that of the outflowing component, that is, $f_{c,\,\mathrm{max,\,r}} \sim f_{c,\,\mathrm{max,\,out}}$ contrary to what was previously seen in Y. Chen et al. (2020). One can consider this element of the model as absorption due to gas with velocities $v_{\mathrm{LOS}} \lesssim 300$ km s^{-1}, similar to but not the same as an ISM component to a down-the-barrel absorption line profile in a galaxy with outflowing material. For our sample, the ratio $f_{c,\,\mathrm{max,\,r}}/f_{c,\,\mathrm{max,\,out}} \simeq 1$ suggests (perhaps unsurprisingly) most of the gas in the CGM ($D_{\mathrm{tran}} < 250$ kpc) is relatively slow moving ($v_{\mathrm{LOS}} \lesssim 300$ km s^{-1}) but there exists an appreciable component of outflowing material.

More quantitatively, Figure 2.12 shows the circular and escape velocities for a $M_{\mathrm{halo}} = 10^{12}$ M$_{\odot}$ NFW halo. These curves treat $r = D_{\mathrm{tran}}$ and do not account for velocity projection effects so the real radii may be larger and LOS velocities may be smaller. As expected, the circular velocity approximately matches the random velocity component since both are constrained by the gravitational potential well of the average host galaxy. We observe the escape velocity at the virial radius $v_{\mathrm{esc}}(R_{\mathrm{vir}}) \approx 400$ km s^{-1} is close to the maximum velocity associated with the outflowing component. While most of the absorbing gas has velocities less than the escape velocity (since those are the velocities where this type of map is most sensitive), a nontrivial fraction has the possibility of escaping the halo. As discussed in Section 2.5, Lyα absorption is not the best probe of high velocity gas since higher ionization lines sample a larger cross-section of the CGM, but the fact that a nominal amount of H I exceeds v_{esc} supports this hypothesis.

As discussed in Y. Chen et al. (2020) and above, the strictly radial dependence of velocity and covering fraction is clearly an oversimplification of a complex environment. With the improved resolution in both v_{LOS} and D_{tran}, this simplification becomes even more suspect. We measure a clumpy distribution of Lyα absorption due to variance in the constituent galaxy stacks; two examples of regions with higher than average opacity can be seen in the left panel of Figure 2.12 at $D_{\mathrm{tran}} \simeq 125$ kpc and $D_{\mathrm{tran}} \simeq 175$ kpc. To model these semianalytically, either non-radial covering fraction and velocity profiles would need to be implemented or a third component would need to be added for this express purpose, but since these features are most likely systematic noise, further complications to the model may be unjustified. That being said, the qualitative picture of outflowing material superposed with ambient CGM gas bound to the galaxy is supported by both the Lyα map and model.

Interestingly, the observed Lyα map (Figure 2.11) has a step in the velocity field at approximately the virial radius for the average foreground galaxy halo ($R_{\rm vir} \simeq 80$ kpc) where the velocity spread decreases from ~ 750 km s^{-1} to ~ 500 km s^{-1}; we denote the approximate virial radius as a green dotted line in the left panel of Figure 2.12. Despite its simplicity, the random velocity component of the model shows a marked downturn in absorption strength at approximately the same projected distance. We conjecture that this could be a site where outflowing and inflowing gas are both present and would therefore result in a smaller average velocity when measured spectroscopically. The data are unable to show the degree (or lack thereof) to which the two components interact or mix but considering that the model treats the outflowing and random velocity components as separate sources of excess absorption, even noninteracting gas streams may produce this "pinch" in the velocity field. In a situation where the two components interact, the effect on the line of sight velocities could be more pronounced.

Table 2.3: Absorption Strength (W_λ) vs. Foreground Galaxy Properties

Composite[a]	W_λ(Lyα)			W_λ(C IV λ 1549)[b]			
	[8, 70] (51)[c] (Å)	[70, 100] (86) (Å)	[100, 250] (188) (Å)	DTB[d] (Å)	[8, 70] (51) (Å)	[70, 100] (86) (Å)	[100, 250] (188) (Å)
$\log(M_*/\mathrm{M}_\odot) = 9.0 \pm 0.5$	0.85 ± 0.20	1.03 ± 0.14	0.63 ± 0.07	1.77 ± 0.03	0.47 ± 0.10	0.71 ± 0.09	0.23 ± 0.05
$\log(M_*/\mathrm{M}_\odot) = 9.6 \pm 0.3$	2.33 ± 0.25	1.70 ± 0.21	1.01 ± 0.07	3.35 ± 0.02	1.04 ± 0.12	0.99 ± 0.13	0.25 ± 0.04
$\log(M_*/\mathrm{M}_\odot) = 10.2 \pm 0.4$	1.74 ± 0.22	2.21 ± 0.16	0.80 ± 0.08	3.69 ± 0.02	1.65 ± 0.11	0.99 ± 0.11	0.44 ± 0.04
$\log[\mathrm{SFR}/(M_\odot\,\mathrm{yr}^{-1})] = 0.6 \pm 0.3$	1.82 ± 0.19	1.31 ± 0.14	0.74 ± 0.06	2.35 ± 0.02	0.75 ± 0.09	0.86 ± 0.08	0.43 ± 0.03
$\log[\mathrm{SFR}/(M_\odot\,\mathrm{yr}^{-1})] = 1.2 \pm 0.3$	1.36 ± 0.15	1.15 ± 0.14	0.77 ± 0.05	3.75 ± 0.01	1.13 ± 0.09	0.98 ± 0.10	0.31 ± 0.03
$\log(\mathrm{sSFR}/\mathrm{Gyr}^{-1}) = -0.2 \pm 0.4$	1.62 ± 0.19	1.27 ± 0.15	0.76 ± 0.06	3.24 ± 0.02	0.90 ± 0.08	0.59 ± 0.08	0.33 ± 0.03
$\log(\mathrm{sSFR}/\mathrm{Gyr}^{-1}) = 0.6 \pm 0.5$	1.38 ± 0.17	1.00 ± 0.15	0.79 ± 0.05	3.05 ± 0.01	0.67 ± 0.10	1.03 ± 0.09	0.18 ± 0.03
$E(B-V) = 0.07 \pm 0.04$	2.03 ± 0.15	1.23 ± 0.14	0.74 ± 0.05	2.95 ± 0.01	0.84 ± 0.07	0.89 ± 0.09	0.19 ± 0.03
$E(B-V) = 0.12 \pm 0.05$	1.18 ± 0.18	1.44 ± 0.14	0.89 ± 0.06	3.63 ± 0.02	1.44 ± 0.09	1.08 ± 0.08	0.28 ± 0.03
Full Sample	1.42 ± 0.09	0.90 ± 0.09	0.76 ± 0.04	3.00 ± 0.05	0.79 ± 0.06	0.67 ± 0.06	0.26 ± 0.02

[a] The pair sample is split into tertiles in M_*; the remaining subsamples are formed by splitting the pair sample in half at the median value of the stellar population parameter. Each subsample's median value and interquartile range are shown; see Figure 2.3 for the precise ranges of each subsample. The corresponding spectra from which these values are derived are shown in Figures 2.13 and 2.14. Values from the full pair sample are shown in the last row for comparison.

[b] W_λ(C IV) is computed by integrating over the full doublet.

[c] In order: the minimum, maximum, and median D_{tran} (in kpc) for each bin.

[d] The DTB W_λ(C IV) are corrected as discussed in Section 2.5 (cf. $W_{\lambda,\mathrm{corr}}$ in Table 2.1).

Table 2.4: Absorption Second Moments (σ) vs. Foreground Galaxy Properties

Composite	σ(Lyα)			σ(C IV λ 1549)			
	[8,70] (51) (km s^{-1})	[70,100] (86) (km s^{-1})	[100,250] (188) (km s^{-1})	DTB (km s^{-1})	[8,70] (51) (km s^{-1})	[70,100] (86) (km s^{-1})	[100,250] (188) (km s^{-1})
$\log(M_*/\mathrm{M}_\odot) = 9.0 \pm 0.5$	209 ± 73	232 ± 64	210 ± 49	473 ± 35	89 ± 89	343 ± 51	457 ± 72
$\log(M_*/\mathrm{M}_\odot) = 9.6 \pm 0.3$	299 ± 28	281 ± 36	215 ± 28	544 ± 8	282 ± 54	352 ± 48	475 ± 40
$\log(M_*/\mathrm{M}_\odot) = 10.2 \pm 0.4$	284 ± 32	359 ± 14	231 ± 35	592 ± 5	360 ± 22	274 ± 52	246 ± 47
$\log[\mathrm{SFR}/(M_\odot\,\mathrm{yr}^{-1})] = 0.6 \pm 0.3$	274 ± 32	266 ± 48	234 ± 29	454 ± 16	142 ± 71	370 ± 28	492 ± 18
$\log[\mathrm{SFR}/(M_\odot\,\mathrm{yr}^{-1})] = 1.2 \pm 0.3$	259 ± 40	282 ± 42	166 ± 36	558 ± 5	353 ± 26	301 ± 36	214 ± 52
$\log(\mathrm{sSFR}/\mathrm{Gyr}^{-1}) = -0.2 \pm 0.4$	300 ± 29	304 ± 34	240 ± 27	516 ± 8	250 ± 44	263 ± 83	420 ± 27
$\log(\mathrm{sSFR}/\mathrm{Gyr}^{-1}) = +0.6 \pm 0.5$	233 ± 48	252 ± 54	172 ± 34	551 ± 8	165 ± 79	298 ± 34	255 ± 83
$E(B-V) = 0.07 \pm 0.04$	319 ± 17	229 ± 51	190 ± 33	501 ± 7	136 ± 54	428 ± 27	338 ± 71
$E(B-V) = 0.12 \pm 0.05$	192 ± 53	325 ± 24	234 ± 20	563 ± 6	401 ± 18	248 ± 75	365 ± 35
Full Sample	261 ± 47	224 ± 21	211 ± 18	514 ± 17	232 ± 46	288 ± 87	378 ± 26

Similar to Table 2.3, now with second moment measurements. The DTB σ(C IV) are measured over the full doublet and corrected as discussed in Section 2.5.

2.7 Dependence of CGM Absorption on Galaxy Properties

The current sample of ($z_{\rm fg}$, $z_{\rm bg}$) galaxy pairs is larger in number, spans a larger range of foreground galaxy properties, and has significantly higher effective spectral resolving power than previous galaxy ($z_{\rm fg}$, $z_{\rm bg}$) pair samples at similar redshifts. In this section, we investigate whether sub-samples (in bins of $D_{\rm tran}$) can reveal significant differences in the absorption W_λ and kinematics (σ) when divided according to inferred properties of the foreground galaxies.

Using SED measurements of the foreground galaxies introduced in Section 2.3, we constructed subsamples based on M_*, SFR, sSFR, and $E(B-V)$. As discussed in Appendix 2.10, the stacked spectra we construct are always "pair limited," i.e., the S/N of the spectra and the corresponding ease of detecting absorption features are both proportional to the number of sightlines being averaged. For this reason, the $D_{\rm tran}$ sampling achievable with the SED-based sub-samples is considerably coarser that what was possible using the full sample.

After some experimentation with various $D_{\rm tran}$ bins, we settled on three independent intervals of $D_{\rm tran}$: $D_{\rm tran} = 8-70$ kpc, $70-100$ kpc, and $100-250$ kpc, which have median $D_{\rm tran}$ of 51, 86, and 188 kpc, respectively; the two inner bins contain a total of 208 and 202 galaxy pairs, respectively. We focus on Lyα and C IV absorption, the only lines that are strong enough to allow for splitting the samples into two or three sub-samples according to galaxy properties while maintaining statistical power.

The distributions of galaxy properties inferred from SED fits for this sample are shown in Figure 2.3. While the $D_{\rm tran} = 100-250$ kpc bin has $\simeq 80\%$ of the total foreground galaxies and is thus representative of the full sample, the number of galaxies in the $D_{\rm tran} = 8-70$ kpc and $D_{\rm tran} = 70-100$ kpc bins is smaller by almost an order of magnitude with respect to the $D_{\rm tran} = 100$– 250 kpc bin. That being said, the overall distributions of galaxy properties sampled within each $D_{\rm tran}$ bin remain similar to one another, and representative of the full sample of foreground galaxies.

Initially, we split the four SED-derived distributions in half at their median value, and constructed "low" and "high" sub-samples; see the leftmost column of Table 2.3. Each subsample based on foreground galaxy properties spans approximately 1.5 dex in M_*, 1 dex in SFR and sSFR, and 0.1 mag-

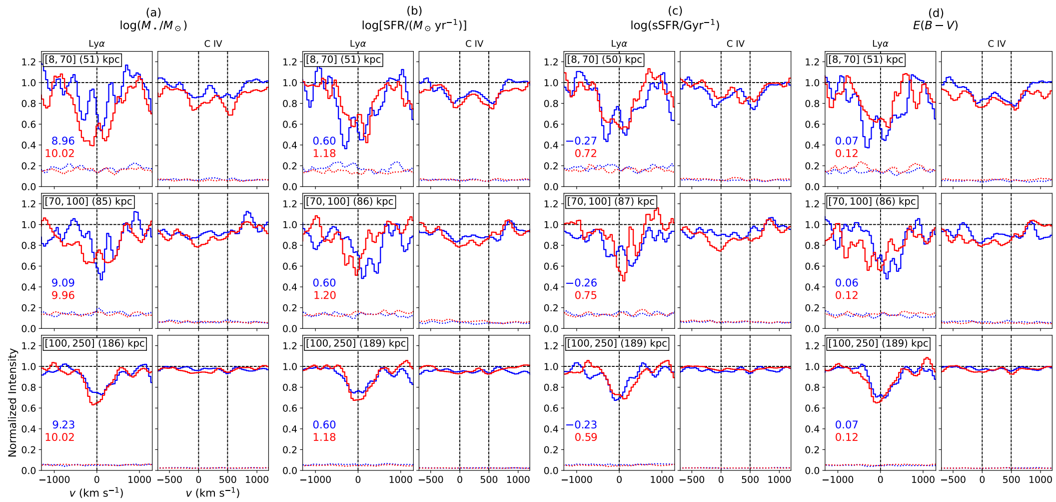

Figure 2.13: Composite spectra in the vicinity of Lyα (left column of each panel) and C IV (right column of each panel) for sub-samples divided less than (blue) and greater than (red) the median value of each of four SED-derived galaxy properties: (a) M_*, (b) SFR, (c) sSFR, and (d) $E(B-V)$. Within each panel, the top spectra compare the results for $D_{\rm tran}$ = 8 − 70 kpc, the middle spectra for $D_{\rm tran}$ = 70 − 100 kpc, and the bottom spectra for $D_{\rm tran}$ = 100 − 250 kpc. The median value of the stellar population parameter is printed in each, color-coded in the same way as the plotted spectra, for the "low" and "high" sub-samples. Error spectra are shown as color-coded dotted lines; the continuum level and systemic velocity of the foreground galaxy are indicated with black dashed lines. Figure 2.3 shows the full distributions of the parameters.

nitudes in $E(B-V)$. For each subsample, we followed the same procedure (see Section 2.3) as the full sample to construct stacked background galaxy spectra that contain foreground objects satisfying a particular galaxy property constraint (e.g. $\log[{\rm SFR}/(M_\odot\,{\rm yr}^{-1})] \leq 0.6$). These stacks were combined using a trimmed mean, renormalized, and line profile measurements were computed for Lyα and C IV. W_λ and σ for each bin and absorption line are given in Tables 2.3 and 2.4, respectively. Spectral cutouts of Lyα and C IV for each galaxy property are shown in Figure 2.13. The top row of plots corresponds to spectra from the $D_{\rm tran}$ = 8 − 70 kpc bin, the middle has $D_{\rm tran}$ = 70 − 100 kpc, and the bottom shows $D_{\rm tran}$ = 100 − 250 kpc composites. The results for C IV are shown in Figure 2.14, discussed below.

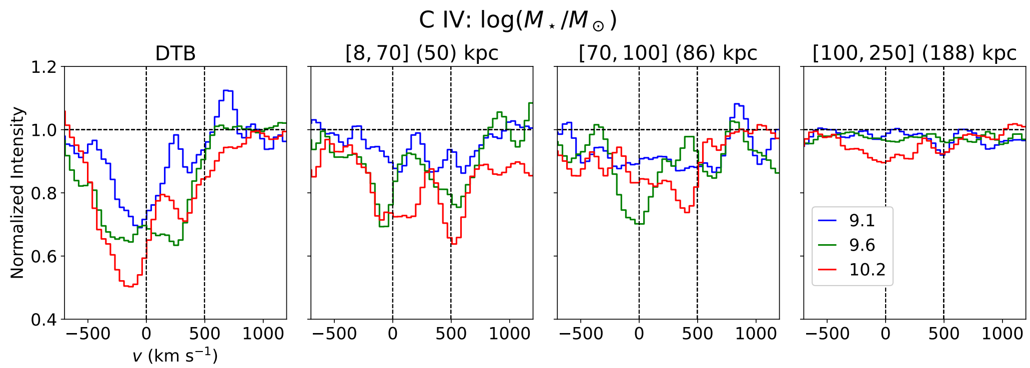

Figure 2.14: C IV absorption profiles for three independent sub-samples of M_*, in four bins of $D_{\rm tran}$: from left to right, DTB ($D_{\rm tran}$ = 0 kpc) spectra, the $D_{\rm tran}$ = 8 – 70 kpc bin, $D_{\rm tran}$ = 70 – 100 kpc bin, and $D_{\rm tran}$ = 100 – 250 kpc bin are shown. Blue, green, and red spectra correspond to the first, second, and third tertiles of M_*. The legend shows the median $\log(M_*/{\rm M}_\odot)$ for each sub-sample.

C IV

The most significant correlation between a galaxy property and the corresponding CGM absorption is found for M_* versus C IV absorption, where the higher-M_* sub-sample has W_λ(CIV) $\simeq 2\times$ greater than the low-M_* bin at all $D_{\rm tran}$ shown in Figure 2.13. Given the difference in C IV strength for the two M_* subsamples, we split the sample into three bins of M_*[12]; the results for C IV in tertiles of M_* are shown in Figure 2.14, where we have included the DTB spectra for each M_* sub-sample. The first three rows of Tables 2.3 and 2.4 summarize the numerical results.

The upper left panel of Figure 2.15 summarizes the W_λ(CIV) measured (as a function of $D_{\rm tran}$) from each mass-binned spectrum. Figure 2.14 shows the C IV absorption profiles for three M_* bins, with median M_* values $\log(M_*/M_\odot)$ = 9.0, 9.6, and 10.2 in four different bins of $D_{\rm tran}$: $\langle D_{\rm tran}\rangle = 0$, $\langle D_{\rm tran}\rangle = 51$, $\langle D_{\rm tran}\rangle = 86$, and $\langle D_{\rm tran}\rangle = 188$ kpc. As the figure shows (see also Table 2.3), the trend of monotonically increasing C IV absorption strength with M_* exists in all four $D_{\rm tran}$ bins, illustrated graphically in the upper lefthand panel of Figure 2.15. The highest mass M_* bin has W_λ(CIV) exceeding that of the lowest-mass bin by factors ranging from 1.9 – 3.5, with the largest difference found for the $\langle D_{\rm tran}\rangle$ = 51 kpc bin, where the spectra for all three M_* bins are detected with very high significance.

[12]Splitting the sample into a larger number of M_* bins results in stacks with an insufficient number of pairs to successfully detect C IV.

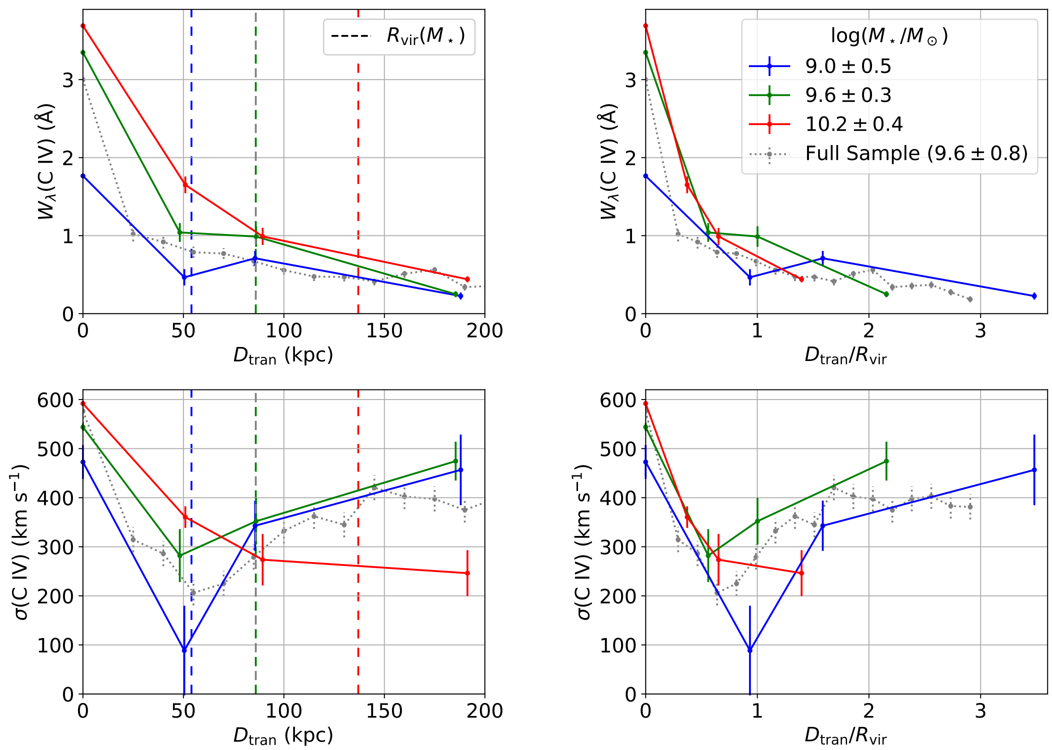

Figure 2.15: Top: W_λ(C IV) vs. D_{tran} (left; see Table 2.3) and projected distance normalized by R_{vir} (right) for the three M_* tertiles (blue, green, and red curves show increasing M_*, as indicated in the legend). Bottom: The line-of-sight velocity second moment σ(C IV) vs. D_{tran} (left; see Table 2.4) and vs. D_{tran}/R_{vir} (right). The plotted values of σ have been corrected for the instrumental contribution as described in Section 2.5. The vertical dashed lines in the two lefthand panels indicate the estimated R_{vir} for the corresponding M_* bin, as discussed in the text. The "Full Sample" data, which provide finer sampling of D_{tran}, are the same as those plotted in Figures 2.5 and 2.6.

It has become common practice to assume that the galactocentric distance to which one expects to observe CGM metals associated with a given galaxy may be related to the virial radius R_{vir} of the corresponding dark matter halos. Figure 2.15a includes vertical dashed, color-coded lines indicating the approximate R_{vir} corresponding each of the three M_* bins. The values adopted are R_{vir} = 53, 86, and 137 kpc for the three M_* bins, based on dark matter halos with $\langle \log(M_{halo}/M_\odot) \rangle = 11.9$ at the median stellar mass $\log(M_*/M_\odot) = 9.6$ for the KBSS sample (R. F. Trainor & Steidel, 2012). We estimated R_{vir} for the other two M_* bins by assuming that the ratio M_*/M_h is the same as that of the full KBSS sample[13]), so that $\langle R_{vir} \rangle \propto M_*^{1/3}$. The upper

[13]The median halo masses for the low-M_* and high M_* bins under this assumption would

right panel of Figure 2.15 shows the same data as the upper left panel, but with $D_{\rm tran}$ scaled by the estimated $R_{\rm vir}$ for each M_* sub-sample. The similar appearance of W_λ(CIV) vs. $D_{\rm tran}/R_{\rm vir}$ for the three M_* sub-samples certainly suggests that $R_{\rm vir}$ may play a significant role in determining the extent of absorbing gas – with the largest changes in the total C IV absorption strength occurring within $R_{\rm vir}$, while all three M_* bins reach a similar "plateau" in W_λ(CIV) between $D_{\rm tran} \sim 1-3\ R_{\rm vir}$.

The average W_λ(CIV) among the M_* bins is affected by both the depth of the absorption features – which depends on the covering fraction and/or the mean N(C IV) as a function of LOS velocity – and on the extent in velocity space of the absorption feature. The latter can be characterized by the second moment σ(C IV), which is shown in the bottom panels of Figure 2.15. The lower left panel shows that the dispersion in velocity of the mean C IV absorption has a similar monotonic behavior of increasing σ(C IV) with M_*, particularly in the inner two bins of $D_{\rm tran}$, and is largely responsible for the most significant difference in absorption strength vs. M_*, in the $\langle D_{\rm tran}\rangle = 51$ kpc bin. The lowest M_*bin reaches a clear minimum σ(C IV) at $\langle D_{\rm tran}\rangle = 51$ kpc, where it is consistent with being unresolved ($\sigma = 89 \pm 89$ km s^{-1}) – and corresponds closely to the estimated $R_{\rm vir}$ for $\langle \log(M_*/M_\odot)\rangle = 9.0$ galaxies.

The values of σ(C IV) for the M_* sub-samples become statistically indistinguishable in the $\langle D_{\rm tran}\rangle = 86$ kpc bin; by $\langle D_{\rm tran}\rangle = 188$ kpc the two lower mass bins have nominal σ(C IV) $\simeq 500$ km s^{-1}, which suggests that, though net C IV absorption is detected, it is not concentrated at the systemic redshift of the foreground galaxy, but is instead nearly uniformly distributed within the velocity window used for the measurement. In contrast, the highest M_* bin has a significantly lower σ(C IV) at large $D_{\rm tran}$, suggesting that the C IV absorbing gas remains gravitationally influenced by the presence of the foreground galaxy, with a line-of-sight velocity dispersion consistent with the circular velocity of the host halos $\log(M_{\rm h}/M_\odot) \simeq 12.5$.

Aside from the M_* dependence of C IV absorption, there is some evidence that the high SFR sub-sample has significantly higher W_λ(C IV) and σ(C IV) than that of the lower-SFR sub-sample, at least for the DTB and $\langle D_{\rm tran}\rangle = 50$ kpc bins (Tables 2.3 and 2.4). A similar trend may be present for the $E(B-V)$ sub-samples, in the sense that more reddened galaxies exhibit stronger C IV

be $\log(M_{\rm halo}/M_\odot) = 11.3$ and 12.5, respectively.

absorption with higher σ(C IV); however, both of these trends might be explained by the correlation of higher SFR and $E(B-V)$ with M_* within the foreground galaxy ensemble.

Lyα

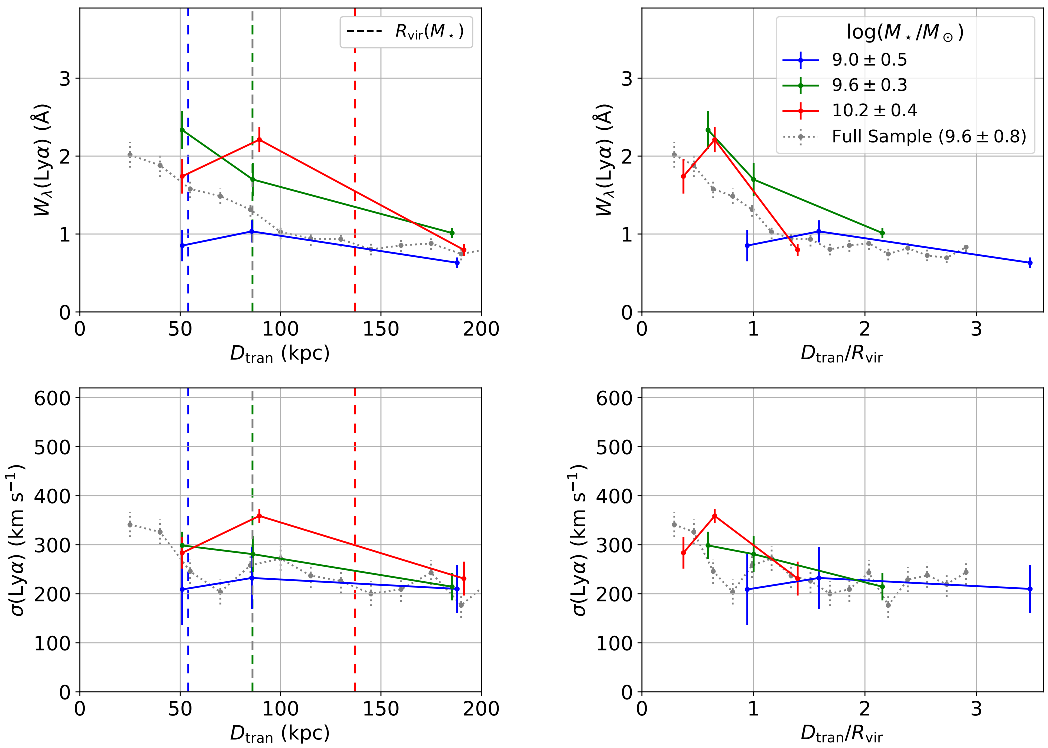

Figure 2.16: As for Figure 2.15, but for Lyα absorption (see Tables 2.3 and 2.4). The "Full Sample" data, which provide finer sampling of $D_{\rm tran}$, are the same as those plotted in Figures 2.5 and 2.6.

While Lyα absorption strength W_λ(Lyα) and velocity dispersion σ(Lyα) generally increase with M_*[14], the trend is not monotonic at all $D_{\rm tran}$, and the differences between M_* sub-samples are significant at $> 2\sigma$ level only within the $\langle D_{\rm tran}\rangle$ = 86 kpc bin, where both W_λ(Lyα) and σ(Lyα) are positively correlated with M_* (Figure 2.16; Tables 2.3 and 2.4). Unlike what was found for C IV (Figure 2.15), there is no significant difference in σ(Lyα) in the $\langle D_{\rm tran}\rangle$ = 188 kpc bin of impact parameter, with values of σ(Lyα) comparable to that of the highest M_* sub-sample for σ(C IV) at the same $D_{\rm tran}$ – likely due to the fact that Lyα remains well-detected ($\gtrsim 10\sigma$) for all 3 M_* sub-samples out to $\gtrsim$ 200 kpc. The large number of galaxy pairs available at

[14]The DTB Lyα absorption is confused by strong Lyα emission in the centers of the foreground galaxies, so we do not attempt a $D_{\rm tran} = 0$ measurement; see Figure 2.7.

large $D_{\rm tran}$, together with a "smoother" local continuum level against which to observe the excess Lyα absorption, helps to suppress the systematic noise in the composite spectra. We discuss the behavior of Lyα kinematics and absorption strength vs. $D_{\rm tran}$ for the full sample in Section 2.6.

The Lyα profiles in the two independent sub-samples of SFR, sSFR, and $E(B-V)$ are largely consistent with one another (Figure 2.13). The profiles become smoother at larger $D_{\rm tran}$ because larger number sightlines are being averaged, but there is no discernible trend across all three bins. Although the sub-samples divided by galaxy properties do not show large variations in Lyα absorption, we again note that the apparent Lyα absorption profiles (both in velocity and apparent optical depth) in the composite spectra of background galaxies for $D_{\rm tran} \lesssim 100$ kpc can be significantly affected by extended Lyα emission from the foreground galaxies. This effect, which depends on the intensity and kinematics of the Lyα emission halos of the foreground galaxies relative to the apparent magnitude of the background galaxies against which the absorption is being measured, may be responsible for some of the stochastic behavior of Lyα absorption profiles. We discuss this issue further in Appendix 2.10, and also in Section 2.6.

2.8 Discussion

The current study further constrains the distribution of baryons in the $z \sim 2$ CGM. Fundamentally, we notice a decrease in W_λ and σ with increasing $D_{\rm tran}$ for all transitions studied. The CGM ionization state changes with $D_{\rm tran}$: W_λ(C II)/W_λ(C IV), W_λ(Si II)/W_λ(Si III), and W_λ(Si II)/W_λ(Si IV) all decrease with $D_{\rm tran}$ consistent with a reduction of cool, dense gas along the line of sight. The decreasing W_λ with approximately constant σ in the low ions can be explained by a decreasing gas column density, either in the metals themselves or in the H I that self-shields them.

Kinematically, σ(Lyα) and σ(C IV) decrease with $D_{\rm tran}$ and both reach a minimum at approximately the virial radius of the average galaxy in our sample. Taken together with the blueshifted absorption features in the DTB spectra, it follows that the gas motions at $D_{\rm tran} \lesssim R_{\rm vir}$ result from optically thick outflows, the fastest of which are localized to within $D_{\rm tran} \lesssim 30$ kpc of the average foreground galaxy. Lyα and C IV within $D_{\rm tran} \lesssim 50$ kpc have absorption at velocities in excess of the escape velocity suggesting that some gas is unbound from the galaxy. This technique is only sensitive to *excess* absorption associated with foreground galaxies so it is not possible to quantify precisely how much gas escapes the system; gas with $v_{\rm LOS} > v_{\rm esc}$ would typically appear as contamination at nearby wavelengths in the composite spectra. We interpret the minimum in the σ vs. $D_{\rm tran}$ distribution as a caustic between outflows that dominated the absorption within $D_{\rm tran} \lesssim$ 100 kpc and gas with velocities less than $v_{\rm circ}$. This represents the extent of the galaxy's influence on its CGM. The absorption at $D_{\rm tran} \simeq R_{\rm vir}$ may result from inflowing gas, which tends to have $\sigma < v_{\rm circ}$ (e.g. Rubin et al., 2012), or the bound ambient CGM. We attribute the increase in σ(C IV) at $D_{\rm tran} \gtrsim 100$ kpc to an increasing number of nearby (but unrelated) C IV systems that serve to broaden the composite C IV absorption profile. These systems are increasingly unlikely to be causally connected with the CGM of the foreground galaxy as $D_{\rm tran}$ increases, but with the current stacking strategy, it is not possible to directly isolate those associated with the foreground system.

In addition to the full sample, the mass-separated Lyα and C IV measurements provide additional clarity into the dynamical signatures of the $z \sim 2$ CGM. The strong dependence of C IV absorption strength on stellar mass suggests that sightlines through higher mass halos are sampling larger CGM volumes. The general agreement between mass subsamples when $D_{\rm tran}$ is normalized by the virial radius further supports this assertion and suggests that $R_{\rm vir}$ – and by extension dark matter halo mass – is a fundamental quantity underpinning the gas distribution of the CGM. Moreover, $R_{\rm vir}$ sets a relative scale over which a galaxy can have a significant effect on its CGM. The overall agreement of σ vs. $D_{\rm tran}/R_{\rm vir}$ may suggest that C IV is similarly distributed throughout halos of varying sizes. Despite the coarse sampling, the slight dependence of σ on M_* (especially at $D_{\rm tran} \lesssim R_{\rm vir}$) supports a picture of feedback where more massive galaxies drive faster outflows, and the outflowing gas associated with more massive galaxies in turn appears to permeate further into the CGM.

Comparison to Prior Observations

The enhanced excess Lyα absorption extending out to the maximum $D_{\rm tran}$ of the sample ($D_{\rm tran} \simeq 250$ kpc) is consistent with Rudie et al. (2012) and Turner et al. (2014) using KBSS QSO lines of sight and Steidel et al. (2010) and Y. Chen et al. (2020) with KBSS galaxy pairs. The measured Lyα equivalent widths and the inferred radial dependence of the covering fraction ($f_c(r) \propto r^{-0.33}$) in particular closely match the dependencies seen in Y. Chen et al. (2020) and Steidel et al. (2010), respectively. The Y. Chen et al. (2020) W_λ(Lyα) measurements are shown in Figure 2.5 (brown curve) for comparison and both W_λ(Lyα) agree well with one another. Note that in Steidel et al. (2010), W_λ(Lyα) at $100 \lesssim \langle D_{\rm tran} \rangle/{\rm kpc} \lesssim 250$ were computed from HIRES spectra of QSO-galaxy pairs while Y. Chen et al. (2020) used galaxy-galaxy pairs for all $D_{\rm tran} \lesssim 4$ Mpc. In addition, we find a reduced in W_λ(Lyα) and σ(Lyα) between $75 \lesssim D_{\rm tran}/{\rm kpc} \lesssim 125$ in accordance with the Y. Chen et al. (2020) results. Given the large overlap in galaxy pairs between Steidel et al. (2010), Y. Chen et al. (2020), and this sample, it is not surprising that the equivalent widths show large agreement.

Outside of the KBSS sample, the anticorrelation between W_λ and $D_{\rm tran}$ for Lyα and metals in the CGM has been well established for galaxies across a range of masses and redshifts. Kacprzak et al. (2020) recently compiled W_λ vs. $D_{\rm tran}$ measurements for Lyα and several far-UV transitions from studies (Bordoloi et al., 2014; Borthakur et al., 2015; Burchett et al., 2016; Johnson et al., 2017; Liang & Chen, 2014; Pointon et al., 2019; Prochaska, Weiner, et al., 2011; Werk et al., 2013) of $9 \leq \log(M_*/{\rm M}_\odot) \leq 11$ galaxies at $z \lesssim 0.3$. Each transition shows a decrease in absorption strength with $D_{\rm tran}$ with the metals showing the most rapid falloff. Analogous to Si II in our sample, at $z \lesssim 1.4$, there is a similar trend between W_λ(Mg II) and σ(Mg II) with $D_{\rm tran}$ (e.g. H.-W. Chen & Zahedy, 2024; Hamanowicz et al., 2020; Martin et al., 2019) in line with the previously listed studies at $z \lesssim 0.3$. While the general trends are similar between low and high redshift star forming galaxies, Lyα and the metal ions have steeper falloffs with $D_{\rm tran}$ at low-z compared to the current $z \sim 2$ sample. The galaxies studied above also tend to have smaller W_λ and overall quieter velocity fields than seen at $z \sim 2$. Indeed, the low-z COS-Burst "starburst" galaxies (**Heckman17**) may offer the most direct comparison in terms of W_λ magnitudes and slope (with $D_{\rm tran}$) to the current sample. It is worth noting that the previously listed studies all use QSOs as their background source which lead to more stochastic gas distributions in comparison to foreground/background galaxy pairs which probe gas on ~ 4 kpc scales (Steidel et al. 2010; the typical half-light diameter of a galaxy in our sample).

At $z \sim 2$, Steidel et al. (2010) modeled gas covering fraction f_c from both H I and metals as power laws of the form $f_c \propto r^{-\gamma}$ and found $0.2 \lesssim \gamma \lesssim 0.6$ at $D_{\rm tran} \lesssim 250$ kpc; applying a similar model to our dataset, we find similarly shallow power law indices: $0.2 \lesssim \gamma \lesssim 0.5$ suggesting a comparable covering fraction evolution with $D_{\rm tran}$. When projected along our line of sight, we observe a faster W_λ falloff in the low ions when compared to the high ions. At face value, this suggests that the column density of the low ions decreases faster than the high ions over the range of projected distances or that the low ions sample a narrower range of CGM velocities and absorbing columns; a result also put forth by Rudie et al. (2019).

While there is good agreement in $v_{\rm LOS}$ between Y. Chen et al. (2020) and this study (see Section 2.5) especially in the high velocity gas at $D_{\rm tran} < 100$ kpc, σ(Lyα) and σ(C IV) are larger by a factor of $\simeq 2$ than the Liang and Chen (2014) velocity measurements of gas surrounding $z < 0.176$ galaxies within $D_{\rm tran} < 250$ kpc. Moreover, Liang and Chen (2014) find gas moving with $v_{\rm LOS} \gtrsim 200$ km s^{-1} almost exclusively arises from $D_{\rm tran} > 250$ kpc sightlines, contrary to our results. The authors speculated that the broad velocity wings may be associated with large-scale filaments; in our case, most of the $v_{\rm LOS} \gtrsim 250$ km s^{-1} excess Lyα absorption likely arises from star formation induced outflows.

Our W_λ(C IV) vs. $D_{\rm tran}$ dependence is consistent with the results of Adelberger et al. (2005), Steidel et al. (2010), and Turner et al. (2014) where the samples have overlap in $D_{\rm tran}$. Adelberger et al. (2005) reported C IV with a velocity spread $\simeq 260$ km s^{-1} for $D_{\rm tran} \lesssim 80$ kpc using galaxy-galaxy pairs and Steidel et al. (2010) extended these measurements to $D_{\rm tran} \simeq 100$ kpc. The W_λ(C IV) measurements from both studies are in agreement with our sample (which recall is a broad superset of theirs); the additional galaxy-galaxy pairs at $D_{\rm tran} > 100$ kpc in our sample enable an analysis that was not possible previously. At $\langle z_{\rm fg} \rangle \sim 2.6$, Méndez-Hernández et al. (2022) measured W_λ(C IV) vs. $D_{\rm tran}$ around 238 star-forming galaxies at $D_{\rm tran} < 173$ kpc. Both this sample and the Méndez-Hernández et al. (2022) measurements are consistent in their slopes and approximate W_λ(C IV) values although the Méndez-Hernández et al. (2022) $D_{\rm tran}$ sampling and spectral resolution are considerably coarser. Surprisingly, the $z \simeq 3.3$ Lyα emitters studied in Muzahid et al. (2021) do not show a W_λ(C IV) vs. $D_{\rm tran}$ dependence. A

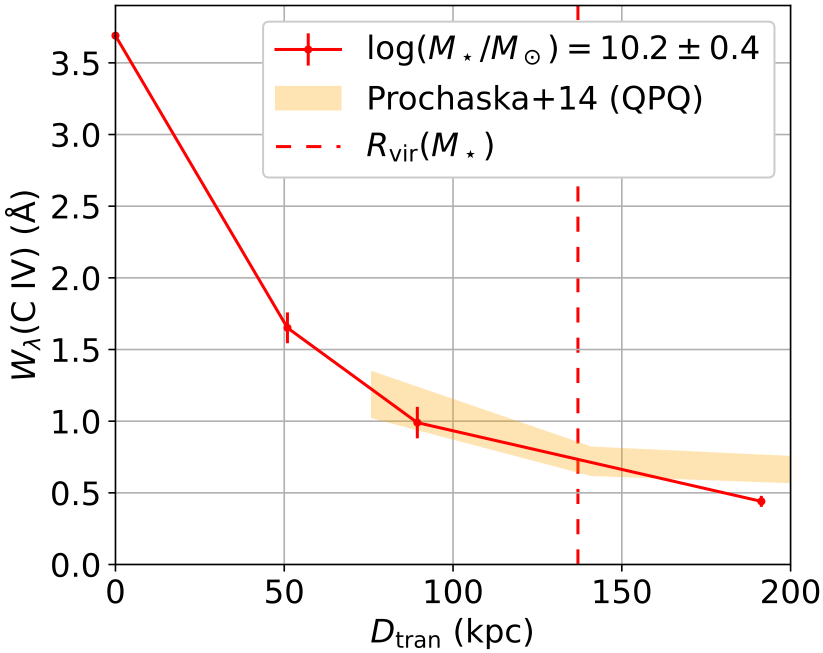

Figure 2.17: W_λ(C IV) vs. D_{tran} for the high mass tertile ($\log(M_*/M_*) \approx 10.2$) of galaxy pairs split by M_* in red (similar color coding to Figure 2.15) and in orange, the average $W_\lambda(1548)$ computed from individual sightlines binned by D_{tran} from the Quasars Probing Quasars (QPQ) survey (Prochaska et al., 2014). The bounds on the orange band represent the dispersion of the individual measurements (see Table 3 in Prochaska et al. 2014). To ensure a fair comparison between samples, we boost the $W_\lambda(1548)$ values by 50% to match the W_λ(C IV) one would measure integrating over a full (optically thin) doublet, as is done in this study. The virial radius for a $\log(M_{halo}/M_*) \approx 12.5$ halo (which both sets of galaxies are expected to inhabit) is plotted as a dashed vertical line.

possible explanation for this discrepancy is that $D_{tran,\,med}$ = 165 kpc for the Muzahid et al. (2021) sample and the largest variability in W_λ(C IV) tends to be at $D_{tran} \lesssim 100$ kpc. Indeed our sample shows only a factor of $\simeq 2$ change in W_λ(C IV) between $D_{tran} \simeq 100$ kpc and $D_{tran} \simeq 250$ kpc.

We estimated that the galaxies in the high mass C IV tertile reside in dark matter halos with masses $M_{halo} \approx 10^{12.5}$ $M_\odot$ (see Section 2.7 and R. F. Trainor and Steidel 2012) and as such, offer an interesting comparison to the sample of $z \simeq 2.3$ QSO-QSO pairs in Prochaska et al. (2014) which probe the CGM around QSOs with comparable halo masses. We find the two sets of W_λ(C IV) measurements agree well and the dependence of W_λ(C IV) on D_{tran} is consistent (Figure 2.17). Evidently, the average C IV halos in the CGM of star-forming galaxies and QSOs with halo masses $M_{\rm halo} \approx 10^{12.5}$ M$_\odot$ are quite similar. In other words, the agreement of W_λ(C IV) between samples suggests the CGM metal distribution at $D_{\rm tran} \gtrsim 70$ kpc ($\sim 0.5R_{\rm vir}$) for halos at these masses appears largely unaffected by the presence of a central QSO.

We observe that $W_\lambda(1548)/W_\lambda(1550)$ transitions from $\simeq 1$ to $\simeq 2$ around $D_{\rm tran} \simeq 60$ kpc (Figure 2.7) and the velocity centroid over the full C IV doublet becomes consistently blueshifted at a similar projected distance (Figure 2.8) suggesting C IV becomes optically thin around that point. At $z \leq 0.1$, Bordoloi et al. (2014) found W_λ(C IV) falls off as a power law with $D_{\rm tran}$ and remained detectable out to $D_{\rm tran} \approx 100$ kpc. At $D_{\rm tran} \simeq 100$ kpc, $W_\lambda(1548) \lesssim 0.1$ Å and $\log[N(\text{C IV})] \lesssim 13.5$; within a factor of $\simeq 2$ of our observed W_λ(C IV) and consistent with optically thin C IV. Using QSO-galaxy pairs at $z \sim 2$, Turner et al. (2014) also computed W_λ(C IV) and N(C IV). In their first and second $D_{\rm tran}$ bins (40 – 130 kpc and 130 – 180 kpc), like Bordoloi et al. (2014), they measured $\log[N(\text{C IV})] \simeq 13.0 - 13.5$ and $W_\lambda(\text{C IV}) \simeq 0.01 - 0.1$ Å again suggesting optically thin C IV at a similar $D_{\rm tran}$ to this study.

The most significant trend when splitting the pair sample up by SED-derived galaxy properties is between C IV absorption strength and M_*, followed tentatively by SFR. The trend of increased W_λ(C IV) in higher mass galaxies is observed at $z \sim 0$ (Burchett et al., 2016), $z \sim 1$ (Kumar et al., 2024) and at $z \sim 2$ (Méndez-Hernández et al., 2022). Bordoloi et al. (2014) also detected a mild correlation between C IV absorption strength and sSFR in $z < 0.1$, $\log(M_*/\text{M}_\odot) \leq 10$ galaxies but we do not observe this at higher redshift. Bordoloi et al. (2018) and Wilde et al. (2021) report a correlation between M_* and Lyα absorption strength at $z < 1$ but evidence for this is not seen in the Méndez-Hernández et al. (2022) $z \sim 2$ sample. These findings can be reconciled since our sample extends to lower stellar masses (by approximately an order of magnitude) and the most significant change we observe in Lyα absorption occurs between the two lowest mass bins in our sample ($\log(M_*/\text{M}_\odot) \simeq 9$ and $\log(M_*/\text{M}_\odot) \simeq 9.6$). It is interesting to note that W_λ(Mg II) depends most strongly on M_* and SFR for galaxies at $z \sim 0.5$ (Bordoloi et al., 2011; H.-W. Chen & Zahedy, 2024; Rubin, Diamond-Stanic, Coil, Crighton, & Moustakas, 2018), the same stellar population parameters that correlate with C IV, but we lack sufficient S/N in the split pair samples to make a more thorough comparison.

With the advent of *JWST*, observations of the CGM surrounding higher redshift galaxies have been facilitated. Using a sample of 29 star-forming galaxies at $2.3 < z < 6.3$ (all but four have $z > 4$) discovered within 300 kpc of a $z \sim 6.33$ QSO, Bordoloi, Simcoe, Matthee, Kashino, Mackenzie, Lilly, Eilers, Liu, DePalma, Yue, and P. Naidu (2024b) find W_λ(Mg II) decreases rapidly with $D_{\rm tran}$ and, like our sample, absorption is detected well beyond the virial radii of their host galaxies. In contrast, the majority of their rest-frame W_λ(Mg II) are below our detection threshold in the $z \sim 2$ composites. The strongest absorption systems are preferentially detected in massive galaxies and those with high SFR. A small fraction of the Mg II complexes have velocity spreads in excess of the galactic escape velocity, and interestingly, the median Δv is redshifted by 135 km s^{-1}. Unlike the net redshifted Lyα we observe at $D_{\rm tran} \sim 100$ kpc, this measurement may simply result from combining a relatively small number of inherently stochastic QSO sightlines. In aggregate however, the trends observed in the Bordoloi, Simcoe, Matthee, Kashino, Mackenzie, Lilly, Eilers, Liu, DePalma, Yue, and P. Naidu (2024b) sample are emblematic of our results seen at $z \sim 2$ and the preponderance of absorption beyond $R_{\rm vir}$ may suggest metals in these systems are not bound to the galaxies in which they were produced.

2.9 Summary

We have measured the mean spatial and kinematic distribution of absorbing gas around $\langle z_{\rm fg} \rangle = 2.03 \pm 0.36$ star forming galaxies at projected distances $8 \leq D_{\rm tran}/{\rm kpc} \leq 250$ using 2738 KBSS foreground/background galaxy pairs (see Figure 2.1 for some examples and Figure 2.2 for sample statistics). The foreground galaxies studied have a median stellar mass $\log(M_*/{\rm M}_\odot) = 9.6$ and span the range $8 \lesssim \log({\rm M}_*/{\rm M}_\odot) \lesssim 11$ (Figure 2.3). For each galaxy foreground/background pair, we shifted background KCWI and LRIS galaxy spectra to the redshift of their associated foreground galaxies and constructed stacks in the rest-frame of the foreground galaxy, binned by projected distance $D_{\rm tran}$ (Figure 2.4). We measured the properties of the foreground absorbing gas using rest-UV interstellar absorption features in the composite spectra. Our principal conclusions are:

1. We detected significant Lyα absorption throughout the full range of

$D_{\rm tran}$ sampled (Figures 2.5 and 2.7a), consistent with previous results using background QSOs (Adelberger et al., 2003, 2005; Rudie et al., 2012; Turner et al., 2014) and background galaxy pairs (Y. Chen et al., 2020; Steidel et al., 2010). The Lyα covering fraction falls off as $f_c \propto r^{-0.33}$, in agreement with the previously listed $z \sim 2$ studies, but noticeably shallower than most results at lower redshift (Table 2.1).

2. After Lyα, C IV is the strongest absorption feature detected in stacks. C IV closely tracks Lyα (f_c(C IV) $\propto r^{-0.27}$) for all measured $D_{\rm tran}$ (Figure 2.5), and both have similar line-of-sight kinematics at $D_{\rm tran} \lesssim 100$ kpc. In addition to the shallower W_λ vs. $D_{\rm tran}$ dependence, the $z \sim 2$ velocity fields are considerably more active than those observed at low-z. The C IV line-of-sight velocity second moment σ(C IV) reaches a minimum at $D_{\rm tran} \simeq 60$ kpc ($\simeq 0.7\,R_{\rm vir}$) signaling the approximate region over which the galaxy has the largest influence on the properties of its CGM (Figures 2.6 and 2.15).

3. Intermediate ionization species (Si III and Si IV) are detected out to $D_{\rm tran} \simeq 200$ kpc, while the absorption strength of low ionization species (e.g., Si II, C II, and O I) decline more steeply with increasing $D_{\rm tran}$ (Table 2.1), with weaker species falling below our detection limit between $D_{\rm tran} \simeq 60$ kpc (e.g., Si II λ1526) and $D_{\rm tran} \simeq 100$ kpc (e.g., O I; Figure 2.5). In general, higher ionization metallic species trace gas with a wider range of LOS velocity dispersions when compared to the low ions (Figures 2.6 and 2.9). Using $W_\lambda(1260)/W_\lambda(1526)$, we estimated the saturation of the Si II transitions with $D_{\rm tran}$ and found that Si II is strongly saturated for $D_{\rm tran} \lesssim 50$ kpc, and becomes optically thin at $D_{\rm tran} \gtrsim 70$ kpc. We showed how absorption strength varies on a per-transition basis (Figure 2.9) and demonstrated that the low and high ions with similar absorption profiles in DTB spectra of the foreground galaxies DTB (e.g., Si II and C II) tend also to exhibit similar velocity profiles at $D_{\rm tran} \simeq 30-50$ kpc when significantly detected (Figure 2.10).

4. We constructed 2-D maps of Lyα absorption strength parametrized as the covering fraction (absorption depth) as functions of $D_{\rm tran}$ and $v_{\rm LOS}$ (Figure 2.11). Lyα absorption spans the full velocity range $|v_{\rm LOS}| \lesssim v_{\rm esc}$ of the average foreground galaxy, with some absorption detected in excess of $v_{\rm esc}$ at all $D_{\rm tran}$, suggesting that a significant fraction of the

CGM may be unbound. As in Y. Chen et al. (2020), we observed a distinct "edge" in the $f_c(\mathrm{Ly}\alpha)$ map at $D_{\mathrm{tran}} \simeq 80$ kpc ($\simeq R_{\mathrm{vir}}$ for the average galaxy in the sample) that corresponds to a local minimum in the line of sight velocity dispersion $\sigma(\mathrm{Ly}\alpha)$, beyond which there is a general flattening of $\sigma(\mathrm{Ly}\alpha)$. We argued that $D_{\mathrm{tran}} \sim 80$ kpc represents a transition from primarily outflowing gas at $D_{\mathrm{tran}} \lesssim 80$ kpc to inflowing and/or ambient CGM gas beyond $D_{\mathrm{tran}} \gtrsim 80$ kpc.

5. We split the pair sample into sub-samples based on foreground galaxy M_*, SFR, sSFR, and reddening parametrized by $E(B-V)$. The strongest observed trend is between C IV absorption strength and M_* (Figures 2.13, 2.14, and 2.15): $W_\lambda(\mathrm{C\ IV})$ increases by a factor of $\simeq 3.5$ at a fixed D_{tran} between galaxies in the lowest ($\log(M_*/\mathrm{M}_\odot) \simeq 9.0$) and highest ($\log(M_*/\mathrm{M}_\odot) \simeq 10.2$) M_* bins. Over the same range in M_*, $W_\lambda(\mathrm{Ly}\alpha)$ differs by a factor of $\simeq 2$ at $D_{\mathrm{tran}} \simeq 70$ kpc, but the difference becomes insignificant beyond $D_{\mathrm{tran}} \sim 150$ kpc (Figure 2.16). While a weaker trend of $W_\lambda(\mathrm{C\ IV})$ with SFR is also observed, it may be a by-product of the well-known M_*–SFR correlation. The self-similarity of $W_\lambda(\mathrm{C\ IV})$ and $\sigma(\mathrm{C\ IV})$ across the M_* sub-samples when D_{tran} is normalized by R_{vir} suggests that dark matter halo mass sets the scale for both the spatial extent and kinematics of the CGM gas distribution at $z \simeq 2$. We show that the foreground galaxy sub-sample with estimated halo mass similar to that of QSOs at $z \sim 2-3$ ($\log(M_{\mathrm{halo}}/M_\odot) \simeq 12.5$) exhibits comparable CGM C IV absorption at $D_{\mathrm{tran}} \gtrsim 70$ kpc where the comparison is possible. Evidently, the presence of an active QSO does not appear to significantly alter the CGM absorption (at least for $D_{\mathrm{tran}} \gtrsim$ 70 kpc) of the host galaxy compared to those without active QSOs (Figure 2.17), which may have implications for our understanding of AGN feedback for relatively massive galaxies during the peak of the QSO era.

KCWI has significantly improved the effective spectral resolution and spatial coverage of the CGM for $D_{\mathrm{tran}} \leq 250$ kpc of typical star-forming galaxies at $z \sim 2$. This sample, which augments the earlier KBSS studies using galaxy-galaxy pairs (Adelberger et al., 2005; Y. Chen et al., 2020; Steidel et al., 2010), represents a data set that is complementary to those using QSO sightlines at $z \sim 2-3$. With the current sample, we have consistently detected Lyα and

C IV over $D_{\rm tran} = 8 - 250$ kpc and improved the $D_{\rm tran}$ sampling of several weaker far-UV resonance transitions for $D_{\rm tran} \lesssim 100$ kpc. For the first time for galaxies at $z \gtrsim 2$ we have shown that significant correlations exist between the CGM properties (absorption strength and LOS velocity dispersion) and their host galaxies extending from $D_{\rm tran} \sim 0$ (DTB) to projected distances well beyond the virial radii of the host halos.

Galaxy-galaxy foreground/background pairs have the advantage of sampling larger swaths of the CGM and converging more efficiently to the mean gas distribution compared to surveys using background QSOs, at the expense of S/N and spectral resolving power for individual sightlines. At small projected distances ($D_{\rm tran} \lesssim 50$ kpc), we have shown that Lyα photons produced in the foreground galaxy and scattered into our line of sight toward a background galaxy affects both the equivalent width and the apparent line-of-sight velocity distribution of Lyα absorption measured in the spectrum of the background galaxy, confirming speculation along similar lines in Y. Chen et al. (2020). IFUs offer a means of "correcting" this contamination given their ability to chart both emission and absorption halos around galaxies contiguously over fields the size of the average $z \sim 2$ CGM. In the future, deep integrations targeting the emission halos around individual galaxies together with background galaxies (or QSOs) sampling absorption in the same galaxy CGM at similar $D_{\rm tran}$ will allow interesting constraints on the structure and kinematics of the clumpy CGM that must be responsible for both.

N. Z. P. thanks Yuanze Ding, Zhihui Li, Evan Nuñez, and Zhuyun Zhuang for thought-provoking discussions, sumptuous meals, and capersome camaraderie during the writing of this paper. N. Z. P. additionally thanks Cameron Hummels for his insights into modeling the results presented in this study. The authors thank Rosalie McGurk, Greg Doppmann, Mateusz Matuszewski, and Don Neill for constructive conversations about KCWI. The authors are indebted to Kurt Adelberger, Milan Bogosavljević, Dawn Erb, Matthew Hunt, David Law, Olivera Rakic, Naveen Reddy, Gwen Rudie, Alice Shapley, Allison Strom, Rachel Theios, Ryan Trainor, and Monica Turner for their efforts towards the KBSS survey over the past ~two decades. The authors thank the referee for thoughtful feedback that improved the final version of this paper. N. Z. P. and C. C. S. were supported in part by NSF grant AST-2009278. This research has made use of the Astrophysics Data System, funded by NASA under Cooperative Agreement 80NSSC21M00561. This work was based on data obtained at W. M. Keck Observatory, which is operated as a scientific partnership among the California Institute of Technology, the University of California, and the National Aeronautics and Space Administration. The Observatory was made possible by the generous financial support of the W. M. Keck Foundation. Finally, the authors wish to recognize and acknowledge the very significant cultural role and reverence that the summit of Maunakea has always had within the Native Hawaiian community. We are most fortunate to have the opportunity to conduct observations from this mountain.

Software: `matplotlib` (Hunter, 2007), `numpy` (Harris et al., 2020), `scipy` (Virtanen et al., 2020), `Astropy` (The Astropy Collaboration et al., 2013, 2018, 2022), `YT` (Turk et al., 2011), `TRIDENT` (Hummels et al., 2017), `tqdm` (da Costa-Luis et al., 2024), `scikit-image` (Van Der Walt et al., 2014), multiprocess (McKerns et al., 2012), corner (Foreman-Mackey, 2016), IRAF[15] (Fitzpatrick et al., 2024; National Optical Astronomy Observatories, 1999; Tody, 1986, 1993), `seaborn` (Waskom, 2021), `plotly` (Inc, 2015), `L.A.COSMIC` (van Dokkum, 2001), IPython (Perez & Granger, 2007), QFitsView (Ott, 2012)

Facilities: Keck:II (KCWI), Keck:I (LRIS), Keck:I (MOSFIRE), Keck:I (HIRES)

2.10 Appendix

Wavelength Trimming

In deciding which galaxies contribute to the galaxy-galaxy pair sample, both Steidel et al. (2010) and Y. Chen et al. (2020) imposed an upper bound on the redshift difference between the foreground and background pairs. The former uses $\Delta z \leq 1$ while the latter imposes $\frac{\Delta z}{1+z_{\rm fg}} < 0.3$; for the median foreground and background galaxy redshifts in our sample, these criteria are very similar. We observe that

$$\lambda_{\rm bg}(1 + z_{\rm bg}) = \lambda_{\rm fg}(1 + z_{\rm fg}), \tag{2.7}$$

or equivalently,

$$\frac{\Delta z}{1 + z_{\rm fg}} = \frac{\lambda_{\rm fg}}{\lambda_{\rm bg}} - 1 \tag{2.8}$$

[15]NOIRLab IRAF is distributed by the Community Science and Data Center at NSF NOIRLab, which is managed by the Association of Universities for Research in Astronomy (AURA) under a cooperative agreement with the U.S. National Science Foundation.

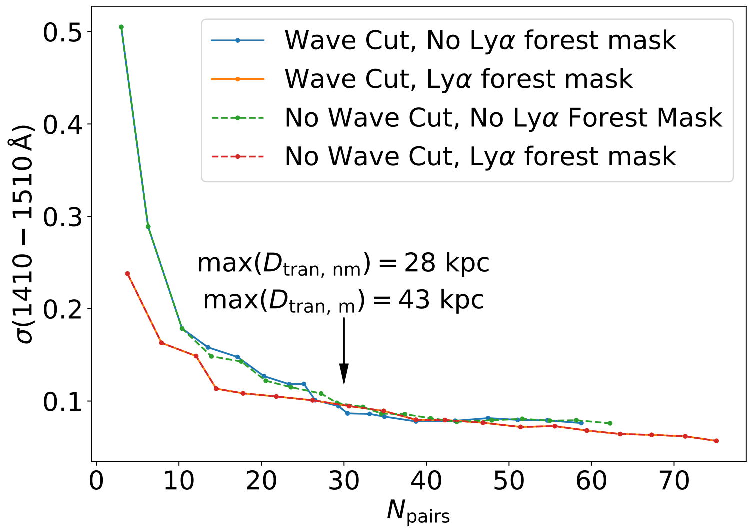

Figure 2.18: Continuum noise (σ) for a given number of pairs (N_{pairs}) depending on wavelength trimming method. The two options include manual wavelength cuts or a redshift dependent rejection that excludes objects with foreground absorption that falls within the Lyα forest of the background spectrum.

where $\Delta z = z_{\text{bg}} - z_{\text{fg}}$ and λ_{fg} and λ_{bg} are the rest wavelengths of a particular transition in the foreground and background frames, respectively. To prevent foreground C IV absorption from being contaminated by unrelated Lyα forest absorption, we chose $\lambda_{\text{fg}} = 1549$ and $\lambda_{\text{bg}} = 1216$ so only pairs with $\frac{\Delta z}{1+z_{\text{fg}}} < 0.27$ are included. Naturally, if one observed significant noise from the background Lyα forest contributing to foreground absorption, this requirement could be strengthened at the cost of many potential foreground/background galaxy pairs; for example, requiring $\frac{\Delta z}{1+z_{\text{fg}}} < 0.15$ would prevent Lyα forest absorption from contributing to the foreground Si IV profiles.

In our sample, we experimented with several such redshift cuts and found that the continuum noise level is indeed reduced, especially when the number of pairs in a bin is small (see the red dashed curve in Figure 2.18). In addition to a blanket cut, we also tried wavelength trimming for each individual spectrum, choosing the highest S/N regions in the bandpass to contribute to the final stacks. This typically involved masking the short wavelength end of the spectrum in the Lyα forest and (in the case of LRIS) the wavelengths near the dichroic cutoff near 5600 Å. The fact that the noise levels in the stacks remain similar with or without a manual wavelength mask suggests that such trimming is not necessary (see the solid vs. dashed curves in Figure 2.18).

While both noise mitigation techniques converge once the number of pairs in a bin exceeds 30, the range of $D_{\rm tran}$ differs. Figure 2.18 shows the maximum $D_{\rm tran}$ in a bin of 30 pairs drawn from a pair list sorted by $D_{\rm tran}$. In other words, when applying a redshift cut, the 30 pairs with the smallest separations probe $D_{\rm tran} \lesssim 43$ kpc; however, if such a cut is not imposed and each spectrum is manually trimmed of noisy regions, the first 30 pairs sorted by impact parameter probe gas within 28 kpc of an average galaxy halo. Since the noise levels in stacks with $N \gtrsim 30$ pairs are comparable and all of the stacks in our sample contain at least thirty pairs, we chose to avoid using the blanket redshift cut (dashed green curve in Figure 2.18), effectively maximizing the number of galaxy pairs contributing to a stack.

HIRES

In order to provide some insight into the cause of asymmetries observed for some of the galaxy-galaxy pair samples, we assembled a sample of QSO-galaxy pairs using existing HIRES spectra of the central QSOs in the KBSS fields (see Rudie et al. 2012; Turner et al. 2014). Briefly, the KBSS QSOs have $\langle z \rangle \simeq 2.7$, and their HIRES spectra have $R \simeq 45{,}000$ with $S/N \simeq 50-100$ pix^{-1} over the observed wavelength range 3100 – 6000 Å. Figure 2.19 shows stacks constructed using the same method as for the galaxy-galaxy pair samples, for 53 foreground galaxies with $D_{\rm tran} \leq 250$ kpc. The results are shown in two broad bins of $D_{\rm tran}$, for the Lyα and C IV transitions. The bins were chosen to be similar to those used for the galaxy-galaxy pair samples discussed in Section 2.7.) We note that the QSO-galaxy pair measurements pertain to foreground galaxies in the same KBSS survey regions and at similar redshifts, but are completely independent of the galaxy-galaxy pair measurements since the QSO sightlines sample different $D_{\rm tran}$ even when probing the same foreground galaxy.

Figure 2.19 shows that, even when the background spectra have very high S/N and spectral resolution, the mean profiles from combining QSO-galaxy pairs can be strongly affected by sample variance – stochastic variation of peculiar velocities and component line strength contributed by different

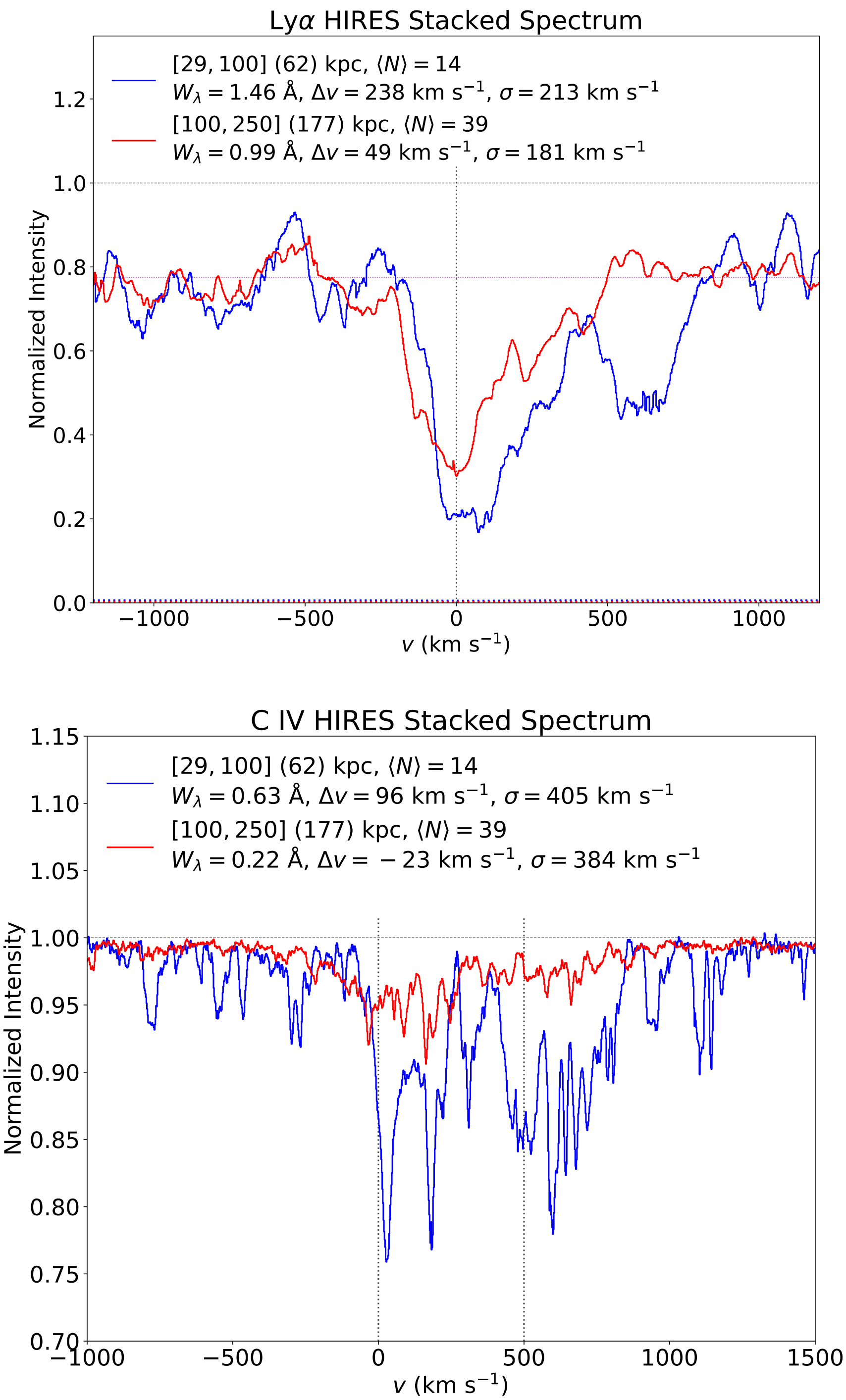

Figure 2.19: Stacked HIRES absorption spectra shifted into the rest frame of the foreground systems centered around the Lyα and C IV transitions. The range of D_{tran} and the number of pairs contributing are enumerated in the plot legend. For each bin, W_λ, Δv, and σ are also shown. The horizontal dotted purple line denotes the suppressed continuum used for the W_λ(Lyα) measurement.

QSO-galaxy pairs – as well as by unrelated absorption lines from other redshifts that fall happen to fall within the same wavelength intervals. Applying outlier rejection in forming the stacks reduces the effects of unrelated absorption features and/or unusual absorption profiles in one or a few individual QSO-galaxy pairs; however, with small pair numbers the average profiles can appear quite asymmetric in velocity (e.g., the blue curves in both panels of Figure 2.19).

For absorption systems with a high incidence rate such as Lyα (lefthand panel of Figure 2.19), an additional effect of combining many systems shifted to the redshift of a foreground galaxy is that the net absorption is superposed on a suppressed local continuum, reflecting the average line blanketing in the Lyα forest at the mean redshift of the foreground galaxy sample – in this case, $\langle z \rangle \sim 2.3$. For stacks with a relatively small number of contributing QSO-galaxy pairs, sample variance in the local Lyα forest can cause "noise" in the net absorption profile due to fluctuations in the local continuum. The apparent continuum fluctuations become smaller for samples with larger numbers of QSO-galaxy pairs, as do the net velocity asymmetries (i.e., centroid shift relative to $v = 0$; compare the blue and red composites in the lefthand panel of Figure 2.19.)

For metal line transitions such as the C IV doublet, when limited to redshifts that place C IV at wavelengths longward of Lyα in the spectrum of the background QSO (as in the righthand panel of Figure 2.19), the continuum remains well-defined. However, small samples may still produce asymmetric C IV profiles that do not resemble a simple velocity-broadened C IV doublet with equivalent width ratio $1 \leq W_\lambda(1548)/W_\lambda(1550) \leq 2$, and the velocity centroid of the absorption may also appear shifted with respect to the foreground galaxy systemic redshift for a similar reason. When a larger number of QSO/galaxy pairs is averaged (red spectrum in the righthand panel of Fig. 2.19) the net profile is much smoother, and has an apparent doublet ratio close to that expected for unsaturated absorption. We observe similar behavior, albeit using galaxy spectra with $\sim 20-30$ times lower resolving power and S/N, in the galaxy-galaxy pair samples covering similar ranges of $D_{\rm tran}$.

For Lyα and C IV, the values of W_λ, Δv, and σ for each $D_{\rm tran}$ bin are shown in the legend of Figure 2.19. We find general agreement in W_λ(Lyα), Δv(Lyα),

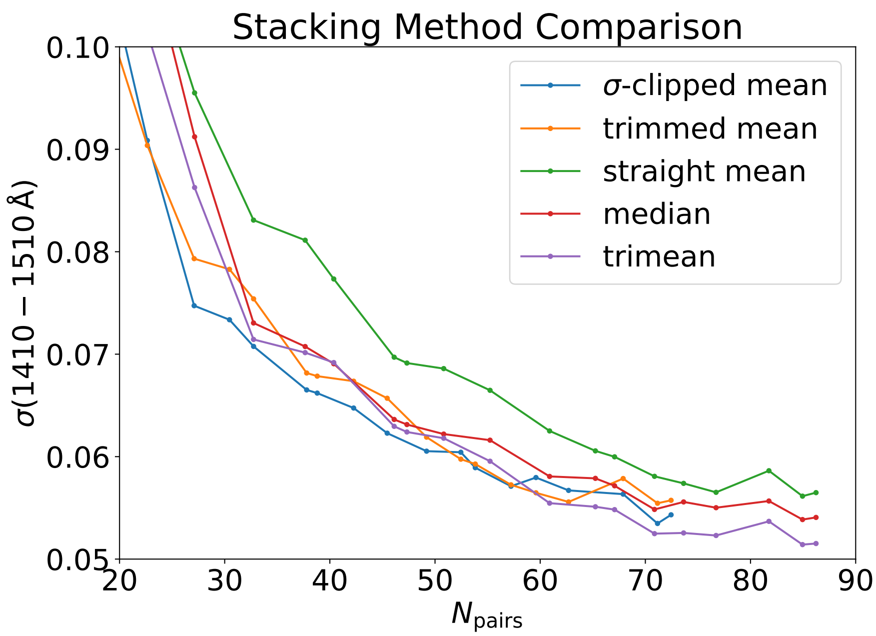

Figure 2.20: Similar to Figure 2.18, the continuum noise level over the 1410–1510 Å wavelength interval as a function of the number of pairs in a bin is plotted for several methods of combining spectra within that bin.

and absorption profile morphology between the HIRES $D_{\rm tran} = 100-250$ kpc stack of Lyα and the galaxy pair stacks over the same range of $D_{\rm tran}$ plotted in Figure 2.13. The computed σ(Lyα) for the HIRES stacks are $50-100$ km s^{-1} lower than their full sample or SED-binned counterparts, but we note that σ depends sensitively on continuum normalization. Similar to the lower resolution stacks, we measure a redshifted velocity centroid at small $D_{\rm tran}$ (Δv = 238 km s^{-1} at $D_{\rm tran}$ = 62 kpc) that approaches the systemic velocity with increasing $D_{\rm tran}$ (Δv = 49 km s^{-1} at $D_{\rm tran}$ = 177 kpc). The C IV profiles all show broad ($\sigma \sim$ 400 km s^{-1}), nearly symmetric absorption in velocity space with a $\simeq$ 100 km s^{-1} shift towards a blueshifted centroid between the inner (blue) and outer (red) bins. This global trend is consistent with a decreasing optical depth where the individual C IV systems transition from an equivalent width ratio $W_\lambda(1548)/W_\lambda(1550)$ of one to two.

Stacking Method

Before deciding on a trimmed mean (averaging the 5th – 95th percentile spectral pixels) for constructing stacks, we experimented with several other stacking options for the final composite spectra. In theory, with high resolution normalized spectra, any absorption manifests as a narrow feature centered at the rest wavelength in the frame of the foreground galaxy. Foreground galaxies without significant absorption will have normalized intensities close to unity. The distribution of intensities at a given rest wavelength is expected to have a mode near unity and a skew towards smaller normalized intensity caused by real absorption. For any distribution, the mean absorption profile will converge faster than the median for a fixed number of galaxy pairs; on the other hand, combining shifted spectra using the pixel-by-pixel mean can result in noise caused by unrelated absorption at other redshifts. This source is clearly exacerbated by averaging over only a few galaxy pairs where background Lyα forest absorption systems can produce large noise spikes at random foreground wavelengths.

In dealing with relatively low resolution ($R \simeq 670$) LRIS spectra, Y. Chen et al. (2020) found that the median of all foreground galaxies in a stack agrees well with a clipped mean using the same spectra, but opted for the median. Now incorporating moderate resolution ($\langle R \rangle \simeq 1500$ at Lyα and $\langle R \rangle \simeq 1900$ at C IV) KCWI spectra, we revisit this issue. Figure 2.20 shows the foreground continuum noise level for a stack as a function of the number of pairs included in the bin. The list of pairs begins at the minimum $D_{\rm tran}$ and is sorted by $D_{\rm tran}$ so more pairs probe larger $D_{\rm tran}$. The stack is either the mean (green), sigma-clipped mean (blue), trimmed mean (orange), median (red), or the trimean (purple; Equation 2.9) of the pixels at each wavelength point in that bin. The trimmed mean clips pixels that are either below the 5th percentile or above the 95th percentile at a given wavelength. In the small sample size limit, this algorithm rejects the minimum and maximum values; for larger samples, more pixels may be rejected (effectively 4 – 6 objects for most of our $D_{\rm tran}$ bins). The trimean is defined as

$$\mathrm{TM} \equiv \frac{1}{2}\left(Q_2 + \frac{Q_1 + Q_3}{2}\right) \tag{2.9}$$

where Q_i are the ith quartiles of the underlying distribution. Although a less efficient estimator than the mean, the trimean emphasizes both the central values and the extrema of a distribution. For our spectra, this measure of central tendency helps mitigate continuum noise while preserving the strength of absorption features.

We note that the straight mean has $\sim 10\%$ higher noise levels overall com-

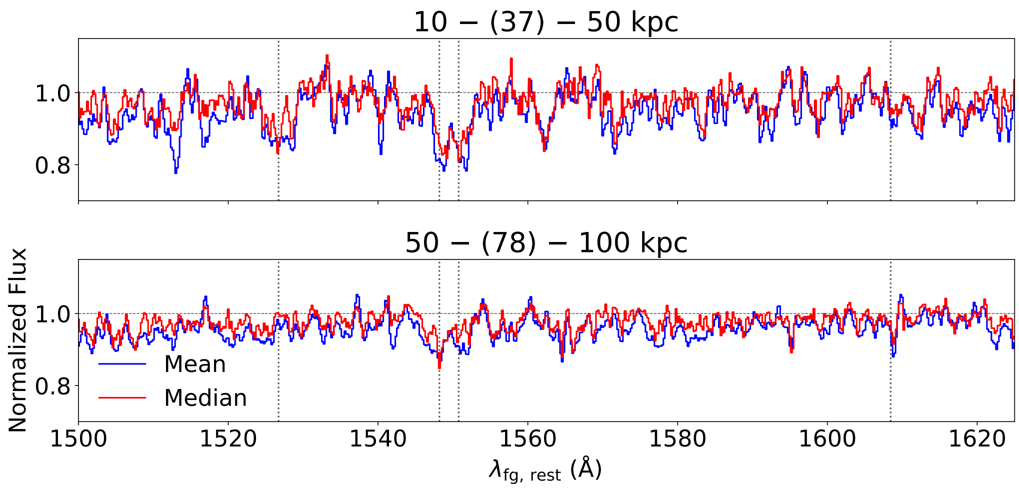

Figure 2.21: Background spectra shifted to the foreground rest frame and stacked using a trimmed mean (blue) and median (red) for two ranges of $D_{\rm tran}$ (*top:* 10 – 50 kpc, *bottom:* 50 – 100 kpc). The vertical dotted lines show Si II λ1526, C IV, and Fe II λ1608 and each input spectrum has been normalized as described in Section 2.4.

pared to the other statistics, which are consistent with one another (to within $\simeq$ 5%). The sigma-clipped mean has a minor advantage for $N < 50$ pairs, while the trimean has the lowest noise for $N > 60$ pairs. With $N > 30$ pairs, each measure of central tendency (straight mean excluded) is consistent with the others, suggesting they are at that point all reflective of the underlying distribution. The straight mean begins to converge to the rest of the metrics with $N > 60$ pairs.

While the continuum noise level is consistent to within $\sim$ 10% regardless of method used, the same is not true for the absorption features. Figure 2.21 shows two $D_{\rm tran}$ bins where the foreground absorption spectra were combined using a trimmed mean (blue) and a median (red). For each absorption line, we observe higher variability near the systemic velocity when using the median over the trimmed mean. As a result, the continuum level in the vicinity of the absorption features is less stable and the equivalent widths one would measure are systematically smaller (see the solid vs. dashed lines in Figure 2.22). Indeed, Figure 2.22 shows spectra combined with a trimmed mean have $W_\lambda \sim$ 50% larger than those measured in median combined spectra, regardless of the line being measured. The approximate W_λ were measured by integrating over $|v| \leq 700$ (500) km s^{-1} around the

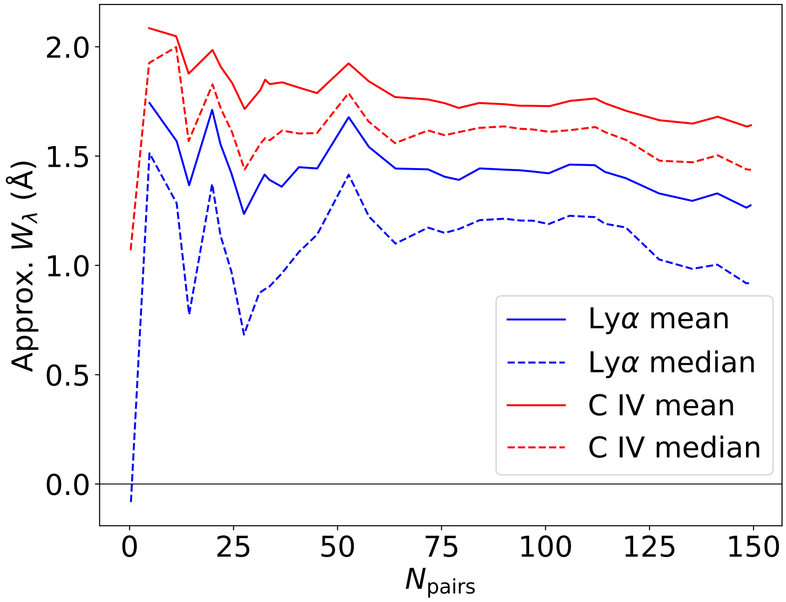

Figure 2.22: Lyα (blue) and C IV (red) approximate equivalent width is measured from stacks with varying numbers of constituent galaxy pairs as a test of line profile convergence. The curves start at $D_{\text{tran}} \simeq 10$ kpc and add pairs with progressively larger separations reaching up to $D_{\text{tran}} \simeq 52$ kpc. Each stack is combined using either a trimmed mean (solid lines) or median (dashed lines).

systemic velocity for Lyα (C IV). When considering small D_{tran}, the contribution of foreground Lyα emission to the background galaxy spectrum (Appendix 2.10) will bias both the median and average toward smaller W_λ, but if the velocity spread between absorption and emission is not the same, the median may show more variability around the systemic velocity than the mean. We therefore choose to use the trimmed mean as it provides the most distinguishable absorption signal when present.

In using the trimmed mean, we experimented with several different bounds (e.g., asymmetric, Q1 & Q3) but found that clipping the top and bottom 2 – 6 (depending on the number of pairs in a bin) background spectra was sufficient for achieving noise levels comparable to that of the median while still detecting strong absorption. Put differently, $\lesssim 5\%$ of the spectra in a particular bin were noisy enough by themselves to result in severe contamination when stacked with $N \gtrsim 30$ others. It is worth remembering that when normalizing each background spectrum, we only allow regions where the spline fit is consistently above the local (DRP-computed) noise

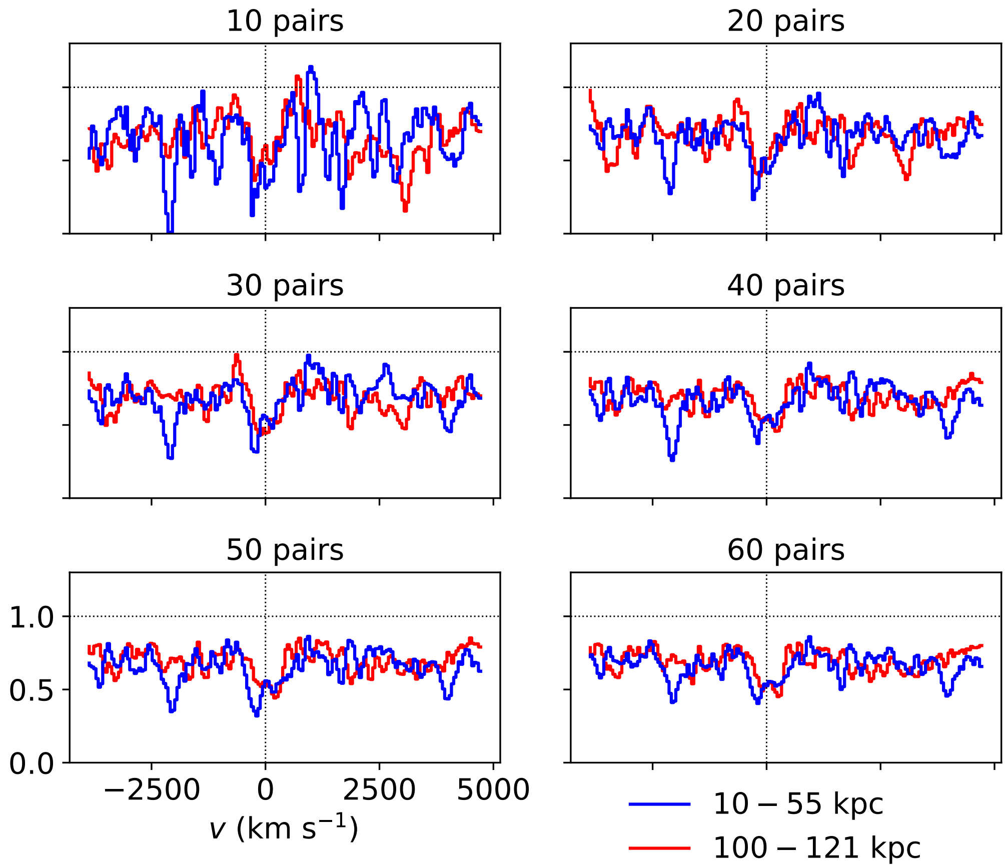

Figure 2.23: A spectral representation of Figures 2.20 and 2.22 showing how Lyα absorption converges to a well-defined profile as more galaxy pairs are averaged. Two bin "starting points" are shown: $D_{\mathrm{tran}} \simeq 10$ kpc in blue and $D_{\mathrm{tran}} \simeq 100$ kpc in red; as more pairs are added, the median D_{tran} increases but Lyα becomes easier to distinguish from the continuum. Note that the continuum is suppressed by the Lyα forest when a sufficient number of pairs are averaged.

level (evaluated in $\Delta\lambda \simeq 50$ Å intervals) to enter into the stack (see Section 2.4). Such a requirement ensures that there is a continuum with at least $S/N \gtrsim 1$ from which to measure absorption. It therefore follows that few of the spectra entering into the stack would need additional trimming.

In addition to noise properties, we investigated the convergence of the Lyα absorption profile for a given number of pairs. Figure 2.23 shows how the number of pairs averaged (using a trimmed mean) influences the net Lyα profile. For transitions measured within the Lyα forest of the background galaxy spectrum, a coherent absorption feature does not materialize until at least 10 pairs are averaged. Once 20 pairs are combined, Lyα is discernible from the continuum and additional pairs help mitigate Lyα forest noise spikes. Lyα absorption strength is reduced with increasing $D_{\rm tran}$ (see Figure 2.5) so a larger number of pairs is required to produce absorption profiles with a comparable S/N. Although there is some sample variance, this effect can be seen by comparing the blue and red spectra in Figure 2.23: for a given number of pairs, the larger $D_{\rm tran}$ bins (red) are marginally noisier around Lyα than their small $D_{\rm tran}$ counterparts.

More quantitatively, Figure 2.22 shows that the W_λ varies considerably for stacks with fewer than 20 pairs due to stochastic background Lyα forest absorption. However, once the number of pairs reaches $N \simeq 30$, W_λ converges and remains roughly constant with increasing numbers of pairs. If one keeps adding pairs to the bin, the average $D_{\rm tran}$ sampled will increase and since pairs at larger $D_{\rm tran}$ tend to have weaker absorption (recall absorption W_λ drops with $D_{\rm tran}$; Figure 2.5), the measured W_λ in the stacks will begin to fall off when $\gtrsim 100$ pairs are included, as seen in Figure 2.22. A similar trend is observed in C IV, albeit with slightly less variability when the number of pairs is small.

Putting all this together, for the trimmed mean stacks, we seek to optimize the number of pairs in each bin such that the continuum noise is minimized and the absorption feature is unambiguous, while still providing as finely sampled of a grid in galactocentric radius as possible. From this analysis and some experimentation with various bins, we find optimum stacks at $D_{\rm tran} \lesssim 50$ kpc contain $N \simeq 30 - 80$ pairs and design the bins used in this study accordingly.

The effects of Lyα emission halos of foreground galaxies

Y. Chen et al. (2020) noted a significant asymmetry in the average excess Lyα profile, both at $D_{\rm tran} \lesssim 40$ kpc and at $50 \lesssim D_{\rm tran}/{\rm kpc} \lesssim 150$ and suggested that the asymmetry results from foreground Lyα emission contaminating the background Lyα absorption feature. In this work, we confirm the presence of net blueshifted Lyα absorption at $D_{\rm tran} \lesssim 40$ and net redshifted absorption at $50 \lesssim D_{\rm tran}/{\rm kpc} \lesssim 150$ (see e.g. Figure 2.11).

For the net redshifted absorption at $D_{\rm tran} \simeq 100$ kpc, we rule out noise arising from a particular set of background spectra (i.e. sample variance) since this feature is larger than the effective resolution element and with

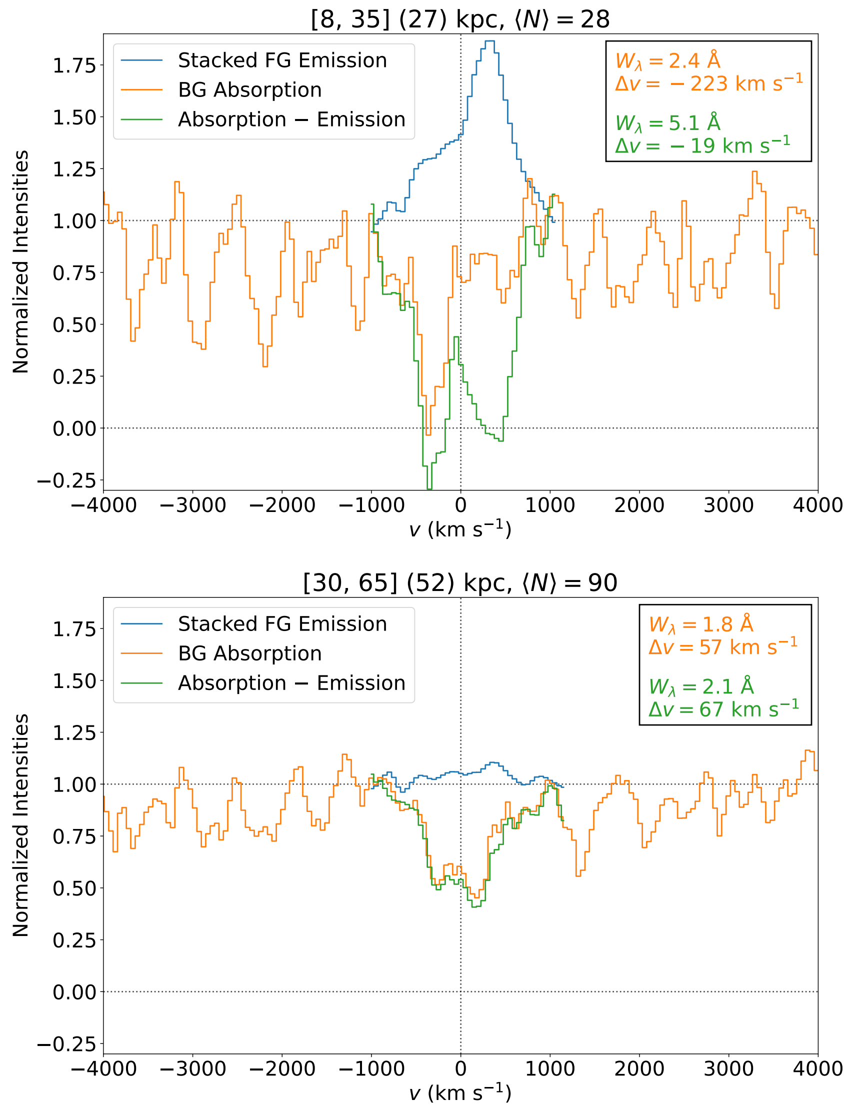

Figure 2.24: The contribution of Lyα emission from the foreground galaxy (blue) to the Lyα absorption profile measured in the background galaxy spectrum (orange) for two D_{tran} bins. The green spectrum is an estimate of the unaffected absorption profile, computed by subtracting the average emission feature from the absorption. W_λ(Lyα) and Δv(Lyα) from the observed and "corrected" spectra are shown in the top right of each plot as a color-coded list. The number of galaxies contributing to each stack is shown in each plot title.

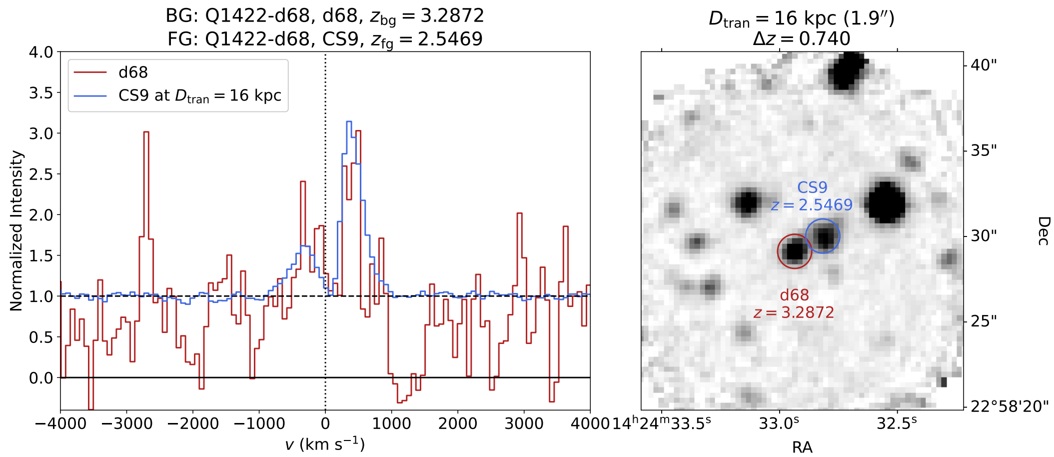

Figure 2.25: *Left:* The spectra of Q1422-d68 (red) and Q1422-d68-CS9 at $D_{\rm tran}$ = 16 kpc (blue) centered around Lyα in the rest frame of CS9. *Right:* White light image of the Q1422-d68 cube with d68 and CS9 circled (same color scheme). We observe emission from CS9 (foreground) contributing to the d68 (background) spectrum effectively masking any absorption within $v_{\rm LOS} \simeq 1000$ km s^{-1} of the systemic velocity.

$\langle N \rangle \sim 400$ galaxies being averaged together, S/N is not a major concern. We also see this effect in the HIRES stacked spectra (Figure 2.19) which have background sources considerably brighter than the foreground galaxies they probe. Since both means of measuring foreground galaxy absorption show redshifted Lyα absorption, the underlying cause may be related to a hitherto unknown bias in the set of background galaxies or another effect that remains to be explained. One possibility put forth by Y. Chen et al. (2020) involves accretion-dominated inflows at large $D_{\rm tran}$ that could result in blueshifted Lyα photons being preferentially scattered in the direction of the observer. Inflowing Lyα would tend to have a blue-dominated profile when scattered into our line of sight and when superposed with symmetric Lyα absorption, the observed net Lyα profile would appear redshifted. While the existing KBSS-KCWI spectra lack the sensitivity to characterize the Lyα emission contribution to the measured Lyα absorption signature at $D_{\rm tran} > R_{\rm vir}$, this possibility cannot yet be ruled out.

We instead focus on understanding the (net blueshifted) Lyα profile at small $D_{\rm tran}$, where in addition to the inherent variability associated with combining Lyα forest absorption systems, Lyα photons in emission from the foreground galaxy modulate absorption measured from the background galaxy spectrum. We build upon the order-of-magnitude calculation presented in

Y. Chen et al. (2020) using a stack of KCWI Lyα halos from Y. Chen et al. (2021, p. 2025) to measure the flux in emission from the foreground galaxy that gets "added" to the background absorption signal. We start by constructing the radial surface brightness (SB) distribution of Lyα for the mean galaxy halo in the sample. The surface brightness integrated over the full Lyα profile is $\sim 2\times10^{-17}$ erg s^{-1} cm^{-2} arcsec^{-2} within $1'' - 2''$ from the center of the average halo. The halo falls off exponentially: at $D_{\rm tran}$ = 20 kpc, the SB is down by a factor of $\sim$ 10, and by $D_{\rm tran}$ = 50 kpc, a factor of $\sim$ 100 (see also Steidel et al. 2011 and Y. Chen et al. 2021).

The emission spectra in Figure 2.24 (shown in blue) were derived by integrating the foreground galaxy surface brightness profile over the $D_{\rm tran}$ of interest weighted by the underlying galaxy pair distribution in that bin. The stack of the foreground galaxies at $D_{\rm tran} \simeq 27$ kpc has an average continuum flux density $f_{\lambda,\rm cont} \sim 5\times10^{-19}$ erg s^{-1} cm^{-2} Å^{-1} and an average Lyα emission flux density close to 2×10^{-18} erg s^{-1} cm^{-2} Å^{-1}. The resultant flux density is normalized with respect to the continuum level and translated up by +1 for ease of visualization.

Figure 2.24 shows absorption and emission profiles for $D_{\rm tran} \simeq 27$ kpc (left) and $D_{\rm tran} \simeq 52$ kpc (right). These $D_{\rm tran}$ represent edge cases but a similar comparison can be made at other $D_{\rm tran}$. Whereas the Y. Chen et al. (2020) order-of-magnitude calculation compared fluxes, the spectra in Figure 2.24 are flux densities normalized by the stacked background galaxy continuum level ($f_{\lambda,\rm abs} \simeq 5\times10^{-19}$ erg s^{-1} cm^{-2} Å^{-1}). The orange curves in both panels show normalized background composite spectra similar to those in the left panel of Figure 2.7.

In Figure 2.24, the noise properties of the emission and absorption spectra depend oppositely on $D_{\rm tran}$. As the range of $D_{\rm tran}$ increases, the S/N of the background absorption spectra increases, while at the same time, the Lyα surface brightness is decreasing and the emission spectra become noisier. The two bins illustrated in Figure 2.24 do not meet the fiducial cutoff for the minimum number of pairs in a impact parameter bin ($N_{\rm pairs} \gtrsim 30$; Appendix 2.10), but represent a compromise where the changing emission and absorption profiles can be seen despite the low S/N. Both spectra are therefore smoothed with a one pixel (σ = 50 km s^{-1}) Gaussian kernel.

At small $D_{\rm tran}$, the Lyα absorption and emission profiles resemble inverted and reflected images of one another (about the intensity and velocity axes respectively). This can be explained simply by considering a symmetric Lyα absorption trough where red-dominated emission contributes to the profile resulting in a blue-dominated absorption trough ($\Delta v_{\rm meas} = -223$ km s^{-1} at $D_{\rm tran} \simeq 27$ kpc). We note that subtracting off the expected foreground emission from the background (modulated) absorption profile (the green curve in Figure 2.24) results in a quasi-symmetric Lyα absorption line ($\Delta v_{\rm corr} = -19$ km s^{-1} at $D_{\rm tran} \simeq 27$ kpc). The ratio of measured to "corrected" equivalent widths suggests that Lyα emission contributed along the line of sight by foreground galaxies reduces the observed absorption strength by $\simeq 47\%$. Since Lyα emission falls off exponentially with $D_{\rm tran}$, we would expect this effect to be reduced significantly by $D_{\rm tran} \simeq 50$ kpc. Indeed, the observed absorption profile in the right panel of Figure 2.24 at $D_{\rm tran} \simeq 50$ kpc is considerably more symmetric since the foreground galaxies modulate the background signal by is modulated by $\simeq 14\%$. While red-dominated foreground Lyα emission can help explain the net blueshifted absorption spectra at $D_{\rm tran} \lesssim 50$ kpc, it is therefore unlikely to contribute significantly at $D_{\rm tran} \simeq 100$ kpc, and thus cannot be the sole contributor to the net redshifted Lyα profiles observed at $50 \lesssim D_{\rm tran}/{\rm kpc} \lesssim 150$.

As a specific example that illustrates an extreme, we plot the Q1422-d68-CS9 galaxy pair in Figure 2.25 which has a separation of $D_{\rm tran} \simeq 16$ kpc. Going off of the full sample W_λ vs. $D_{\rm tran}$ evolution (Figure 2.5), at $D_{\rm tran} \simeq 16$ kpc, the average Lyα absorption system has $W_\lambda({\rm Ly}\alpha) \simeq 2$ Å. Instead, the background (d68, red) spectrum at the wavelength of Lyα in the foreground shows *emission* with a red-dominated profile similar to that of foreground galaxy (CS9, blue). Only once the Lyα emission from foreground galaxy has diminished and no longer contributes (at $|v| \simeq 1000$ km s^{-1}) do we observe absorption. For this particular system, it is likely that the unaffected absorption signal would cover $|v_{\rm LOS}| \lesssim 1000$ km s^{-1}, but a brighter background source (e.g. a QSO) would be needed to confirm this. This effect represents one of the pitfalls in using comparably luminous sources as pairs especially at small $D_{\rm tran}$ where Lyα emission contributes to the background galaxy signal.

Chapter 3

NONRESONANT EMISSION IN KBSS-KCWI GALAXIES AT $z \sim 2$

Prusinski, N. Z., Steidel, C. C., & Chen, Y. (2026). Nonresonant emission in KBSS-KCWI galaxies at $z \sim 2$. *in prep*.

Nikolaus Z. Prusinski: Cahill Center for Astronomy and Astrophysics, California Institute of Technology, MC 249-17, Pasadena, CA 91125, USA; nik@astro.caltech.edu

Charles C. Steidel: Cahill Center for Astronomy and Astrophysics, California Institute of Technology, MC 249-17, Pasadena, CA 91125, USA; ccs@astro.caltech.edu

Yuguang Chen: Department of Physics, The Chinese University of Hong Kong, Shatin, N.T., Hong Kong SAR, China; yuguangchen@cuhk.edu.hk

ABSTRACT

We investigate the spatial structure and kinematics of nonresonant Si II* emission in 50 $\langle z \rangle = 2.25$ star-forming galaxies. KBSS-KCWI spectra were used to spatially resolve the Si II* gas distribution. Si II* kinematics are most characteristic of an absorption line ISM component and on average nonresonant emission is shifted by Δv(Si II*) $\simeq$ 40 km s^{-1} with respect to the systemic velocity from nebular spectra. Nonresonant emission (and by extension, optically thick gas) extends beyond the galaxy continuum. The radial surface brightness falloff of Si II* is steeper than that of Lyα. The Si II* velocity spread similarly decreases with $D_{\rm tran}$ and when aligned along the major axis of the galaxy, stacks of nonresonant Si II* show marginal ($\lesssim 2\sigma$) evidence for excess emission along the galaxy *minor* axis. Growing the effective spectroscopic aperture, we find a significant fraction of Si II* emission associated with a galaxy resides well beyond its continuum.

3.1 Introduction

The current picture of galaxy evolution places star forming galaxies at the center of a "cosmic ecosystem" where pristine gas flows in from the cosmic web, sustaining star formation. Star formation in turn gives rise to numerous baryonic feedback processes which drive the evolution of galaxies through the expulsion of metal-enriched gas potentially to circumgalactic and intergalactic scales. The circumgalactic medium (CGM) contains the majority of gas associated with galaxies (Peeples et al., 2014), making it an excellent laboratory for studying the effects of baryonic feedback.

Large-scale galactic winds have been observed in star-forming galaxies across all redshifts (M82, Steidel et al. 2010; Weiner et al. 2009, $z > 6$ JWST) and appear to be ubiquitous in starburst galaxies with star formation rate surface densities $\Sigma_{\rm SFR} \gtrsim 0.1$ $M_\odot$ yr^{-1} kpc^{-2} (Heckman, 2002). While the precise energy and momentum budget is uncertain, it is clear that supernovae (e.g., Leitherer et al., 1999; Veilleux et al., 2005), radiation pressure from stars acting on gas (Murray et al., 2011), and cosmic ray pressure (e.g., Hopkins, 2025) all play a role in driving galactic winds. For galaxies with stellar masses $M_* \lesssim 10^{10.5}$ $M_\odot$, star formation-induced baryonic feedback processes are likely to have their largest effect during the so-called "cosmic noon" (i.e. $z \sim 2$) when global star formation rate (SFR) and baryonic accretion rate were at their peak (Behroozi et al., 2013; Faucher-Giguère et al., 2011; Madau & Dickinson, 2014). This redshift is also observationally conducive using ground-based facilities in that many of the rest-frame far-UV and optical diagnostics fall in spectral windows with high atmospheric throughput.

Historically, outflows have been observed using resonant interstellar absorption lines through "down-the-barrel" (DTB) spectroscopy (see Veilleux et al. 2020 for a review). While the most accessible lines change with redshift — in general, Na–D at $z \sim 0$; Fe II and Mg II at $z \sim 1$ (Erb et al., 2012; Martin et al., 2012; Prusinski et al., 2021; Rubin et al., 2011); and O I, Si II, C II, C IV at $z \sim 2$ (Steidel et al., 2010) — the overall technique remains similar (e.g., Savage & Sembach, 1991). Blueshifted resonant absorption lines against the (background) galaxy continuum describe the velocity and covering fraction of outflowing material.

DTB absorption line spectroscopy provides the line-of-sight (LOS) kinemat-

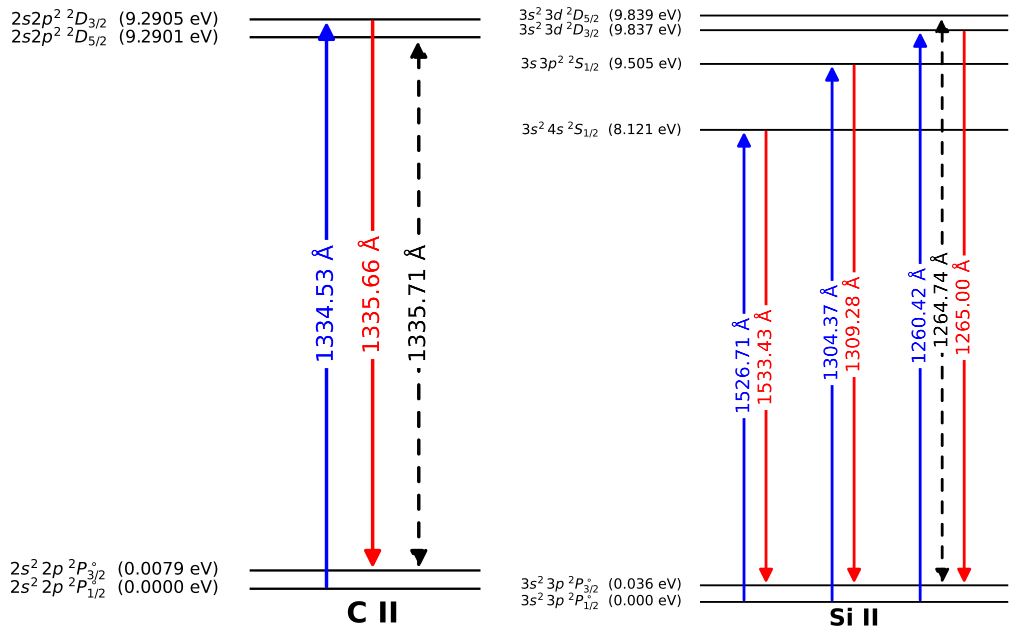

Figure 3.1: *Left:* C II Grotrian diagram. *Right:* Si II Grotrian diagram. Resonant transitions (and their rest wavelengths) are depicted by upward blue arrows; nonresonant "fluorescent" transitions are in red. Excited levels and their energies with respect to the ground state are shown on the left of each subplot. Black dashed lines show nearby transitions. Transition probabilities for each of the transitions shown here are listed in Table 3.1.

ics but it is generally not possible to determine the distribution of absorbing gas. However, with the advent of integral field units (IFUs), it has recently become possible to spatially map outflows via nebular emission lines (e.g., Hα and [O III]). With IFU observations of emission lines, it is (in principle) possible to determine the effective area of the emitting region and compute (e.g.) mass outflow rates ($\dot{M} \propto m_H N v_{\rm out} r_{\rm eff}$). Measures of outflow properties in emission are subject to two primary limitations: nebular emission lines like Hα preferentially trace high density gas ($\varepsilon \propto n_e^2$; cf. absorption lines whose strength $\tau \propto \int n_e \, d\ell$) and the precision to which high velocity gas can be detected is highly dependent on the spectral S/N.

Resolved rest-UV integral field spectroscopy offers a promising avenue for understanding the physics of outflows at $z \sim 2$. The strongest rest-UV transition (by far) is Lyα, followed by resonant metallic features. In recent years, considerable effort has been dedicated to the study of Lyα in absorption (e.g., Y. Chen et al., 2021; Prusinski et al., 2025; Rudie et al., 2012; Steidel et al., 2010) and in emission (e.g., Bacon et al., 2021; Y. Chen et al., 2021; Steidel et al., 2011; Wisotzki et al., 2016, 2018) around $z \sim 2$ star-forming galaxies, but the resonant nature of the line requires sophisticated modeling to extract physically meaningful results (e.g., Erb et al., 2023; Z. Li & Gronke, 2022; Z. Li et al., 2026). Fundamentally, the resonant nature of Lyα prevents a unique radiative transfer solution to a 1-D emission profile. Some rest-UV resonant transitions (e.g., Si II, C II, O I, Fe II) on the other hand have fine structure levels just above their ground state sharing the same excited state (Figure 3.1). The presence of such levels allows resonantly excited ions to emit through either the resonant (blue upward arrows in Figure 3.1) or nonresonant (red downward arrows in Figure 3.1) channel. At high optical depths in the resonance line, excited ions will preferentially decay through the nonresonant (sometimes referred to as "fluorescent") channel (Figure 5 in Scarlata and Panagia 2015).

Nonresonant emission originating from reprocessed absorbed UV continuum photons has been observed in star-forming galaxies across a range of redshifts. At $z \sim 0$, space-based UV observations (typically with *HST*/COS) target the far-UV Si II* transitions (e.g. Scarlata & Panagia, 2015; B. Wang et al., 2020), intermediate redshift ($1 \lesssim z \lesssim 2$) ground-based studies focus on the near-UV Fe II* features (e.g. Erb et al., 2012; Finley et al., 2017; Kornei et al., 2013; Rubin et al., 2011; Tang et al., 2014; Yuma et al., 2013; Zhu et al., 2015), and at $z \gtrsim 2$, O I*, C II*, and Si II* are observable from the ground leading to additional study (Jones et al., 2012; Kusakabe et al., 2024; Shapley et al., 2003).

Low and intermediate redshift studies of nonresonant emission have typically focused on star-forming galaxies and studied Fe II* in the context of large-scale galactic outflows traced by blueshifted Fe II and Mg II. In general, they find that Fe II* is produced via the reprocessing of continuum photons absorbed in the Fe II resonant channel and that Fe II* is spatially more extended than the galaxy continuum (Erb et al., 2012). Importantly, emission filling appears to have the largest effect in purely resonant transitions (e.g. Mg II, Fe II 2382) because the resonant channel is the only means of re-emitting the absorbed photon. Transitions like Si II with excited fine structure levels are less susceptible to emission filling because the nonresonant Si II* offers an alternate emission pathway in addition to the resonant channel (Finley et al., 2017).

Nonresonant emission was observed in the $z \sim 3$ Lyman Break Galaxy (LBG) survey using stacks of several hundred LBG spectra (Shapley et al., 2003; Steidel et al., 2003). Shapley et al. (2003) found relatively narrow and redshifted Si II* (Δv(Si II*) = 100 km s^{-1}); the latter of which was attributed to either low S/N or contamination by the resonant feature (e.g. Si II λ1260). More recently, Steidel et al. (2018) measured nonresonant Si II* in a stack of $\simeq 100$ $z \sim 3$ Keck Lyman Continuum Spectroscopic Survey (KLCS) star-forming galaxies, all with existing KBSS-MOSFIRE data (and therefore more accurate systemic redshifts). Si II* emission was shown to be consistent with the systemic velocity and Si II* had a velocity width that closely matched the red wing of the resonant Si II absorption. Si II* emission strength was also correlated with Lyα emission equivalent width suggesting that galaxies with more compact optically thick gas distributions were more likely to leak Lyα (and by extension LyC) photons.

Nonresonant transitions were explored in detail at $z \sim 1$ by Prochaska, Kasen, and Rubin (2011) and Erb et al. (2012) but the first IFU-based measurements at $z \gtrsim 2$ were made by Kusakabe et al. (2024) who mapped Si II* in the MUSE eXtremely Deep Field with a sample of 14 galaxies. They find extended Si II* λ1533 halos in their UV-bright galaxies and show that photon conservation holds in one object through a comparison of the absorption and emission equivalent widths.

In this paper, we explore the structure and kinematics of Si II* emission in a sample of 50 KBSS-KCWI galaxies. This paper is organized as follows: Section 3.2 describes the KCWI observations and data reduction; Section 3.3 provides an overview of the data products and spectral formats used in this work; Section 3.4 focuses on the kinematics of Si II* emission measured DTB; Section 3.5 investigates the variation of Si II* emission with projected distance ($D_{\rm tran}$), azimuthal angle, and introduces a test of photon conservation; the results are discussed in Section 3.6; and outline our conclusions in Section 3.7. Where required throughout the paper, we assume a flat ΛCDM cosmology with $H_0 = 70$ km s^{-1} Mpc^{-1}, $\Omega_m = 0.3$, $\Omega_\Lambda = 0.7$. At the average redshift of the sample ($\langle z \rangle \simeq 2.3$; Figure 3.2), 1″ therefore corresponds to 8.2 (physical) kpc.

3.2 Observations & Sample Selection

The rest-UV spectra used in this paper come from KBSS-KCWI (Y. Chen et al. 2021, 2026 in preparation; Prusinski et al. 2025), which comprises 186 star-forming galaxies observed with KCWI in 46 unique IFU pointings. Each KBSS-KCWI field has a $\sim 20''$ diameter (170 kpc at $\langle z \rangle = 2.3$) and a typical total integration time of 5 hr. The KCWI spectra were obtained between 2017 September and 2022 June using the medium slicer and low-resolution blue grating (BL; central wavelength = 4500 Å) to achieve spectral resolving power $\langle R \rangle \approx 1800$ over the 3530 − 5530 Å bandpass.

Detailed KCWI data reduction procedures are described in Y. Chen et al. (2021) and Prusinski et al. (2025); in short, individual exposures were reduced using a customized version of the KCWI Data Reduction Pipeline (DRP; Neill, Matuszewski, and Martin 2023; Neill, Matuszewski, Martin, et al. 2023) and stacked using the `KCWIKit` package (Prusinski & Chen, 2024). `KCWIKit` also contains scripts to mitigate instrument systematics not corrected by the standard KCWI DRP making it especially useful in KCWI post-processing.

KBSS-KCWI galaxies have extensive multiwavelength ancillary data that provide stellar population parameter measurements and inferences. The stellar mass (M_*), star formation rate (SFR), specific star formation rate (sSFR $\equiv M_*/\mathrm{SFR}$) and reddening ($E(B-V)_{\mathrm{SED}}$) can be inferred for each galaxy from broadband spectral energy distribution (SED) fitting (see Steidel et al. 2016, 2018 and Theios et al. 2019 for thorough descriptions of the methodology). KBSS space- and ground-based near-IR imaging is also important for quantifying galaxy morphology (discussed further in Section 3.5).

Rest-frame optical spectra from KBSS-MOSFIRE (Steidel et al., 2014; Strom et al., 2017, 2018) are especially helpful in the kinematic analysis below. KBSS-MOSFIRE galaxies have systemic redshift precision $\delta v_{\mathrm{MOSFIRE}} = 18$ km s^{-1} (Steidel et al., 2014), a factor of $\simeq 4$ more precise than is possible with KCWI in the rest-UV ($\sigma_{\mathrm{KCWI}} \simeq 71$ km s^{-1}). Rest-frame optical nebular lines also permit estimates of several stellar population parameters. Dynamical masses ($\mathrm{M_{dyn}}$) were measured following Erb et al. (2006) and Theios et al. (in prep) using the Hα velocity dispersion, $\sigma(\mathrm{H}\alpha)$, such that $\mathrm{M_{dyn}} = C\,[\sigma(\mathrm{H}\alpha)]^2\, r/G$. As discussed in detail by Erb et al. (2006), the value of C

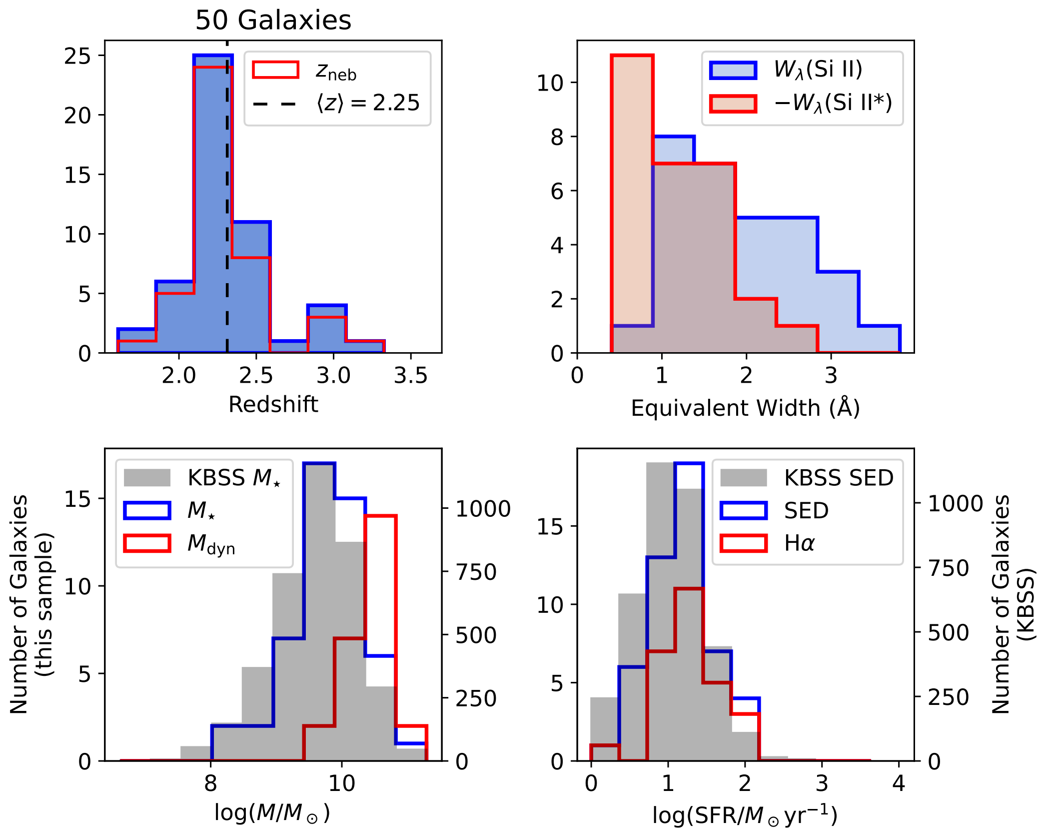

Figure 3.2: Physical and inferred properties about this sample (red and blue histograms; number counts on left ordinate) and the parent KBSS sample (gray histograms; right ordinate, where applicable). *Top Left:* The galaxy redshift distribution; 37/50 galaxies have systemic redshifts measured from nebular emission lines observed with MOSFIRE. *Top Right:* DTB equivalent width distribution for Si II $\lambda1526$ (blue) and Si II* $\lambda1533$ (red). *Bottom Left:* Stellar (blue) and dynamical (red) masses estimated from SED fitting and the Hα emission line width, respectively. *Bottom Right:* Star formation rate estimates from SED fitting (blue) and Hα (red). The gray KBSS histograms are derived from SED fitting.

depends on the mass distribution of the galaxy and its velocity field (both of which are somewhat uncertain in the current sample). In line with Erb et al. (2006), we assumed a disk geometry which results in $C \simeq 3.4$, and let r be the half-light radius of the Hα emission line along the MOSFIRE slit. Reddening was inferred from the Balmer decrement ($E(B-V)_{\rm BD}$) as discussed in Theios et al. (2019), and star formation rate surface densities were estimated from the Hα luminosity as $\Sigma_{\rm SFR} = \frac{\rm SFR}{\pi r^2}$, where r has the same definition as above (see again Theios et al. 2019). We explore the relationship between galaxy properties and nonresonant emission in Section 3.4.

Shapley et al. (2003) hypothesized that nonresonant emission is generated from continuum pumping of the resonance transition which subsequently decays via either the resonant or nonresonant channel. We therefore selected KBSS-KCWI galaxies where at least one of Si II λ1260, Si II λ1304, or Si II λ1526 was detected. In order for such lines to be detected in the KBSS-KCWI cubes, galaxies must have $1.3 \leq z \leq 3.3$ and we further required W_λ(Si II) ≥ 0.2 Å. From the sample of 186 star-forming galaxies in KBSS-KCWI, 50 objects satisfy both criteria. Most of the galaxies with resonant absorption also have corresponding nonresonant Si II* emission, which will be the primary focus of this paper. 37/50 (74%) of the galaxies have nebular redshifts from KBSS-MOSFIRE and all 50 galaxies have spatially extended morphologies that permit a robust position angle measurement (Section 3.5). The redshift, W_λ, M_*, $\mathrm{M_{dyn}}$, and SFR distributions for the sample are shown in Figure 3.2.

3.3 Data Formats & Measurements

Beyond the native KCWI "cube" format that provides surface brightness as a function of spatial position and wavelength, i.e. SB$(\alpha, \delta, \lambda)$, this study also makes use of cylindrically projected two dimensional (CP2D) spectra. CP2D spectra were introduced and visualized in Y. Chen et al. (2021); at a high level, CP2D spectra are 2-D projections of the 3-D mosaicked KCWI IFU cubes that show surface brightness in concentric, azimuthally averaged bins moving outward from the center of a particular object i.e., SB$(\lambda, D_{\mathrm{tran}})$. Equivalently, one can think of a CP2D spectrum as a projection that provides a radial surface brightness profile vs. wavelength. Additional details for the interested reader are provided in Y. Chen et al. (2021); this data format will be put to use in Section 3.5.

This work also makes use of 1-D DTB spectra, extracted from the ~ 5 hr stacked KCWI cubes. The details of how the 1-D spectra are extracted from the cubes are discussed in Prusinski et al. (2025), but in brief, the whitelight image of a cube (formed by collapsing the cube along the wavelength axis) together with `SExtractor` (Bertin & Arnouts, 1996) was used to define a spatial extraction aperture. Each spaxel in that aperture contributes to the final 1-D average galaxy spectrum, but is weighted by the $(S/N)^2$ of the white light signal. On average, the DTB extraction region is approximately the size of the seeing disk ($\simeq 0.9''$ FWHM).

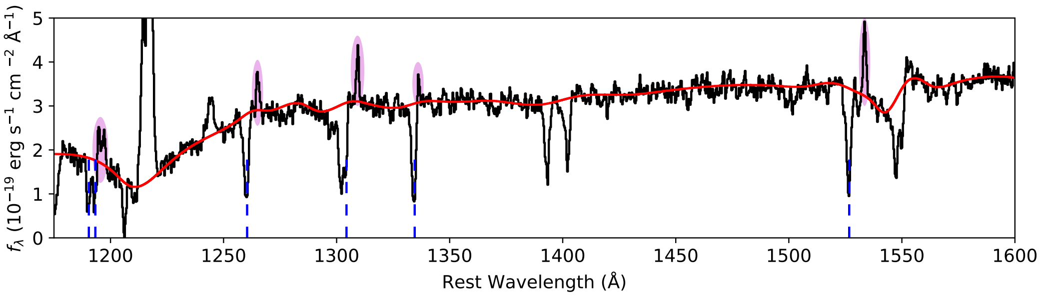

Figure 3.3: DTB extraction from stack of all 50 KBSS-KCWI spectra in the sample ($\langle z \rangle = 2.25$). The spline continuum fit is shown in red. Resonant absorption lines are shown with blue vertical dashed lines and corresponding nonresonant emission lines are highlighted in magenta. Rest wavelengths for all transitions are in Table 3.1.

All of the nonresonant emission measurements below are made using continuum subtracted spectra. Throughout this paper, the general procedure is to stack and then continuum subtract to avoid adding additional spectral noise due to continuum fitting (exceptions, where they appear, are noted). Given a one dimensional spectrum, we fit a low-order spline, masking regions around strong UV absorption or emission features. Spline knots were placed in approximately 50 Å increments and set equal to the median flux density over that wavelength range. Additional knots were used to fit out the broad ($\sim$ 2,000 km s^{-1}) stellar wind component from the C IV λ1548 line (see e.g. Crowther et al. 2006; Rix et al. 2004; Steidel et al. 2016) so that only Si II* λ1533 emission is retained. Figure 3.3 shows an example continuum fit for the full galaxy stack.

Moving to higher dimensions, CP2D spectra can be subtracted row by row using this approach, as each row in the CP2D image is a spectrum at a particular D_{tran}. Where needed, the KCWI cubes were continuum subtracted on a spaxel-by-spaxel basis.[1] The cube continuum subtraction strategy used here differs slightly from the one used in Y. Chen et al. (2021) who fit a single BPASSv2.2 (Stanway & Eldridge, 2018) stellar population synthesis (SPS) model to each KCWI-observed galaxy and scaled that model by the median flux of each spaxel in the cube containing continuum from that particular galaxy. We found that the spline and SPS continuum subtraction methods yielded consistent results with residuals between the best-fit BPASS continua and the spline fit at the level of the flux uncertainty in the KCWI data cubes.

[1]This is of course the most computationally expensive continuum subtraction strategy.

At the same time, we did not find large spaxel-to-spaxel discrepancies that might signal the need for a less spatially variable approach. We therefore opted for the spline method due to its simplicity.

We experimented with several methods for fitting and measuring absorption and emission features in the KCWI spectra[2] but ultimately concluded that at this spectral resolution, the absorption and emission features were well fit by Gaussians (see e.g. Figure 3.5). Gaussian fitting also worked well at low S/N since the fit parameters were less affected by noise spikes in the spectrum compared to more direct methods. Velocity centroids (Δv) and dispersions (σ) are therefore directly from the Gaussian fits and are comparable to first and second moments of the line profiles at high-S/N. This approach matches what was done for the KBSS-MOSFIRE kinematic measurements which we compare to below. Rest-frame equivalent widths (W_λ) are still computed via direct integration over the line profile, using the 1st and 99th Gaussian percentiles as bounds ($\Delta v \pm 3\sigma$). This particular choice of bounds is relatively insensitive to small errors in continuum placement.

Since KCWI and MOSFIRE have different instrumental resolutions ($\sigma_{\rm KCWI} \simeq 71\,{\rm km\,s^{-1}}$; $\sigma_{\rm MOSFIRE} \simeq 35\,{\rm km\,s^{-1}}$), in order to make a fair comparison between velocity dispersions measured between using instruments, it is necessary to correct the measured velocity widths of spectral features. We have quadrature subtracted the appropriate instrumental contribution from all velocity dispersion measurements presented to facilitate comparison between the two instruments.

We now discuss the principal results of this paper, beginning with a discussion of the kinematics of nonresonant emission observed DTB (Section 3.4) then we move on to the properties of spatially extended Si II* (Section 3.5).

3.4 DTB Emission

Table 3.1 lists the resonant/nonresonant pairs observable in our rest-UV spectra. In this paper, we preferentially focus on rest-frame wavelengths longward of Lyα since the nonresonant emission in the sample is already comparatively "weak" with respect to other interstellar transitions and the Si II* lines in the Lyα forest fall at observed wavelengths with low KCWI

[2](Multi-component) Gaussian fit mean and width; W_{90}; direct integration of the line profile and its moments; $v_{\rm max}$ defined as the velocity where the line reaches the continuum.

Table 3.1: Rest-UV Absorption and Emission Features

Line	λ_{vac} (Å)	A_{ul}^{a} (s^{-1})	P_{ul}^{b} (%)	ΔE^{c} (eV)
C II	1334.5323	2.41×10^{8}	83.5	
C II*	1335.6628	4.76×10^{7}	16.5	0.0079
Si II	1190.4158	6.53×10^{8}	15.9	
Si II	1193.2897	2.69×10^{9}	65.8	
Si II*	1194.5002	3.45×10^{9}	84.1	0.0356
Si II*	1197.3938	1.40×10^{9}	34.2	0.0356
Si II	1260.4221	2.57×10^{9}	84.5	
Si II*	1265.0020	4.73×10^{8}	15.5	0.0356
Si II	1304.3702	3.64×10^{8}	36.9	
Si II*	1309.2757	6.23×10^{8}	63.1	0.0356
Si II	1526.7066	3.81×10^{8}	33.6	
Si II*	1533.4316	7.52×10^{8}	66.4	0.0356

[a] Einstein *A* coefficients.
[b] Probability of de-excitation to listed level from the excited state.
[c] Energy of the excited fine structure level above the ground state.

detector throughput. As discussed in Section 3.2, we require Si II* to be present in the DTB galaxy spectrum and we focus on that ion over C II* and O I* (which are available for a large fraction of the sample). Not only does Si II have multiple resonant/nonresonant pairs in the KCWI bandpass, but the Si II* nonresonant transitions have greater wavelength separation from their resonant counterparts than the C II/C II* and O I/O I* transitions (see Figure 3.5 for a visual). For the same reason, we make measurements using, in order of availability and S/N: Si II* λ1533, then Si II* λ1265. Note that Si II λ1304 is also generally avoided since it is the weakest of the three Si II transitions and as such would be expected to produce the fewest nonresonant photons (Table 3.1). Si II λ1526 is weaker than Si II λ1260 but is still often saturated and has a comparable strength to Si II λ1260 at all but the highest DTB blueshifted velocities (Figure 3.4). The DTB absorption lines are too broad to separate C II λ1334 and C II* λ1335 so we use Si II λ1260 as a proxy for C II λ1334 since they have a similar presentation.

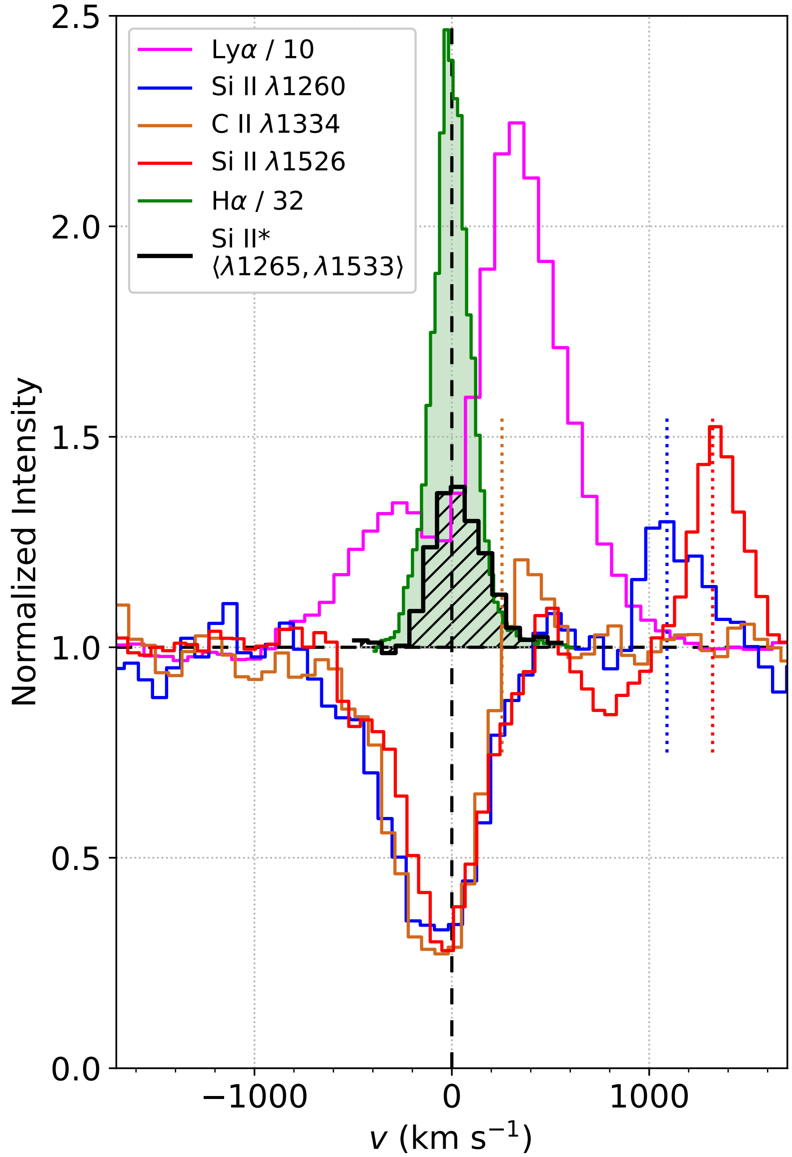

Figure 3.4: Rest-frame UV and optical features from continuum-normalized stacked KCWI and MOSFIRE spectra (respectively) plotted on the same velocity scale. Transitions (and scalings for Lyα and Hα) are listed in the figure legend. The black hatched histogram is the average of the Si II* λ1265 and Si II* λ1533 emission line profiles.

Kinematics of DTB Si II*

For each of the galaxies in the sample, we perform multi-component fits to the absorption and emission lines present; Figure 3.5 shows an example of a galaxy with all of the rest-UV nonresonant features detection with relatively high S/N. In general, σ(Si II*) is less than σ(Si II) (similarly, σ(C II*) < σ(C II)

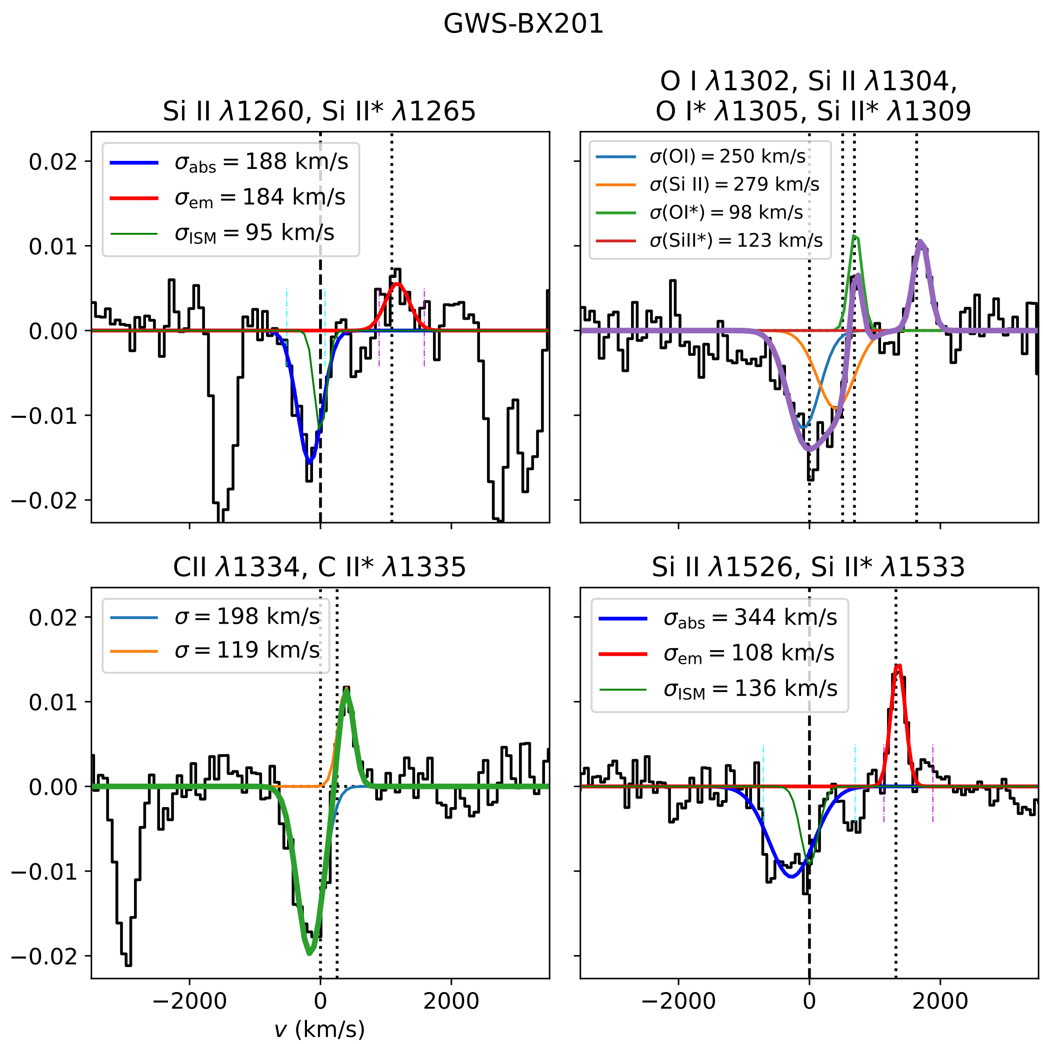

Figure 3.5: Example Gaussian fits to continuum-subtracted DTB resonant absorption and nonresonant emission lines in the rest-frame UV. For Si II, full absorption line is fit in blue, the Si II ISM component is in green (fit using only the red wing of the absorption line), and the Si II* fit is in red. For O I and Si II λ1304, each component is listed in the legend and the sum of all components is in purple. The C II panel is similar, but the total fit is in green. Each transition is denoted by vertical dotted lines. Neighboring absorption lines in the Si II λ1260 and C II λ1334 panels are intervening absorption systems from foreground galaxies.

and σ(O I*) < σ(O I)) and W_λ(Si II*) is approximately half of W_λ(Si II) (Figure 3.2).

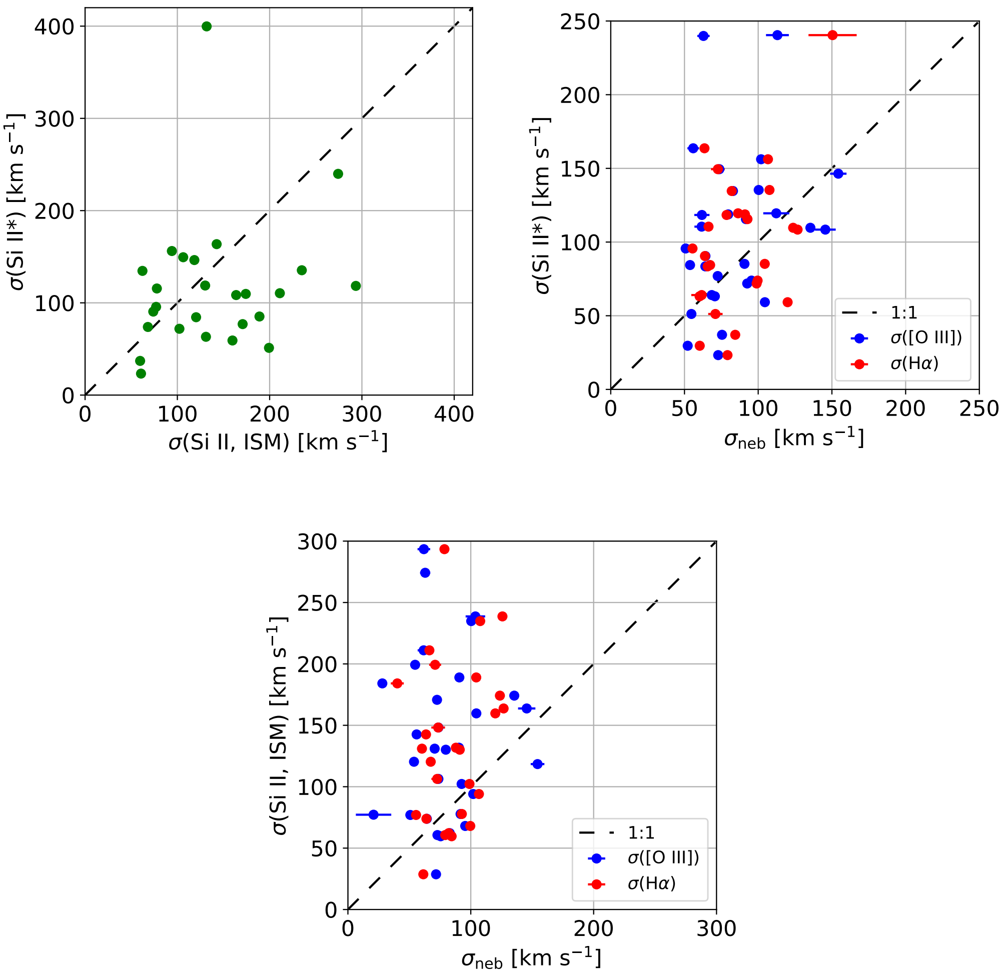

Figure 3.6: *Top Left:* Rest-frame UV nonresonant emission line width vs. width of ISM component derived from the resonant absorption feature associated with each respective fluorescent line. *Top Right:* Rest-frame UV nonresonant emission line width, computed from Gaussian fits vs. rest-frame optical nebular emission line widths for the same set of galaxies. *Bottom Center:* Derived rest-frame UV absorption line ISM component widths vs. rest-frame nebular emission line widths. In all three plots, σ(Si II, ISM) represents a median of σ(1260, ISM) and σ(1526, ISM) i.e., the median of the derived Gaussian widths of the ISM components for Si II λ1260 and Si II λ1526. Similarly, σ(Si II*) represents an average of σ(1265) and σ(1533) for a particular object, where available.

In low-resolution absorption line studies of galaxies with outflows, blueshifted interstellar absorption lines are expected to have contributions from both outflowing material and the ISM of the galaxy. A common practice is to separate the absorption line profile into two components: an "ISM" component (typically modeled as a Gaussian centered at the systemic velocity) and an "outflowing" component which comprises the remaining absorbed flux not included in the ISM component (e.g. Coil et al., 2011; Martin et al., 2012; Weiner et al., 2009). Motivated by the fact that σ(Si II*) < σ(Si II), we fit a Gaussian ISM absorption component centered at Δv(Si II) = 0 km s^{-1} to test if the resonant absorption "ISM" component more closely resembles the nonresonant emission line. The "ISM" component is fit using only the red wing of the absorption line (v(Si II) > 0 km s^{-1}) with amplitude not exceeding the absorption line flux (see the green curves in Figure 3.5 for a sample fit). Figure 3.6a shows a comparison between σ(Si II*) and the velocity spread associated with the ISM derived from Si II absorption.

The general agreement between σ(Si II*) and σ(Si II, ISM) suggests that most of the nonresonant emission is tracing ISM gas and not necessarily outflowing material. This finding further supports the hypothesis that Si II* is tracing reprocessed absorption line photons from optically thick regions of the galaxy. Most of the optically thick gas in the galaxy likely resides in its ISM and would be expected to take on the approximate ISM kinematics.

To further test this connection, we compared the Si II* kinematics to that of the bright nebular emission lines in the rest-optical (e.g. Hα and [O III]) which are expected to trace gas in the H II regions of the galaxy. Figure 3.6b shows a comparison between σ(Si II*) and $\sigma_{\rm neb}$. Figure 3.6b shows both σ(Hα) and σ([O III]) but both nebular lines have been shown to have similar velocity dispersions (Steidel et al., 2014). While the points generally cluster around the one-to-one line, σ(Si II*) exceeds $\sigma_{\rm neb}$ for a majority of the sample. A similar comparison can be made (Figure 3.6c) between σ(Si II, ISM) and $\sigma_{\rm neb}$, both of which are ostensibly tracing predominantly ISM gas. Here the distinction is more obvious in that Si II and Si II* have a wider range of velocities compared to the nebular lines.

While the nonresonant lines could potentially have a contribution from outflowing gas (as suggested by e.g. Prochaska, Kasen, and Rubin 2011), a likely explanation is that the UV interstellar lines have a different weighting than the optical emission lines. The interstellar absorption line optical depth $\tau_{\rm IS} \propto \int n_e \, dl$, where n_e is the electron number density and the integral is computed along the line of sight. Since a fraction of these electrons decay through the nonresonant channels, $\varepsilon_{\rm IS} \propto \frac{A_{ul_i}}{\Sigma_i A_{ul_i}} \int n_e \, dl$ In contrast, rest-optical recombination (and collisionally excited) line emissivity $\varepsilon_{\rm recomb} \propto n^2$. The rest-UV lines therefore sample a larger cross-section of the ISM (and CGM) gas and if that gas takes on a larger velocity dispersion relative to the rest-optical lines (as is suggested by Figure 3.6b) it could explain the disparity between the two apparent ISM metrics.

Si II* Velocity Centroid

Unlike the resonant far-UV absorption lines, which use the galaxy continuum as a backlight and are sensitive only to gas "in front of" the galaxy, nonresonant emission can trace gas along the line of sight from both the "front" and "back" sides of the galaxy. Nonresonant emission lines therefore may provide a more complete census of high optical depth gas throughout the galaxy. In a spherically symmetric dust-free geometry, an equal number of photons would be produced on both sides of the galaxy resulting in a symmetric fluorescent emission line profile centered at $\Delta v = 0$ km s^{-1}. Any asymmetries in the spatial or kinematic distribution of the gas would then naturally induce changes to the emission line profile.

Stacks of nonresonant emission spectra from different galaxies would also be expected to converge to a symmetric velocity distribution centered at $v_{\rm sys}$. Studies of Si II* and Fe II* in moderately-sized galaxy samples have observed velocity centroids close to zero in composite spectra at low (B. Wang et al., 2020), intermediate (Coil et al., 2011; Erb et al., 2012; Kornei et al., 2013), and high redshift (Steidel et al., 2016). We note that Fe II has a similar ground state splitting to Si II in that several fluorescent channels are available to resonantly-excited electrons. Fe II* and Si II* are therefore expected to be produced in a similar manner (Prochaska, Kasen, & Rubin, 2011).

At higher redshifts ($z \sim 2 - 3$), there have been several attempts to measure rest-UV nonresonant emission lines using different galaxy subsamples (Shapley et al., 2003; Steidel et al., 2016, 2018). On average, Δv(Si II*) is consistent with $v_{\rm sys}$, given the redshift uncertainties and spectral resolution of each subsample. Despite their low significance in earlier work, Si II* λ1265 and Si II* λ1533 have consistently showed a redshifted velocity centroid where measured. We revisit these measurements with the current sample

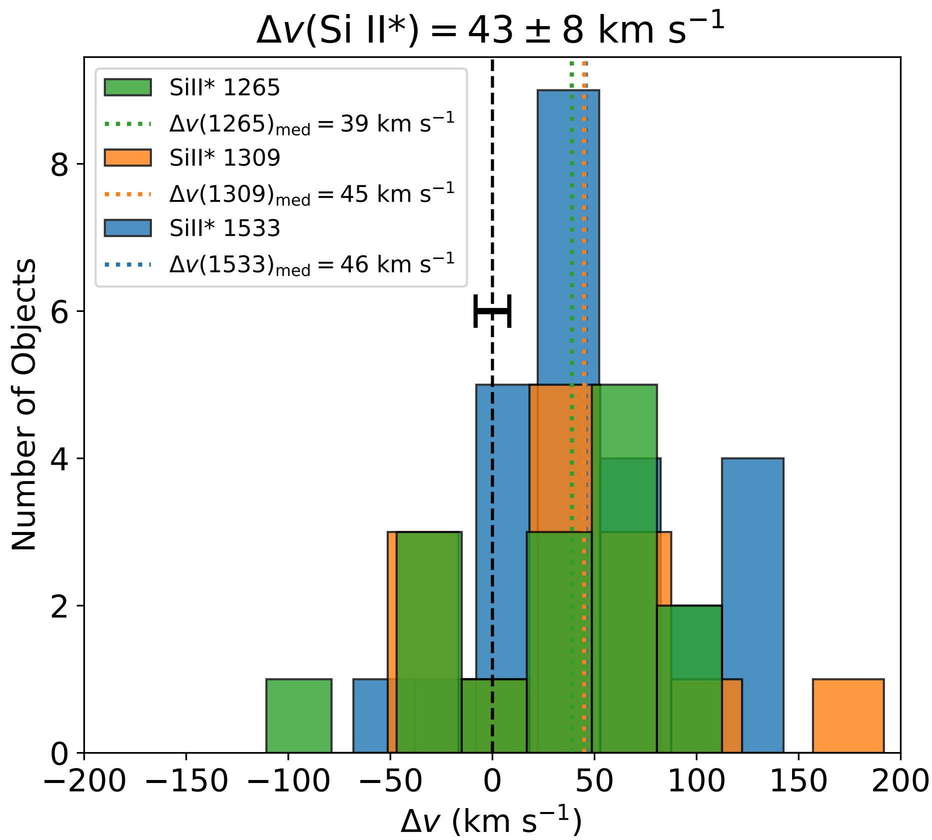

Figure 3.7: Histogram of several Si II* velocity centroids (Δv) derived from Gaussian fits for the 37 objects with systemic redshifts from MOSFIRE nebular emission lines: $\Delta v(1265)$, $\Delta v(1309)$, $\Delta v(1533)$. Median velocity centroids are overplotted in color-coded in dotted lines and listed in the legend. The average redshift uncertainty is 8 km s^{-1}.

noting that KBSS-KCWI offers the highest spectral resolution measurements to date ($\langle R \rangle \simeq 1800$) and this subsample contains a higher fraction of galaxies with nebular redshifts (74%) over previous studies. Figure 3.7 shows the distribution of velocity centroids for Si II* λ1265, Si II* λ1309, and Si II* λ1533. While O I* and C II* are present for a large fraction of the sample, their proximity to neighboring transitions (at this spectral resolution) compromises the accuracy of their velocity centroid measurements. For this reason, we restrict our discussion to the relatively clean Si II* lines.

For the sample of KBSS-KCWI galaxies with nebular redshifts, we find Si II* emission redshifted by $\Delta v_{\rm med} \simeq 40$ km s^{-1} with respect to the systemic velocity of the galaxy.[3] Given the wavelength ranges in which these fluo-

[3] Where there is overlap, KBSS-LM1 spectra (Steidel et al., 2016) show a similar velocity

rescent transitions reside it is reasonable that this type of offset could result from an error in continuum fitting. Our testing suggests the fitting strategy we have chosen is efficient and fairly robust against many different Si II and Si II* presentations but we note that $\Delta v(1265)$ could be redshifted if there is broad absorption in the Si II $\lambda1260$ red wing, and $\Delta v(1533)$ could be similarly redshifted if the C IV $\lambda1548$ wing is not correctly fit out by the spline. Another possible explanation for the systematic redshift could be due to a population of collisionally-excited electrons in the Si II excited fine structure level ($^2P^\circ_{3/2}$) that produce Si II* $\lambda1265$, Si II* $\lambda1309$, or Si II* $\lambda1533$ *absorption*. Such a situation would only occur however is very high-density environments ($n_e = 10^{9-13}$ cm^{-3}; Keenan et al. 1992; Shapley et al. 2003) which seems unlikely for our current sample.

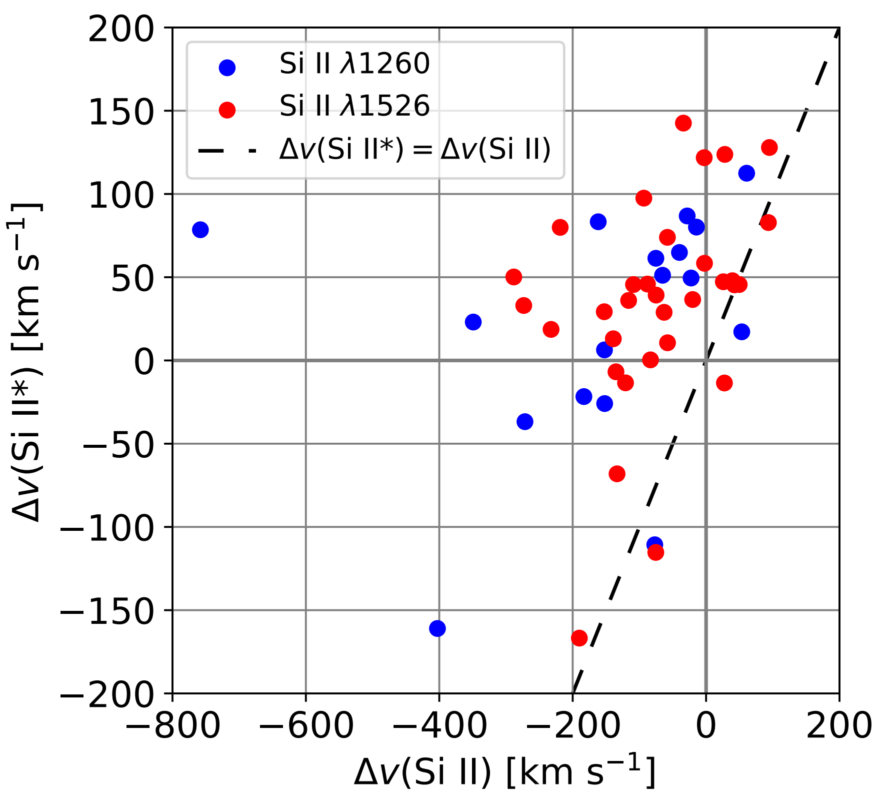

Figure 3.8: Δv(Si II*) vs. Δv(Si II) for the strongest nonresonant transitions: $\Delta v(1265)$ vs. $\Delta v(1260)$ in blue and $\Delta v(1533)$ vs. $\Delta v(1526)$ in red. A dashed one-to-one line is overplotted in black.

Despite being marginally redshifted from the systemic velocity on average,

shift.

Δv(Si II*) is weakly correlated with Δv(Si II) (fit to the full resonant absorption profile). Figure 3.8 compares the velocity centroids of the resonant and nonresonant transitions for Si II λ1260 (1265) and Si II λ1526 (1533). In general, galaxies with more blueshifted absorption (i.e. outflows with higher velocities or covering fractions) tend to also have blueshifted nonresonant emission. The scatter and comparatively narrow range of Δv(Si II*) (with respect to Δv(Si II)) again point to an emission source dominated by fluorescent ISM photons and a subdominant outflowing component. Put differently, the weak outflowing material in these galaxies has a considerably lower density than the ISM.

Dependence of Si II* on galaxy properties

We compared the Si II* emission strength and kinematics with the set of galaxy physical and stellar population parameters available but find remarkably few correlations. The lack of correlations is perhaps not surprising in light of previous kinematic studies of $z \sim 2$ Lyman-break galaxies (e.g., Steidel et al. 2010 and Theios et al. in prep).

Comparing Si II and Si II*, σ(Si II*) is uncorrelated with Δv(Si II) and σ(Si II) except insofar as σ(Si II*) is related to σ(Si II, ISM). This lack of a correlation also appears independent of velocity metric (see Section 3.3).

In terms of stellar population parameters, Δv(1260) and Δv(1526) are correlated with $\Sigma_{\rm SFR}$ (also see Theios et al. in prep) and based on Figure 3.8, it makes sense that we find Δv(1265) and Δv(1533) to be correlated with $\Sigma_{\rm SFR}$. While the Si II and Si II* velocity centroids are correlated with $\Sigma_{\rm SFR}$, σ(Si II) and σ(Si II*) show no correlation with $\Sigma_{\rm SFR}$. Higher mass galaxies tend to have Δv(Si II*) closer to the systemic velocity, perhaps due to the fact that there is more mass in the ISM in those systems. Higher mass galaxies do not appear to have larger σ(Si II*) however.

Erb et al. (2012) and Tang et al. (2014) both find tentative evidence for blueshifted Fe II* emission in high $E(B-V)$ composite spectra of $z \sim 1$ galaxies. Models of nonresonant emission have suggested that galaxies with higher dust content (and therefore higher $E(B-V)$) produce more blueshifted emission profiles (e.g. Prochaska, Kasen, & Rubin, 2011). This idea can be appreciated in the case of an outflow geometry, where nonresonant photons produced in the outflow on the “back side” of the galaxy

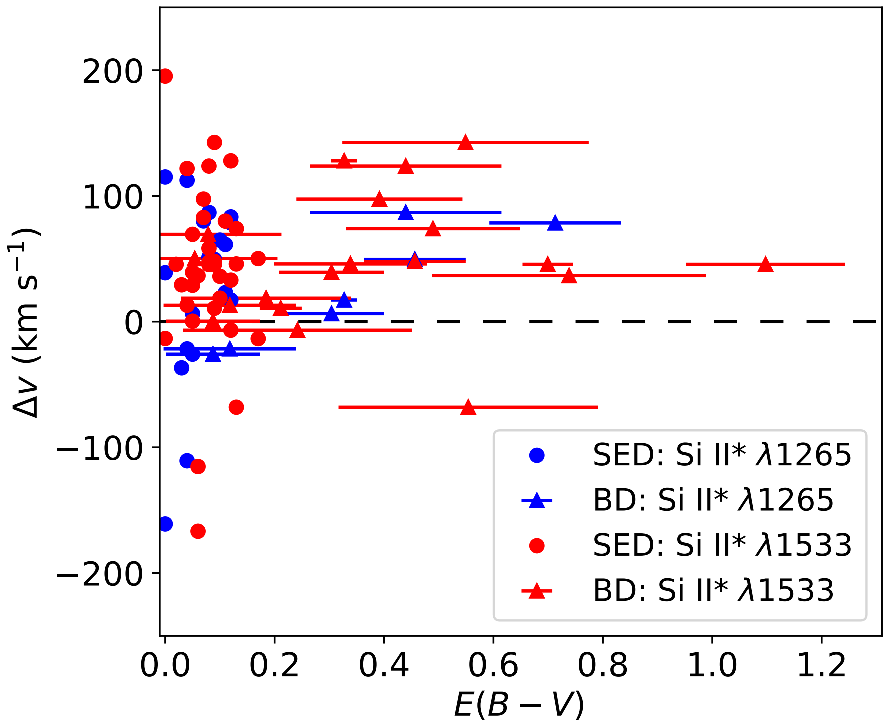

Figure 3.9: Si II* λ1265 (blue) and Si II* λ1533 (red) velocity centroids against two measures of $E(B-V)$ for the sample: $E(B-V)_{\rm SED}$ (circles) and $E(B-V)_{\rm BD}$ (triangles) which are computed from galaxy SED fits and Balmer decrements, respectively.

would appear redshifted with respect to the systemic velocity. Such photons would then be preferentially absorbed by dust since they have a longer path length along the line of sight, with respect to (blueshifted) photons produced on the side of the galaxy nearest the observer. The net fluorescent line profile for the dusty galaxy would therefore appear blueshifted. We test this hypothesis with the current sample by comparing both $E(B-V)_{\rm SED}$ and $E(B-V)_{\rm BD}$ against Δv(Si II*) but find no correlation (Figure 3.9).

3.5 Extended Nonresonant Emission

Absorption-line studies at $z \sim 2$ have shown that star-forming galaxies have extended reservoirs of neutral hydrogen (Y. Chen et al., 2020; Rudie et al., 2012) and metals (Prusinski et al., 2025; Turner et al., 2014) detectable at Mpc scales from the host (for neutral hydrogen and the high ions). Studies of Lyα have also revealed halos in emission (e.g. Y. Chen et al., 2021). Here we present the first maps of spatially resolved metallic emission at $z \sim 2$.

The maps below were constructed by stacking all 50 galaxies in the sample. Each constituent galaxy contains a subset of the possible nonresonant UV emission lines, dependent largely on redshift and continuum S/N. Additionally, before stacking, each galaxy was coarsely normalized by its median 1400 – 1500 Å continuum flux density so that the final cube would have approximately equal contributions from each object. Aside from the surface brightness scaling, no other continuum subtraction was performed on individual cubes entering into the stack; the average continuum was subtracted from the final stacked cube in the manner described in Section 3.3. In the following subsections, we introduce the radial dependence of Si II* with $D_{\rm tran}$ (Section 3.5), how Si II* emission depends on galaxy azimuthal angle (Section 3.5), and then explore the properties of Si II* at large $D_{\rm tran}$ (Section 3.5).

The radial variation of Si II*

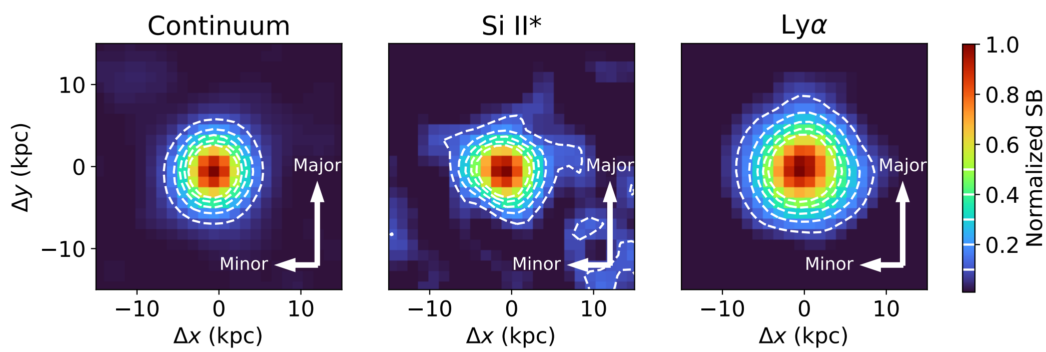

Figure 3.10: Stacked rest-UV continuum (left), Si II* (center), and Lyα images for galaxies aligned along their major axis. Both Si II* λ1265 and Si II* λ1533 are averaged to produce the center Si II* image; the continuum map is a whitelight image between 1410 – 1500 Å. Each image has had its intensity normalized by the peak (central) value in the image. Since the stacked galaxies are co-aligned along their major axis, the continuum image shows a slight elongation in that direction. The Si II* emission appears marginally extended the minor axis.

Figure 3.10 shows a collection of pseudo-narrowband images for a stack of the 50 KBSS-KCWI galaxies in this sample.[4] The continuum whitelight image is made by summing over the 1400 – 1500 Å bandpass where strong UV interstellar absorption lines do not contaminate the signal; the Lyα

[4]Figure 3.10 comprises *rotated* galaxies but as discussed in Section 3.5, the difference in morphology between a “rotated” and “straight” stack is quite small.

map is constructed similarly by summing over the spectral extent of Lyα (1212 – 1220 Å) in the continuum subtracted cube. The Si II* map is an average of the Si II λ1260 and Si II* λ1533 continuum-subtracted emission line intensities. A $\simeq$ 600 km s^{-1} wavelength window centered on the rest wavelength of each feature was used so that the full velocity extent of the emission line was captured. Each pseudo-narrowband image is normalized by its brightest (central) pixel for ease of comparison.

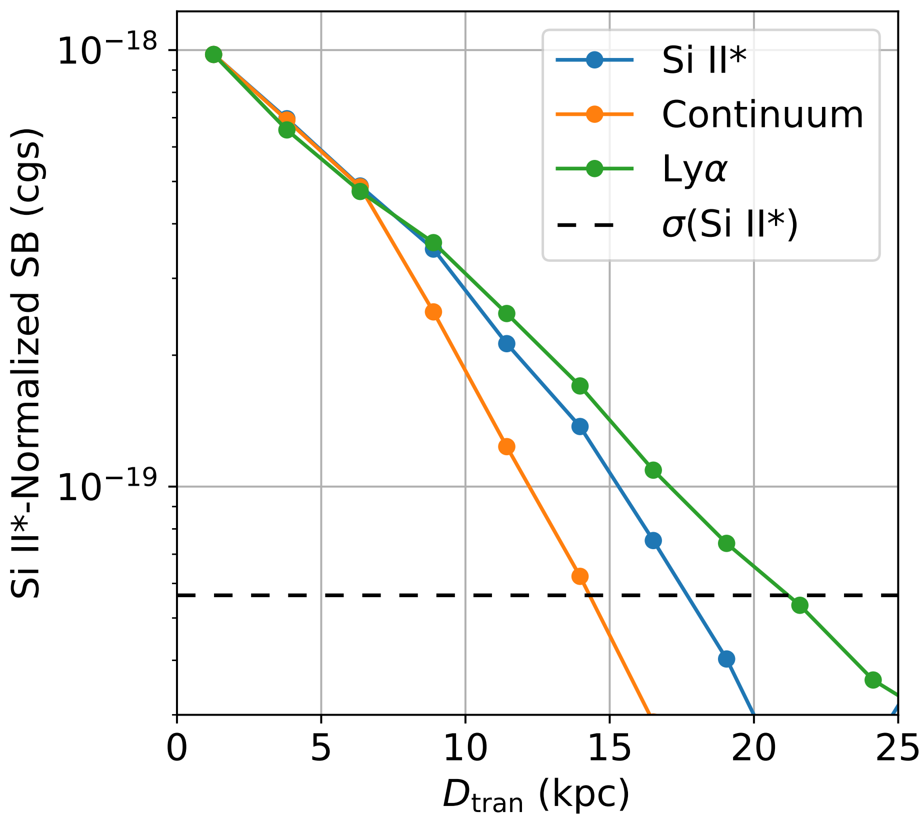

Figure 3.11: *Left:* Surface brightness profiles for Si II* (whose central SB sets the normalization), the rest-UV continuum (1410 – 1510 Å), and Lyα. Si II* is slightly more extended than the galaxy continuum.

From Figure 3.10, it is clear that Si II* has a noisier morphology than both the galaxy continuum light and Lyα emission. Lyα also has a somewhat more compact (centrally-concentrated) distribution than has been observed for larger KBSS galaxy subsets (Y. Chen et al., 2021; Steidel et al., 2011). The radial distribution of each image is shown in Figure 3.11 Si II* again represents an average over the Si II* λ1265 and Si II* λ1533 lines. In general, Si II* is slight extended beyond the average galaxy continuum. Together with Lyα, all three distributions fall off similarly, but Si II* falls off faster than Lyα. Lyα may be expected to be more spatially extended than Si II* owing to its comparatively larger scattering cross-section, its resonant nature that results in numerous scatterings before escaping along our line of sight, and the overall abundance of H I relative to the metals. A further discussion of Lyα will appear in Chen et al. (in prep). The Si II* emission lines are $\sim 20\times$ weaker than Lyα so, even when stacked, it is only possible to trace its radial profile out to $D_{\rm tran} \simeq 20$ kpc before reaching the KBSS-KCWI noise floor. However, as we will discuss in Section 3.5, diffuse Si II* emission is present to at least $D_{\rm tran} \simeq 50$ kpc for a fraction of the galaxies in this sample.

Kinematically, we have shown that Si II* takes on a smaller range of velocities than its associated resonant transitions (e.g. Figure 3.6a) DTB, and at $D_{\rm tran} >$ 0 kpc, the picture stays the same where σ(Si II*) is consistently less than than σ(Si II). Similar to Figure 3.11, Figure 3.12 shows the radial dependence of the line-of-sight velocity spread for both Si II* λ1265 and Si II* λ1533. Where measurable, $\sigma(1265) > \sigma(1533)$ which could be explained by the fact that the $W_\lambda(1260)/W_\lambda(1526)$ ratio is a tracer of saturation. Previous KLCS work (e.g. Steidel et al. 2018) has shown that high velocity outflowing Si II observed DTB is less saturated than the absorbing gas closer to the systemic velocity. In other words, $W_\lambda(1260) > W_\lambda(1526)$ and by extension $\sigma(1260) > \sigma(1526)$. It is possible that the difference in σ for the resonant transition is manifested in the nonresonant transition since a fraction of the absorption photons are getting reprocessed through the nonresonant channel.

Figure 3.12 also includes a comparison between DTB emission and projected sightlines from foreground/background galaxy pairs at $D_{\rm tran} > 0$ kpc in absorption. Interstellar absorption lines require a background source of illumination, normally the galaxy continuum, in order to be observed. In (Prusinski et al., 2025), background galaxies were used as the backlight to measure extended absorption in the halos of KBSS galaxies at $z \sim 2$. Figure 3.12 combines DTB Si II velocity dispersions with the relevant results from Prusinski et al. (2025). Note that the observed DTB σ(Si II) have been multiplied by a factor of 2 to estimate the total velocity spread one would observe at $D_{\rm tran} = 0$ kpc. While the effective spatial sampling is considerably different between the two samples (see Prusinski et al. (2025) for details), it is interesting to note that the absorption and emission share a comparable decrease in their velocity dispersions with increasing $D_{\rm tran}$.

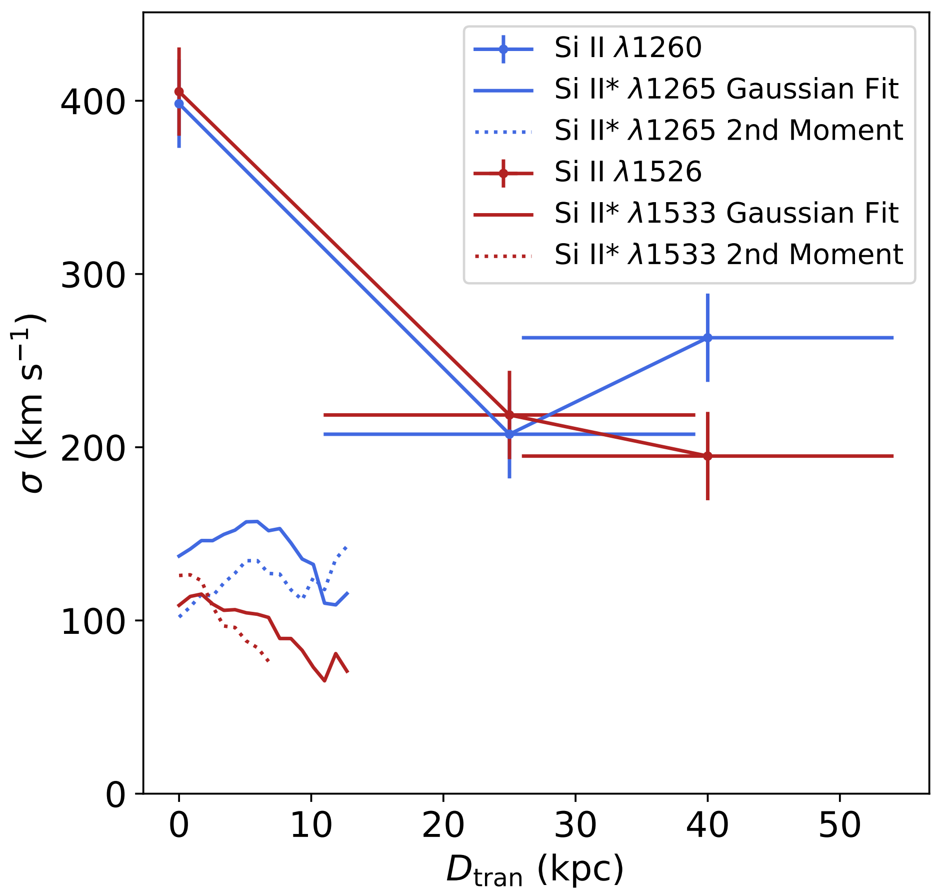

Figure 3.12: Si II* velocity spread (σ) vs. D_{tran} for Si II* λ1265 (blue) and Si II* λ1533 (red). Velocity dispersions are computed by fitting a Gaussian to the emission line (solid line) and by taking the second moment of the line profile (dotted line). Velocity dispersions for the associated resonant Si II transitions are also shown using the same color coding. DTB σ(Si II) are measured with this sample; σ(Si II) at $D_{\text{tran}} > 0$ kpc are from Prusinski et al. (2025). Following Prusinski et al. (2025), the observed DTB σ(Si II) have been upscaled by a factor of 2 to approximate the total velocity spread that would be observed along a line of sight through the full galaxy at $D_{\text{tran}} = 0$ kpc.

The dependence of Si II* on azimuthal angle

At $z \lesssim 1$, observations and simulations have supported a picture of the CGM where gas accretion occurs primarily along the major axis of the galaxy and star-formation-induced galactic winds expel metal-enriched ejecta via (biconical) outflows along the minor axis (S. Dutta et al., 2026; Péroux et al., 2020; Veilleux et al., 2005; Zhang et al., 2024). However, at $z \sim 2$, the morphology of Lyα emission halos and rest-UV absorption measured with transverse sightlines ($D_{\rm tran} > 0$ kpc) appear independent of galaxy orientation (Y. Chen et al., 2021; Méndez-Hernández et al., 2022). Given this dichotomy (and potential redshift evolution), it is fair to ask if nonresonant emission halos show evidence of an azimuthal dependence.

To answer the question of CGM azimuthal asymmetry, it is necessary to have robust measurements of galaxy major axis position angle (PA). We adopt the conventions and methodology of Y. Chen et al. (2021) who computed PAs for 33/50 galaxies in the current sample. Y. Chen et al. (2021) used four separate methods to compute galaxy PA; since all techniques showed mutual agreement to within ±10°, we choose to use the second moment of the pixel intensity on high spatial resolution images of each galaxy for our PA measurement.

The details of the second moment method are described in Y. Chen et al. (2021) but fundamentally PAs are computed based on the second moment of the intensity relative to the flux-weighted centroid of the galaxy. We use the existing 33 previous measurements and derive the PA of the remaining 17 galaxies using the highest spatial resolution imaging available from KBSS ancillary data products. In decreasing order of priority we used images from: *JWST* F277W, *HST* ACS, WFC3-IR/F140W, F160W, KBSS-MOSFIRE J, H, and K_s band, and finally ground-based optical narrowband imaging (UG$\mathcal{R}$). This prioritization scheme is the same as adopted by Y. Chen et al. (2021), with the addition of *JWST* rest-optical imaging. We find (as did Y. Chen et al. 2021) that convolving the high spatial resolution images by a symmetric 2D Gaussian kernel resulted in more consistent PA measurements across the sample.

We perform the ensuing morphological analysis on the the full sample of 50 galaxies since they all exhibit a non-circular morphology with a clearly defined PA. In other words, the image second moments along the major and minor axes of each galaxy are significantly different. Figure 3.13 shows the distribution of PAs for the sample. As discussed by Y. Chen et al. (2021), there is a pronounced, but statistically insignificant excess at PA $\sim 10-40°$. A source of uncertainty in this type of measurement is the connection (or lack thereof) between the "kinematic" PA (that is set by the dynamics in the galaxy/CGM) and the "morphological" PA (the quantity we are measuring from imaging) of a galaxy. Where there was overlap, Y. Chen et al. (2021) found reasonable agreement between "morphological" and "kinematic" PAs, but we caution that a majority of the current sample does not have high spatial resolution kinematic information.

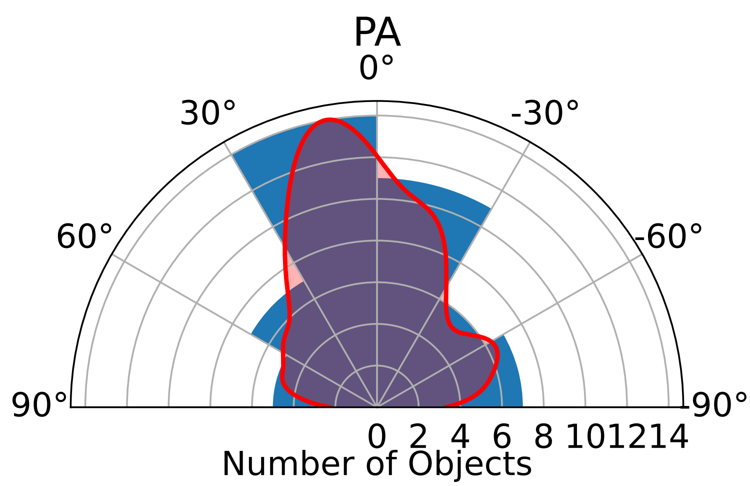

Figure 3.13: Distribution of PAs (blue histogram) and kernel density estimate (red).

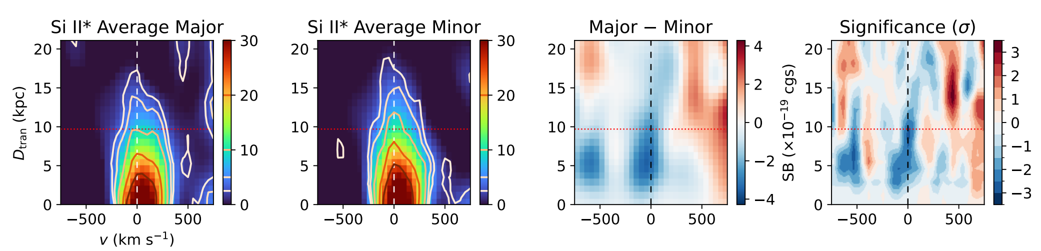

Figure 3.14: Cylindrical deprojection of the Si II* map shown in Figure 3.10 restricted to emission from the major and minor axes, respectively. Si II* emission along the minor axis is moderately elevated within $D_{\rm tran} \lesssim 20$ kpc, albeit at $\lesssim 2\sigma$ significance.

With PA measurements in hand, we formed a stacked cube with galaxies coaligned along their major axes. For each object, a $6'' \times 6''$ pixel cutout was masked of all neighboring sources, rotated by its measured PA, and projected onto a common grid with the same $0.3'' \times 0.3''$ spatial sampling of the original cube. In practice, the rotation and reprojection took place in one step and with only one (bilinear) interpolation. As in Section 3.5, the individual objects were coarsely normalized (using the median continuum level between 1400 and 1500 Å) before stacking so that each galaxy contributed approximately equally to the net spectrum. The PA-aligned stacked cube was also continuum subtracted so that line emission could be extracted using the approach discussed in Section 3.3.

Psuedo-narrowband images extracted from the PA-aligned stack are shown in Figure 3.10. Since galaxies comprising the stack are lined up along their major axes (as determined from continuum imaging), the continuum shows an elongation along that axis. Lyα is the most symmetric distribution out of the three images and Si II* shows excess emission along the minor axis of the average galaxy, but we caution that this image is the noisiest out of the three. We compute 2-D Gaussian fits to each of the images. The continuum FWHM values (after subtracting in quadrature the $0\overset{''}{.}9$ seeing disk), are 8.8 ± 0.1 kpc (major axis) $\times$ 7.4 ± 0.1 kpc (minor axis) – a 19% difference; for Lyα, we find 15.7 ± 0.2 kpc (major axis) $\times$ 15.8 ± 0.2 kpc (minor axis) – less than a 1% difference and consistent with Y. Chen et al. (2021); and for Si II*, the fit returns 7.7 ± 0.4 kpc (major axis) $\times$ 9.4 ± 0.4 kpc (minor axis) – a 22% excess toward the minor axis.

To better assess the discrepancy between emission along the major and minor axes we converted the PA-aligned, stacked cube into two CP2D spectra based on azimuthal angle. Normally, CP2D spectra azimuthally average over the full circular annulus, but in this case, we follow Y. Chen et al. (2021) and construct "minor" and "major" axis CP2D spectra for ease of comparison. Each CP2D spectrum azimuthally averages over a disjoint 180° region of the original cube, since the "opening angle" of any potential collimated emission is unknown. CP2D spectra with Si II* emission separated based on galaxy major and minor axis are shown in Figure 3.14. The Si II* surface brightness measurements come from Si II* $\lambda1265$ and Si II* $\lambda1533$, averaged together in velocity space. Figure 3.14 also shows the residual CP2D spectrum and its significance. In these units, σ is defined as the standard deviation of the surface brightnesses between 1400 – 1500 Å at large $D_{\rm tran}$ ($D_{\rm tran} \gtrsim 50$ kpc), where there is not expected to be any signal. The residual CP2D spectrum in Figure 3.14 indicates that excess emission along the minor axis is present near the systemic velocity for $D_{\rm tran} \lesssim 20$ kpc and the most significant difference is seen at $D_{\rm tran} \simeq 10$ kpc.

Similar to what was done in Figure 3.11, we also took vertical cuts in the CP2D map and produced 1-D radial surface brightness profiles along both axes for the continuum and Si II*; the distributions are shown in Figure 3.15. The trends seen in 2-D — excess Si II* emission along the minor axis of the galaxy and a slight excess of continuum emission along the major axis — are still present. Interestingly, the nonresonant emission shows a quick downturn before the continuum reaches the KCWI noise floor.

Si II* at $D_{\rm tran} \gg 0$ kpc

In principle, except for Lyα, interstellar absorption lines have no source function, which implies that the flux "removed" along the line of sight in Si II absorption should be reprocessed as either Si II resonant emission or Si II* nonresonant emission. Resonant emission would be expected if optically thick Si II resonantly scatters until it reaches an optically thin medium and the photons can escape unimpeded along our line of sight. However, optically thick regions of ISM and CGM are generally sufficiently extended such that Si II has to undergo many scatterings before escaping; nonresonant Si II* emission therefore becomes a much more probable emission channel. Indeed, most Si II photons in optically thick regions are expected to escape through nonresonant Si II* channels.

If photons escape isotropically and dust is minimal, photon conservation would suggest that given a sufficiently large aperture, it would be possible to capture all of the nonresonant emission along the line of sight and the equivalent width in the absorption and nonresonant emission feature would be equal and opposite. A number of studies focusing on low-z star-forming galaxies have attempted to test Si II* photon conservation but usually W_λ(Si II) exceeds W_λ(Si II*) by a considerable margin (e.g. Gazagnes et al., 2023; Jones et al., 2012; Shapley et al., 2003; Steidel et al., 2018). That being said, when larger apertures are used, the cumulative flux in the

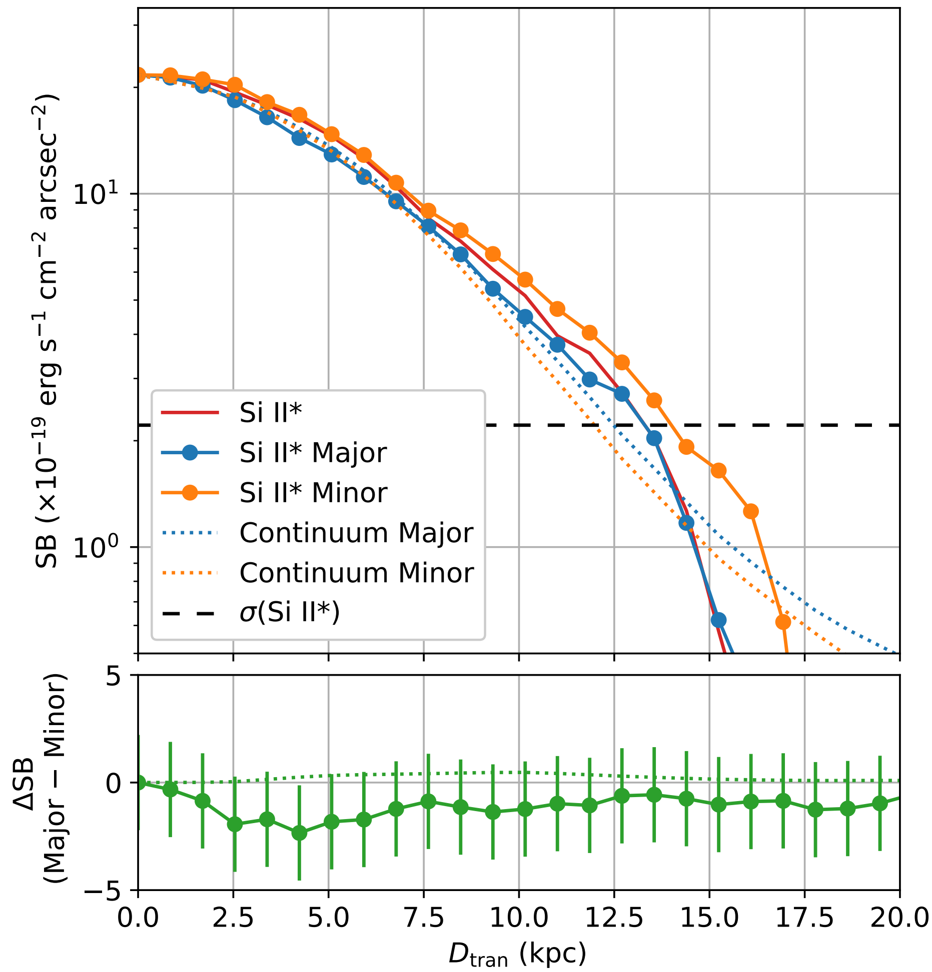

Figure 3.15: *Top:* Radial surface brightness profiles for Si II* on average (red solid line), Si II* along the major (blue) and minor (orange) axes (connect-the-dot style), and the rest-UV continuum (dotted lines), also broken down by axis and following the same color coding. The approximate noise level for Si II* is shown as a dashed black line. *Bottom:* Difference in SB between the major and minor axes of the stack in Si II* (green connect-the-dot) and the continuum (dotted green). Galaxies aligned along their major axis appear to have excess Si II* emission along their minor (at the $\sim 2.5\sigma$ level).

nonresonant channel approaches the flux removed by the associated resonant absorption line suggesting that slit losses (or relatively small apertures more generally) are responsible for the discrepancy in equivalent widths (Gazagnes et al., 2023; Kusakabe et al., 2024; B. Wang et al., 2020). As a proof of concept, Kusakabe et al. (2024) used a $z = 2.34$ galaxy observed with VLT/MUSE to show that an aperture that included 80% of the galaxy continuum light included only 50% of the total detectable Si II* emission. An aperture approximately three times larger was required to recover (in emission) the flux that was "removed" by Si II absorption.

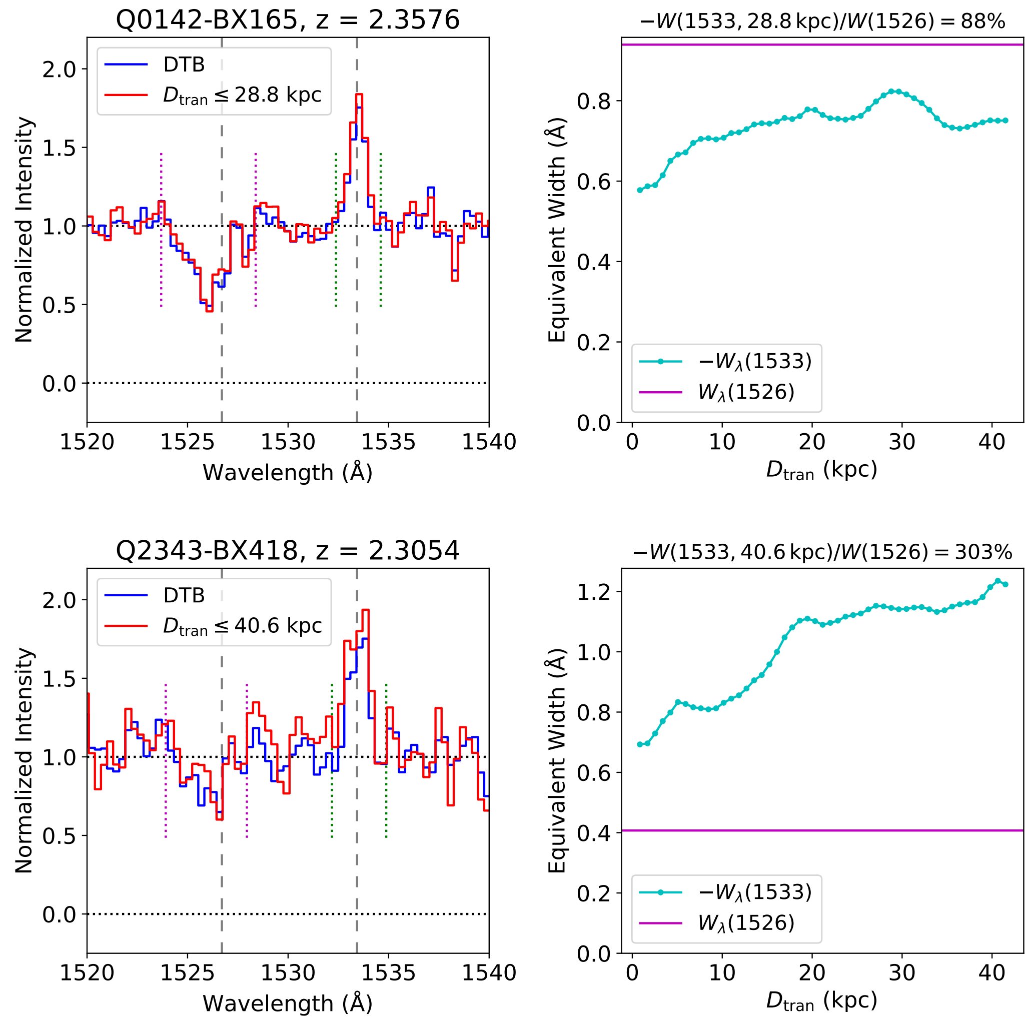

Figure 3.16: *Left:* Spectral extraction from two different apertures: DTB (0.8″ = 7 kpc) and the peak of the W_λ distribution. *Right:* Si II* λ1533 emission equivalent width measured in progressively larger apertures compared with DTB Si II λ1526 absorption equivalent width. In the absence of dust, W_λ in the absorption line should equal W_λ in emission.

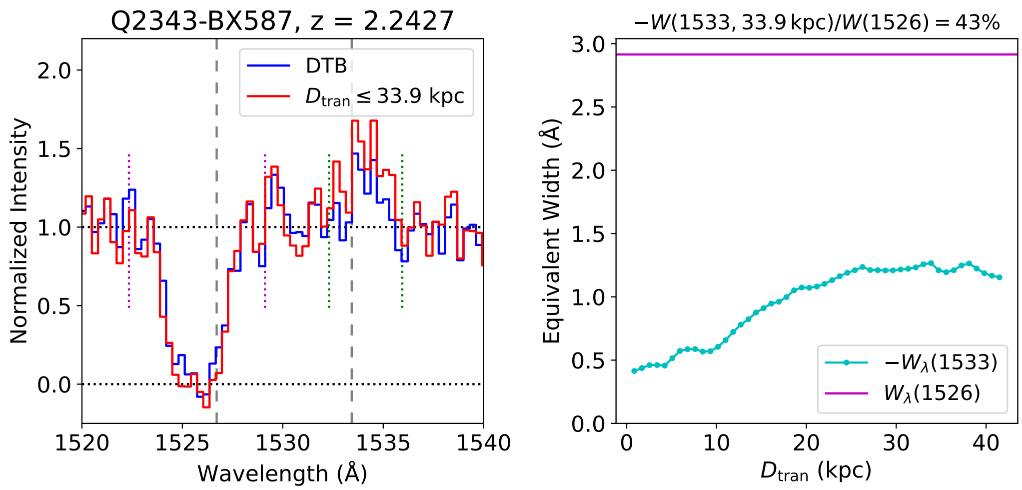

Figure 3.16 (cont.)

Like Kusakabe et al. (2024), the IFU nature of KBSS-KCWI spectra allows testing of the "zero source function" hypothesis on the current sample of galaxies. For this test, we used individual objects from the sample instead of making a combined stack. Figure 3.16 shows two galaxies where we have measured how nonresonant Si II* λ1533 emission equivalent width changes for ever-increasing apertures. We measured $W_\lambda(1526)$ from a 0.8″ diameter circular ("DTB") aperture to establish a baseline for the amount of flux removed by resonant absorption. The spatial resolution of KCWI does not permit us to measure $W_\lambda(1526)$ as a function of D_{tran}. In emission, we measure $W_\lambda(1533)$ within progressively larger circular apertures centered on the galaxy i.e., $W_\lambda(1533, \leq D_{\text{tran}})$. For both galaxies in Figure 3.16, $W_\lambda(1533)$ grows with D_{tran} although the ratio $-W_\lambda(1533)/W_\lambda(1526)$ is quite different.

Q0142-BX165 and Q2343-BX587 are representative of many of the galaxies in the sample in that $-W_\lambda(1533)/W_\lambda(1526)$ asymptotically approaches unity with increasing D_{tran} suggesting either a relatively small amount of dust in the ISM and/or CGM or simply not all of the emission is being captured within our expanded apertures ($D_{\text{tran}} \lesssim 40$ kpc). On the other hand, Q2343-BX418 starts with $-W_\lambda(1533)/W_\lambda(1526) > 1$ and continues to grow. Physically, this implies that there is a significant Si II emission line filling and our estimate of $W_\lambda(1526)$ is underestimated. The comparatively sharp red wing of Si II λ1526 lends additional support for this claim.

3.6 Discussion

The strong similarity in the kinematics of Si II*, the fit ISM components to Si II resonant absorption, and KBSS-MOSFIRE nebular spectra suggest that Si II* emission is primarily produced through continuum pumping of the resonance transition, followed by spontaneous emission in both the resonant and nonresonant channels, first suggested in Shapley et al. (2003). Si II* appears to preferentially trace optically thick gas where a majority of Si II photons are reprocessed through the fluorescent Si II* channel. The fact that Si II* extends beyond the galaxy continuum shows that optically thick gas is present in the CGM; the latter conclusion has been repeatedly established via CGM absorption studies (e.g. Prusinski et al., 2025) but this study in emission provides another piece of supporting evidence.

Galactic wind models have proposed that the majority of observed nonresonant line emission could be produced via scattered photons in an outflow (e.g. Prochaska, Kasen, & Rubin, 2011). The Si II* velocity centroid appears to shift in accordance with the resonant Si II line, which could mean that a substantial fraction of the Si II* photons are produced in a bulk outflow, but the comparatively low Si II* emission line widths relative to their resonant Si II counterparts challenge this hypothesis. It is possible that the KCWI spectra are of insufficient resolution and/or S/N to detect a second broad component in Si II* emission. We observe that in KBSS-MOSFIRE, it is necessary to have $S/N \sim 50$ in Hα or [O III] before a single Gaussian no longer provides a good fit to the line profile due to the presence of a broad emission line base (Theios et al. 2026)

The presence of extended Si II* emission that favors the minor axis of the average galaxy is interesting in the context of $z \sim 2$ CGM studies. Despite several lower-z observations and simulations, to date, there has been little evidence at $z \sim 2$ that galaxy morphology is correlated with the structure of its CGM gas distribution. While most galaxies at low-z have had time to form disks and, by extension, temporally coherent angular momentum vectors, the majority of galaxies at high-z, with very few exceptions,[5] have not. In any case, the fact that Si II* shows a directional preference, while Lyα does not, suggests that galaxy- and inner-CGM-scale variations may get

[5] GWS-CC50 (Cheng et al. in prep.), the 'Big Wheel' (W. Wang et al., 2025), Q2343-BX442 (Law et al., 2012) to name a few.

washed out through Lyα scattering.

In terms of photon conservation, it is difficult to compare the current KBSS-KCWI sample with just one galaxy in Kusakabe et al. (2024), but our spectroscopic aperture in general needs to be at least a factor of two larger than what was used on their galaxy in order to achieve $W_\lambda(1526) \simeq W_\lambda(1533)$. Such a discrepancy may have to do with the underlying systematics between the MUSE and KCWI cubes or that the gas giving rise to Si II* emission is more tenuous in the current sample at $z \sim 2$ compared to that system.

Steidel et al. (2018) established that W_λ(Si II*) is correlated with W_λ(Lyα) and LyC escape. It remains to do a comparison with Lyα. It also remains to self-consistently model the Si II ion incorporating the multiple absorption and emission lines present in a given spectrum. This can be done using `PEACOCK` (Z. Li et al., 2026) or potentially `RASCAS` and/or `Cloudy`.

3.7 Summary

We have investigated the spatial structure and kinematics of nonresonant Si II* emission in 50 $\langle z \rangle = 2.25$ star-forming galaxies (see Figure 3.2 for additional physical properties). KBSS-KCWI spectra were used to spatially resolve the Si II* gas distribution. Our main conclusions are:

1. Si II* kinematics are most characteristic of an absorption line ISM component (Figures 3.5 and 3.6a)

2. Nonresonant emission is shifted by Δv(Si II*) $\simeq 40$ km s^{-1} with respect to the systemic velocity of the galaxy obtained from rest-frame optical nebular emission lines (Figure 3.7).

3. Nonresonant emission (and by extension, optically thick gas) extends beyond the galaxy continuum (Figure 3.10). The radial surface brightness falloff of Si II* is steeper than that of Lyα (Figure 3.11). The Si II* velocity spread similarly decreases with $D_{\rm tran}$ (Figure 3.12), consistent with studies using background sightlines (e.g. Prusinski et al., 2025).

4. When aligned along the major axis of the galaxy, stacks of nonresonant Si II* show evidence (at the $\simeq 2\sigma$ level) of excess emission along the galaxy *minor* axis (Figures 3.10, 3.14, 3.15).

5. A significant fraction of Si II* emission associated with a galaxy arises in its CGM (well beyond the galaxy continuum) (Figure 3.16).

Clearly nonresonant UV emission represents a powerful (but still little utilized) tool for exploring the nature of optically thick gas in and around galaxies.

N.Z.P. and C.C.S. were partially supported by NSF grant AST-2009278. N. Z. P. thanks Mandy Chen, Isaac Cheng, Claudia Scarlata, Cameron Hummels, Yuanze Ding, Zhihui Li, Evan Nuñez, and Zhuyun Zhuang for catalyzing discussions during the writing of this paper. The authors thank Rosalie McGurk, Mateusz Matuszewski, and Don Neill for constructive conversations about KCWI. This research has made use of the Astrophysics Data System, funded by NASA under Cooperative Agreement 80NSSC21M00561. Finally, the authors wish to recognize and acknowledge the very significant cultural role and reverence that the summit of Maunakea has always had within the Native Hawaiian community. We are most fortunate to have the opportunity to conduct observations from this mountain.

Software: `matplotlib` (Hunter, 2007), `numpy` (Harris et al., 2020), `scipy` (Virtanen et al., 2020), `Astropy` (The Astropy Collaboration et al., 2013, 2018, 2022), `YT` (Turk et al., 2011), `TRIDENT` (Hummels et al., 2017), `tqdm` (da Costa-Luis et al., 2024), `scikit-image` (Van Der Walt et al., 2014), multiprocess (McKerns et al., 2012), corner (Foreman-Mackey, 2016), IRAF[6] (Fitzpatrick et al., 2024; National Optical Astronomy Observatories, 1999; Tody, 1986, 1993), `seaborn` (Waskom, 2021), `plotly` (Inc, 2015), `L.A.COSMIC` (van Dokkum, 2001), IPython (Perez & Granger, 2007), QFitsView (Ott, 2012), MOSPEC (Strom et al., 2017)

Facilities: Keck:I (MOSFIRE), Keck:II (KCWI)

[6]NOIRLab IRAF is distributed by the Community Science and Data Center at NSF NOIRLab, which is managed by the Association of Universities for Research in Astronomy (AURA) under a cooperative agreement with the U.S. National Science Foundation.

Chapter 4

KCWI DATA REDUCTION

Approximately two years of effort have been dedicated to the red channel of KCWI, both on the hardware and software front. In 2022 June, KCWI went off-sky for red channel integration. I participated in Caltech assembly, integration, and testing of the camera, dichroic, and red detector. I characterized the red detector focus plane and helped with fabrication, installation, and testing of the seven red channel VPH gratings. I constructed photon transfer curves for the red detector to measure and ensure the gain, linearity, and read noise were within tolerance. Once in Hawaii, I peaked each of the gratings using arc spectra, and installed (and calibrated) an additional blue channel high resolution grating that made a new observing mode possible. Once on sky, I used standard stars to conduct an end-to-end throughput analysis for each grating/slicer combination and assessed the need for a second order blocking filter. During commissioning, I acted as a liaison between the broader Keck community of astronomers and the instrument team as we sourced science verification targets. In particular, I oversaw the choice of commissioning targets, took the data during each of the commissioning nights, reduced said data, and distributed it back to the observers and the broader astronomical community. These efforts have contributed to making KCWI the most popular dark-time instrument at Keck.

The results unpinning this thesis would not be possible without the Keck Cosmic Web Imager (KCWI) and, perhaps of more importance, the KCWI Data Reduction Pipeline (DRP) which converts 2-D KCWI detector images into 3-D flux-calibrated data cubes. The KCWI DRP has been described elsewhere (e.g. Y. Chen, 2022; Y. Chen et al., 2021; Neill, Matuszewski, Martin, et al., 2023; Prusinski et al., 2025) and provides a general framework for reducing KCWI data but reaching the sensitivities required for these thesis projects (especially Section 5) necessitated improvements in several stages.

The KBSS-KCWI survey contains KCWI spectra taken with the “Medium BL” configuration. The slicer sets the FoV ($16'' \times 20.4''$) and spatial sampling

($0\farcs69 \times 0\farcs29$); combined with the low-resolution "BL" grating, an average spectral resolving power $\langle R \rangle \approx 1800$ is achieved over the $3530 - 5530$ Å passband. Individual exposures are twenty minutes and each survey field is observed for a total time of ~ 5 hours. Small dithers and/or sky position angle (PA) changes between exposures allow for square pixels with a finer spatial sampling ($0\farcs3 \times 0\farcs3$) in the stacked cubes. Ultimately, the stacked cubes have a spatial resolution of $\simeq 0.7 - 1''$, limited by the seeing with a small contribution from the regridding while stacking.

4.1 KCWI Standard DRP Improvements

KBSS-KCWI exposures are initially processed through the KCWI DRP. At a high level, exposures are bias subtracted, cosmic ray rejected, flat fielded, sky subtracted, transformed into cube format, corrected for differential atmospheric refraction (DAR), and flux calibrated. The details of these procedures are described in e.g. Y. Chen et al. (2021) and Prusinski et al. (2025). On the software front, the red channel of KCWI behaves similarly to the blue with a few pernicious exceptions; notably cosmic ray rejection (Section 4.1) and sky subtraction (Section 4.1) require different treatment between channels. Over the course of this thesis, each of the major steps in the DRP have been investigated and solutions devised to correct the DRP's shortcomings: the highlights are discussed in the following subsections.

Bias

The blue and red detectors are run in two-amplifier mode where each half of the detector has a different bias level. Despite the construction and subtraction of a master bias there is still an *additive* print-through of the two different bias levels of both amplifiers. This effect is shown in Figures 4.1 and 4.8 (to a lesser degree). This was one of the motivations for the developing the median filter used in Y. Chen et al. (2021). Partly through my efforts, the blue and red detector gains were remeasured during red channel commissioning with deltas $\sim 0.001\, e^{-}$/DN. It remains to be seen if adopting the new gain values precludes the need for a median filter or if the bias requires a "second-order" correction.

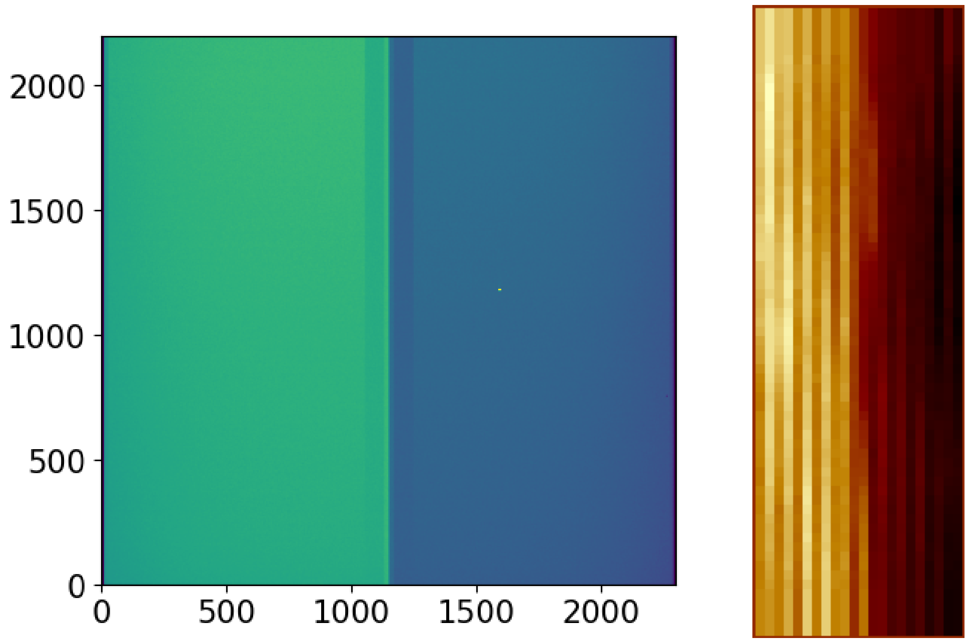

Figure 4.1: *Left:* KCWI blue channel master bias in detector coordinates. *Right:* a whitelight image of the `.med.fits` cube that is subtracted from the DRP-constructed cube. Peak to valley, there is a $\simeq 2e^-$ residual between each amplifier left after bias subtraction. The median cube also shows slice to slice variations at the level of $\simeq 0.2e^-$.

Cosmic Ray Rejection

The blue channel DRP uses `astroscrappy` (Robitaille et al., 2025), a port of `L.A.COSMIC` (van Dokkum, 2001), which uses a Laplacian kernel to flag pixels affected by cosmic rays. The pixel value is replaced by a local median. This approach works well for the "hot-pixel"-type blue channel cosmic rays but fails for cosmic rays that affect the red detector (see Figure 4.2 for an example). Red channel cosmic rays affect more pixels (CRs cover $\simeq 0.8\%$ of the detector in a typical 5 minute exposure in 2×2 binning; see Table 4.1) and can have quite a diverse range of morphologies (e.g. bursts, snakes; Figure 4.2).

Exposure Time (minutes)	Binning	Detector coverage (%)
5	1×1	0.59
10	1×1	1.13
5	2×2	0.77
10	2×2	~ 1.5

Table 4.1: KCWI Red Channel Detector Cosmic Ray Statistics

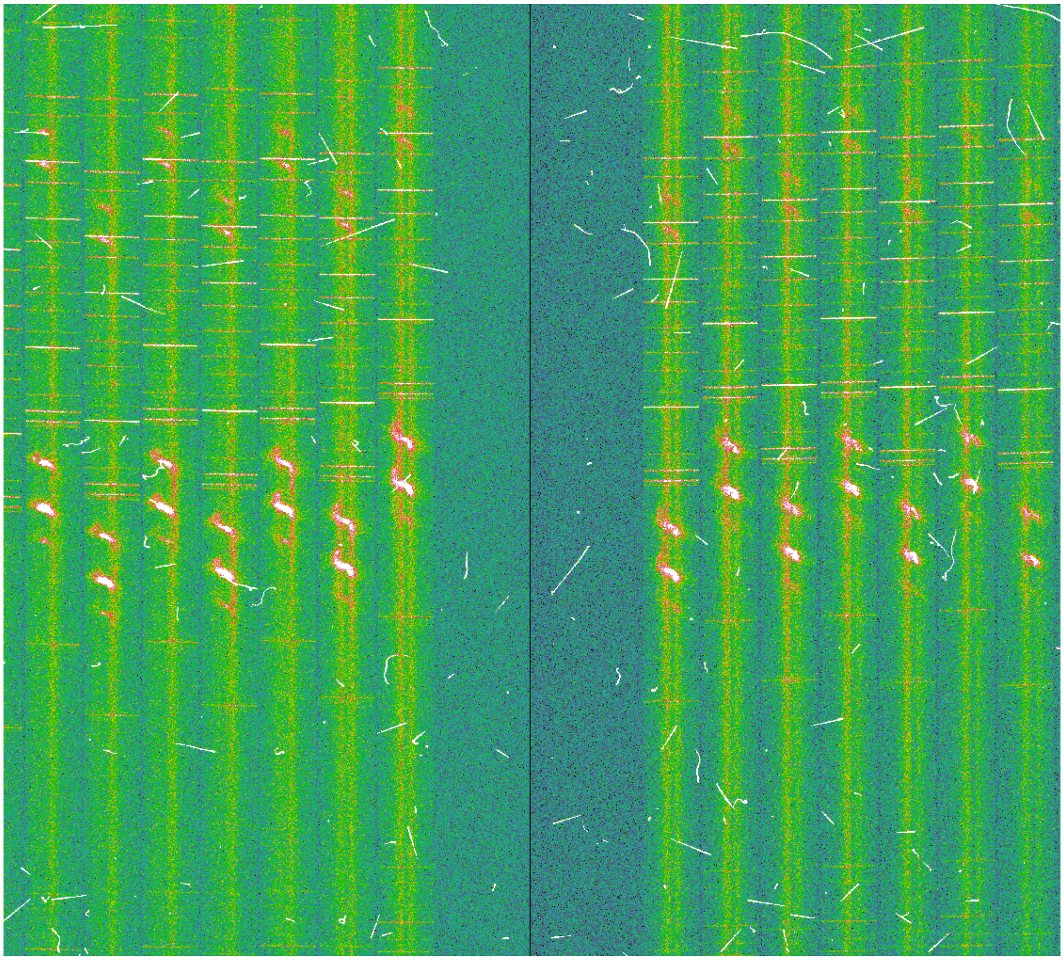

Figure 4.2: A zoomed-in KCWI red channel science frame before cosmic ray rejection. Cosmic rays take on a range of morphologies and span the detector.

If exposures are taken one by one at the telescope, the DRP reduces each exposure in the same fashion and performs only the `astroscrappy` cosmic ray rejection, which is not particularly well-suited for the red channel cosmic rays. If three exposures were taken as a group, the DRP creates a master object (`_mobj.fits`) file based on the median of the three exposures. Four or more grouped exposures are combined via a straight average which clearly leaves a cosmic ray imprint on faint emission in pixels where both are present.

In `KCWIKit`, I have implemented an approach to cosmic ray rejection that maintains the statistical power of using multiple frames. This approach requires that at least two red-channel exposures were taken at the same sky position, the same PA, and in the same configuration, with little change in the observing conditions (seeing, presence of clouds) between the two exposures. I presented an iterative approach: similar exposures are combined to construct a master object frame; each constituent exposure is then subtracted from the master object frame; the difference image contains primarily cosmic ray pixels from which a binary mask can easily be constructed by sigma-clipping. Each constituent image can then be re-reduced, employing its associated cosmic ray mask. For cases where only two science frames exist, the master object frame can be constructed using the pixel-wise minimum; with three or more frames, the pixel-wise median the natural choice. The upshot of this approach is that the effective exposure time (on average) remains close to ($t_{\rm exp} \times N_{\rm exp}$) instead of just $t_{\rm exp}$ (in the case of taking the median of $N_{\rm exp}$). Several scripts have been constructed for grouping red-channel frames ex post facto and interleaving them with blue-channel exposures.

The approach implemented in `KCWIKit` is by no means the only way of removing CRs. Aside from by-eye masking (which I implemented), there is no easy way to remove cosmic rays on single exposures. There have been efforts to look at cosmic ray morphology (most cosmic rays have a fairly uniform width); contrast over the ray and contrast compared to the expected signal; and location and angle with respect to slice boundaries, sky lines, and the object trace (Matuszewski et al. in preparation). A more "modern" technique, `Cosmic-CoNN` (Xu et al., 2021, 2022, 2023), is under development with the goal of using a neural network to detect cosmic rays on single frames (Peng, Xu, et al. in preparation). The possibility of observers only obtaining one red channel frame on a target is possible (especially in the case of rapidly changing weather), and having the ability to make effective use of that data is an important DRP use case. The solutions developed for KCWI can be easily adapted for LRIS-R which uses the same detector.

Flat-fielding

The sky background is expected to be approximately uniform across the KCWI FoV ($\simeq 20'' \times 16''$ for the "Medium BL" configuration) and the current default means of sky subtraction (a b-spline fit to all of the sky pixels on the detector) necessitates a flat field. The default afternoon calibration script collects six internal and three dome flats for each requested configuration. In good conditions, these are supplemented by twilight flats taken in either the evening or morning.

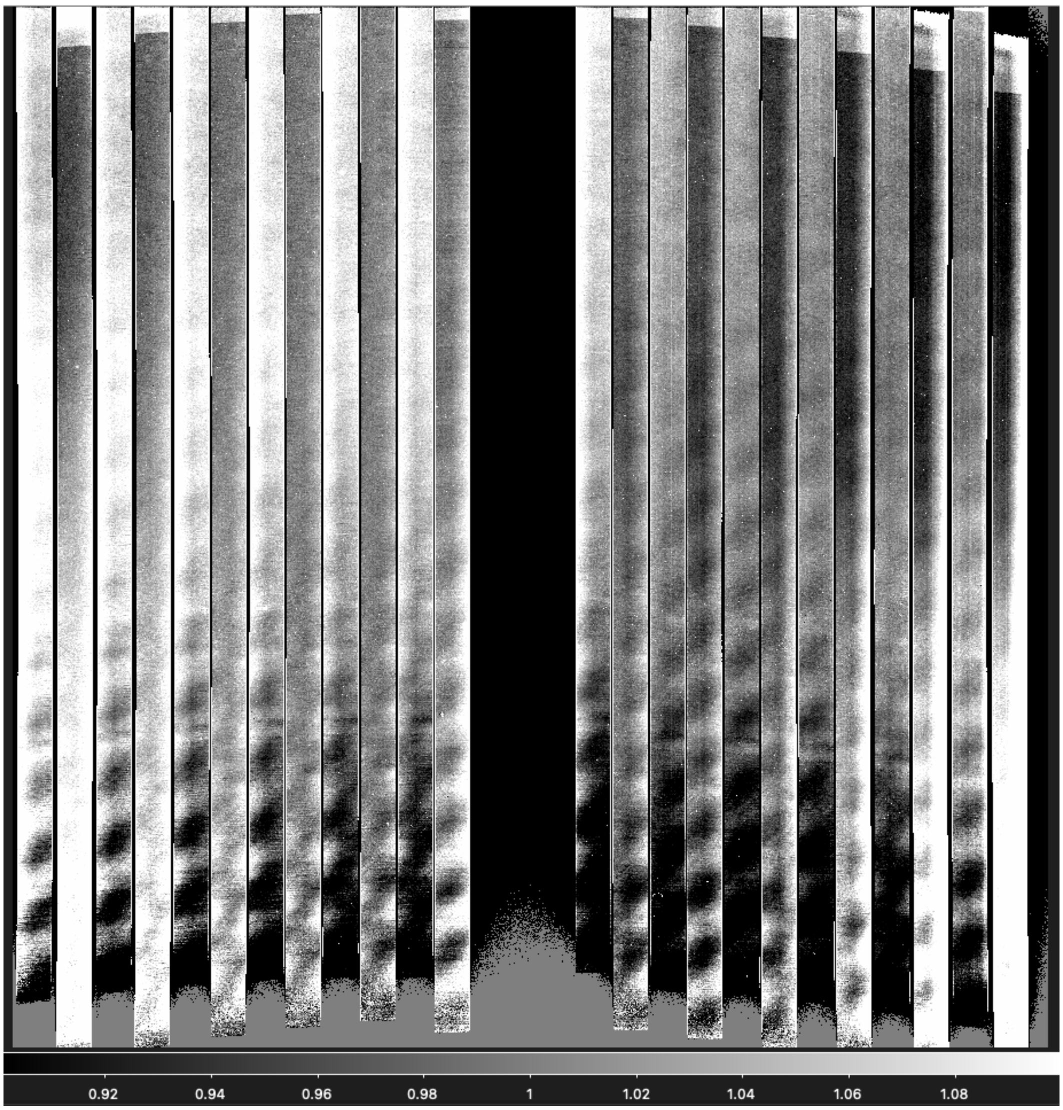

Figure 4.3: A normalized KCWI flat field that is the product of the master internal flat and a smoothed master twilight flat. The large scale detector gradients are captured, without significant twilight sky line print through.

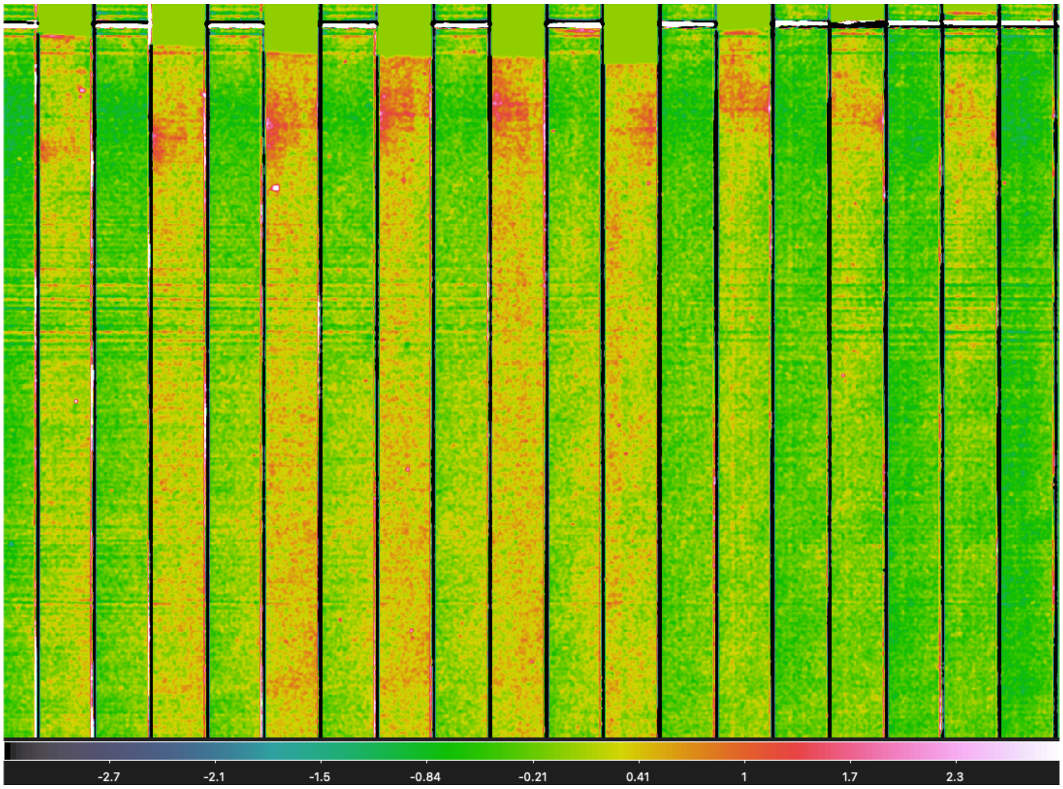

Figure 4.4: 2-D "Sky Flat" approximately centered on N I λ5199 made by combining two years' worth of continuum source masked KBSS science frames (`icube.fits`) and deprojecting. All frames were taken in the "Medium BL" configuration and units are in e^{-}. In regions without prominent sky features, the background noise level $\sigma \simeq 0.5e^{-}$; around N I, $\sigma \simeq 1.5e^{-}$.

Broadly speaking, the internal and dome flats are useful in correcting pixel-to-pixel variations and twilight flats are essential in removing large-scale detector illumination gradients. Internal flats use a calibration unit that mimics the telescope pupil but therefore suffer from vignetting. Dome flats do not suffer from this issue but the Keck dome lamps currently do not have significant flux in the near-UV ($\lambda \lesssim 4000$ Å) which prevents accurate flat fielding at those wavelengths. Twilight flats have the advantage of using the full telescope optical path and sufficient throughput in the near-UV; their one drawback is the night sky spectrum which needs to be fitted out before such frames can be used. By default, the sky spectrum is fit with a b-spline; under- and over-subtraction of sky can therefore result in wavelength-dependent gradients in the flattened images.

What one desires is a well-exposed flat field that simultaneously corrects pixel-to-pixel variations and large-scale detector gradients.[1] At present, two attempts have been made on the blue channel: first, a combined master flat that is the product of the master internal flat and a smoothed master twilight (Figure 4.3); second, a "sky flat" made using two years' worth of skies (Figure 4.4), all taken in the same "Medium BL" configuration. The first approach uses a heavily smoothed twilight flat to mitigate any sky lines that have not been properly subtracted. The second approach combines sky pixels from several dozen nights (several hundred individually masked exposures) and constructs an average (quasi-)detector image. The large scale gradients in Figure 4.4 are the result of improper flat fielding on each of the science frames; the sky spectrum print-through results from poor sky subtraction in either the twilight flats used to flat field the constituent exposures or the science frames themselves.[2] In either case, this "sky flat" shows where flat fielding is subpar not to mention several second-order effects (e.g. shadowing) and has the potential to correct individual frames, thereby improving overall sky subtraction.

Sky Subtraction

The galaxies that comprise this thesis have surface brightnesses $\lesssim 1\%$ of the night sky background surface brightness under dark lunar conditions. The ability to extract meaningful information about the galaxies therefore hinges upon accurate sky subtraction. As introduced in Section 4.1, the KCWI DRP default sky subtraction routine collects all pixels on a science frame, performs a $\pm 1\sigma$ rejection and fits a low-order spline to the remaining pixels. It is also possible to create sky masks around science targets so they do not bias the sky model high (and therefore lead to oversubtraction of the sky). Considerable effort has been spent masking individual frames in the KBSS-KCWI survey with positive results (e.g. Y. Chen, 2022; Y. Chen et al., 2021).

While a $\pm 1\sigma$ clip tends to work well for a wide range of science cases, a *wavelength-dependent* rejection is even more useful! The [O I]λ5577 night sky line is by far the strongest feature in the blue channel bandpass and prior to

[1] In principle, the dome flats will meet these criteria on the red channel, but this claim is still being investigated.

[2] As an aside, when PCA sky subtraction routines are implemented on KCWI data cubes, the first few components tend to capture these flat fielding artifacts, not bona fide sky features.

this fix, the $\pm 1\sigma$ rejection would only mask that feature, practically ignoring the rest of the wavelength range. Currently, the $\pm 1\sigma$ clip occurs in 40 Å chunks, but it would be useful to tune this parameter further in future.

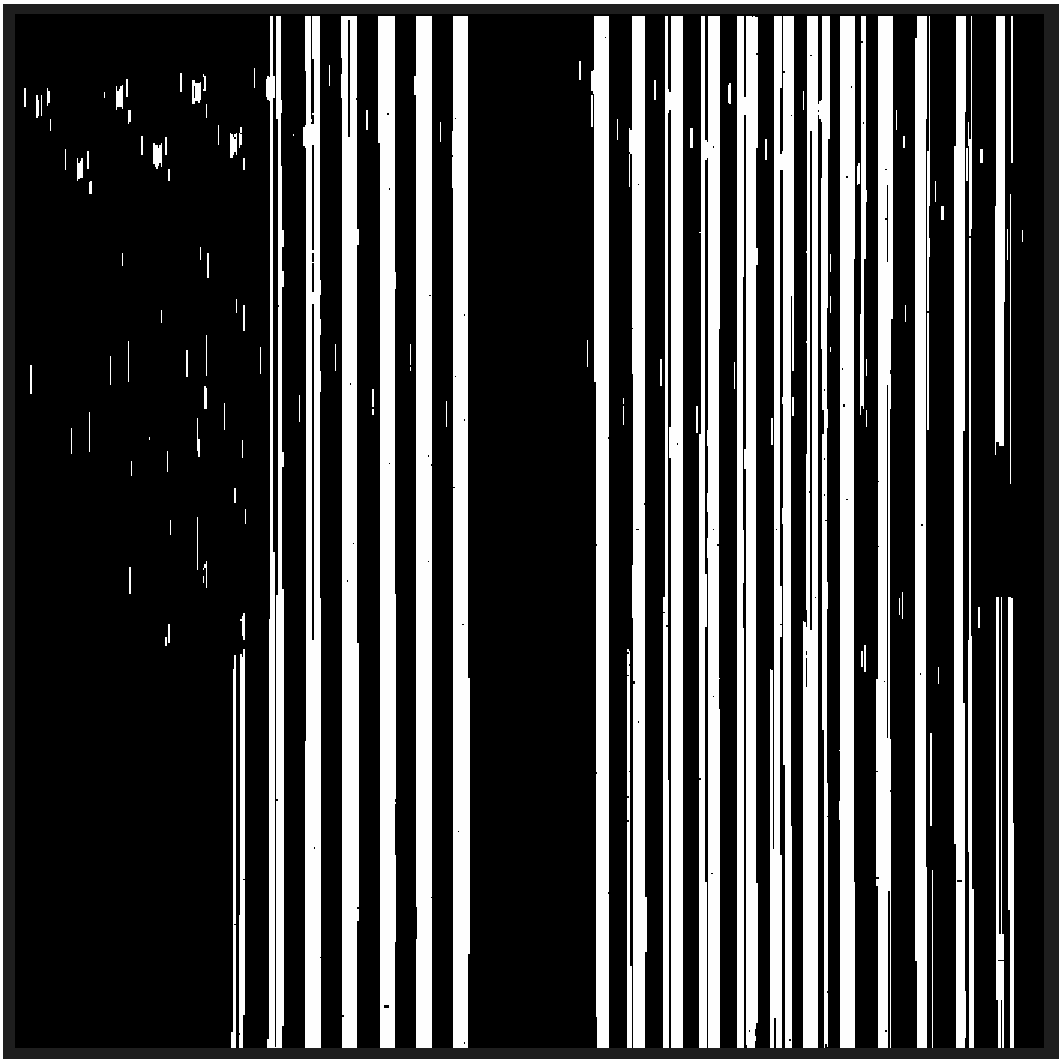

Figure 4.5: An example of a deprojected sky mask (seen here in detector coordinates) used in a KBSS-KCWI field. Note the presence of continuum and line emission.

The best sky subtraction can only occur when "all" of the objects in a frame have been masked so that only sky pixels remain. However, only a subset of the objects visible in a $\simeq 5$ hour stack are visible in a 20 minute exposure which, in the approach described above, results in stacks with oversubtracted skies. The solution I have implemented is:

1. Run a "first pass" sky subtraction using the wavelength dependent

b-spline described above on every exposure

2. Stack those exposures

3. Create a sky mask on the stacked cube

4. Deproject that mask back to detector coordinates (Figure 4.5 shows an example)

5. Sky subtract each exposure using its respective mask made by deprojecting the stacked cube mask

6. Restack the cubes, now with improved sky subtraction.

For the moment, the stacked cube masks are two dimensional, constructed from whitelight images of the cube (hence why e.g. the width of the masked region does not change with wavelength in detector coordinates), but the next obvious step is to make 3-D (wavelength-dependent) masks. The `CubEx` package (Cantalupo et al. in prep) would be a natural choice for making such masks. 3-D masks have the advantage of accounting for objects with extended (e.g. Lyα) emission and have already been used successfully in the median filtering procedure typically performed on KBSS-KCWI data cubes (Y. Chen et al., 2021).

On the red channel, I have worked on a sky subtraction PCA tool (`KSkyWizard`[3]; Zhuang et al. in preparation), ported from `ZAP` (Peng et al. 2026; Soto et al. 2016; Peng et al. in preparation[4]) originally used on VLT/MUSE and now usable with KCWI frames. While the `KSkyWizard` PCA works well for bright targets, I am actively developing a physically-informed model that will fit a red sky model (in the optical) to each raw KCWI frame and account for the changing focus/illumination with wavelength (see Section 5.1).

Interpolation in Cube Construction and DAR Correction

Converting from 2-D detector coordinates to the 3-D cube format requires some form of interpolation. The DAR correction, which effectively sets up a larger spatial grid and imposes a wavelength-dependent spatial shift, also requires interpolation. Experimentation between different interpolation orders has revealed bright point-like features (e.g. CRs, Lyα emitters with

[3]https://github.com/zhuyunz/KSkyWizard
[4]https://github.com/jasonpeng17/zap_for_kcwi

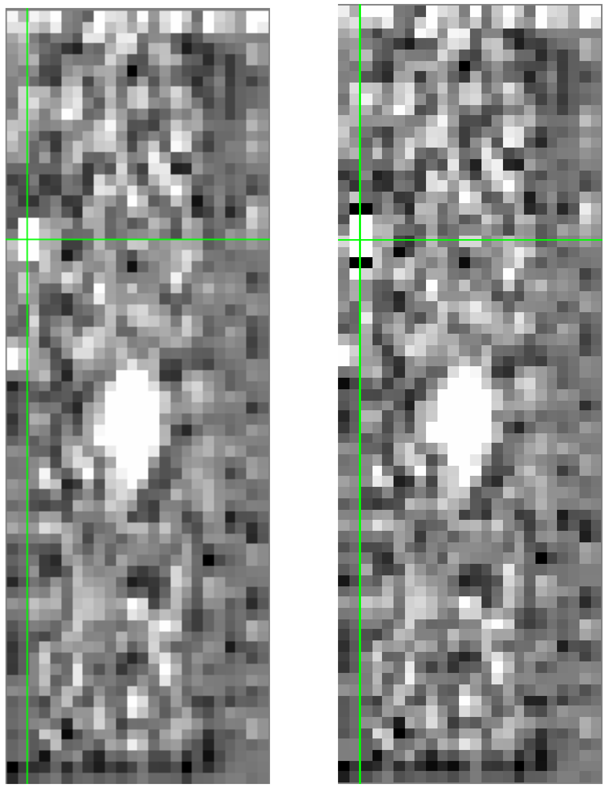

Figure 4.6: One wavelength slice (0.5 Å narrowband image) of a twenty minute KCWI blue channel QSO pointing with a cosmic ray hit, identified by green crosshairs. The cosmic ray flux is apportioned differently depending on the interpolation order used to construct the cube. *Left:* linear interpolation, *Right:* cubic interpolation.

weak continua) are particularly susceptible to interpolation errors. Figure 4.6 shows how higher-order interpolation can result in a "diffraction-like" pattern around the object. The simplest solution here is to use linear interpolation where possible.

Flux Calibration

The introduction of the red channel and dichroic in the optical path has created a need to improve how one flux calibrates the KCWI cubes. The standard DRP takes an average of the majority of the pixels in the standard star cube and fits a polynomial to the spectrum. The dichroic leads to an exponential cutoff around 5600 Å that cannot be properly fit by a polynomial. `KSkyWizard` helps with this fitting and adopts a more manual approach. The dichroic cutoff (equivalently, half-power point) varies spatially however (Figure 4.7), and proper flux calibration requires that one take account of

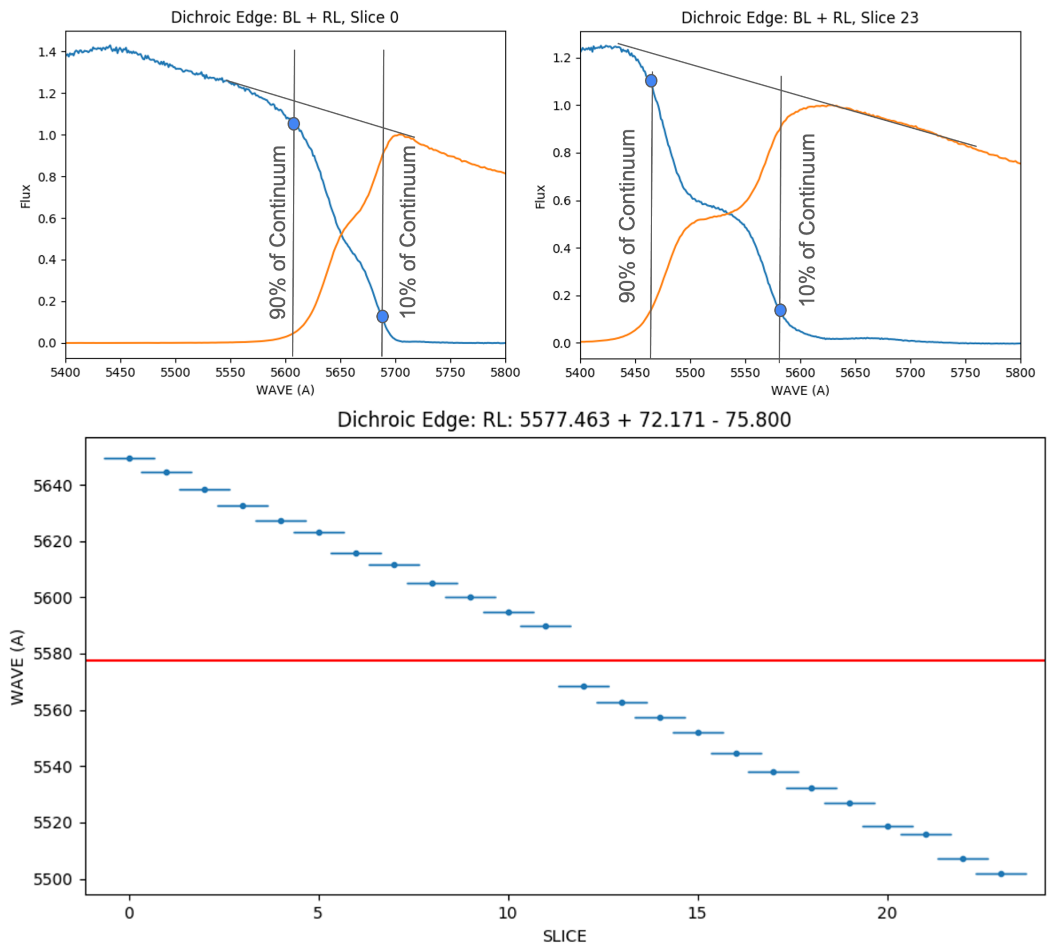

Figure 4.7: *Top:* The KCWI dichroic cutoff mapped as a function of wavelength for the the two edge slices: slice 1 (left) and slice 24 (right). The blue (orange) curve shows the blue (red) channel wavelength-dependent throughput. *Bottom:* The dichroic half power point as a function of slice. The transition band is from approximately 5465 – 5685 Å. Figure courtesy of Don Neill and Matt Matuszewski.

this.

4.2 KCWIKit

A large fraction of the suggestions and DRP improvements discussed in Section 4.1 are implemented in `KCWIKit` (Prusinski & Chen, 2024). I am the lead developer of this software, which offers masking and median filtering scripts (Figure 4.8) to be used while running the KCWI DRP, and a step-by-step KCWI DRP implementation for finer control over the reduction process. Once the DRP has finished, `KCWIKit` can be used to stack the output cubes via the `Montage` (Jacob et al., 2010) package. Various functions cross-

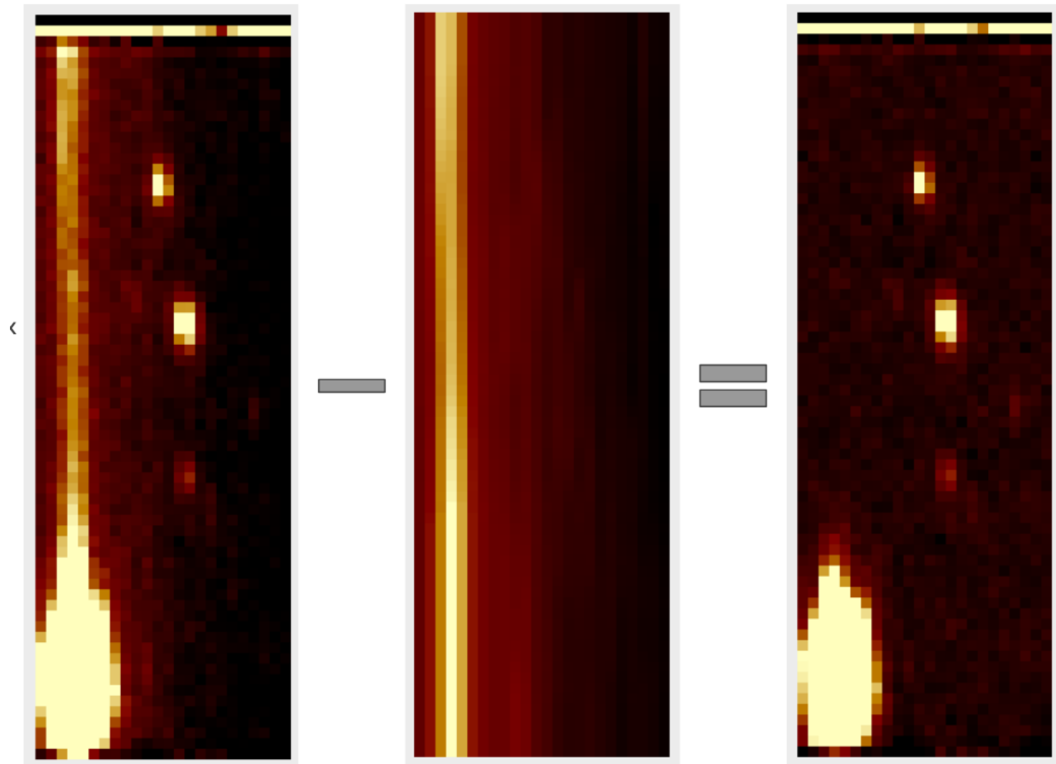

Figure 4.8: A cartoon representation of the median filter routine. Whitelight images of the science frame (left), the median of the science ignoring continuum sources (center), and the median filtered cube (right). The latter is used for all subsequent analysis.

correlate and mosaic the constituent cubes and the final stacked cubes are WCS corrected. Helper functions can then be used to deproject the stacked cube into lower-dimensional representations should the user desire.

Mosaicking

The underlying stacking code in `KCWIKit` has existed since Y. Chen et al. (2021) (a sample stack is shown in Figure 4.9). As a Keck Visiting Scholar, I improved `KCWIKit` to stack both red and blue channel cubes and ensure consistent astrometric alignment. I also implemented an outlier rejection scheme when stacking data from multiple nights and/or PAs to eliminate cosmic rays (if all former attempts to do so have failed). Of particular interest on the red channel is the ability to stack data at the same spatial resolution but with different red grating angles. The red channel features a 5600 − 10800 Å passband, but at one time only $\Delta\lambda \simeq 3500$ Å can fit on the red detector. Observers typically choose a central wavelength that captures most of their

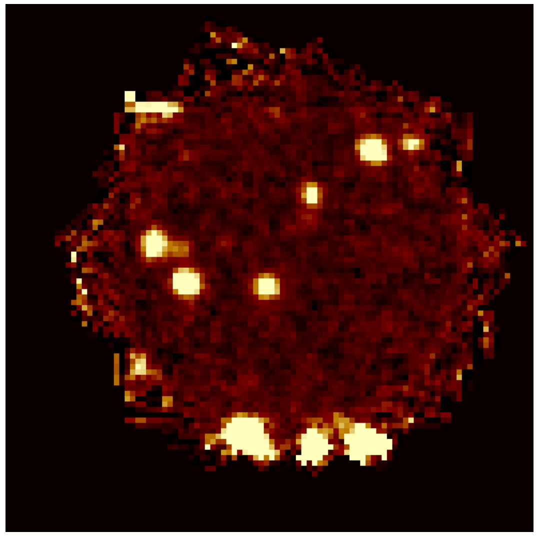

Figure 4.9: A whitelight image of the GWS-MM37 KBSS-KCWI field. The total integration time in this stack is ≃ 5 hours.

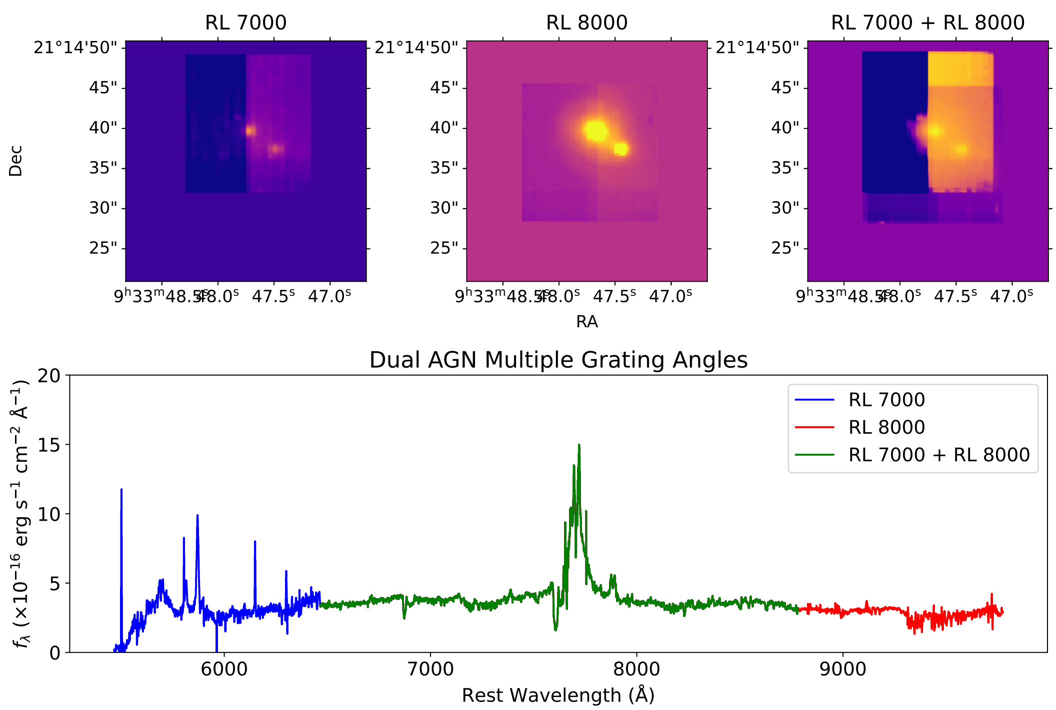

Figure 4.10: A series of KCWI red channel exposures taken at different spatial positions and in different instrument configurations are stacked. *Top:* Whitelight images for sets of stacked exposures taken with central wavelength 7000 Å (left) and 8000 Å (center); all images are combined in the right panel. *Bottom:* The final extracted spectrum color coded by the setups contributing to each wavelength.

features of interest, but with my improvements, it is now possible to combine data from multiple different central wavelengths into one large cube (Figure 4.10). This functionality has been tested on a limited basis and it is clear that accurate flux calibration is required between all of the constituent datasets.

Chapter 5

MPC-SCALE JETS

High-power jets driven by supermassive black holes (SMBHs) for millions of years are the largest galaxy-made structures in the Universe. These "megajets" are one of the most spectacular forms of feedback, pumping electrons, atomic nuclei, and magnetic fields into the IGM. Over the last few years, thanks to sensitivity gains of large-scale radio surveys, such as the LOFAR Two-metre Sky Survey (LoTSS; Shimwell et al. 2017), it has become clear that megajets — previously thought to be rare and cosmologically insignificant — are not only common, but possibly the dominant source of black hole feedback to the Cosmic Web. Indeed, about 10^4 out of the $6 \cdot 10^5$ radio-detected AGN in LoTSS DR2 produce Mpc-scale jets (i.e. ~2%; M. J. Hardcastle et al., 2025; Mostert et al., 2024). Correcting for the strong evolutionary surface brightness decay that hampers the detection of the largest jet systems, the true incidence of Mpc-scale jets may amount to ~10% of all radio AGN.

Recently, Oei, Hardcastle, et al. (2024) reported the joint LOFAR–uGMRT–Keck I Telescope discovery of a 7 Mpc–long black hole jet system at a redshift of $z = 0.896$, powered by a radiative-mode active SMBH. This structure, niknamed Porphyrion, is currently the largest known structure generated by an astrophysical body. State-of-the-art modeling (M. Hardcastle, 2018) suggests that the jets, by that time, had undergone fueling by the active SMBH for $\Delta t = 1.9^{+0.7}_{-0.2}$ Gyr. Spanning about 66% of the radius of a typical cosmic void at its redshift, the outflow shows that the sphere of influence of individual SMBHs can reach the scale of the Cosmic Web. The age of the jets, in combination with the inferred two-sided jet power $Q = 1.3 \pm 0.1 \cdot 10^{39}$ W, suggests a spectacular time-integrated energy release into the IGM of $E = Q \cdot \Delta t = 8^{+2}_{-1} \cdot 10^{55}$ J. This amount is comparable with the energy freed during galaxy cluster mergers (e.g. Van Weeren et al., 2009), suggesting that the outflow is among the most energetic post–Big Bang events to have occurred in its region of the Cosmic Web. As numerical simulations of smaller systems indicate that energy carried by jets predominantly goes into the heating of the IGM, Oei, Hardcastle, et al. (2024) argue that Porphyrion may have heated its Cosmic Web filament by $\Delta T \sim 10^7$ K.

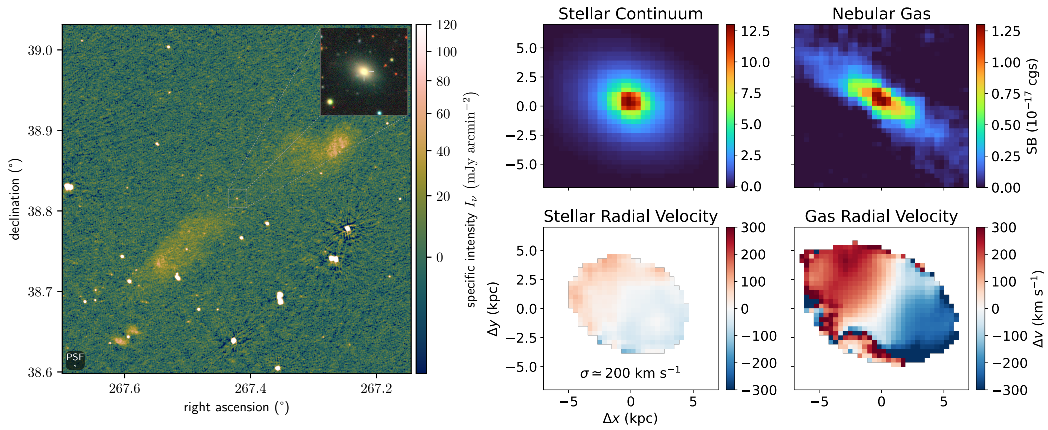

Figure 5.1: *Left:* LOFAR image (at 144 MHz) showing a 1.5 Mpc jet system at $z = 0.06$. The inset shows a 100 kpc × 100 kpc DESI optical cutout of the host galaxy. The jets have emerged from the host's minor axis. *Right:* Preliminary KCWI psuedo-narrowband images (top) and first moment maps (bottom) showing the radial motion of stars and gas. The gas (traced by [O II]) shows evidence of bulk rotation with an angular momentum vector aligned with the jet axis. The gas appears kinematically decoupled from the stars which have a random velocity dispersion $\sigma \simeq 200$ km s^{-1}. The proposed study will test if this situation holds for a sample of $\simeq 50$ Mpc-scale jet systems.

The discovery of Porphyrion is part of a productive, large-scale radio campaign aimed at quantifying the impact of black hole energy transport on the IGM. By eye and with machine learning, the International LOFAR Telescope (ILT) team has increased the number of known Mpc-scale black hole jets by an order of magnitude, from about 1,300 to more than 11,400. Bayesian forward modelling of the Mpc-scale jet population suggests that, at least in the Local Universe, the comoving number density of actively powered Mpc-scale jets is $\sim$10 (100 Mpc)$^{-3}$. This line of work has thus revealed that Mpc-scale jets are a relatively common phenomenon — i.e. about as common as luminous shorter jets.

5.1 Angular momenta of galaxies hosting Mpc-scale jets

Although megajets have recently emerged as a leader in contributions to galactic baryonic processes, the physical triggers for giant jet formation remain unknown. I am spearheading a Keck/KCWI survey of elliptical galaxies hosting Mpc-scale jets with the goal of figuring out why some galaxies generate giant jets and others do not. At present we have KCWI spectra of $\sim$ 30 hosts at $z \sim 0.1$ and preliminary reductions have revealed kpc-scale

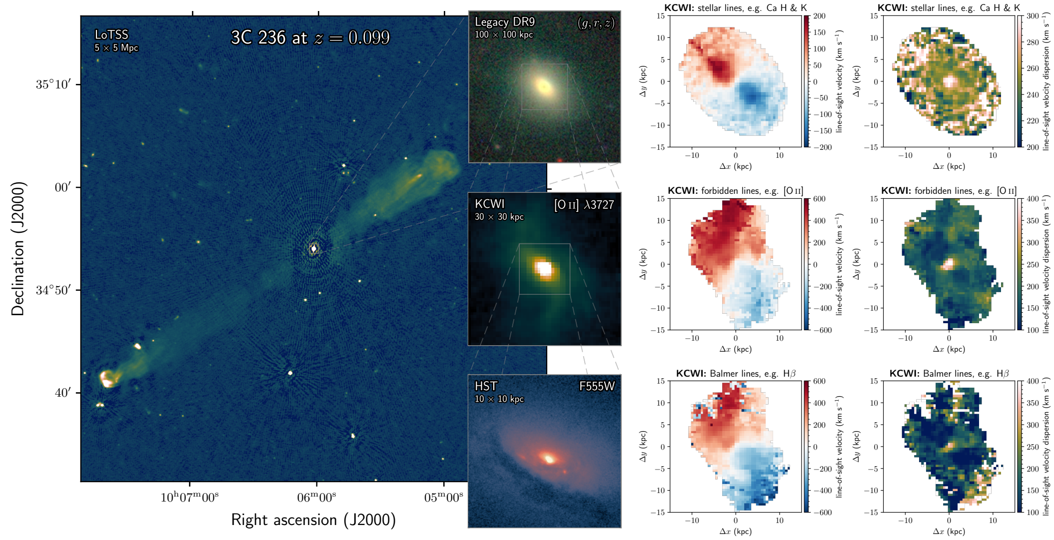

Figure 5.2: KCWI results for 3C236, with a sky-projected length l_p = 4.5 Mpc the largest jet system known in the 1970s–2000s. We show a 6″ LoTSS image with Legacy Survey, KCWI, and HST insets, covering a factor 500 in spatial extent: from 5 × 5 Mpc to 10 kpc × 10 kpc (left). KCWI observations provide a spectral dimension that complements large-scale *Rubin*-like ground-based surveys and *Roman*-like space-based surveys. Through Ca H and K, [O II] λ3727, Hβ, and other lines, our pPXF-processed host galaxy data reveal a rotating disk of stars and gas perpendicular to the jet axis of ~10 kpc–scale extent (right). From the central stellar velocity dispersion, we estimate an SMBH mass $M_\bullet \simeq 2 \cdot 10^9\ M_\odot$. The gaseous velocity dispersion shows elongated, ~3 kpc–long structures along the jet axis, as well as depressions in the perpendicular direction.

rotating disks with nebular emission (Hα and [O II]), perpendicular to the jet axes (examples are shown in Figures 5.1 and 5.2).

An important objective of this project is to explain the conditions in the host galaxy that give rise to stable jet orientations over Gyr timescales. I will start by using KCWI kinematic maps to test the extent to which galaxy-scale and core angular momentum vectors predict the SMBH jet axis. In other words, do the stars and/or gas in the galaxy "know about" the Mpc-scale jet? Zheng et al. (2024) recently combined radio measurements of jet position angles with host elliptical galaxy position angles (from DESI imaging) and showed that longer jets tend to be preferentially aligned with their host's minor axis. This result appears to hold for megajets (Figure 5.3). The kinematic information garnered from KCWI data cubes will anchor these measurements. If a tight correlation exists, as hinted at by preliminary

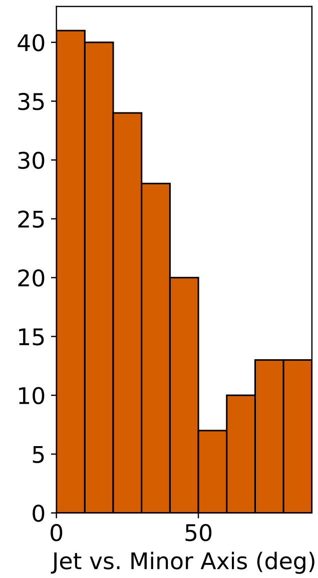

Figure 5.3: The angle between host-galaxy minor axis and the jet axis for several recently observed jets. In projection, Mpc-scale jets are 3× more likely to protrude from the stellar minor axis than from the stellar major axis.

results in Figures 5.1 and 5.2, then this would suggest that longer jets may stem from ellipticals with large-scale angular momentum, either throughout the entire galaxy or in a kinematically decoupled core, which could supply the central SMBH with long-lived, disk-like accretion. Stable jet orientations over cosmological timescales may then be plausible.

The giant jet–derived conclusion that AGN activity at high two-sided jet powers (for Porphyrion, $Q \sim 10^{39}$ W) can be sustained for hundreds of millions of years or even billions of years, suggests an atypical star formation state in these host galaxies. KCWI observations allow for a detailed investigation of jet-mediated star formation quenching in an extreme regime, probing the limits of the effectiveness of jet-mediated quenching. Additionally, galactic core spaxels probe the ongoing existence of massive stars in the nuclear region. Jets emerging from the galactic nucleus entrain atomic nuclei from the winds of massive stars, and could spread heavy elements through the Cosmic Web once they reach Mpc-scale sizes. The (non-)detection of massive stars could lead to a better understanding of the elemental enrichment of the Cosmic Web through cosmological black hole jets.

Finally, these measurements allow for improved SMBH mass determinations

($M_\bullet$). Strikingly, for a significant fraction of the largest jet systems, estimates of $M_\bullet$ do not exist at all; additionally, when such estimates exist, they are based on the widths of stellar emission lines in a single SDSS fiber spectrum. However, in order to unravel the physics of giant jet growth, SMBH masses are important: under the Blandford–Znajek mechanism (Blandford & Znajek, 1977), and at fixed magnetic field strength and spin, the two-sided jet power $Q \propto M_\bullet^2$. The simultaneous availability of high-quality galaxy morphology, internal angular momentum, jet orientation, SMBH mass, and radio luminosity data in cosmological black hole jet systems will enable a new era of precision studies into the yet-elusive physics underpinning one of the Universe's most spectacular phenomena.

Our initial success has motivated a search to understand if these galaxies hosting Mpc-scale jets change over cosmic time; in the latest observations, we have expanded the redshift range out to $z \lesssim 0.5$ i.e. ~ 5 Gyr of cosmic time. The next step is to fully reduce, analyze, and interpret these data. As shown in Figure 5.2, full spectral fitting to the KCWI data cubes and extracting kinematic information through first and second moment maps are the initial step in this process.

Sky Subtraction Strategy

Megajets are predominately generated in elliptical galaxies and the peak of the redshift distribution (mostly due to LOFAR sensitivity constraints) is at $\langle z \rangle \sim 0.7$. Most of the elliptical galaxies observed with KCWI therefore cover the full field of view and it is necessary to use an external reference for sky subtraction. Since the sky intensity varies with time and wavelength, precision sky subtraction is nontrivial. However, the problem becomes tractable with some simplifying assumptions and realizations.

Over the relatively small KCWI FoV, the sky is approximately uniform i.e.

$$f_{\text{sky}}(\alpha, \delta, \lambda) = f_{\text{sky}}(\lambda).$$

The total observed flux density f_λ at a particular voxel can therefore be written as a sum of sky and object contributions:

$$f_\lambda(\alpha, \delta, \lambda) = f_{\text{sky}}(\lambda) + f_{\text{obj}}(\alpha, \delta, \lambda).$$

Using an external sky frame means $f_{\text{sky}}(\lambda)$ can be replaced with $\xi(\lambda) f_{\text{sky, ext}}(\lambda)$ where $f_{\text{sky, ext}}(\lambda)$ is now a known reference spectrum and $\xi(\lambda)$ accounts for the temporal variation in sky intensity. Ideally, $\xi(\lambda)$ would be a sky scaling factor ≈ 1 for most of the wavelength range, but a wavelength dependent correction may be required near OH sky features which vary independently of the sky continuum.

The equation

$$f_\lambda(\alpha, \delta, \lambda) = \xi(\lambda) f_{\mathrm{sky,\,ext}}(\lambda) + f_{\mathrm{obj}}(\alpha, \delta, \lambda).$$

still has too many unknowns for a unique solution, but imaging surveys like Legacy (Dey et al., 2019) can in principle provide $f_{\mathrm{obj}}(\alpha, \delta)$ over several wavelength ranges (e.g. g-band). Each galaxy was also observed at two PAs, which could be of some use in solving for the spatial flux density dependence. The elliptical galaxies are expected to have broad features (relative to the night sky lines), so it may be possible to require a locally smooth spectrum, effectively interpolating over the "sharp" night sky features. Taking this approach or using an external object spectrum (from e.g. SDSS) may be the missing link in solving for the true object flux densities.

Above, I provided a fairly general approach to sky subtraction when there are no sky pixels on the IFU. In spectral regions without strong sky features and a locally smooth sky continuum, precise sky subtraction may not be required to extract reasonably meaningful kinematic measurements. Since one of the primary goals of this project is to understand the angular momenta of these systems, that will ultimately dictate the necessary sky subtraction precision.

5.2 Emission from the WHIM compressed on shock fronts from Mpc-scale black hole jets

Numerical simulations predict that most extragalactic jet energy is transferred to the IGM through supersonic shocks that propagate approximately perpendicular to these Mpc-scale jets (e.g. Stimpson et al., 2023). In decreasing order of importance, this transfer increases the thermal, kinetic, and potential energy of the downstream IGM. SMBH systems therefore represent a largely unexplored, but indispensable source of heating and mixing of the warm–hot IGM (WHIM). Despite this, bow shocks driven by megajets have never been observed.

High-power SMBH jets arising from galaxies push away the IGM that lies in their path. The formation of a low-density, high-temperature, turbulent

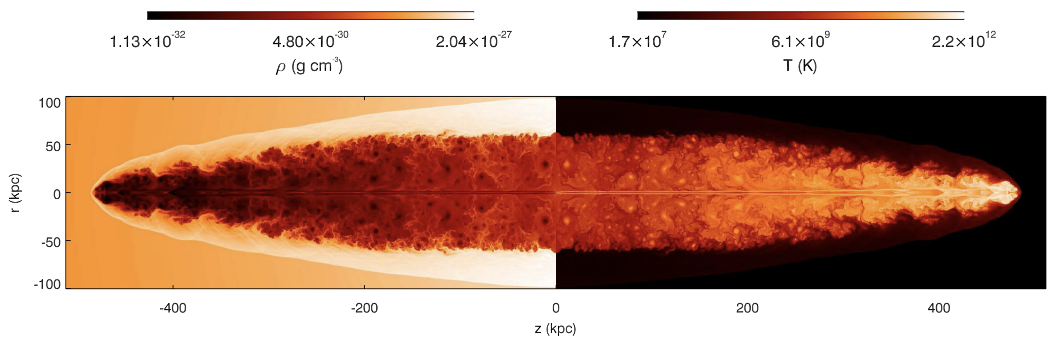

Figure 5.4: Large-scale, relativistic (magneto)hydrodynamic simulations of SMBH jets universally predict that jets drive supersonic shocks into the Cosmic Web. These shock fronts cause strong compression of the IGM (factors of $\sim 10^1$–10^2), and thus locally enhance the rest-frame UV emissivity due to collisionally excited lines by a factor $\sim 10^2$–10^4. This would render the WHIM at Mpc-scale distances from galaxies visible to KCWI. We show the density (left) and temperature (right) around a Perucho et al. (2014) jet with a kinetic power of 10^{38} W after 50 Myr of activity.

"cocoon" around the jet, filled with relativistic electrons flowing from the jet tip implies that the IGM must be compressed elsewhere. As the left panel of Figure 5.5 shows, the jet cocoon (dark) is fully enveloped by a region with shocked ambient medium (light) which lies in the wake of a thin shock front layer (lightest). In this shock front layer, I estimate the ambient medium is compressed by a factor $\beta \sim 10$. In "undisturbed" circumstances, rest-frame UV emission from the $z \sim 2$ IGM would lie several orders of magnitude below the KCWI detection threshold, even after many hours of integration. The presence of a jet, however, results in a significant local compression of the ambient medium. Since the UV line emissivity is proportional to the (hydrogen) density squared, n_{H}^2, even moderate compression can result in significantly more luminous emission. The objective of this project is to observe these shock fronts via collisionally excited emission that is produced as the jets sweep up and compress the local IGM. To the best of my knowledge, such a measurement would be the first detection of the WHIM in a cosmic void and would open up a new means of mapping the distribution of metals in the IGM (through rest-frame UV emission). The latter remains a critical frontier in accounting for the baryons in the universe and understanding the large-scale effects of galactic feedback.

Local Universe observations (Oei, Van Weeren, et al., 2024) suggest that Mpc-scale jets arise predominantly (75%) in filaments of the Cosmic Web,

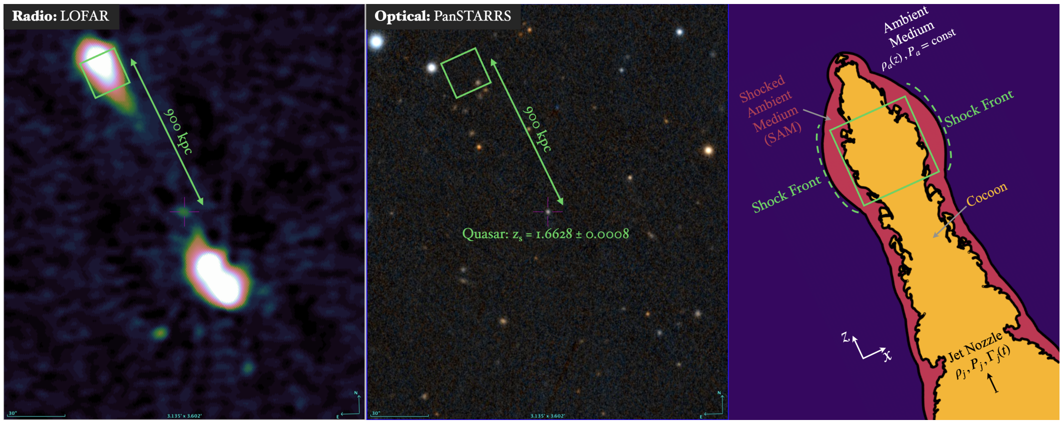

Figure 5.5: Meter-wavelength radio interferometers, such as the International LOFAR Telescope, can reveal Mpc-scale jet systems at cosmological distances, which drive supersonic shocks into the warm–hot intergalactic medium (WHIM). These shocks may allow a intriguing new pathway to observe the WHIM in the optical with KCWI. For the jet system generated by J150012.22+604941.1, a quasar-hosting galaxy at a spectroscopic redshift $z_{\text{spec}} = 1.6628 \pm 0.0008$, we show a radio image (left), an optical image (center), and an annotated schematic of a simulated analogon from Whitehead and Matthews (2023). We show the KCWI medium slicer FOV ($20'' \times 16''$) in green.

and in galaxy groups in particular; the remaining 25% exist in clusters. Since the IGM in clusters boasts temperatures $T \sim 10^7$–10^8 K and emits primarily in the X-ray, this project focuses on jets in filaments, where the plasma is colder ($T \sim 10^5$–10^6 K) and a considerable fraction of collisionally excited emission can observed in the rest-UV. To detect such emission with KCWI, the radio jets must lie at $z \sim 2$. Mostert et al. (2024) have recently assembled the largest catalog ($N \sim 10^4$) of Mpc-scale jet systems to date; Figure 5.5 illustrates one example of the measurement technique.

In light of the high IGM temperatures, it is fair to ask if KCWI is the correct instrument for the job. Unlike other instruments, KCWI was tailor-made for detecting diffuse emission from the Cosmic Web and this is precisely what is being observed. While there is also likely collisionally excited X-ray emission present, current facilities do not have the sensitivity to map such low-SB emission at large galactocentric distances (e.g. Simionescu et al., 2021) and the IFU format allows for additional flexibility given that the precise location of this emission in these systems is not well constrained.

Using a suite of CHIANTI (Del Zanna et al., 2021) simulations (see Figure 5.6),

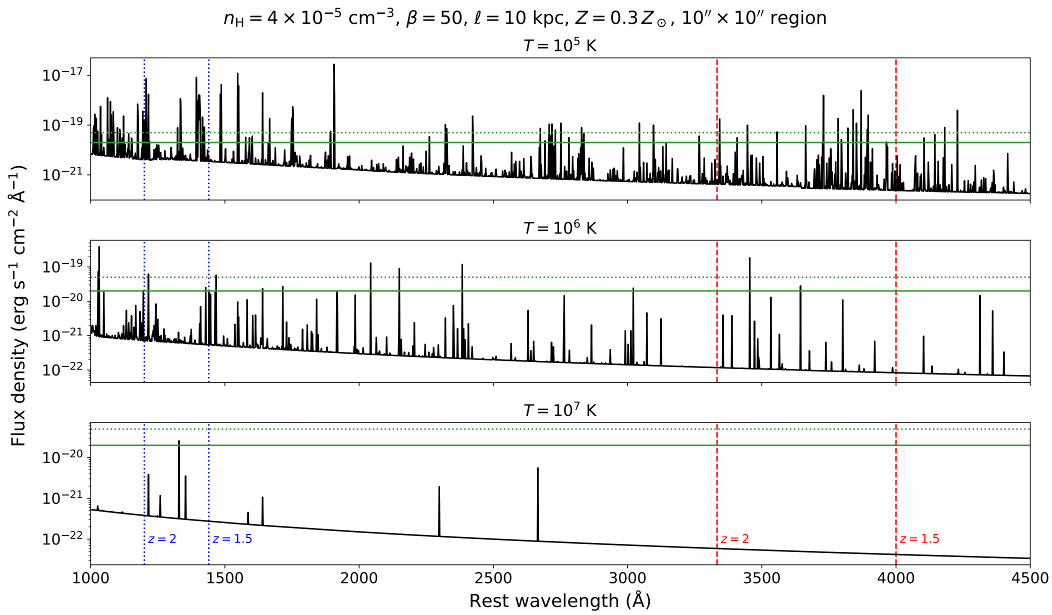

Figure 5.6: CHIANTI emission spectra for shocked WHIM temperatures $T \sim 10^5$–10^7 K (top to bottom), and unshocked WHIM density $n_{\rm H}$, compression factor β, effective LoS distance ℓ, and metallicity Z given in the title. The estimated flux densities assume integration over a $10'' \times 10''$ region (approximately 16–25% of the FoV, depending on the choice of KCWI slicer). The solid (dotted) green line shows the five-hour empirically derived limiting flux density ($S/N \simeq 1$) for the large (medium) slicer and low-resolution grating set. The color-coded vertical dotted (dashed) line denotes the blue (red) end of the KCWI bandpass for redshifts $z = 1.5$ and $z = 2$. The strongest lines are tabulated in Table 5.1.

I constructed mock emission spectra for gas temperatures $5 \le \log(T/{\rm K}) \le 7$ and densities expected in a WHIM region compressed by a Mpc-scale jet. In addition to the aforementioned $n_{\rm H}^2$ dependence, the expected surface brightness (SB) of the collisionally excited emission depends sensitively on the IGM's temperature, metallicity (Z; Mernier et al. 2018), and is proportional to the emission's line-of-sight (LoS) path length (ℓ).

The most luminous collisionally excited species for $T \sim 10^{5-7}$ K gas that fall within the KCWI bandpass at $z \lesssim 2$ are listed in Table 5.1. Based on my CHIANTI emission line modeling, I anticipate these species to have SBs $\sim 10^{-20}$ erg s^{-1} cm^{-2} Å^{-1} arcsec^{-2}; if one integrates over a $10'' \times 10''$ region, the flux densities are $\sim 10^{-18}$ erg s^{-1} cm^{-2} Å^{-1}. Reaching this SB limit will

Line	Rest wavelength (Å)	Peak flux density ($\mathrm{erg\,s^{-1}\,cm^{-2}\,Å^{-1}}$)
C III	1908.73	1.3×10^{-17}
O III	1666.15	8.2×10^{-18}
Si IV	1393.76	4.1×10^{-18}
O IV	1404.81	3.6×10^{-18}
Fe XI	2649.50	3.0×10^{-19}
Fe IX	2498.84	1.0×10^{-19}
Fe X	3455.27	9.3×10^{-20}
Si IX	2149.99	9.1×10^{-20}
Fe XXI	1354.06	8.5×10^{-20}
N V	1238.82	8.0×10^{-20}

Table 5.1: Brightest 10 collisionally excited emission lines observable at $z \lesssim 2$ in the rest-UV with KCWI. The physical conditions are the same as those in Fig. 5.6 and temperatures fall in the range $T \sim 10^5$–10^7 K. This list includes both resonant and nonresonant transitions sorted by intensity. Ions further down the list tend to reach their peak intensities in hotter gas.

result in an emission line $S/N \sim 2$–3. The SB approximately obeys:

$$\mathrm{SB} \sim 10^{-20}\,\mathrm{erg\,s^{-1}\,cm^{-2}\,\mathring{A}^{-1}\,arcsec^{-2}} \times \left(\frac{n_\mathrm{H}}{4\times10^{-5}\,\mathrm{cm^{-3}}}\right)^2 \left(\frac{\beta}{50}\right)^2 \left(\frac{\ell}{10\,\mathrm{kpc}}\right) \left(\frac{Z}{0.3\,Z_\odot}\right)^2 \left(\frac{T}{10^6\,\mathrm{K}}\right)^{-2}. \quad (5.1)$$

This SB level is achievable with KCWI in $\simeq 5$ hours using the large slicer and low-resolution grating set. If the hot IGM is interspersed with cooler clouds ($T \sim 10^4$ K), as e.g. inner hotspots in restarted jets hint at (Kaiser et al., 2000), the signal would be strongly enhanced. It is important to note these values represent reasonable estimates for each quantity in our exposure time calculations, but these values are uncertain and are expected to vary strongly among jets and environments.

I am a founding member of the *Jets on a WHIM* Collaboration which has secured four nights of KCWI time so far for this project. Encouragingly, my early data reduction efforts have revealed tentative emission consistent with O IV $\lambda1404$ and $\lambda1407$ that covers a sizable fraction of the IFU and has peak flux densities within a factor of ~ 3 from the CHIANTI modeling. This ambitious project attempts the first direct observation of shock-induced baryonic heating in the WHIM. If confirmed, these data will be combined with LOFAR VLBI maps and a suite of jet models to ascertain the temperatures, densities, and local magnetic field strengths in the compressed

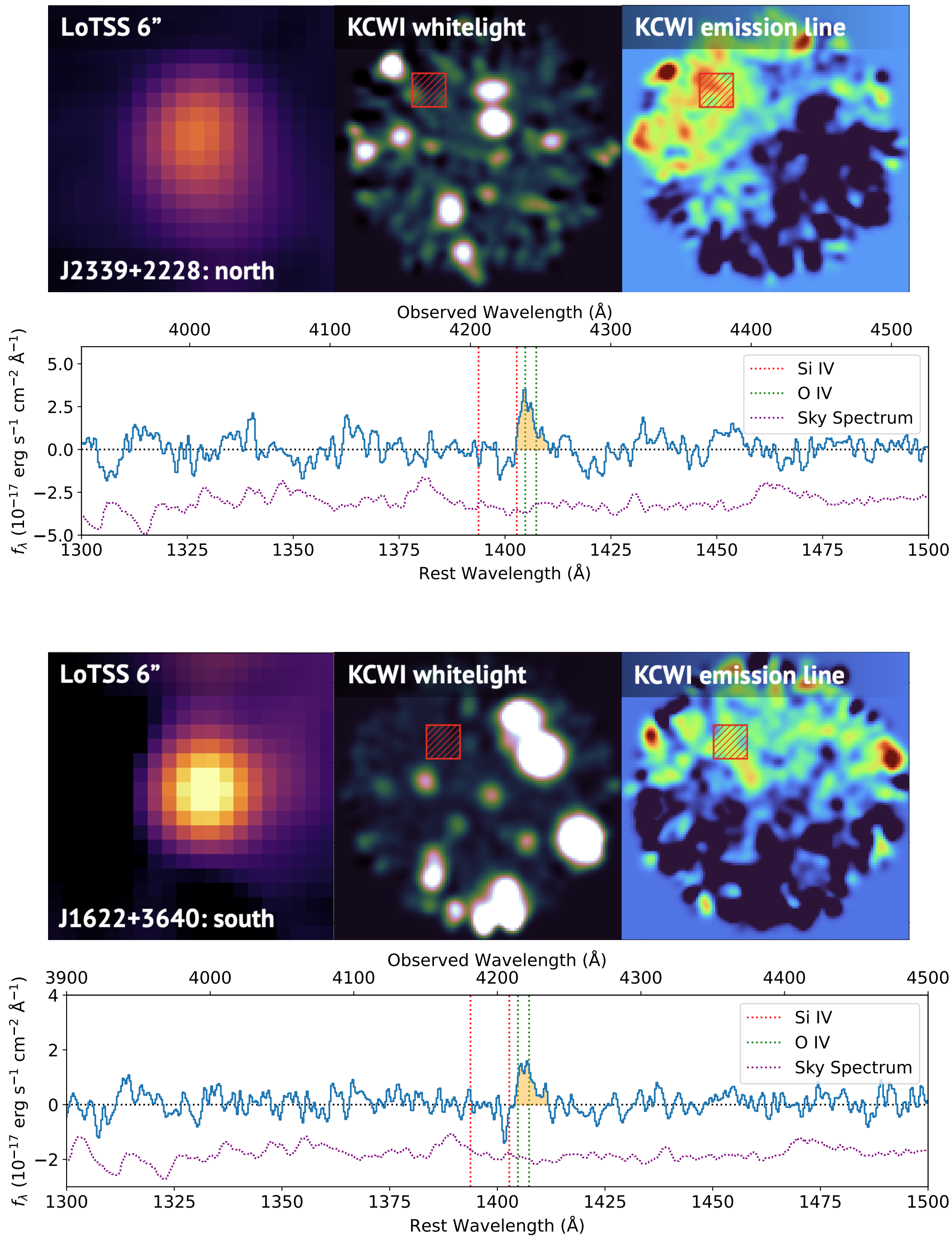

Figure 5.7: Two examples of jet systems observed in 2025 with KCWI: the northern lobe of Mpc-scale jet system J2339+2228 (top; $z_{\rm spec} = 2.009$) and the southern lobe of Mpc-scale jet system J1622+3640 (bottom; $z_{\rm spec} = 1.999$). Each panel shows a LoTSS jet image, a KCWI whitelight image (integrating over 3500–5500 Å), an emission line map (wavelength bounds highlighted in the spectrum in yellow), and the spectrum extracted from a subset of the emission region (red hatched box). The night sky spectrum (scaled and translated for readability) is displayed as a diagnostic. Early data reduction efforts suggest emission consistent with O IV λ1404 or λ1407.

WHIM. In the optimistic case, it may be possible to uncover the extent to which megajets distribute metals from their host galaxies into the distant WHIM.

Uncertainties and potential roadblocks

Since several nights' worth of data have already been collected for this project, I describe below several strategies for sky subtraction that will be attempted and one (of many!) source of uncertainty in making this kind of measurement.

Since the collisionally-excited emission is expected to cover the full KCWI field of view, care must be taken to ensure that signal is not being subtracted off as part of normal sky subtraction. Four approaches are planned, in increasing level of complexity:

1. The first attempt at reduction followed the normal data reduction procedure for KBSS-KCWI galaxies closely. Flat-fielding was performed using the master twilight flat; the sky was subtracted using masks constructed from the deprojected stack (see Section 4.1); and no median filter was used for fear of subtracting off any weak omnipresent signal. Stacks of multiple jet lobes have revealed O IVλ1404 and λ1407, O III] $\lambda\lambda$1660, 1666, and C III$\lambda\lambda$1907, 1909 (all with marginal significance).

2. An incremental improvement would be to adopt the current gains measured during KCWI-R commissioning, use a combined flat that takes advantage of both the internal and (smoothed) twilight frames, plus all of the additional non-standard DRP improvements above.

3. Dedicated off-field skies can be used to ensure that any real signal is not subtracted away (discussed in detail below). In other words, even "sky background" pixels not associated with objects in the deprojected stacks may contain real signal and the default b-spline fit may subtract off.

4. In principle, the exposures of lobes at different redshifts could be used as sky frames for a given object. This has the highest probability of bringing out any real features and minimizing instrument systematics, provided the sky scaling between exposures is correct.

As discussed in Section 5.1, even with an external sky frame, the sky scaling factor $\xi(\lambda)$ is crucial in establishing the true background level. The advantage of this project, however, is each science frame is likely to have at least some sky pixels (even after stringent masking). Given a flat field, the true sky as a function of wavelength can be computed. I outline a potentially viable approach for sky subtracting these frames.

For simplicity, I will assume each detector slice has some combination of emission from the WHIM ($f_{\rm WHIM}$), sky ($f_{\rm sky}$), and unrelated objects ($f_{\rm obj}$). The average spectrum on the first slice[1] can then be written as:

$$f_{\rm tot,\,1}(\lambda) = f_{\rm WHIM,\,1}(\lambda) + f_{\rm sky}(\lambda) + f_{\rm obj}(\lambda).$$

Assuming the deprojected masks I construct exclude all object flux, $f_{\rm obj}(\lambda) = 0$. Substituting in the scaled external sky spectrum, the total flux density on slice one is therefore:

$$f_{\rm tot,\,1}(\lambda) = f_{\rm WHIM,1}(\lambda) + \xi(\lambda) f_{\rm sky,\,ext}(\lambda)$$

and all that remains is to find $\xi(\lambda)$.

Since $f_{\rm WHIM}$ varies spatially (slice to slice) but ξ does not[2], it is possible to take a variant of the standard KCWI b-spline approach and solve slice by slice

$$f_{\rm WHIM,\,1}(\lambda) + \xi(\lambda) f_{\rm sky,\,ext}(\lambda) = 0 \quad (5.2)$$
$$f_{\rm WHIM,\,2}(\lambda) + \xi(\lambda) f_{\rm sky,\,ext}(\lambda) = 0 \quad (5.3)$$
$$\vdots \quad (5.4)$$
$$f_{\rm WHIM,\,24}(\lambda) + \xi(\lambda) f_{\rm sky,\,ext}(\lambda) = 0. \quad (5.5)$$

This system of equations will return a set of 24 sky scaling factors $\xi_i(\lambda)$, $i \in \{1, \ldots, 24\}$ that reflect the spatially varying WHIM emission. Defining $\hat{\xi}$ as the minimum (possibly the median or mean) of the set of sky scaling factors and computing

$$f_{\rm WHIM,\,i}(\lambda) = f_{\rm tot,\,i}(\lambda) - \hat{\xi}(\lambda) f_{\rm sky,\,ext}(\lambda)$$

[1]Since sky subtraction will happen in 2-D (detector coordinates), a slice is a reasonable choice of spatial "unit." Sky subtraction could potentially occur in the 3-D cube format, at which point $f_{\rm tot}(\alpha, \delta, \lambda)$ and $f_{\rm WHIM}(\alpha, \delta, \lambda)$ would be more appropriate notation. In either case, the relevant distinction is which pixels are masked and which pixels can be used to represent the sky.

[2]in an idealized case without additional sources of noise

slice by slice (i is the slice number) will return a sky subtracted 2-D frame with only WHIM emission. These frames can then be converted into cubes and stacked.

For this sky subtraction strategy to work, it is necessary to have a version of the "true" sky spectrum. The external sky spectrum can come from known sky pixels on the science frame, an external sky frame, or another science frame containing mostly sky and weak WHIM emission *at a different redshift*. If one employs the above (or the standard KCWI b-spline) approach to pixels that include WHIM emission, that emission has a probability of being subtracted off.

Redshift uncertainties are another potential hindrance to this project. The galaxies launching Mpc-scale jets at $z \sim 2$ in the sample are all active QSOs. I am in the process of determining fiducial redshifts for each object, but the redshift uncertainty associated with QSOs has been well-established (DESI Collaboration et al., 2026; Lyke et al., 2020). For the current sample, we estimate that uncertainty to be $20 - 125$ km s^{-1}, on par with the estimated LOS velocities from the collisionally excited emission.

Chapter 6

CONCLUSIONS AND FUTURE DIRECTIONS

This thesis has attempted to characterize the distribution of gas and metals and how they flow into and out of galaxies, largely focusing at $z \sim 2$ with the Keck Baryonic Structure Survey. KCWI IFU observations of KBSS galaxies in absorption and emission have made these novel results possible. I recapitulate some of these results below, showing where my work has made contributions to the field of galaxy evolution, and outline some future avenues of study that naturally stem from this thesis.

In Chapter 2, (Prusinski et al., 2025), I constructed the largest ensemble to date of foreground–background KBSS galaxy pairs within projected distances $D_{\rm tran} \leq 250$ kpc (the approximate scale of the CGM surrounding $z \sim 2-3$ star-forming galaxies), and produced the most statistically robust maps of the average $z \sim 2$ CGM. The maps of Lyα covering fraction vs. $D_{\rm tran}$ and line-of-sight velocity I produced chart the changing gravitational influence the galaxy has over its CGM. At small $D_{\rm tran}$, absorption arises due to outflowing gas but near the virial radius of the average foreground galaxy, the maps show a distinct transition where absorption due to radial inflows or ambient CGM gas likely begins to dominate. For the first time with a sample of this kind, there was a sufficient number of pairs to split the ensemble based on Spectral Energy Distribution (SED) derived foreground galaxy properties. There is a strong and monotonic correlation between C IV absorption strength and stellar mass at all $D_{\rm tran}$. Altogether, these results suggest that dark matter halo mass strongly affects the kinematics, covering fraction, and spatial extent of CGM gas, a significant fraction of which may be unbound. Below, I introduce an extension to this project focusing on individual foreground galaxies.

6.1 Multiple background sightlines to individual foreground galaxies

In Chapter 2, (Prusinski et al., 2025), I studied the average $z \sim 2$ CGM *en masse* and connected stellar population parameters (notably M_*) measured in foreground galaxies down-the-barrel with CGM properties inferred from transverse sightlines ($D_{\rm tran} > 0$ kpc). Crucially, I studied many foreground

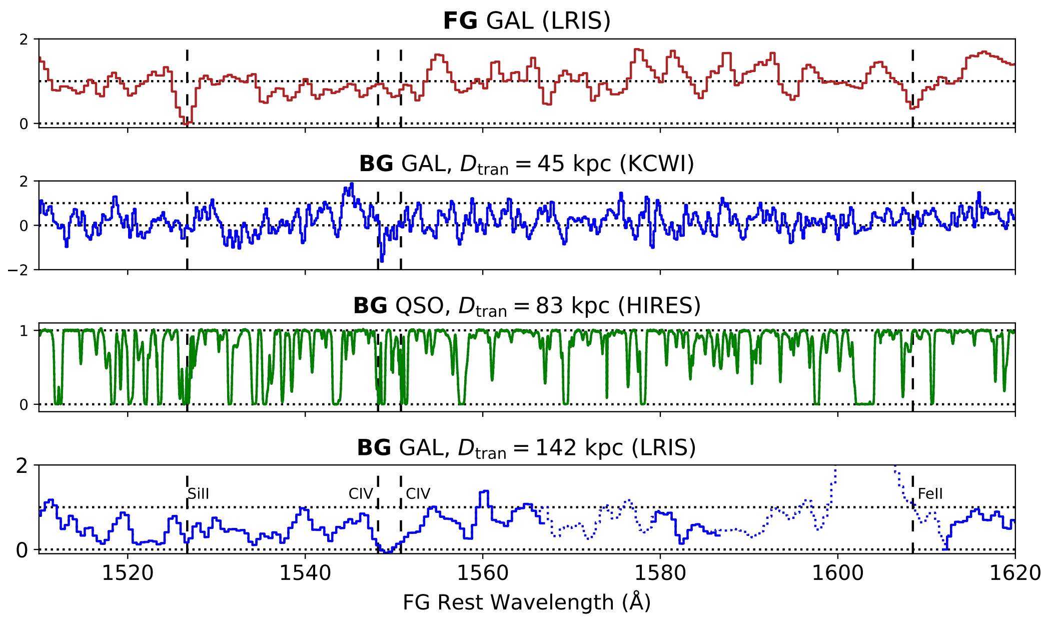

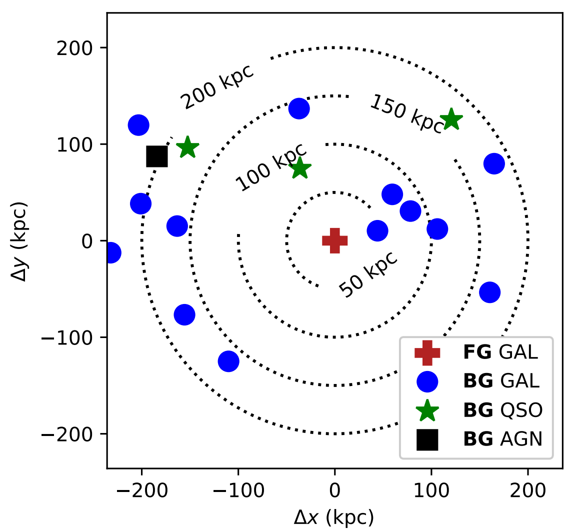

Figure 6.1: *Top:* The CGM of a foreground galaxy (red) imparts absorption on the spectra of background sightlines (color set by background object type) at several projected distances. *Left:* The background galaxy sightline distribution on the sky relative to the foreground galaxy (red plus sign in the center). This grid can probe CGM gas distribution asymmetries.

galaxies using a similarly large set of background sightlines. Now, I propose to "flip this study on its head" and exploit the fact that multiple background sightlines can intersect one common foreground halo (Figure 6.1 illustrates how this works). In essence, I will investigate a robust subset of foreground galaxies that have numerous spectra along background sightlines to map out individual foreground galaxies' CGM as a function of 2-D spatial position (not just D_{tran}).

While the results on the average CGM are constraining, considering individual galaxies offers a new "lens" in which to study CGM gas. To date, studies of individual galaxies have been relegated to the local universe (e.g. M31 with AMIGA; Lehner et al. 2025) where their CGM subtend large areas on the sky such that many independent background galaxy and QSO sightlines are available. With increasing redshift, fewer bright background sightlines are available and fainter background sources (i.e. galaxies) are required to maintain the same spatial sampling. The galaxy distribution in KBSS is unique in that $\simeq 40$ foreground galaxies have $10 \lesssim N_{\rm bg} \lesssim 20$ background sightlines within the average virial radius of the foreground galaxy, a spatial sampling comparable to AMIGA at $z \sim 2$.

Fundamentally, I am interested in measuring the *asymmetry of the CGM gas distribution*, which will be detectable for the first time at these redshifts. Studies like AMIGA (Lehner et al., 2025) at $z \sim 0$ have found radial variation in absorption column densities and kinematics but little change with azimuthal angle, contrary to what might be naively expected in the "classic" CGM picture (inflowing gas enters along the major axis of a galaxy and gets expelled along the minor; Tumlinson et al. 2017; Veilleux et al. 2005). It is worth emphasizing that, except for stellar mass M_*, the $z \sim 2-3$ galaxies in KBSS are a disjoint population with respect to $z \sim 0$ galaxies in most stellar population parameters (e.g. star formation rate [SFR], specific SFR [sSFR], excitation, Hα luminosity). In general, $z \sim 2$ KBSS galaxies have $\simeq 30\times$ higher SFRs, sSFRs, and Hα luminosities than their $z \sim 0$ counterparts (Strom et al., 2017). Along these lines, $z \sim 2$ star-forming galaxies have considerably more active velocity fields and outflows appear to have a more dramatic effect on their CGM (Prusinski et al., 2025) than at $z \sim 0$. Asymmetries in the gas distribution, if present, are therefore expected to be more pronounced at $z \sim 2$.

In addition to CGM morphology, asymmetries in the gas kinematics are also of interest. In particular, individual sightlines allow for the possibility of detecting bulk rotation (something not detectable in an average). Y. Chen et al. (2020) and Prusinski et al. (2025) found that the velocity centroid of the Lyα absorption feature varies with $D_{\rm tran}$. At $D_{\rm tran} \lesssim 50$ kpc, preferentially redshifted foreground Lyα emission contributes to symmetric background absorption resulting in net blueshifted profiles and Lyα emission from radial inflows beyond the virial radius ($R_{\rm vir}$) is suspected to lead to a net redshifted profile near $D_{\rm tran} \simeq 100$ kpc. Both studies averaged many sightlines and were therefore insensitive to the direction of the bulk gas motion, but the proposed study using individual sightlines will be able to test this hypothesis.

This extension project offers CGM constraints on a variety of scales. As an example, KBSS contains HIRES spectra of several closely separated hyper-luminous QSOs that can be used to calculate the gas coherence scale. Rudie et al. (2019) showed an example (using KBSS foreground galaxy BX182) of how this can be done with the KBSS Q0142 QSO. The background QSO is lensed by a $z = 0.49$ foreground galaxy and two images are formed $2''.2$ apart (400 pc in projection), but this type of analysis is not limited to simply one galaxy and can easily be expanded to multiple foreground galaxies in the field. On CGM scales, the brightest QSO in the universe (observed to date), Q1549 (HS1549+1919), resides in a proto-cluster environment at $z = 2.84$ along with three other ($\mathcal{R} \sim 23-24$) AGN, all within a radius of $20''$ (156 pkpc) from the bright QSO. Their proximity makes these AGN useful since each $z \lesssim 2.8$ galaxy in the Q1549 field will have at least four lines of sight through its CGM on physical scales comparable to $R_{\rm vir}$. The Q1623 field is another example of a field where three HLQSOs (KP76 – 78) are located within $2-3'$ (~ 1 pMpc) of one another at $2.46 \leq z \leq 2.61$ that have the potential to trace Lyα and C IV at large separations from foreground galaxies at $z \lesssim 2.4$.

In practice, this project will utilize existing Keck/LRIS and KCWI spectra of background galaxies at spectral resolution $R \simeq 1500$, together with QSO sightlines ($R \sim 45{,}000$). Coupled with the wealth of ancillary data collected over the past ~two decades, this project will take full advantage of the KBSS dataset and directly tackle questions the survey was tailor-made to answer from the start.

Chapter 3 of this thesis involved mapping $z \sim 2$ CGM gas in emission with a novel diagnostic. Using KCWI, I studied optically thick regions through nonresonant emission associated with rest-frame far-UV metallic transitions. Lyα is by far the strongest emission line in the UV but remains notoriously difficult to interpret since it resonantly scatters in high density gas. In short, there is no unique radiative transfer solution to an observed (1-D) Lyα profile because observed Lyα photons have typically undergone many scatterings since their production. However, many of the far-UV low ionization metallic species (e.g. Si II, C II, O I) have fine structure levels just above their ground states. At high optical depths, in addition to resonant absorption, there is a finite probability of spontaneous de-excitation to the excited fine structure level just above the ground state. The latter transition produces photons with slightly longer wavelengths with respect to the resonant interstellar line, making this emission off-resonance and optically thin. The fact that these transitions (e.g. Si II*, C II*) are off-resonance and can escape without modulation by radiative transfer effects makes them extremely useful in tracing the morphology and kinematics of high-density gas that would otherwise be unobservable in UV emission.

I found that the nonresonant lines appear as "emission-line counterparts" to fit ISM-components of resonant absorption lines. In other words, the range of velocities observed in nonresonant emission is consistent with that of the ISM of $z \sim 2$ galaxies. Optically thick gas is present out to at least $D_{\rm tran} \lesssim 20$ kpc from the average $z \sim 2$ galaxy and shows a similar trend to the galaxy pair studies (Chapter 2) of decreasing LOS velocity spread (σ) with $D_{\rm tran}$. There also appears to be an tentative azimuthal dependence to the Si II* halos favoring their minor axes.

The Si II*, C II*, and O I* emission lines are not the only emission features that can be explored in the rest-UV. Collisionally-excited metallic emission in the far-UV, if observed, has the potential to reveal pockets of rapidly cooling CGM gas. Feedback from massive stars, supernovae, and AGN inject large amounts of energy into CGM gas and are predicted to drive the warm-hot phase of the CGM ($T \gtrsim 10^6$ K). Recent simulations (e.g. Sravan et al., 2016) have predicted that this shock-heated gas cools through metallic line emission in the far-UV and may be visible with deep KCWI observations. A systematic search for such emission in KBSS-KCWI data cubes could constrain the most metal-enriched regions of the CGM and the role galactic winds play in metal disbursement.

A well-characterized data reduction pipeline is essential to making all of these results possible (Chapter 4). At the same time, it is clear that our understanding of how SMBHs are coupled to their host galaxies, their CGM, and IGM is sorely lacking. The ongoing work in Chapter 5 represents two approaches addressing the origins of AGN feedback in the most egregious cases in the (relatively) nearby universe, and the potential for AGN-induced metal disbursement into the WHIM, respectively. Below I propose a new project that has the potential to make strides in understanding AGN feedback at high-redshift by assessing the effect QSOs have on their environments.

6.2 The effect of QSOs on circumgalactic Lyα absorption

AGN feedback is a prime example of an astrophysical phenomenon that is commonly invoked but not yet well constrained. Jets and AGN have been shown to be essential manifestations of feedback, supplying (in principle) a necessary amount of kinetic energy to quench star formation in massive galaxies (e.g. Heckman & Best, 2023; Heckman et al., 2024), but $z \sim 2$ galaxies with and without active QSOs appear to have remarkably similar metal distributions in their CGM (at least for $D_{\rm tran} \gtrsim 70$ kpc; see Figure 2.17). Moreover, observational studies of AGN are particularly timely given that subgrid models of AGN feedback in simulations are becoming critical to distinguishing the physics of galaxy evolution (e.g. Schaye et al., 2026).

Focusing on how QSOs influence their environment, I propose to use background galaxies around $\simeq 50$ KBSS QSOs to investigate the response of the IGM to QSO ionizing radiation (i.e. the transverse proximity effect [TPE]) with the finest spatial and temporal sampling to date. Transverse lines of sight to KBSS QSOs at $D_{\rm tran} > 0$ kpc will achieve a coarse measure of the radiative history of the QSO and determine the bulk (an)isotropy of the QSO radiation field. Such a study was proposed in concept at the beginning of KBSS (Adelberger, 2004) but at the time, the number of background galaxies was insufficient to overcome the predicted cosmic variance. We are now in a position where $\simeq 50$ background galaxies at $D_{\rm tran} \leq 2$ Mpc can sample the CQM around KBSS foreground QSOs. The high density of background galaxies with respect to foreground QSOs makes KBSS arguably the best sample to chart the ionization gradients in the IGM surrounding QSOs through variations in Lyα forest absorption. At the same time, much of the software I have developed for working with galaxy-galaxy pairs can be naturally extended for this use case.

The TPE results from copious amounts of ionizing radiation emanating from bright QSOs which serves to reduce the amount of neutral hydrogen in their vicinity. As a result, redshifts near the QSO redshift would be expected to show an observed decrease in intergalactic Lyα absorption (typically measured in the Lyα forest). The apparent paucity of absorption in the circum-QSO medium (CQM) is termed the QSO "proximity effect."

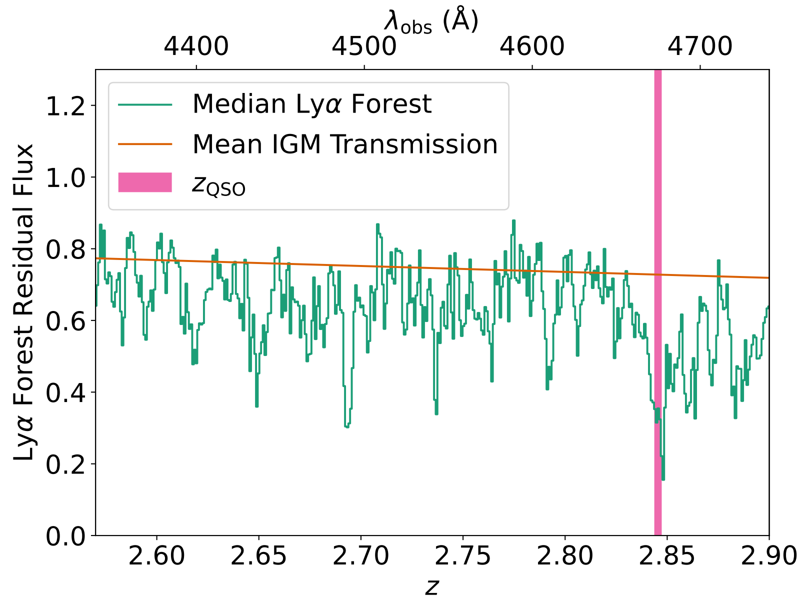

Figure 6.2: The Lyα forest in the vicinity of the brightest QSO in the universe: HS1549+1919, measured by stacking 25 background KBSS galaxy sightlines within $D_{tran} \simeq 2$ Mpc of the QSO. The excess Lyα absorption near z_{QSO} suggests there is considerable H I in the vicinity of the QSO despite its prodigious ionizing flux. The proposed study will look for spatial variation in the neutral hydrogen around such QSOs.

Changes in QSO luminosity over time will lead to different hydrogen ionization fractions within the QSO's light cone as a function of distance.

There have been several attempts to study the transverse proximity effect (TPE) including around three (out of $\simeq 50$) KBSS QSOs, with mixed results. The high ionization fractions induced by the QSO might lead one to predict shallower Lyα absorption systems in the Lyα forest near the QSO redshift but to the contrary, many studies (e.g. Croft, 2004; Crotts & Fang, 1998; Gonçalves et al., 2008; Schirber et al., 2004) have instead found *excess* Lyα absorption near z_{QSO} (see Figure 6.2). This effect has been explained by either anisotropic ionizing radiation fields around QSOs or the fact that QSOs at $z \sim 2$ tend to reside in group-size halos i.e. where an overabundance of neutral gas is expected (Kirkman & Tytler, 2008). The grid of background sightlines to the QSO in the proposed study will make it possible to test the validity of these assumptions. In KBSS, Gonçalves et al. (2008) looked at the Q1623-KP76 – 78 QSO triplet (where the ionizing flux from foreground QSOs is 10 – 200× that of the metagalactic background) with deep Keck/HIRES

($R \sim 45{,}000$) observations. Rather than focusing solely on Lyα, Gonçalves et al. (2008) folded metal absorption systems into their analysis. Encouragingly, photoionization models suggested that the atypical properties seen in metal absorption systems close to QSOs were best explained by the presence of a strong UV radiation field (i.e. the QSO proximity effect).

The primary objective of this study is to detect order-of-magnitude changes in the QSO's luminosity with a temporal resolution ~ 5 Myr over the previous 50–100 Myr. By measuring the spatial extent of gas clearly affected by QSO radiation relative to unrelated foreground systems, this study will establish independent QSO lifetime estimates for the sample. The sparsely sampled grid of background sightlines to the QSO will test previous assumptions on QSO radiation field anisotropies. If Lyα forest spatial asymmetries are detected, I will measure QSO light cone opening angles with respect to the line of sight. Such asymmetries could be compared for different types of QSOs as a direct test of unified AGN models.

Clearly the field of galaxy evolution has a long way to go before a prescriptive formulation of "galaxies" is possible, but the results presented in this thesis move our collective understanding of baryonic feedback forward and open up new areas of inquiry. This thesis represents the cutting edge in baryon cycle observations at $z \sim 2$, offering new views into the physics of feedback. Looking forward, newly-commissioned facilities (e.g. 4MOST, PFS) and upcoming facilities on the ground (e.g., E-ELT, TMT) and in space (e.g., *Roman*, SCWI) are poised to continue unraveling the subtleties underpinning galactic evolution (especially at high-z).[1]

[1]A jejune individual could summarize this sentence with the platitude "the future is bright."

BIBLIOGRAPHY

Adelberger, K. L. (2004). Measuring the Radiative Histories of High-Redshift QSOs with the Transverse Proximity Effect. *The Astrophysical Journal*, *612*(2), 706–723. https://doi.org/10.1086/422804

Adelberger, K. L., Shapley, A. E., Steidel, C. C., Pettini, M., Erb, D. K., & Reddy, N. A. (2005). The Connection between Galaxies and Intergalactic Absorption Lines at Redshift 2<\raisebox-0.5ex\textasciitildez<\raisebox-0.5ex\textasciitilde3 [_eprint: astro-ph/0505122]., *629*(2), 636–653. https://doi.org/10.1086/431753

Adelberger, K. L., Steidel, C. C., Shapley, A. E., Hunt, M. P., Erb, D. K., Reddy, N. A., & Pettini, M. (2004). Optical Selection of Star-forming Galaxies at Redshifts $1 < z < 3$. *The Astrophysical Journal*, *607*(1), 226–240. https://doi.org/10.1086/383221

Adelberger, K. L., Steidel, C. C., Shapley, A. E., & Pettini, M. (2003). Galaxies and Intergalactic Matter at Redshift z 3: Overview. *The Astrophysical Journal*, *584*(1), 45–75. https://doi.org/10.1086/345660

Afruni, A., Lopez, S., Anshul, P., Tejos, N., Noterdaeme, P., Berg, T. A. M., Ledoux, C., Solimano, M., Gonzalez-Lopez, J., Gronke, M., Barrientos, F., & Johnston, E. J. (2023). Directly constraining the spatial coherence of the z 1 circumgalactic medium. *Astronomy & Astrophysics*, *680*, A112. https://doi.org/10.1051/0004-6361/202347867

Anderson, M. E., Gaspari, M., White, S. D. M., Wang, W., & Dai, X. (2015). Unifying x-ray scaling relations from galaxies to clusters. *Monthly Notices of the Royal Astronomical Society*, *449*(4), 3806–3826. https://doi.org/10.1093/mnras/stv437

Bacon, R., Mary, D., Garel, T., Blaizot, J., Maseda, M., Schaye, J., Wisotzki, L., Conseil, S., Brinchmann, J., Leclercq, F., Abril-Melgarejo, V., Boogaard, L., Bouché, N. F., Contini, T., Feltre, A., Guiderdoni, B., Herenz, C., Kollatschny, W., Kusakabe, H., . . . Zoutendijk, S. L. (2021). The MUSE Extremely Deep Field: The cosmic web in emission at high redshift. *Astronomy & Astrophysics*, *647*, A107. https://doi.org/10.1051/0004-6361/202039887

Bahcall, J. N., & Spitzer, L., Jr. (1969). Absorption lines produced by galactic halos. *The Astrophysical Journal*, *156*, L63. https://doi.org/10.1086/180350

Behroozi, P. S., Wechsler, R. H., & Conroy, C. (2013). THE AVERAGE STAR FORMATION HISTORIES OF GALAXIES IN DARK MATTER HALOS FROM $z = 0$-8. *The Astrophysical Journal*, *770*(1), 57. https://doi.org/10.1088/0004-637X/770/1/57

Bergeron, J., & Boissé, P. (1991). A sample of galaxies giving rise to Mg II quasar absorption systems., *243*, 344.

Bertin, E., & Arnouts, S. (1996). SExtractor: Software for source extraction., *117*, 393–404. https://doi.org/10.1051/aas:1996164

Bigwood, L., Amon, A., Schneider, A., Salcido, J., McCarthy, I. G., Preston, C., Sanchez, D., Sijacki, D., Schaan, E., Ferraro, S., Battaglia, N., Chen, A., Dodelson, S., Roodman, A., Pieres, A., Ferté, A., Alarcon, A., Drlica-Wagner, A., Choi, A., . . . Yamamoto, M. (2024). Weak lensing combined with the kinetic Sunyaev–Zel'dovich effect: A study of baryonic feedback. *Monthly Notices of the Royal Astronomical Society*, *534*(1), 655–682. https://doi.org/10.1093/mnras/stae2100

Blandford, R. D., & Znajek, R. L. (1977). Electromagnetic extraction of energy from kerr black holes. *mnras*, *179*, 433–456. https://doi.org/10.1093/mnras/179.3.433

Bordoloi, R., Lilly, S. J., Knobel, C., Bolzonella, M., Kampczyk, P., Carollo, C. M., Iovino, A., Zucca, E., Contini, T., Kneib, J.-P., Le Fevre, O., Mainieri, V., Renzini, A., Scodeggio, M., Zamorani, G., Balestra, I., Bardelli, S., Bongiorno, A., Caputi, K., . . . Welikala, N. (2011). THE RADIAL AND AZIMUTHAL PROFILES OF Mg II ABSORPTION AROUND 0.5 < z < 0.9 zCOSMOS GALAXIES OF DIFFERENT COLORS, MASSES, AND ENVIRONMENTS. *The Astrophysical Journal*, *743*(1), 10. https://doi.org/10.1088/0004-637X/743/1/10

Bordoloi, R., Prochaska, J. X., Tumlinson, J., Werk, J. K., Tripp, T. M., & Burchett, J. N. (2018). On the CGM Fundamental Plane: The Halo Mass Dependency of Circumgalactic H i. *The Astrophysical Journal*, *864*(2), 132. https://doi.org/10.3847/1538-4357/aad8ac

Bordoloi, R., Simcoe, R. A., Matthee, J., Kashino, D., Mackenzie, R., Lilly, S. J., Eilers, A.-C., Liu, B., DePalma, D., Yue, M., & P. Naidu, R. (2024a). EIGER IV. The Cool 10^4 K Circumgalactic Environment of High-redshift Galaxies Reveals Remarkably Efficient Intergalactic Medium Enrichment. *The Astrophysical Journal*, *963*(1), 28. https://doi.org/10.3847/1538-4357/ad1b63

Bordoloi, R., Simcoe, R. A., Matthee, J., Kashino, D., Mackenzie, R., Lilly, S. J., Eilers, A.-C., Liu, B., DePalma, D., Yue, M., & P. Naidu, R. (2024b). EIGER IV. The Cool 10^4 K Circumgalactic Environment of High-redshift Galaxies Reveals Remarkably Efficient Intergalactic Medium Enrichment., *963*(1), Article 28, 28. https://doi.org/10.3847/1538-4357/ad1b63

Bordoloi, R., Tumlinson, J., Werk, J. K., Oppenheimer, B. D., Peeples, M. S., Prochaska, J. X., Tripp, T. M., Katz, N., Davé, R., Fox, A. J., Thom, C., Ford, A. B., Weinberg, D. H., Burchett, J. N., & Kollmeier, J. A.

(2014). THE COS-DWARFS SURVEY: THE CARBON RESERVOIR AROUND SUB- *L* * GALAXIES. *The Astrophysical Journal*, *796*(2), 136. https://doi.org/10.1088/0004-637X/796/2/136

Borthakur, S., Heckman, T., Tumlinson, J., Bordoloi, R., Thom, C., Catinella, B., Schiminovich, D., Davé, R., Kauffmann, G., Moran, S. M., & Saintonge, A. (2015). CONNECTION BETWEEN THE CIRCUMGALACTIC MEDIUM AND THE INTERSTELLAR MEDIUM OF GALAXIES: RESULTS FROM THE COS-GASS SURVEY. *The Astrophysical Journal*, *813*(1), 46. https://doi.org/10.1088/0004-637X/813/1/46

Bouche, N., Cresci, G., Davies, R., Eisenhauer, F., Forster Schreiber, N. M., Genzel, R., Gillessen, S., Lehnert, M., Lutz, D., Nesvadba, N., Shapiro, K. L., Sternberg, A., Tacconi, L. J., Verma, A., Cimatti, A., Daddi, E., Renzini, A., Erb, D. K., Shapley, A., & Steidel, C. C. (2007). Dynamical Properties of z 2 Star-forming Galaxies and a Universal Star Formation Relation. *The Astrophysical Journal*, *671*(1), 303–309. https://doi.org/10.1086/522221

Bouché, N., Murphy, M. T., Kacprzak, G. G., Péroux, C., Contini, T., Martin, C. L., & Dessauges-Zavadsky, M. (2013). Signatures of Cool Gas Fueling a Star-Forming Galaxy at Redshift 2.3. *Science*, *341*(6141), 50–53. https://doi.org/10.1126/science.1234209

Burchett, J. N., Tripp, T. M., Bordoloi, R., Werk, J. K., Prochaska, J. X., Tumlinson, J., Willmer, C. N. A., O'Meara, J., & Katz, N. (2016). A DEEP SEARCH FOR FAINT GALAXIES ASSOCIATED WITH VERY LOW REDSHIFT C iv ABSORBERS. III. THE MASS- AND ENVIRONMENT-DEPENDENT CIRCUMGALACTIC MEDIUM. *The Astrophysical Journal*, *832*(2), 124. https://doi.org/10.3847/0004-637X/832/2/124

Byrohl, C., & Nelson, D. (2023). The cosmic web in Lyman-alpha emission. *Monthly Notices of the Royal Astronomical Society*, *523*(4), 5248–5273. https://doi.org/10.1093/mnras/stad1779

Chen, H.-W., & Zahedy, F. S. (2024, December). The Circumgalactic Medium [arXiv:2412.10579 [astro-ph]]. https://doi.org/10.48550/arXiv.2412.10579

Chen, H.-W., Zahedy, F. S., Boettcher, E., Cooper, T. M., Johnson, S. D., Rudie, G. C., Chen, M. C., Walth, G. L., Cantalupo, S., Cooksey, K. L., Faucher-Giguère, C.-A., Greene, J. E., Lopez, S., Mulchaey, J. S., Penton, S. V., Petitjean, P., Putman, M. E., Rafelski, M., Rauch, M., . . . Weiner, B. J. (2020a). The Cosmic Ultraviolet Baryon Survey (CUBS) – I. Overview and the diverse environments of Lyman limit systems at z < 1. *Monthly Notices of the Royal Astronomical Society*, *497*(1), 498–520. https://doi.org/10.1093/mnras/staa1773

Chen, H.-W., Zahedy, F. S., Boettcher, E., Cooper, T. M., Johnson, S. D., Rudie, G. C., Chen, M. C., Walth, G. L., Cantalupo, S., Cooksey, K. L., Faucher-Giguère, C.-A., Greene, J. E., Lopez, S., Mulchaey, J. S., Penton, S. V., Petitjean, P., Putman, M. E., Rafelski, M., Rauch, M., . . . Weiner, B. J. (2020b). The Cosmic Ultraviolet Baryon Survey (CUBS) - I. Overview and the diverse environments of Lyman limit systems at z < 1., *497*(1), 498–520. https://doi.org/10.1093/mnras/staa1773

Chen, Y. (2022, January). *The Absorption and Emission of Neutral Hydrogen Around High-Redshift Star-Forming Galaxies* [PhD Thesis]. California Institute of Technology, Division of Physics, Mathematics and Astronomy.

Chen, Y., Steidel, C. C., Erb, D. K., Law, D. R., Trainor, R. F., Reddy, N. A., Shapley, A. E., Pahl, A. J., Strom, A. L., Lamb, N. R., Li, Z., & Rudie, G. C. (2021). The KBSS–KCWI survey: The connection between extended Ly haloes and galaxy azimuthal angle at z 2–3. *Monthly Notices of the Royal Astronomical Society*, *508*(1), 19–43. https://doi.org/10.1093/mnras/stab2383

Chen, Y., Steidel, C. C., Hummels, C. B., Rudie, G. C., Dong, B., Trainor, R. F., Bogosavljević, M., Erb, D. K., Pettini, M., Reddy, N. A., Shapley, A. E., Strom, A. L., Theios, R. L., Faucher-Giguère, C.-A., Hopkins, P. F., & Kereš, D. (2020). The Keck Baryonic Structure Survey: Using foreground/background galaxy pairs to trace the structure and kinematics of circumgalactic neutral hydrogen at z 2. *Monthly Notices of the Royal Astronomical Society*, *499*(2), 1721–1746. https://doi.org/10.1093/mnras/staa2808

Coil, A. L., Weiner, B. J., Holz, D. E., Cooper, M. C., Yan, R., & Aird, J. (2011). OUTFLOWING GALACTIC WINDS IN POST-STARBURST AND ACTIVE GALACTIC NUCLEUS HOST GALAXIES AT 0.2 < z < 0.8. *The Astrophysical Journal*, *743*(1), 46. https://doi.org/10.1088/0004-637X/743/1/46

Connor, L., & Ravi, V. (2021). A detection of circumgalactic gas with fast radio bursts [arXiv: 2107.13692]. *arXiv:2107.13692 [astro-ph]*. Retrieved July 30, 2021, from http://arxiv.org/abs/2107.13692

Crighton, N. H. M., Bielby, R., Shanks, T., Infante, L., Bornancini, C. G., Bouché, N., Lambas, D. G., Lowenthal, J. D., Minniti, D., Morris, S. L., Padilla, N., Péroux, C., Petitjean, P., Theuns, T., Tummuangpak, P., Weilbacher, P. M., Wisotzki, L., & Worseck, G. (2011a). The VLT LBG Redshift Survey- II. Interactions between galaxies and the IGM at z 3., *414*, 28–49. https://doi.org/10.1111/j.1365-2966.2011.17247.x

Crighton, N. H. M., Bielby, R., Shanks, T., Infante, L., Bornancini, C. G., Bouché, N., Lambas, D. G., Lowenthal, J. D., Minniti, D., Morris, S. L., Padilla, N., Péroux, C., Petitjean, P., Theuns, T., Tummuangpak, P., Weilbacher, P. M., Wisotzki, L., & Worseck, G. (2011b). The VLT LBG Redshift Survey- II. Interactions between galaxies and the IGM at z 3: VLT LBG Redshift Survey - II. *Monthly Notices of the Royal Astronomical Society*, *414*(1), 28–49. https://doi.org/10.1111/j.1365-2966.2011.17247.x

Croft, R. A. C. (2004). Ionizing Radiation Fluctuations and Large-Scale Structure in the Ly\ensuremath\alpha Forest [_eprint: astro-ph/0310890]. *The Astrophysical Journal*, *610*(2), 642–662. https://doi.org/10.1086/421839

Crotts, A. P. S., & Fang, Y. (1998). Reobservation of Close QSO Groups: The Size Evolution and Shape of Ly\ensuremath\alpha Forest Absorbers [_eprint: astro-ph/9702185]. *The Astrophysical Journal*, *502*(1), 16–47. https://doi.org/10.1086/305872

Crowther, P. A., Prinja, R. K., Pettini, M., & Steidel, C. C. (2006). On the reliability of C IV 1549 as an abundance indicator for high-redshift star-forming galaxies. *Monthly Notices of the Royal Astronomical Society*, *368*(2), 895–902. https://doi.org/10.1111/j.1365-2966.2006.10164.x

da Costa-Luis, C., Larroque, S. K., Altendorf, K., Mary, H., richardsheridan, Korobov, M., Yorav-Raphael, N., Ivanov, I., Bargull, M., Rodrigues, N., Chen, G., Dektyarev, M., mjstevens777, Pagel, M. D., Zugnoni, M., JC, CrazyPython, Newey, C., Lee, A., . . . McCracken, J. (2024, August). Tqdm: A fast, Extensible Progress Bar for Python and CLI. https://doi.org/10.5281/zenodo.595120

Del Zanna, G., Dere, K. P., Young, P. R., & Landi, E. (2021). CHIANTI – an atomic database for emission lines – Paper XVI: Version 10, further extensions [arXiv: 2011.05211]. *The Astrophysical Journal*, *909*(1), 38. https://doi.org/10.3847/1538-4357/abd8ce

DESI Collaboration, Abdul Karim, M., Adame, A. G., Aguado, D., Aguilar, J., Ahlen, S., Alam, S., Aldering, G., Alexander, D. M., Alfarsy, R., Allen, L., Allende Prieto, C., Alves, O., Anand, A., Andrade, U., Armengaud, E., Avila, S., Aviles, A., Awan, H., . . . Zu, Y. (2026). Data release 1 of the dark energy spectroscopic instrument. *The Astronomical Journal*, *171*(5), 285. https://doi.org/10.3847/1538-3881/ae4c43

Dey, A., Schlegel, D. J., Lang, D., Blum, R., Burleigh, K., Fan, X., Findlay, J. R., Finkbeiner, D., Herrera, D., Juneau, S., Landriau, M., Levi, M., McGreer, I., Meisner, A., Myers, A. D., Moustakas, J., Nugent, P., Patej, A., Schlafly, E. F., . . . Zhou, Z. (2019). Overview of the DESI Legacy Imaging Surveys., *157*(5), Article 168, 168. https://doi.org/10.3847/1538-3881/ab089d

Dutta, R., Fumagalli, M., Fossati, M., Bielby, R. M., Stott, J. P., Lofthouse, E. K., Cantalupo, S., Cullen, F., Crain, R. A., Tripp, T. M., Prochaska, J. X., Battaia, F. A., Burchett, J. N., Fynbo, J. P. U., Murphy, M. T., Schaye, J., Tejos, N., & Theuns, T. (2021). Metal-enriched halo gas across galaxy overdensities over the last 10 billion years [arXiv: 2109.10927]. *arXiv:2109.10927 [astro-ph]*. Retrieved September 27, 2021, from http://arxiv.org/abs/2109.10927

Dutta, R., Fumagalli, M., Fossati, M., Lofthouse, E. K., Prochaska, J. X., Arrigoni Battaia, F., Bielby, R. M., Cantalupo, S., Cooke, R. J., Murphy, M. T., & O'Meara, J. M. (2020). MUSE Analysis of Gas around Galaxies (MAGG) – II: Metal-enriched halo gas around z 1 galaxies. *Monthly Notices of the Royal Astronomical Society*, *499*(4), 5022–5046. https://doi.org/10.1093/mnras/staa3147

Dutta, S., Muzahid, S., Schaye, J., Johnson, S., Herenz, E. C., Pessa, I., Augustin, R., Bouché, N. F., Braspenning, J., Cantalupo, S., Das, S., & Wendt, M. (2026, February). MUSEQuBES: Probing Anisotropies in Gas and Metal Distributions in the Circumgalactic Medium [arXiv:2602.17593 [astro-ph]]. https://doi.org/10.48550/arXiv.2602.17593

Erb, D. K., Li, Z., Steidel, C. C., Chen, Y., Gronke, M., Strom, A. L., Trainor, R. F., & Rudie, G. C. (2023). The Circumgalactic Medium of Extreme Emission Line Galaxies at z2: Resolved Spectroscopy and Radiative Transfer Modeling of Spatially Extended Ly Emission in the KBSS-KCWI Survey*. *The Astrophysical Journal*, *953*(1), 118. https://doi.org/10.3847/1538-4357/acd849

Erb, D. K., Quider, A. M., Henry, A. L., & Martin, C. L. (2012). GALACTIC OUTFLOWS IN ABSORPTION AND EMISSION: NEAR-ULTRAVIOLET SPECTROSCOPY OF GALAXIES AT $1 < z < 2$. *The Astrophysical Journal*, *759*(1), 26. https://doi.org/10.1088/0004-637X/759/1/26

Erb, D. K., Steidel, C. C., Shapley, A. E., Pettini, M., Reddy, N. A., & Adelberger, K. L. (2006). The Stellar, Gas, and Dynamical Masses of Star-forming Galaxies at z 2. *The Astrophysical Journal*, *646*(1), 107–132. https://doi.org/10.1086/504891

Faber, J. T., Ravi, V., Ocker, S. K., Sherman, M. B., Sharma, K., Connor, L., Law, C., Kosogorov, N., Hallinan, G., Harnach, C., Hellbourg, G., Hobbs, R., Hodge, D., Hodges, M., Lamb, J. W., Rasmussen, P., Somalwar, J. J., Weinreb, S., & Woody, D. P. (2024, May 23). A heavily scattered fast radio burst is viewed through multiple galaxy halos. https://doi.org/10.48550/arXiv.2405.14182

Faucher-Giguère, C.-A., Kereš, D., & Ma, C.-P. (2011). The baryonic assembly of dark matter haloes: Baryonic halo assembly. *Monthly Notices of the Royal Astronomical Society*, *417*(4), 2982–2999. https://doi.org/10.1111/j.1365-2966.2011.19457.x

Faucher-Giguère, C.-A., & Oh, S. P. (2023). Key Physical Processes in the Circumgalactic Medium. *Annual Review of Astronomy and Astrophysics*, *61*(1), 131–195. https://doi.org/10.1146/annurev-astro-052920-125203

Faucher-Giguère, C.-A., & Quataert, E. (2012). The physics of galactic winds driven by active galactic nuclei: AGN outflow physics. *Monthly Notices of the Royal Astronomical Society*, *425*(1), 605–622. https://doi.org/10.1111/j.1365-2966.2012.21512.x

Finley, H., Bouché, N., Contini, T., Epinat, B., Bacon, R., Brinchmann, J., Cantalupo, S., Erroz-Ferrer, S., Marino, R. A., Maseda, M., Richard, J., Schroetter, I., Verhamme, A., Weilbacher, P. M., Wendt, M., & Wisotzki, L. (2017). Galactic winds with MUSE: A direct detection of Fe ii* emission from a $z = 1.29$ galaxy. *Astronomy & Astrophysics*, *605*, A118. https://doi.org/10.1051/0004-6361/201730428

Fitzpatrick, M., Placco, V., Bolton, A., Merino, B., Ridgway, S., & Stanghellini, L. (2024, January). Modernizing IRAF to Support Gemini Data Reduction [arXiv:2401.01982 [astro-ph]]. Retrieved August 26, 2024, from http://arxiv.org/abs/2401.01982

Foreman-Mackey, D. (2016). Corner.py: Scatterplot matrices in Python. *The Journal of Open Source Software*, *1*(2), 24. https://doi.org/10.21105/joss.00024

Foreman-Mackey, D., Hogg, D. W., Lang, D., & Goodman, J. (2013). Emcee : The MCMC Hammer. *Publications of the Astronomical Society of the Pacific*, *125*(925), 306–312. https://doi.org/10.1086/670067

Freeman, W. R., Siana, B., Kriek, M., Shapley, A. E., Reddy, N., Coil, A. L., Mobasher, B., Muratov, A. L., Azadi, M., Leung, G., Sanders, R., Shivaei, I., Price, S. H., DeGroot, L., & Kereš, D. (2019). The MOSDEF survey: Broad emission lines at z = 1.4–3.8*. *The Astrophysical Journal*, *873*(2), 102. https://doi.org/10.3847/1538-4357/ab0655

Gazagnes, S., Mauerhofer, V., Berg, D. A., Blaizot, J., Verhamme, A., Garel, T., Erb, D. K., Arellano-Córdova, K. Z., Brinchmann, J., Chisholm, J., Hayes, M., Henry, A., James, B. L., Jaskot, A., Jurlin, N., Martin, C. L., Maseda, M., Scarlata, C., Skillman, E. D., . . . Xu, X. (2023). Interpreting the Si II and C II line spectra from the COS Legacy Spectroscopic SurveY using a virtual galaxy from a high-resolution radiation-hydrodynamic simulation [arXiv:2305.19177 [astro-ph]]. *The Astrophysical Journal*, *952*(2), 164. https://doi.org/10.3847/1538-4357/acda2c

Gonçalves, T. S., Steidel, C. C., & Pettini, M. (2008). Detection of the Transverse Proximity Effect: Radiative Feedback from Bright QSOs1. *The*

Astrophysical Journal, *676*(2), 816–835. https://doi.org/10.1086/527313

Hamanowicz, A., Péroux, C., Zwaan, M. A., Rahmani, H., Pettini, M., York, D. G., Klitsch, A., Augustin, R., Krogager, J.-K., Kulkarni, V., Fresco, A., Biggs, A. D., Milliard, B., & Vernet, J. D. R. (2020). MUSE-ALMA haloes V: Physical properties and environment of z 1.4 H i quasar absorbers. *Monthly Notices of the Royal Astronomical Society*, *492*(2), 2347–2368. https://doi.org/10.1093/mnras/stz3590

Hardcastle, M. J., Pierce, J. C. S., Duncan, K. J., Gürkan, G., Gong, Y., Horton, M. A., Mingo, B., Röttgering, H. J. A., & Smith, D. J. B. (2025). Radio AGN selection in LoTSS DR2. *Monthly Notices of the Royal Astronomical Society*, *539*(2), 1856–1878. https://doi.org/10.1093/mnras/staf622

Hardcastle, M. (2018). Interpreting radiative efficiency in radio-loud AGNs. *Nature Astronomy*, *2*(4), 273–274. https://doi.org/10.1038/s41550-018-0424-1

Harris, C. R., Millman, K. J., Van Der Walt, S. J., Gommers, R., Virtanen, P., Cournapeau, D., Wieser, E., Taylor, J., Berg, S., Smith, N. J., Kern, R., Picus, M., Hoyer, S., Van Kerkwijk, M. H., Brett, M., Haldane, A., Del Río, J. F., Wiebe, M., Peterson, P., . . . Oliphant, T. E. (2020). Array programming with NumPy. *Nature*, *585*(7825), 357–362. https://doi.org/10.1038/s41586-020-2649-2

Heckman, T. M. (2002, January). Galactic Superwinds Circa 2001 [_eprint: astro-ph/0107438]. In J. S. Mulchaey & J. T. Stocke (Eds.), *Extragalactic Gas at Low Redshift* (p. 292, Vol. 254).

Heckman, T. M., & Best, P. N. (2023). A Global Inventory of Feedback. *Galaxies*, *11*(1), 21. https://doi.org/10.3390/galaxies11010021

Heckman, T. M., Roy, N., Best, P. N., & Kondapally, R. (2024). Mergers, Radio Jets, and Quenching Star Formation in Massive Galaxies: Quantifying Their Synchronized Cosmic Evolution and Assessing the Energetics. *The Astrophysical Journal*, *977*(1), 125. https://doi.org/10.3847/1538-4357/ad8f3e

Hopkins, P. F. (2025, September). Cosmic Rays on Galaxy Scales: Progress and Pitfalls for CR-MHD Dynamical Models [arXiv:2509.07104 [astro-ph]]. https://doi.org/10.48550/arXiv.2509.07104

Hopkins, P. F., Kereš, D., Oñorbe, J., Faucher-Giguère, C.-A., Quataert, E., Murray, N., & Bullock, J. S. (2014). Galaxies on FIRE (Feedback In Realistic Environments): Stellar feedback explains cosmologically inefficient star formation. *Monthly Notices of the Royal Astronomical Society*, *445*(1), 581–603. https://doi.org/10.1093/mnras/stu1738

Hopkins, P. F., Quataert, E., & Murray, N. (2012). Stellar feedback in galaxies and the origin of galaxy-scale winds: Stellar feedback and galactic winds. *Monthly Notices of the Royal Astronomical Society*, *421*(4), 3522–3537. https://doi.org/10.1111/j.1365-2966.2012.20593.x

Hummels, C. B., Smith, B. D., & Silvia, D. W. (2017). Trident: A Universal Tool for Generating Synthetic Absorption Spectra from Astrophysical Simulations. *The Astrophysical Journal*, *847*(1), 59. https://doi.org/10.3847/1538-4357/aa7e2d

Hunter, J. D. (2007). Matplotlib: A 2D Graphics Environment. *Computing in Science & Engineering*, *9*(3), 90–95. https://doi.org/10.1109/MCSE.2007.55

Inc, P. T. (2015). Collaborative data science [Place: Montreal, QC Publisher: Plotly Technologies Inc.]. https://plot.ly

Jacob, J. C., Katz, D. S., Berriman, G. B., Good, J., Laity, A. C., Deelman, E., Kesselman, C., Singh, G., Su, M.-H., Prince, T. A., & Williams, R. (2010, October). Montage: An Astronomical Image Mosaicking Toolkit [Published: Astrophysics Source Code Library, record ascl:1010.036].

Johnson, S. D., Chen, H.-W., Mulchaey, J. S., Schaye, J., & Straka, L. A. (2017). The Extent of Chemically Enriched Gas around Star-forming Dwarf Galaxies. *The Astrophysical Journal Letters*, *850*(1), L10. https://doi.org/10.3847/2041-8213/aa9370

Jones, T., Stark, D. P., & Ellis, R. S. (2012). KECK SPECTROSCOPY OF FAINT $3 < z < 7$ LYMAN BREAK GALAXIES. III. THE MEAN ULTRAVIOLET SPECTRUM AT z 4. *The Astrophysical Journal*, *751*(1), 51. https://doi.org/10.1088/0004-637X/751/1/51

Kacprzak, G. G., Nielsen, N. M., Nateghi, H., Churchill, C. W., Pointon, S. K., Nanayakkara, T., Muzahid, S., & Charlton, J. C. (2020). Evidence for galaxy quenching in the green valley caused by a lack of a circumgalactic medium. *Monthly Notices of the Royal Astronomical Society*, *500*(2), 2289–2301. https://doi.org/10.1093/mnras/staa3461

Kaiser, C. R., Schoenmakers, A. P., & Rottgering, H. J. A. (2000). Radio galaxies with a 'double-double' morphology–II. The evolution of double-double radio galaxies and implications for the alignment effect in FRII sources. *Monthly Notices of the Royal Astronomical Society*, *315*(2), 381–394. https://doi.org/10.1046/j.1365-8711.2000.03431.x

Keenan, F. P., Cook, J. W., Dufton, P. L., & Kingston, A. E. (1992). Solar SI II line ratios from the high-resolution telescope and spectrograph. *The Astrophysical Journal*, *387*, 726. https://doi.org/10.1086/171121

Kereš, D., Katz, N., Weinberg, D. H., & Davé, R. (2005). How do galaxies get their gas? *Monthly Notices of the Royal Astronomical Society*, *363*(1), 2–28. https://doi.org/10.1111/j.1365-2966.2005.09451.x

Kirkman, D., & Tytler, D. (2008). The transverse proximity effect in the z 2 Lyman forest suggests quasi-stellar object episodic lifetimes of 1 Myr. *Monthly Notices of the Royal Astronomical Society*, *391*(3), 1457–1471. https://doi.org/10.1111/j.1365-2966.2008.13994.x

Kluyver, T., Ragan-Kelley, B., Pérez, F., Granger, B., Bussonnier, M., Frederic, J., Kelley, K., Hamrick, J., Grout, J., Corlay, S., Ivanov, P., Avila, D., Abdalla, S., Willing, C., & team, J. d. (2016). Jupyter Notebooks - a publishing format for reproducible computational workflows. In F. Loizides & B. Scmidt (Eds.), *Positioning and Power in Academic Publishing: Players, Agents and Agendas* (pp. 87–90). IOS Press. https://eprints.soton.ac.uk/403913/

Kornei, K. A., Shapley, A. E., Martin, C. L., Coil, A. L., Lotz, J. M., & Weiner, B. J. (2013). FINE-STRUCTURE Fe II* EMISSION AND RESONANT Mg II EMISSION IN z 1 STAR-FORMING GALAXIES. *The Astrophysical Journal*, *774*(1), 50. https://doi.org/10.1088/0004-637X/774/1/50

Kumar, S., Chen, H.-W., Qu, Z., Chen, M. C., Zahedy, F. S., Johnson, S. D., Muzahid, S., & Cantalupo, S. (2024). On the Nature of the C IV-bearing Circumgalactic Medium at z~1 [arXiv:2408.15824 [astro-ph]]. *The Open Journal of Astrophysics*, *7*. https://doi.org/10.33232/001c.124930

Kusakabe, H., Mauerhofer, V., Verhamme, A., Garel, T., Blaizot, J., Wisotzki, L., Richard, J., Boogaard, L. A., Leclercq, F., Guo, Y., Claeyssens, A., Contini, T., Herenz, E. C., Kerutt, J., Maseda, M. V., Michel-Dansac, L., Nanayakkara, T., Ouchi, M., Pessa, I., & Schaye, J. (2024). The MUSE eXtremely Deep Field: Detections of circumgalactic Si II* emission at z 2. *Astronomy & Astrophysics*, *691*, A255. https://doi.org/10.1051/0004-6361/202451009

Law, D. R., Shapley, A. E., Steidel, C. C., Reddy, N. A., Christensen, C. R., & Erb, D. K. (2012). High velocity dispersion in a rare grand-design spiral galaxy at redshift z = 2.18. *Nature*, *487*(7407), 338–340. https://doi.org/10.1038/nature11256

Le Fèvre, O., Béthermin, M., Faisst, A., Jones, G. C., Capak, P., Cassata, P., Silverman, J. D., Schaerer, D., Yan, L., Amorin, R., Bardelli, S., Boquien, M., Cimatti, A., Dessauges-Zavadsky, M., Giavalisco, M., Hathi, N. P., Fudamoto, Y., Fujimoto, S., Ginolfi, M., . . . Zucca, E. (2020). The ALPINE-ALMA [CII] survey: Survey strategy, observations, and sample properties of 118 star-forming galaxies at $4 < z < 6$. *Astronomy & Astrophysics*, *643*, A1. https://doi.org/10.1051/0004-6361/201936965

Leclercq, F., Bacon, R., Verhamme, A., Garel, T., Blaizot, J., Brinchmann, J., Cantalupo, S., Claeyssens, A., Conseil, S., Contini, T., Hashimoto, T., Herenz, E. C., Kusakabe, H., Marino, R. A., Maseda, M., Matthee, J., Mitchell, P., Pezzulli, G., Richard, J., . . . Wisotzki, L. (2020). The MUSE *Hubble* Ultra Deep Field Survey: XIII. Spatially resolved spectral properties of Lyman haloes around star-forming galaxies at $z > 3$. *Astronomy & Astrophysics*, *635*, A82. https://doi.org/10.1051/0004-6361/201937339

Lehner, N., Howk, J. C., Collins, L., Sameer, Wakker, B. P., Augustin, R., Barger, K. A., Berg, M. A., Bordoloi, R., Brown, T. M., Cashman, F. H., Faucher-Giguère, C.-A., Fox, A. J., French, D. M., Gilbert, K. M., Guhathakurta, P., O'Meara, J. M., O'Shea, B. W., Peeples, M. S., . . . Williams, B. F. (2025, June). Project AMIGA: The Inner Circumgalactic Medium of Andromeda from Thick Disk to Halo [arXiv:2506.16573 [astro-ph]]. https://doi.org/10.48550/arXiv.2506.16573

Leitherer, C., Schaerer, D., Goldader, J. D., Delgado, R. M. G., Robert, C., Kune, D. F., de Mello, D. F., Devost, D., & Heckman, T. M. (1999). Starburst99: Synthesis Models for Galaxies with Active Star Formation. *The Astrophysical Journal Supplement Series*, *123*(1), 3–40. https://doi.org/10.1086/313233

Li, J.-T., Bregman, J. N., Wang, Q. D., Crain, R. A., Anderson, M. E., & Zhang, S. (2017). The circum-galactic medium of massive spirals. II. probing the nature of hot gaseous halo around the most massive isolated spiral galaxies. *The Astrophysical Journal Supplement Series*, *233*(2), 20. https://doi.org/10.3847/1538-4365/aa96fc

Li, Z., & Gronke, M. (2022). Deciphering the Lyman- emission line: Towards the understanding of galactic properties extracted from Ly spectra via radiative transfer modelling. *Monthly Notices of the Royal Astronomical Society*, *513*(4), 5034–5051. https://doi.org/10.1093/mnras/stac1207

Li, Z., Gronke, M., & Steidel, C. C. (2024). ALPACA : A new semi-analytical model for metal absorption lines emerging from clumpy galactic environments. *Monthly Notices of the Royal Astronomical Society*, *529*(1), 444–463. https://doi.org/10.1093/mnras/stae469

Li, Z., Heckman, T., Gronke, M., Xu, X., Henry, A., Schneider, E., Abruzzo, M., Berg, D., James, B., Martin, C., & Chisholm, J. (2026, March). Kinematically Coherent Multiphase Galactic Winds in Star-Forming Galaxies Revealed by Unified Radiative Transfer Modeling of UV Emission and Absorption Lines [arXiv:2603.06546 [astro-ph]]. https://doi.org/10.48550/arXiv.2603.06546

Liang, C. J., & Chen, H.-W. (2014). Mining circumgalactic baryons in the low-redshift universe. *Monthly Notices of the Royal Astronomical Society*, *445*(2), 2061–2081. https://doi.org/10.1093/mnras/stu1901

Lofthouse, E. K., Fumagalli, M., Fossati, M., O'Meara, J. M., Murphy, M. T., Christensen, L., Prochaska, J. X., Cantalupo, S., Bielby, R. M., Cooke, R. J., Lusso, E., & Morris, S. L. (2020). MUSE Analysis of Gas around Galaxies (MAGG) – I: Survey design and the environment of a near pristine gas cloud at z 3.5. *Monthly Notices of the Royal Astronomical Society*, *491*(2), 2057–2074. https://doi.org/10.1093/mnras/stz3066

Lyke, B. W., Higley, A. N., McLane, J. N., Schurhammer, D. P., Myers, A. D., Ross, A. J., Dawson, K., Chabanier, S., Martini, P., Busca, N. G., Mas Des Bourboux, H. D., Salvato, M., Streblyanska, A., Zarrouk, P., Burtin, E., Anderson, S. F., Bautista, J., Bizyaev, D., Brandt, W. N., . . . Weaver, B. A. (2020). The sloan digital sky survey quasar catalog: Sixteenth data release. *The Astrophysical Journal Supplement Series*, *250*(1), 8. https://doi.org/10.3847/1538-4365/aba623

Madau, P., & Dickinson, M. (2014). Cosmic Star-Formation History. *Annual Review of Astronomy and Astrophysics*, *52*(1), 415–486. https://doi.org/10.1146/annurev-astro-081811-125615

Martin, C. L., Ho, S. H., Kacprzak, G. G., & Churchill, C. W. (2019). Kinematics of Circumgalactic Gas: Feeding Galaxies and Feedback. *The Astrophysical Journal*, *878*(2), 84. https://doi.org/10.3847/1538-4357/ab18ac

Martin, C. L., Shapley, A. E., Coil, A. L., Kornei, K. A., Bundy, K., Weiner, B. J., Noeske, K. G., & Schiminovich, D. (2012). DEMOGRAPHICS AND PHYSICAL PROPERTIES OF GAS OUTFLOWS/INFLOWS AT $0.4 < z < 1.4$. *The Astrophysical Journal*, *760*(2), 127. https://doi.org/10.1088/0004-637X/760/2/127

McKerns, M. M., Strand, L., Sullivan, T., Fang, A., & Aivazis, M. A. G. (2012, February). Building a Framework for Predictive Science [arXiv:1202.1056 [cs]]. Retrieved August 26, 2024, from http://arxiv.org/abs/1202.1056

McLean, I. S., Steidel, C. C., Epps, H. W., Konidaris, N., Matthews, K. Y., Adkins, S., Aliado, T., Brims, G., Canfield, J. M., Cromer, J. L., Fucik, J., Kulas, K., Mace, G., Magnone, K., Rodriguez, H., Rudie, G., Trainor, R., Wang, E., Weber, B., & Weiss, J. (2012, September). MOSFIRE, the multi-object spectrometer for infra-red exploration at the Keck Observatory. In I. S. McLean, S. K. Ramsay, & H. Takami (Eds.), *Ground-based and airborne instrumentation for astronomy iv* (84460J, Vol. 8446). https://doi.org/10.1117/12.924794

Méndez-Hernández, H., Cassata, P., Ibar, E., Amorín, R., Aravena, M., Bardelli, S., Cucciati, O., Garilli, B., Giavalisco, M., Guaita, L., Hathi, N., Koekemoer, A., Le Brun, V., Lemaux, B. C., Maccagni, D., Ribeiro, B., Tasca, L., Tejos, N., Thomas, R., . . . Zucca, E. (2022). Metal content of the circumgalactic medium around star-forming galaxies at z 2.6 as revealed by the VIMOS Ultra-Deep Survey. *Astronomy & Astrophysics*, *666*, A56. https://doi.org/10.1051/0004-6361/202142553

Mernier, F., Biffi, V., Yamaguchi, H., Medvedev, P., Simionescu, A., Ettori, S., Werner, N., Kaastra, J. S., Plaa, J. d., & Gu, L. (2018). Enrichment of the hot intracluster medium: Observations [arXiv:1811.01967 [astro-ph]]. *Space Science Reviews*, *214*(8), 129. https://doi.org/10.1007/s11214-018-0565-7

Morrissey, P., Matuszewski, M., Martin, D. C., Neill, J. D., Epps, H., Fucik, J., Weber, B., Darvish, B., Adkins, S., Allen, S., Bartos, R., Belicki, J., Cabak, J., Callahan, S., Cowley, D., Crabill, M., Deich, W., Delecroix, A., Doppman, G., . . . Zarzaca, R. (2018). The Keck Cosmic Web Imager Integral Field Spectrograph. *The Astrophysical Journal*, *864*(1), 93. https://doi.org/10.3847/1538-4357/aad597

Mostert, R. I. J., Oei, M. S. S. L., Barkus, B., Alegre, L., Hardcastle, M. J., Duncan, K. J., Röttgering, H. J. A., Van Weeren, R. J., & Horton, M. (2024). Constraining the giant radio galaxy population with machine learning and Bayesian inference. *Astronomy & Astrophysics*, *691*, A185. https://doi.org/10.1051/0004-6361/202348897

Münch, G., & Zirin, H. (1961). Interstellar Matter at Large Distances from the Galactic Plane., *133*, 11. https://doi.org/10.1086/146999

Murray, N., Ménard, B., & Thompson, T. A. (2011). RADIATION PRESSURE FROM MASSIVE STAR CLUSTERS AS A LAUNCHING MECHANISM FOR SUPER-GALACTIC WINDS. *The Astrophysical Journal*, *735*(1), 66. https://doi.org/10.1088/0004-637X/735/1/66

Muzahid, S., Schaye, J., Cantalupo, S., Marino, R. A., Bouché, N. F., Johnson, S., Maseda, M., Wendt, M., Wisotzki, L., & Zabl, J. (2021). MUSE-QuBES: Characterizing the circumgalactic medium of redshift 3.3 Ly emitters. *Monthly Notices of the Royal Astronomical Society*, *508*(4), 5612–5637. https://doi.org/10.1093/mnras/stab2933

National Optical Astronomy Observatories. (1999, November). IRAF: Image Reduction and Analysis Facility [Published: Astrophysics Source Code Library, record ascl:9911.002].

Navarro, J. F., Frenk, C. S., & White, S. D. M. (1996). The Structure of Cold Dark Matter Halos [_eprint: astro-ph/9508025]., *462*, 563. https://doi.org/10.1086/177173

Navarro, J. F., Frenk, C. S., & White, S. D. M. (1997). A Universal Density Profile from Hierarchical Clustering [_eprint: astro-ph/9611107]., *490*(2), 493–508. https://doi.org/10.1086/304888

Neill, D., Matuszewski, M., & Martin, C. (2023, January). Kderp: Keck Cosmic Web Imager Data Extraction and Reduction Pipeline in IDL [Published: Astrophysics Source Code Library, record ascl:2301.018].

Neill, D., Matuszewski, M., Martin, C., Brodheim, M., & Rizzi, L. (2023, January). KCWI_drp: Keck Cosmic Web Imager Data Reduction Pipeline in Python [_eprint: 2301.019 Published: Astrophysics Source Code Library, record ascl:2301.019].

Oei, M. S. S. L., Hardcastle, M. J., Timmerman, R., Gast, A. R. D. J. G. I. B., Botteon, A., Rodriguez, A. C., Stern, D., Calistro Rivera, G., Van Weeren, R. J., Röttgering, H. J. A., Intema, H. T., De Gasperin, F., & Djorgovski, S. G. (2024). Black hole jets on the scale of the cosmic web. *Nature*, *633*(8030), 537–541. https://doi.org/10.1038/s41586-024-07879-y

Oei, M. S. S. L., Van Weeren, R. J., Hardcastle, M. J., Gast, A. R. D. J. G. I. B., Leclercq, F., Röttgering, H. J. A., Dabhade, P., Shimwell, T. W., & Botteon, A. (2024). Luminous giants populate the dense Cosmic Web: The radio luminosity–environmental density relation for radio galaxies in action. *Astronomy & Astrophysics*, *686*, A137. https://doi.org/10.1051/0004-6361/202347115

Ott, T. (2012, October). QFitsView: FITS file viewer [_eprint: 1210.019 Published: Astrophysics Source Code Library, record ascl:1210.019].

Peeples, M. S., Werk, J. K., Tumlinson, J., Oppenheimer, B. D., Prochaska, J. X., Katz, N., & Weinberg, D. H. (2014). A BUDGET AND ACCOUNTING OF METALS AT z 0: RESULTS FROM THE COS-HALOS SURVEY. *The Astrophysical Journal*, *786*(1), 54. https://doi.org/10.1088/0004-637X/786/1/54

Peng, Z., Martin, C. L., Huang, J., Prusinski, N. Z., Huang, C., Zhuang, Z., Li, Y., Wong, T. L. S., Yang, J., & Hennawi, J. F. (2026). When Stars Mimic Monsters: Spectral Evidence for an η Carinae−like Giant Eruption in SBS 0335−052 E., *1001*(2), Article 218, 218. https://doi.org/10.3847/1538-4357/ae589b

Perez, F., & Granger, B. E. (2007). IPython: A System for Interactive Scientific Computing. *Computing in Science & Engineering*, *9*(3), 21–29. https://doi.org/10.1109/MCSE.2007.53

Péroux, C., & Howk, J. C. (2020). The Cosmic Baryon and Metal Cycles. *Annual Review of Astronomy and Astrophysics*, *58*(1), 363–406. https://doi.org/10.1146/annurev-astro-021820-120014

Péroux, C., Nelson, D., van de Voort, F., Pillepich, A., Marinacci, F., Vogelsberger, M., & Hernquist, L. (2020). Predictions for the angular dependence of gas mass flow rate and metallicity in the circumgalactic medium. *Monthly Notices of the Royal Astronomical Society*, *499*(2), 2462–2473. https://doi.org/10.1093/mnras/staa2888

Perucho, M., Martí, J. M., Laing, R. A., & Hardee, P. E. (2014). On the deceleration of Fanaroff–Riley Class I jets: Mass loading by stellar winds. *Monthly Notices of the Royal Astronomical Society*, *441*(2), 1488–1503. https://doi.org/10.1093/mnras/stu676

Planck Collaboration, Aghanim, N., Akrami, Y., Ashdown, M., Aumont, J., Baccigalupi, C., Ballardini, M., Banday, A. J., Barreiro, R. B., Bartolo, N., Basak, S., Battye, R., Benabed, K., Bernard, J.-P., Bersanelli, M., Bielewicz, P., Bock, J. J., Bond, J. R., Borrill, J., . . . Zonca, A. (2020). *Planck* 2018 results: VI. Cosmological parameters. *Astronomy & Astrophysics*, *641*, A6. https://doi.org/10.1051/0004-6361/201833910

Pointon, S. K., Kacprzak, G. G., Nielsen, N. M., Muzahid, S., Murphy, M. T., Churchill, C. W., & Charlton, J. C. (2019). Relationship between the Metallicity of the Circumgalactic Medium and Galaxy Orientation. *The Astrophysical Journal*, *883*(1), 78. https://doi.org/10.3847/1538-4357/ab3b0e

Prochaska, J. X., Kasen, D., & Rubin, K. (2011). SIMPLE MODELS OF METAL-LINE ABSORPTION AND EMISSION FROM COOL GAS OUTFLOWS. *The Astrophysical Journal*, *734*(1), 24. https://doi.org/10.1088/0004-637X/734/1/24

Prochaska, J. X., Lau, M. W., & Hennawi, J. F. (2014). QUASARS PROBING QUASARS. VII. THE PINNACLE OF THE COOL CIRCUMGALACTIC MEDIUM SURROUNDS MASSIVE z 2 GALAXIES. *The Astrophysical Journal*, *796*(2), 140. https://doi.org/10.1088/0004-637X/796/2/140

Prochaska, J. X., Weiner, B., Chen, H.-W., Mulchaey, J., & Cooksey, K. (2011). PROBING THE INTERGALACTIC MEDIUM/GALAXY CONNECTION. V. ON THE ORIGIN OF Ly AND O VI ABSORPTION AT z < 0.2. *The Astrophysical Journal*, *740*(2), 91. https://doi.org/10.1088/0004-637X/740/2/91

Prusinski, N. Z., & Chen, Y. (2024, April). KCWIKit: KCWI Post-Processing and Improvements [Published: Astrophysics Source Code Library, record ascl:2404.003].

Prusinski, N. Z., Erb, D. K., & Martin, C. L. (2021). Connecting Galactic Outflows and Star Formation: Inferences from H Maps and Absorption-line Spectroscopy at 1 z 1.5* †. *The Astronomical Journal*, *161*(5), 212. https://doi.org/10.3847/1538-3881/abe85b

Prusinski, N. Z., Steidel, C. C., & Chen, Y. (2025, September). Mapping the $z\sim 2$ Circumgalactic Medium using KBSS Galaxy Pairs [arXiv:2503.20037 [astro-ph]]. https://doi.org/10.48550/arXiv.2503.20037

Rauch, M., Sargent, W. L. W., & Barlow, T. A. (2001). Small-Scale Structure at High Redshift. II. Physical Properties of the C IV Absorbing Clouds [_eprint: astro-ph/0104216]., *554*(2), 823–840. https://doi.org/10.1086/321402

Ravi, V. (2019). Measuring the circumgalactic and intergalactic baryon contents with fast radio bursts. *The Astrophysical Journal*, *872*(1), 88. https://doi.org/10.3847/1538-4357/aafb30

Reddy, N. A., Steidel, C. C., Erb, D. K., Shapley, A. E., & Pettini, M. (2006). A Spectroscopic Survey of Redshift 1.4<\raisebox-0.5ex\textasciitildez<\raisebox-0.5ex\textasciitilde3.0 Galaxies in the GOODS-North Field: Survey Description, Catalogs, and Properties [_eprint: astro-ph/0609296]., *653*(2), 1004–1026. https://doi.org/10.1086/508851

Richards, G. T., Strauss, M. A., Fan, X., Hall, P. B., Jester, S., Schneider, D. P., Vanden Berk, D. E., Stoughton, C., Anderson, S. F., Brunner, R. J., Gray, J., Gunn, J. E., Ivezić, Ž., Kirkland, M. K., Knapp, G. R., Loveday, J., Meiksin, A., Pope, A., Szalay, A. S., . . . Snedden, S. A. (2006). The Sloan Digital Sky Survey Quasar Survey: Quasar Luminosity Function from Data Release 3. *The Astronomical Journal*, *131*(6), 2766–2787. https://doi.org/10.1086/503559

Rix, S. A., Pettini, M., Leitherer, C., Bresolin, F., Kudritzki, R.-P., & Steidel, C. C. (2004). Spectral Modeling of Star-forming Regions in the Ultraviolet: Stellar Metallicity Diagnostics for High-Redshift Galaxies. *The Astrophysical Journal*, *615*(1), 98–117. https://doi.org/10.1086/424031

Robitaille, T., Conseil, S., Sipőcz, B., McCully, C., Tollerud, E., Droettboom, M., Lim, P. L., Bradley, L., Bray, E. M., Craig, M., Deil, C., Price-Whelan, A., Barbary, K., Ginsburg, A., Robert, C., Kerzendorf, W., Gupta, A., D'Avella, D., Burke, D., . . . Günther, H. M. (2025, October). *Astropy/astroscrappy: V1.3.0* (Version v1.3.0). Zenodo. https://doi.org/10.5281/zenodo.17495347

Rubin, K. H. R., Diamond-Stanic, A. M., Coil, A. L., Crighton, N. H. M., & Moustakas, J. (2018). Galaxies Probing Galaxies in PRIMUS. I. Sample, Spectroscopy, and Characteristics of the Mg II–absorbing Circumgalactic Medium. *The Astrophysical Journal*, *853*(1), 95. https://doi.org/10.3847/1538-4357/aa9792

Rubin, K. H. R., Diamond-Stanic, A. M., Coil, A. L., Crighton, N. H. M., & Stewart, K. R. (2018). Galaxies Probing Galaxies in PRIMUS. II. The Coherence Scale of the Cool Circumgalactic Medium. *The Astrophysical Journal*, *868*(2), 142. https://doi.org/10.3847/1538-4357/aad566

Rubin, K. H. R., Prochaska, J. X., Ménard, B., Murray, N., Kasen, D., Koo, D. C., & Phillips, A. C. (2011). LOW-IONIZATION LINE EMISSION FROM A STARBURST GALAXY: A NEW PROBE OF A GALACTIC-

SCALE OUTFLOW. *The Astrophysical Journal*, *728*(1), 55. https://doi.org/10.1088/0004-637X/728/1/55

Rubin, K. H. R., Xavier Prochaska, J., Koo, D. C., & Phillips, A. C. (2012). THE DIRECT DETECTION OF COOL, METAL-ENRICHED GAS ACCRETION ONTO GALAXIES AT z 0.5. *The Astrophysical Journal*, *747*(2), L26. https://doi.org/10.1088/2041-8205/747/2/L26

Rudie, G. C., Steidel, C. C., Pettini, M., Trainor, R. F., Strom, A. L., Hummels, C. B., Reddy, N. A., & Shapley, A. E. (2019). Column Density, Kinematics, and Thermal State of Metal-bearing Gas within the Virial Radius of z 2 Star-forming Galaxies in the Keck Baryonic Structure Survey. *The Astrophysical Journal*, *885*(1), 61. https://doi.org/10.3847/1538-4357/ab4255

Rudie, G. C., Steidel, C. C., Trainor, R. F., Rakic, O., Bogosavljević, M., Pettini, M., Reddy, N., Shapley, A. E., Erb, D. K., & Law, D. R. (2012). THE GASEOUS ENVIRONMENT OF HIGH- z GALAXIES: PRECISION MEASUREMENTS OF NEUTRAL HYDROGEN IN THE CIRCUMGALACTIC MEDIUM OF z 2-3 GALAXIES IN THE KECK BARYONIC STRUCTURE SURVEY. *The Astrophysical Journal*, *750*(1), 67. https://doi.org/10.1088/0004-637X/750/1/67

Savage, B. D., & Sembach, K. R. (1991). The analysis of apparent optical depth profiles for interstellar absorption lines. *The Astrophysical Journal*, *379*, 245. https://doi.org/10.1086/170498

Scarlata, C., & Panagia, N. (2015). A SEMI-ANALYTICAL LINE TRANSFER MODEL TO INTERPRET THE SPECTRA OF GALAXY OUTFLOWS. *The Astrophysical Journal*, *801*(1), 43. https://doi.org/10.1088/0004-637X/801/1/43

Schaye, J., Chaikin, E., Schaller, M., Ploeckinger, S., Huško, F., McGibbon, R. J., Trayford, J. W., Benítez-Llambay, A., Correa, C., Frenk, C. S., Richings, A. J., Forouhar Moreno, V. J., Bahé, Y. M., Borrow, J., Durrant, A., Gebek, A., Helly, J. C., Jenkins, A., Lacey, C. G., . . . Nobels, F. S. J. (2026). The COLIBRE project: Cosmological hydrodynamical simulations of galaxy formation and evolution. *Monthly Notices of the Royal Astronomical Society*, *548*(1), stag375. https://doi.org/10.1093/mnras/stag375

Schirber, M., Miralda-Escude, J., & McDonald, P. (2004). The Transverse Proximity Effect: A Probe to the Environment, Anisotropy, and Megayear Variability of QSOs. *The Astrophysical Journal*, *610*(1), 105–116. https://doi.org/10.1086/421451

Shapley, A. E., Steidel, C. C., & Pettini, M. (2003). REST-FRAME ULTRAVIOLET SPECTRA OF z $ 3 LYMAN BREAK GALAXIES. *588*(1).

Shimwell, T. W., Röttgering, H. J. A., Best, P. N., Williams, W. L., Dijkema, T. J., de Gasperin, F., Hardcastle, M. J., Heald, G. H., Hoang, D. N., Horneffer, A., Intema, H., Mahony, E. K., Mandal, S., Mechev, A. P., Morabito, L., Oonk, J. B. R., Rafferty, D., Retana-Montenegro, E., Sabater, J., . . . Zwart, J. T. L. (2017). The LOFAR Two-metre Sky Survey. I. Survey description and preliminary data release., *598*, Article A104, A104. https://doi.org/10.1051/0004-6361/201629313

Shull, J. M., Smith, B. D., & Danforth, C. W. (2012). THE BARYON CENSUS IN A MULTIPHASE INTERGALACTIC MEDIUM: 30% OF THE BARYONS MAY STILL BE MISSING. *The Astrophysical Journal*, *759*(1), 23. https://doi.org/10.1088/0004-637X/759/1/23

Siegel, J., Amon, A., McCarthy, I. G., Bigwood, L., Yamamoto, M., Bulbul, E., Greene, J. E., McCullough, J., Schaller, M., & Schaye, J. (2025, September). Joint X-ray, kinetic Sunyaev-Zeldovich, and weak lensing measurements: Toward a consensus picture of efficient gas expulsion from groups and clusters [arXiv:2509.10455 [astro-ph]]. https://doi.org/10.48550/arXiv.2509.10455

Silk, J., & Rees, M. J. (1998). Quasars and galaxy formation [_eprint: astro-ph/9801013]. *Astronomy & Astrophysics*, *331*, L1–L4. https://doi.org/10.48550/arXiv.astro-ph/9801013

Simionescu, A., Ettori, S., Werner, N., Nagai, D., Vazza, F., Akamatsu, H., Pinto, C., De Plaa, J., Wijers, N., Nelson, D., Pointecouteau, E., Pratt, G. W., Spiga, D., Vacanti, G., Lau, E., Rossetti, M., Gastaldello, F., Biffi, V., Bulbul, E., . . . Werk, J. (2021). Voyage through the hidden physics of the cosmic web. *Experimental Astronomy*, *51*(3), 1043–1079. https://doi.org/10.1007/s10686-021-09720-0

Soto, K. T., Lilly, S. J., Bacon, R., Richard, J., & Conseil, S. (2016). ZAP - enhanced PCA sky subtraction for integral field spectroscopy., *458*(3), 3210–3220. https://doi.org/10.1093/mnras/stw474

Spitzer, L., Jr. (1956). On a Possible Interstellar Galactic Corona., *124*, 20. https://doi.org/10.1086/146200

Sravan, N., Faucher-Giguère, C.-A., van de Voort, F., Kereš, D., Muratov, A. L., Hopkins, P. F., Feldmann, R., Quataert, E., & Murray, N. (2016). Strongly time-variable ultraviolet metal-line emission from the circumgalactic medium of high-redshift galaxies. *Monthly Notices of the Royal Astronomical Society*, *463*(1), 120–133. https://doi.org/10.1093/mnras/stw1962

Stanway, E. R., & Eldridge, J. J. (2018). Re-evaluating old stellar populations. *Monthly Notices of the Royal Astronomical Society*, *479*(1), 75–93. https://doi.org/10.1093/mnras/sty1353

Steidel, C. C., Adelberger, K. L., Shapley, A. E., Pettini, M., Dickinson, M., & Giavalisco, M. (2003). Lyman Break Galaxies at Redshift z 3: Survey Description and Full Data Set. *The Astrophysical Journal*, *592*(2), 728–754. https://doi.org/10.1086/375772

Steidel, C. C., Bogosavljević, M., Shapley, A. E., Kollmeier, J. A., Reddy, N. A., Erb, D. K., & Pettini, M. (2011). DIFFUSE Ly EMITTING HALOS: A GENERIC PROPERTY OF HIGH-REDSHIFT STAR-FORMING GALAXIES. *The Astrophysical Journal*, *736*(2), 160. https://doi.org/10.1088/0004-637X/736/2/160

Steidel, C. C., Bogosavljević, M., Shapley, A. E., Reddy, N. A., Rudie, G. C., Pettini, M., Trainor, R. F., & Strom, A. L. (2018). The Keck Lyman Continuum Spectroscopic Survey (KLCS): The Emergent Ionizing Spectrum of Galaxies at z 3. *The Astrophysical Journal*, *869*(2), 123. https://doi.org/10.3847/1538-4357/aaed28

Steidel, C. C., Erb, D. K., Shapley, A. E., Pettini, M., Reddy, N., Bogosavljević, M., Rudie, G. C., & Rakic, O. (2010). THE STRUCTURE AND KINEMATICS OF THE CIRCUMGALACTIC MEDIUM FROM FAR-ULTRAVIOLET SPECTRA OF z 2-3 GALAXIES. *The Astrophysical Journal*, *717*(1), 289–322. https://doi.org/10.1088/0004-637X/717/1/289

Steidel, C. C., Rudie, G. C., Strom, A. L., Pettini, M., Reddy, N. A., Shapley, A. E., Trainor, R. F., Erb, D. K., Turner, M. L., Konidaris, N. P., Kulas, K. R., Mace, G., Matthews, K., & McLean, I. S. (2014). STRONG NEBULAR LINE RATIOS IN THE SPECTRA of z 2-3 STAR FORMING GALAXIES: FIRST RESULTS FROM KBSS-MOSFIRE. *The Astrophysical Journal*, *795*(2), 165. https://doi.org/10.1088/0004-637X/795/2/165

Steidel, C. C., Shapley, A. E., Pettini, M., Adelberger, K. L., Erb, D. K., Reddy, N. A., & Hunt, M. P. (2004). A Survey of Star-forming Galaxies in the 1.4<\raisebox-0.5ex\textasciitildeZ<\raisebox-0.5ex\textasciitilde 2.5 Redshift Desert: Overview [_eprint: astro-ph/0401439]., *604*(2), 534–550. https://doi.org/10.1086/381960

Steidel, C. C., Strom, A. L., Pettini, M., Rudie, G. C., Reddy, N. A., & Trainor, R. F. (2016). RECONCILING THE STELLAR AND NEBULAR SPECTRA OF HIGH-REDSHIFT GALAXIES. *The Astrophysical Journal*, *826*(2), 159. https://doi.org/10.3847/0004-637X/826/2/159

Stimpson, M., Hardcastle, M. J., & Krause, M. G. H. (2023). Numerical modelling of the lobes of radio galaxies – Paper V: Universal pressure profile cluster atmospheres. *Monthly Notices of the Royal Astronomical Society*, *526*(3), 3421–3440. https://doi.org/10.1093/mnras/stad2933

Strom, A. L., Steidel, C. C., Rudie, G. C., Trainor, R. F., & Pettini, M. (2018). Measuring the Physical Conditions in High-redshift Star-forming Galaxies: Insights from KBSS-MOSFIRE. *The Astrophysical Journal*, *868*(2), 117. https://doi.org/10.3847/1538-4357/aae1a5

Strom, A. L., Steidel, C. C., Rudie, G. C., Trainor, R. F., Pettini, M., & Reddy, N. A. (2017). Nebular Emission Line Ratios in z 2–3 Star-forming Galaxies with KBSS-MOSFIRE: Exploring the Impact of Ionization, Excitation, and Nitrogen-to-Oxygen Ratio. *The Astrophysical Journal*, *836*(2), 164. https://doi.org/10.3847/1538-4357/836/2/164

Tang, Y., Giavalisco, M., Guo, Y., & Kurk, J. (2014). PROBING OUTFLOWS IN $z = 1$ 2 GALAXIES THROUGH Fe II/Fe II* MULTIPLETS. *The Astrophysical Journal*, *793*(2), 92. https://doi.org/10.1088/0004-637X/793/2/92

The Astropy Collaboration, Price-Whelan, A. M., Sipőcz, B. M., Günther, H. M., Lim, P. L., Crawford, S. M., Conseil, S., Shupe, D. L., Craig, M. W., Dencheva, N., Ginsburg, A., VanderPlas, J. T., Bradley, L. D., Pérez-Suárez, D., de Val-Borro, M., (Primary Paper Contributors), Aldcroft, T. L., Cruz, K. L., Robitaille, T. P., . . . (Astropy Contributors). (2018). The Astropy Project: Building an Open-science Project and Status of the v2.0 Core Package. *The Astronomical Journal*, *156*(3), 123. https://doi.org/10.3847/1538-3881/aabc4f

The Astropy Collaboration, Price-Whelan, A. M., Lim, P. L., Earl, N., Starkman, N., Bradley, L., Shupe, D. L., Patil, A. A., Corrales, L., Brasseur, C. E., Nöthe, M., Donath, A., Tollerud, E., Morris, B. M., Ginsburg, A., Vaher, E., Weaver, B. A., Tocknell, J., Jamieson, W., . . . Astropy Project Contributors. (2022). The Astropy Project: Sustaining and Growing a Community-oriented Open-source Project and the Latest Major Release (v5.0) of the Core Package*. *The Astrophysical Journal*, *935*(2), 167. https://doi.org/10.3847/1538-4357/ac7c74

The Astropy Collaboration, Robitaille, T. P., Tollerud, E. J., Greenfield, P., Droettboom, M., Bray, E., Aldcroft, T., Davis, M., Ginsburg, A., Price-Whelan, A. M., Kerzendorf, W. E., Conley, A., Crighton, N., Barbary, K., Muna, D., Ferguson, H., Grollier, F., Parikh, M. M., Nair, P. H., . . . Streicher, O. (2013). Astropy: A community Python package for astronomy. *Astronomy & Astrophysics*, *558*, A33. https://doi.org/10.1051/0004-6361/201322068

Theios, R. L., Steidel, C. C., Strom, A. L., Rudie, G. C., Trainor, R. F., & Reddy, N. A. (2019). Dust Attenuation, Star Formation, and Metallicity in z 2–3 Galaxies from KBSS-MOSFIRE. *The Astrophysical Journal*, *871*(1), 128. https://doi.org/10.3847/1538-4357/aaf386

Tody, D. (1986, January). The IRAF Data Reduction and Analysis System. In D. L. Crawford (Ed.), *Instrumentation in astronomy VI* (p. 733, Vol. 627). https://doi.org/10.1117/12.968154

Tody, D. (1993, January). IRAF in the Nineties. In R. J. Hanisch, R. J. V. Brissenden, & J. Barnes (Eds.), *Astronomical Data Analysis Software and Systems II* (p. 173, Vol. 52).

Trainor, R., & Steidel, C. C. (2013). CONSTRAINTS ON HYPERLUMINOUS QSO LIFETIMES VIA FLUORESCENT Ly EMITTERS AT Z 2.7. *The Astrophysical Journal*, *775*(1), L3. https://doi.org/10.1088/2041-8205/775/1/L3

Trainor, R. F., & Steidel, C. C. (2012). THE HALO MASSES AND GALAXY ENVIRONMENTS OF HYPERLUMINOUS QSOs AT *z* 2.7 IN THE KECK BARYONIC STRUCTURE SURVEY. *The Astrophysical Journal*, *752*(1), 39. https://doi.org/10.1088/0004-637X/752/1/39

Trainor, R. F., Steidel, C. C., Strom, A. L., & Rudie, G. C. (2015). THE SPECTROSCOPIC PROPERTIES OF Ly -EMITTERS AT *z* 2.7: ESCAPING GAS AND PHOTONS FROM FAINT GALAXIES. *The Astrophysical Journal*, *809*(1), 89. https://doi.org/10.1088/0004-637X/809/1/89

Tumlinson, J., Peeples, M. S., & Werk, J. K. (2017). The Circumgalactic Medium. *Annual Review of Astronomy and Astrophysics*, *55*(1), 389–432. https://doi.org/10.1146/annurev-astro-091916-055240

Turk, M. J., Smith, B. D., Oishi, J. S., Skory, S., Skillman, S. W., Abel, T., & Norman, M. L. (2011). Yt: A MULTI-CODE ANALYSIS TOOLKIT FOR ASTROPHYSICAL SIMULATION DATA. *The Astrophysical Journal Supplement Series*, *192*(1), 9. https://doi.org/10.1088/0067-0049/192/1/9

Turner, M. L., Schaye, J., Steidel, C. C., Rudie, G. C., & Strom, A. L. (2014). Metal-line absorption around z 2.4 star-forming galaxies in the Keck Baryonic Structure Survey. *Monthly Notices of the Royal Astronomical Society*, *445*(1), 794–822. https://doi.org/10.1093/mnras/stu1801

van Dokkum, P. G. (2001). Cosmic-Ray Rejection by Laplacian Edge Detection. *Publications of the Astronomical Society of the Pacific*, *113*(789), 1420–1427. https://doi.org/10.1086/323894

Van Der Walt, S., Schönberger, J. L., Nunez-Iglesias, J., Boulogne, F., Warner, J. D., Yager, N., Gouillart, E., & Yu, T. (2014). Scikit-image: Image processing in Python. *PeerJ*, *2*, e453. https://doi.org/10.7717/peerj.453

Van Weeren, R. J., Röttgering, H. J. A., Bagchi, J., Raychaudhury, S., Intema, H. T., Miniati, F., Enßlin, T. A., Markevitch, M., & Erben, T. (2009). Radio observations of ZwCl 2341.1+0000: A double radio relic cluster.

Astronomy & Astrophysics, *506*(3), 1083–1094. https://doi.org/10.1051/0004-6361/200912287

Veilleux, S., Cecil, G., & Bland-Hawthorn, J. (2005). Galactic Winds. *Annual Review of Astronomy and Astrophysics*, *43*(1), 769–826. https://doi.org/10.1146/annurev.astro.43.072103.150610

Veilleux, S., Maiolino, R., Bolatto, A. D., & Aalto, S. (2020). Cool outflows in galaxies and their implications. *The Astronomy and Astrophysics Review*, *28*(1), 2. https://doi.org/10.1007/s00159-019-0121-9

Virtanen, P., Gommers, R., Oliphant, T. E., Haberland, M., Reddy, T., Cournapeau, D., Burovski, E., Peterson, P., Weckesser, W., Bright, J., Van Der Walt, S. J., Brett, M., Wilson, J., Millman, K. J., Mayorov, N., Nelson, A. R. J., Jones, E., Kern, R., Larson, E., . . . Vázquez-Baeza, Y. (2020). SciPy 1.0: Fundamental algorithms for scientific computing in Python. *Nature Methods*, *17*(3), 261–272. https://doi.org/10.1038/s41592-019-0686-2

Wang, B., Heckman, T. M., Zhu, G., & Norman, C. A. (2020). A Systematic Study of Galactic Outflows via Fluorescence Emission: Implications for Their Size and Structure. *The Astrophysical Journal*, *894*(2), 149. https://doi.org/10.3847/1538-4357/ab88b4

Wang, W., Cantalupo, S., Pensabene, A., Galbiati, M., Travascio, A., Steidel, C. C., Maseda, M. V., Pezzulli, G., De Beer, S., Fossati, M., Fumagalli, M., Gallego, S. G., Lazeyras, T., Mackenzie, R., Matthee, J., Nanayakkara, T., & Quadri, G. (2025). A giant disk galaxy two billion years after the Big Bang. *Nature Astronomy*, *9*(5), 710–719. https://doi.org/10.1038/s41550-025-02500-2

Waskom, M. (2021). Seaborn: Statistical data visualization. *Journal of Open Source Software*, *6*(60), 3021. https://doi.org/10.21105/joss.03021

Weiner, B. J., Coil, A. L., Prochaska, J. X., Newman, J. A., Cooper, M. C., Bundy, K., Conselice, C. J., Dutton, A. A., Faber, S. M., Koo, D. C., Lotz, J. M., Rieke, G. H., & Rubin, K. H. R. (2009). Ubiquitous outflows in DEEP2 spectra of star-forming galaxies at z=1.4 [arXiv: 0804.4686]. *The Astrophysical Journal*, *692*(1), 187–211. https://doi.org/10.1088/0004-637X/692/1/187

Weldon, A., Reddy, N., Topping, M., Shapley, A., Sanders, R., Du, X., Price, S., Coil, A., Siana, B., Mobasher, B., Fetherolf, T., Shivaei, I., & Rezaee, S. (2022). The MOSDEF-LRIS Survey: Connection between Galactic-scale Outflows and the Properties of z~2 star-forming Galaxies [arXiv: 2203.09539]. *arXiv:2203.09539 [astro-ph]*. Retrieved March 21, 2022, from http://arxiv.org/abs/2203.09539

Werk, J. K., Prochaska, J. X., Thom, C., Tumlinson, J., Tripp, T. M., O'Meara, J. M., & Meiring, J. D. (2012). THE COS-HALOS SURVEY: KECK LRIS AND MAGELLAN MagE OPTICAL SPECTROSCOPY. *The Astrophysical Journal Supplement Series*, *198*(1), 3. https://doi.org/10.1088/0067-0049/198/1/3

Werk, J. K., Prochaska, J. X., Thom, C., Tumlinson, J., Tripp, T. M., O'Meara, J. M., & Peeples, M. S. (2013). THE COS-HALOS SURVEY: AN EMPIRICAL DESCRIPTION OF METAL-LINE ABSORPTION IN THE LOW-REDSHIFT CIRCUMGALACTIC MEDIUM. *The Astrophysical Journal Supplement Series*, *204*(2), 17. https://doi.org/10.1088/0067-0049/204/2/17

Whitehead, H. W., & Matthews, J. H. (2023). Studying the link between radio galaxies and AGN fuelling with relativistic hydrodynamic simulations of flickering jets. *Monthly Notices of the Royal Astronomical Society*, *523*(2), 2478–2497. https://doi.org/10.1093/mnras/stad1582

Wilde, M. C., Werk, J. K., Burchett, J. N., Prochaska, J. X., Tchernyshyov, K., Tripp, T. M., Tejos, N., Lehner, N., Bordoloi, R., O'Meara, J. M., & Tumlinson, J. (2021). CGM^2 I: The Extent of the Circumgalactic Medium Traced by Neutral Hydrogen. *The Astrophysical Journal*, *912*(1), 9. https://doi.org/10.3847/1538-4357/abea14

Wisotzki, L., Bacon, R., Blaizot, J., Brinchmann, J., Herenz, E. C., Schaye, J., Bouché, N., Cantalupo, S., Contini, T., Carollo, C. M., Caruana, J., Courbot, J.-B., Emsellem, E., Kamann, S., Kerutt, J., Leclercq, F., Lilly, S. J., Patrício, V., Sandin, C., . . . Wendt, M. (2016). Extended Lyman haloes around individual high-redshift galaxies revealed by MUSE. *Astronomy & Astrophysics*, *587*, A98. https://doi.org/10.1051/0004-6361/201527384

Wisotzki, L., Bacon, R., Brinchmann, J., Cantalupo, S., Richter, P., Schaye, J., Schmidt, K. B., Urrutia, T., Weilbacher, P. M., Akhlaghi, M., Bouché, N., Contini, T., Guiderdoni, B., Herenz, E. C., Inami, H., Kerutt, J., Leclercq, F., Marino, R. A., Maseda, M., . . . Wendt, M. (2018). Nearly all the sky is covered by Lyman- emission around high-redshift galaxies. *Nature*, *562*(7726), 229–232. https://doi.org/10.1038/s41586-018-0564-6

Xu, C., Dong, B., Stier, N., McCully, C., Howell, D. A., Sen, P., & Höllerer, T. (2022). Interactive segmentation and visualization for tiny objects in multi-megapixel images. *Proceedings of the IEEE/CVF Conference on Computer Vision and Pattern Recognition (CVPR)*, 21447–21452.

Xu, C., McCully, C., Dong, B., Howell, D. A., & Sen, P. (2021, June). *Cosmic-conn lco cr dataset* (Version 0.1.0). Zenodo. https://doi.org/10.5281/zenodo.5034763

Xu, C., McCully, C., Dong, B., Howell, D. A., & Sen, P. (2023). Cosmic-conn: A cosmic-ray detection deep-learning framework, data set, and toolkit. *The Astrophysical Journal*, *942*(2), 73. https://doi.org/10.3847/1538-4357/ac9d91

Yuma, S., Ouchi, M., Drake, A. B., Simpson, C., Shimasaku, K., Nakajima, K., Ono, Y., Momose, R., Akiyama, M., Mori, M., & Umemura, M. (2013). FIRST SYSTEMATIC SEARCH FOR OXYGEN-LINE BLOBS AT HIGH REDSHIFT: UNCOVERING AGN FEEDBACK AND STAR FORMATION QUENCHING. *The Astrophysical Journal*, *779*(1), 53. https://doi.org/10.1088/0004-637X/779/1/53

Zhang, H., Li, M., & Zaritsky, D. (2024, August). The Anisotropic Circumgalactic Medium of Sub-L* Galaxies [arXiv:2408.07102 [astro-ph]]. Retrieved August 17, 2024, from http://arxiv.org/abs/2408.07102

Zheng, X., Zhang, Y., & Röttgering, H. (2024). Alignments in the orientation of radio jets from AGN and their host galaxies. *Astronomy & Astrophysics*, *686*, A169. https://doi.org/10.1051/0004-6361/202347096

Zhu, G. B., Comparat, J., Kneib, J.-P., Delubac, T., Raichoor, A., Dawson, K. S., Newman, J., Yèche, C., Zhou, X., & Schneider, D. P. (2015). NEAR-ULTRAVIOLET SPECTROSCOPY OF STAR-FORMING GALAXIES FROM eBOSS: SIGNATURES OF UBIQUITOUS GALACTIC-SCALE OUTFLOWS. *The Astrophysical Journal*, *815*(1), 48. https://doi.org/10.1088/0004-637X/815/1/48